Technische Universität München
Physik Department
E19a Interfaces and Nonlinear Dynamics

Spatio-temporal pattern formation during the anodic electrodissolution of silicon in ammonium fluoride solution

Iljana Miethe

Vollständiger Abdruck der von der Fakultät für Physik der Technischen Universität München zur Erlangung des akademischen Grades eines

Doktors der Naturwissenschaften (Dr. rer. nat.)

genehmigten Dissertation.

Vorsitzender: Univ.-Prof. Dr. Roland Netz

Prüfer der Dissertation:

1. Univ.-Prof. Dr. Katharina Krischer
2. apl. Prof. Dr. Martin S. Brandt

Die Dissertation wurde am 25.02.2010 bei der Technischen Universität München eingereicht und durch die Fakultät für Physik am 22.04.2010 angenommen.

Contents

1 Introduction **1**

2 Anodic Electrodissolution of Silicon **5**

2.1 Potential Distribution 5

2.2 Chemical and Electrochemical Reactions 8

3 Experimental Setup **15**

3.1 Electrochemical Setup 15

3.2 Optical Setup 19

3.3 Chemical Pretreatment and Experimental Preparations 23

3.4 Data Acquisition and Online Processing 24

4 Correlations between Current Density and Ellipso-microscopic Signal **29**

4.1 Voltage Characteristics of Current Density and Ellipso-microscopic Signal . . 29

4.2 The Domain of Dry Oxide 31

4.3 Etch Back 33

4.4 Analytic Relationship between Ellipso-microscopic Signal and Current Density 35

4.5 Discussion and Outlook 39

5 Spatially Averaged Dynamics on p-type silicon **47**

5.1 Parameter Dependency 47

5.2 Oscillation Mechanism 59

5.3 Summary and Outlook 68

6 Spatially Averaged Dynamics on n-type silicon **71**

6.1 Impact of Illumination 71

6.2 Stirring 80

6.3 Discussion and Outlook 83

7 Spatial Pattern Formation **87**

7.1 Temporal Dynamics and Spatial Pattern Formation 88

7.2 Immobile, Labyrinthine Cluster Pattern 99
7.3 Moving Clusters and Coexistence of Oscillations with Different Frequencies . 107
7.4 Discussion and Outlook 112

8 Summary **115**

A Overview of Experiments **119**

B Glossary **123**

References **129**

Chapter 1

Introduction

Electrochemistry is a useful tool for the treatment of metal and semiconductor surfaces. The anodic electrodissolution of silicon not only allows for smoothing of the surface via electropolishing but also for the tailoring of specific optical and physical surface properties. For example, Rauscher *et al.* (1995) showed that by exploiting nonlinear instabilities smooth silicon surfaces can be prepared with a density of states much lower than when prepared by other methods. Lewerenz *et al.* (2009) produced thin film photovoltaic cells by combining a dynamic instability of the electrodissolution of silicon with chemical etching and electrochemical metal deposition.

The plethora of applications of the anodic electrodissolution of silicon has spurred many studies of the kinetics of the anodic oxidation of silicon with various electrochemical methods and techniques from surface science. Hence, a large body of fundamental studies exists. Yet, as stressed by Zhang (2001) in a monograph on the electrochemistry of silicon, "many details of the phenomena observed in the complex system of [the] silicon|electrolyte interface are still not understood".

In a typical electrodissolution experiment, a silicon wafer is immersed in a fluoride containing electrolyte and an anodic bias is applied. The positive potential of the silicon electrode leads to the electrochemical oxidation of the electrode. Simultaneously, the fluoride species from the electrolyte etch the silicon oxide formed electrochemically. Since holes at the silicon surface are necessary for the electrooxidation, an appreciable current density is only obtained with p-type silicon samples. In the case of n-type silicon it is necessary to illuminate the sample. With both types of silicon, current density oscillations are observed when a sufficiently high voltage is applied.

Although the current oscillations were already discovered more than fifty years ago (Turner, 1958), fundamental questions remained unsolved. The first one concerns the physical mechanism causing the oscillatory instability, the second one relates to the possibility that the temporal oscillations are accompanied by spatial pattern formation. Closely related to the second question is the origin of the synchronization across the spatially extended system, which results to observable macroscopic oscillations of the current density.

As for the physical mechanism, there are several suggestions in literature: (i) Lewerenz and Aggour (1993) ascribe the oscillations to stress that results from the difference in molecular volume between silicon and its anodic oxide. The stress induces cracks in the oxide that are responsible for the current flow and at which etching occurs preferentially. Oxidation stops when the oxide layer at bottom of the defect lines reaches a critical, so-called passivating thickness. In contrast, (ii) Lehmann (1996) related the current density oscillations to morphology changes of the silicon oxide with the oxide thickness and postulated that two oxide

morphologies are etched at different rates. (iii) In the so-called current burst model by Föll *et al.* (2006), field-dependent ionic breakthrough events were postulated. The breakthrough occurs at higher values of the electric field than the closure of the resulting pore, which introduces hysteresis in the system that causes the oscillatory instability. Only the latter of these three approach was cast in a mathematical model. The microscopic reaction steps were simulated with a Monte Carlo ansatz limiting the modeling to electrode areas of 100 times $100\,\mathrm{nm}^2$ (Foca *et al.*, 2007).

Thus, the existing models do not give an unambiguous picture of the oscillation mechanism. Gerischer and Lübke (1988) stated two decades ago that "the appearance of oscillations [...] can only be caused by nonlinear correlations between formation and dissolution of the oxide". Yet, a macroscopic model that can consolidate the existing microscopic approaches and is sufficient to explain the oscillations is still missing. Furthermore, up to the present the identification of bifurcations is missing. The determination of activator and inhibitor has yet to be accomplished. The synchronization of the local oscillators is a spatial phenomenon, therefore its analysis calls for a thorough investigation of possible pattern formation.

Spatially extended oscillatory systems are known to exhibit mesoscopic pattern formation as well investigated in the Belousov-Zhabotinsky reaction (Zhabotinsky, 1991) or the heterogeneously catalyzed oxidation of carbon monoxide on platinum (Ertl, 1991). Pattern formation during oscillatory electrochemical reactions has been investigated on metal working electrodes (*e.g.* Krischer, 2003), but not on semiconductor electrodes.

Up to the start of the present investigations the possible spatio-temporal pattern formation at the electrified silicon|oxide|electrolyte interface was essentially unexplored. Space averaging methods probing the oxide layer thickness have been used to investigate the temporal dynamics. The spatial patterning of the oxide layer was also investigated, but mostly with *ex situ* methods that lack a resolution of the temporal dynamics.

All theoretical considerations assume local, *i.e.* microscopic, oscillating domains and try to link macroscopic oscillations to the synchronization of these small domains. In this picture, damped oscillations, which are often observed when the potential is stepped from open-circuit potential to several volts, result from a synchronization of micro-oscillators due to the voltage step and subsequent desynchronization due to small local differences of the surface properties (*e.g.* Chazalviel and Ozanam, 1992; Grzanna *et al.*, 2000a,b). In the case of the current burst model, synchronization is ascribed to the concerted oxide formation at neighboring sites, which may be desynchronized by the reduction of the electric field across the oxide layer in the vicinity of an active pore (Carstensen *et al.*, 1999).

It has never been discussed that the electric potential at the interface might lead to macroscopic oscillations, as it is the case in a classical oscillatory reaction-diffusion system. The main objective of this thesis is to fill these gaps in the understanding of the oscillatory electrodissolution of silicon. Therewith this thesis lies at the intersection between semiconductor electrochemistry and nonlinear dynamics. Nonlinear dynamics is the study of the temporal evolution of systems governed by equations where superposition fails (Strogatz, 1994), *i.e.* whose activity is definable by a set of nonlinear equations, or relationships between active variables and dependent functions. This includes oscillations of different periodicities and chaos.

In this thesis, spatially and temporarily resolved *in situ* measurements of the oxide layer thickness are used to investigate the synchronization and the pattern formation during the electrodissolution of silicon. Measurements of the thickness of the anodic oxide layer on the silicon electrode using ellipsometry were successfully conducted by Lewerenz (1992) and Blackwood *et al.* (1992). Ellipso-microscopic surface imaging was used to study the dynam-

ics of pitting corrosion of stainless steel (Rotermund *et al.*, 1995). To monitor the oxide layer thickness dynamics during the electrodissolution of silicon, ellipso-microscopy is set up, adapted to the present purpose.

In Chapter 2 of this thesis, a description of the basic chemical and electrochemical concepts necessary for the understanding of the electrodissolution of silicon is given. This includes a summary of the state of the art of the understanding of the etch reactions, and of how the oxidation reactions depend on the applied potential. In Chapter 3, the components of the experimental setup are described in detail, as are sample preparation and data acquisition.

In Chapter 4, the response of the averaged ellipso-microscopic signal to potential scans and potential step experiments is discussed. The functional relation of this signal to the oxide layer thickness is investigated theoretically and oxide layer thickness and current density are correlated during oscillations in the case of p-type silicon. In Chapter 5, an analysis of the influence of parameters, such as the resistance in series with the silicon working electrode and the applied potential, on the averaged dynamics of p-type silicon, follows. Combining the results, an oscillation mechanism is derived.

In Chapter 6, the focus lies on spatially averaged oscillatory dynamics of n-type silicon. The influence of the illumination intensity on the stability and the form of the oscillations is studied and compared to the effect of stirring. In Chapter 7, spatial pattern formation is discussed for p-type silicon and n-type silicon. Firstly, it is shown how the type of pattern depends on applied potential, series resistance and illumination intensity. Secondly, observed cluster patterns are analyzed in more detail using a frequency demodulation technique (Lin *et al.*, 2000) and their origin is discussed from the perspective of nonlinear dynamics. Finally, the results obtained in this thesis are summarized in Chapter 8. The appendix compiles an overview of the experiments, and contains a detailed glossary and the references.

Chapter 2

Anodic Electrodissolution of Silicon

In this chapter, the basic mechanisms governing the electrodissolution of silicon in fluoride containing electrolyte are reviewed. The interfacial region between bulk silicon and the electrolyte is shaped by the interplay between oxide formation and etching. Silicon is electrochemically oxidized in the direction of the silicon bulk (Fig. 2.1a). Simultaneously, the oxidized species are chemically etched at their interface with the electrolyte (Fig. 2.1b). Depending on the relative rates of these two processes, an oxide layer may form on the electrode surface.

In Sec. 2.1, the potential distribution is examined at the biased silicon|electrolyte interface and silicon|oxide|electrolyte double interface. In Sec. 2.2, the dependency of oxidation and etching reactions on the applied voltage and the fluoride concentration are discussed.

2.1 Potential Distribution

The understanding of the potential distribution across the entire interface region, *i.e.* the region between bulk silicon and the bulk electrolyte, is vital for the understanding of the oxidation of silicon. Usually, experiments are conducted in a classical three electrode setup (Fig. 2.1c) under potential controlled conditions. Here, a voltage, U, is applied between the silicon working electrode and reference electrode. Current flows between working electrode and counter electrode. The voltage between working electrode and counter electrode, U_{pot}, is adjusted by the potentiostat in such a way that U is equal to a prescribed value.

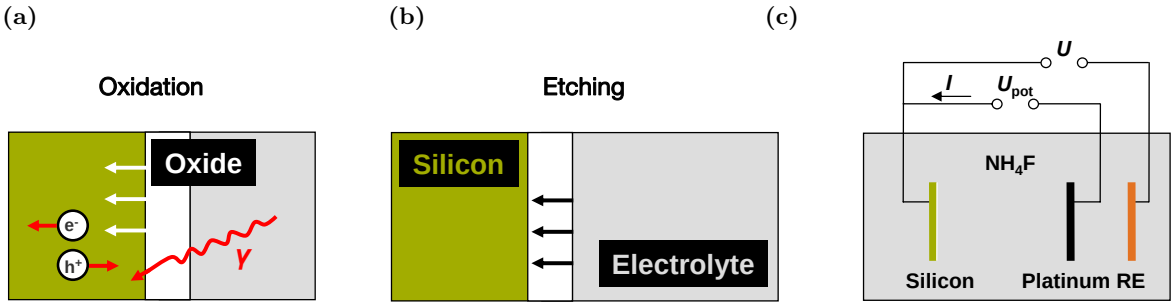

Figure 2.1: During the electrodissolution of silicon in fluoride containing electrolyte, silicon is simultaneously **(a)** electrochemically oxidized and **(b)** chemically etched. In the case of n-type silicon, illumination is necessary to create holes for the anodic oxidation. **(c)** A classic three electrode setup with working electrode (silicon), counter electrode (platinum) and reference electrode (RE) is used.

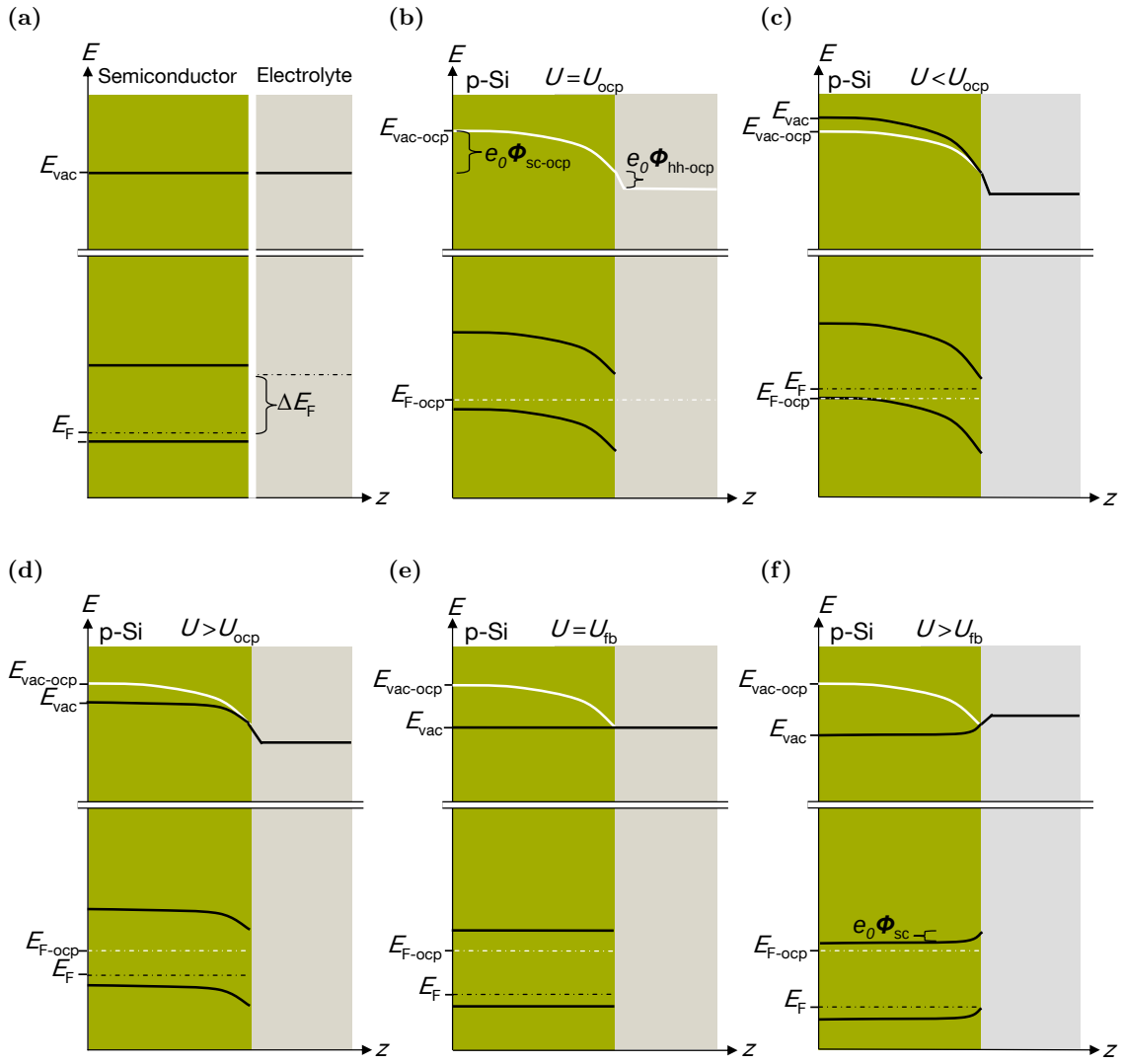

Figure 2.2: Energy-distance diagrams across the silicon|electrolyte interface. The vacuum energy is depicted at the top part of each panel. In the bottom part, the Fermi energy, the energy of the valence band and the energy of the conduction band across the p-semiconductor|electrolyte interface are shown: **(a)** before contact, **(b)** at open-circuit potential, **(c)** under a cathodic bias, **(d)** under a small anodic bias, **(e)** under flat band conditions, and **(f)** under a large anodic bias [adapted from Miethe (2004)]. Energy levels at open-circuit conditions are indicated in white.

Firstly, the potential distribution across the silicon|electrolyte interface under open-circuit conditions is discussed. Before silicon and the electrolyte are brought into contact, they have different Fermi levels (Fig. 2.2a). When immersing silicon into the electrolyte, their Fermi levels adjust, which leads to charge separation. The charge is distributed mainly across a space charge layer in the silicon, because its charge carrier concentration is lower than the one in the electrolyte. The formation of a space charge layer leads to the bending of valence and conduction band. The much thinner charged region which forms on the side of the electrolyte is referred to as Helmholtz double layer. It will be neglected in the following, because it is very thin and the potential drop across it is much smaller than the one across the space charge layer of silicon.

The band bending in the silicon electrode is accompanied by a dependency of the vacuum energy, E_{vac}, on position because the work functions neither in silicon nor in the electrolyte

are affected by their contact.

Fig. 2.2b illustrates the distribution of the electrical potential at open-circuit potential, U_{ocp}, where the sum of the potential drop in the semiconductor, $\Phi_{\mathrm{sc-ocp}}$, and in the Helmholtz layer, $\Phi_{\mathrm{hh-ocp}}$, is equal to ΔE_{F}:

$$-e_0 \left(\Phi_{\mathrm{sc-ocp}} + \Phi_{\mathrm{hh-ocp}}\right) = \Delta E_{\mathrm{F}} \tag{2.1}$$

Secondly, it is discussed how the potential distribution changes when a bias is applied. At open-circuit potential, the band bending leads to a depletion of the majority charge carriers of p-type silicon, *i.e.* holes, at the interface. Applying a cathodic bias increases Φ_{sc}, *i.e.* it leads to a further depletion of holes (Fig. 2.2c). In contrast, applying an anodic bias decreases the depletion of holes at the interface (Fig. 2.2d). At the flat-band potential, U_{fb}, the band bending disappears altogether (Fig. 2.2e):

$$-e_0 \left(U_{\mathrm{fb}} - U_{\mathrm{ocp}}\right) = \Delta E_{\mathrm{F}} \tag{2.2}$$

At applied voltages larger than U_{fb}, holes accumulate in the space charge region (Fig. 2.2f). This is also true for n-type silicon. Holes are minority charge carriers in the case of n-type silicon, therefore here holes accumulate in the so-called depletion or inversion layer at potentials larger than U_{fb}. In the case of n-type silicon, U_{fb} is larger than in the case of p-type silicon, because of the their different Fermi level.

In the presence of an oxide and a continuous current flow as in the experiments discussed below, the distribution of the potential drops is more complicated. In Fig. 2.3a an equivalent circuit for the anodically biased silicon|oxide|electrolyte double interface is shown (Morrison, 1980). The silicon electrode is composed of the bulk, a space charge layer, surface states and the back contact. The latter can be charged (C_{cont}) and has an ohmic resistance, R_{cont}. The bulk can be described by an ohmic resistor, R_{sample}. The surface states consisting of an ohmic resistor, R_{ss}, and a capacitor, C_{ss}, in series, are connected in parallel with the Faradaic impedance, Z_{F}, and the capacitor of the space charge layer, C_{sc}. An optional series resistance, R_{ser}, and the resistance of the electrolyte, R_{sol}, are connected in series with the semiconductor. Furthermore, the chargeable oxide layer and the Helmholtz layer are also connected in series each consisting of a resistor and a capacitor.

For the experiments in this thesis, several simplifications hold. The back contact is ohmic, therefore C_{cont} can be neglected. The Helmholtz layer capacity, C_{hh}, is usually very large compared to C_{sc} and C_{ox}, and is also neglected. R_{hh} is set to zero, because of the lack of an electrochemical reaction at the silicon oxide|electrolyte interface. The resulting simplified equivalent circuit is depicted in Fig. 2.3b with the contributions to R_{ext} resulting from the back contact of the silicon electrode, R_{cont}, the sample resistance, R_{sample}, the solution resistance, R_{sol}, and a possible external series resistor, R_{ser}. All ohmic resistances are combined to R_{ext}:

$$R_{\mathrm{ext}} = R_{\mathrm{ser}} + R_{\mathrm{cont}} + R_{\mathrm{sample}} + R_{\mathrm{sol}} \tag{2.3}$$

The additionally applied potential, $U - U_{\mathrm{ocp}}$, is divided into different potential drops:

$$U - U_{\mathrm{ocp}} = -\frac{\Delta E_{\mathrm{F}}}{e_0} + \Phi_{\mathrm{sc}} + \Phi_{\mathrm{hh}} + \Phi_{\mathrm{ox}} + \Phi_{\mathrm{ext}} \tag{2.4}$$

with:

$$\Phi_{\mathrm{ext}} = JAR_{\mathrm{ext}} \tag{2.5}$$

and Φ_{ox} being the potential drop across the oxide layer. This distribution is depicted in Fig. 2.4. $-\Delta E_{\mathrm{F}}/e_0$ is not a potential drop in the system, but rather a potential drop necessary to overcome the difference of the Fermi levels at open-circuit potential.

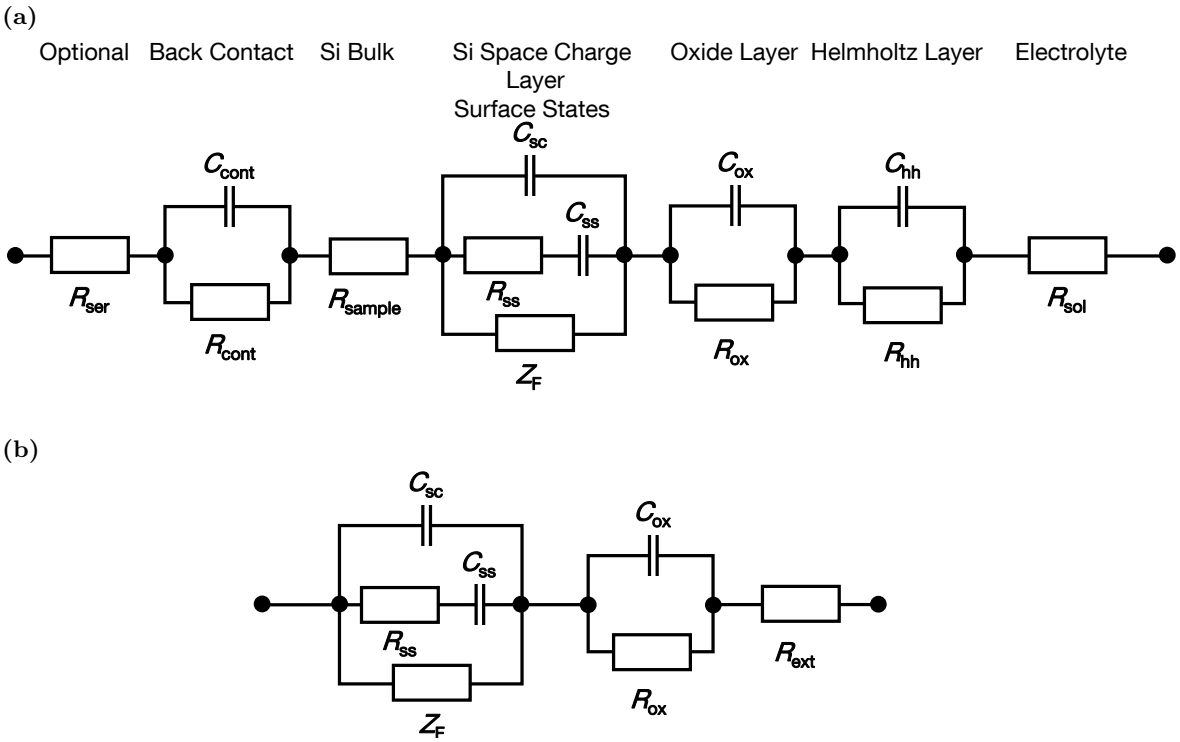

Figure 2.3: **(a)** Equivalent circuit for a biased semiconductor with an oxide layer in an electrolyte. (Morrison, 1980). **(b)** Simplified version of the equivalent circuit.

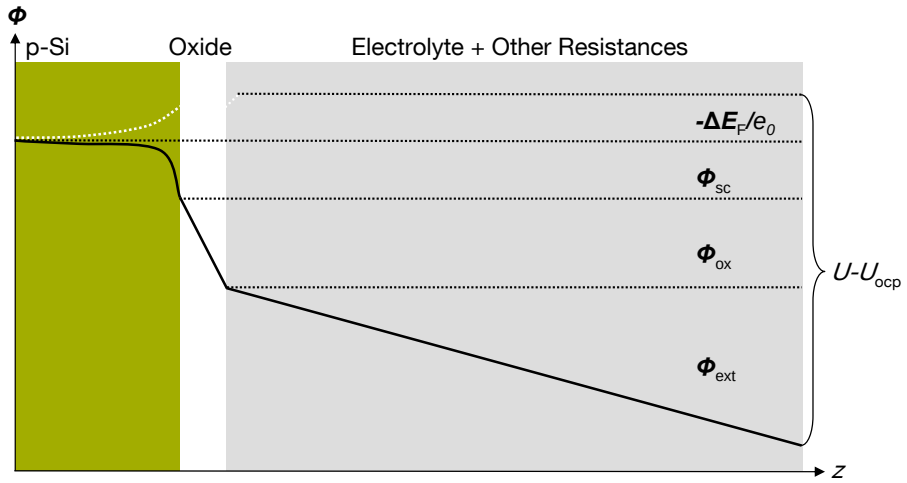

Figure 2.4: Distribution of the additionally applied voltage, $U - U_{\mathrm{ocp}}$, over the potential drop in the semiconductor, Φ_{sc}, the potential drop across the oxide layer, Φ_{ox}, and the potential drop across the ohmic resistances, Φ_{ext}. The potential drop necessary to overcome the difference of Fermi level energies at open-circuit potential, $-\Delta E_{\mathrm{F}}/e_0$, is drawn in white. The potential drops are not drawn to scale.

2.2 Chemical and Electrochemical Reactions

Fig. 2.5 depicts a typical $J - U$ characteristic for p-type silicon in an acidic, ammonium fluoride containing electrolyte. Under sufficient illumination, the $J - U$ characteristic of n-type silicon looks similar, apart from a shift in the applied voltage to more negative values (Eddowes, 1990) that results from a different flat band potential. Thus the $J-U$ characteristic

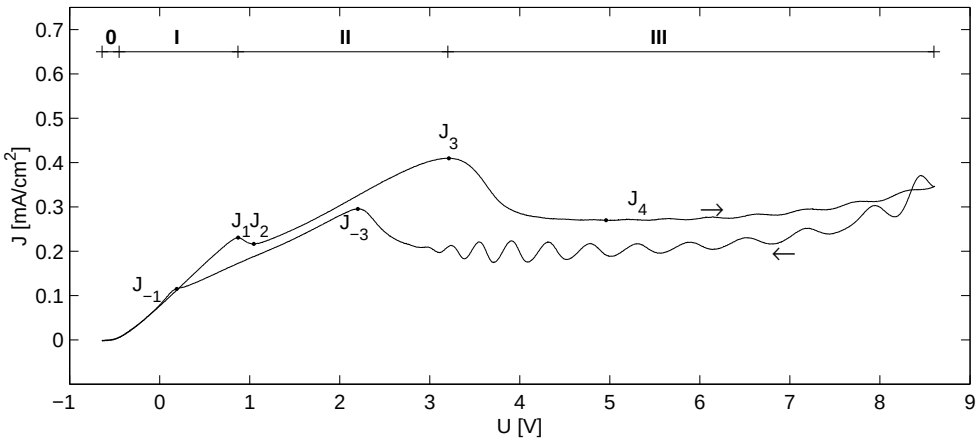

Figure 2.5: A typical $J-U$ characteristic during the anodic electrodissolution of silicon in acidic ammonium fluoride solution with the two characteristic peaks, J_1 and J_3, the minimum between them, J_2, and the current density plateau, J_4. This notation has been used in the literature for several years (*e.g.* Zhang, 2001; Lehmann and Föll, 1988). The two characteristic peaks during the backwards scan are indicated with J_{-3} and J_{-1}. The domains indicated at the top of the graph represent different reaction dynamics, namely **0**: hydrogen termination, **I**: porous silicon formation, **II**: 'wet' oxide formation, **III**: 'dry' oxide formation. Experimental conditions: p-type silicon with $R_{\text{ext}} = 100\,\text{k}\Omega$, $A = 4.91\,\text{mm}^2$, $c_{\text{NH}_4\text{F}} = 0.05\,\text{mol/l}$, pH = 2.4, scan rate, $v_{\text{scan}} = 10\,\text{mV/s}$.

is mainly determined by (electro)chemical rather than electrical properties of silicon. The $J-U$ characteristic is characterized by two current density peaks, J_1 and J_3, in the positive scan, and hysteresis between the forward and backward scan. It can be divided into four domains (Blackwood *et al.*, 1992) that are discussed after taking a closer look at the etching fluoride species in solution.

At a sufficiently high anodic bias, silicon oxide forms on the electrode surface. This is etched in acidic electrolyte solutions that contain ammonium fluoride. However, the etch rate depends on the fluoride concentration and the pH. The species active in the etching process are not F^- ions, but HF molecules and $HF_2{}^-$ ions (Cattarin *et al.*, 2000).

The dependency of the etch rate on the pH is exponential (Yahyaoui *et al.*, 2003), because the etch rate is affected by the dissolution equilibrium of ammonium fluoride. In dilute solutions, three fluoride species, $HF_2{}^-$, HF, and F^-, exist in equilibrium.

$$\text{HF} \rightleftarrows \text{H}^+ + \text{F}^- \tag{2.6}$$

$$\text{HF}_2{}^- \rightleftarrows \text{HF} + \text{F}^- \tag{2.7}$$

In Fig. 2.6, the concentration profiles of the three fluoride species using the equilibrium constants, $K_1 = 1.3\ 10^{-3}$ mol/l, and $K_2 = 1.04\ 10^{-1}$ mol/l (Judge, 1971) for reactions (2.6) and (2.7), respectively, are shown as a function of the pH of the electrolyte solution.

The etching chemistry depends on the type of oxidized silicon present on the electrode surface. The $J-U$ characteristic in Fig. 2.5 reflects the interplay between electrochemical oxidation and chemical dissolution steps. In domain **0**, no current density is observed. Silicon is not oxidized in this domain, therefore no etching takes place.

Below the critical current density, J_1, and at low U, silicon dissolution is divalent in domain **I** (Memming and Schwandt, 1966) where silicon electrooxidation is assisted by fluoride and involves hole capture and electron injection:

$$\text{Si} + 2\text{F}^- + \nu_{\text{cap}} h^+ \longrightarrow \text{SiF}_2 + \nu_{\text{inj}} e^- \tag{2.8}$$

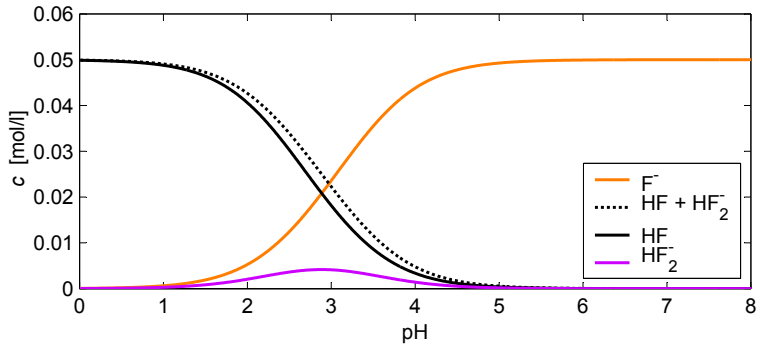

Figure 2.6: Concentration of $HF_2{}^-$, HF, and F^-, as a function of the pH in an electrolyte solution with an ammonium fluoride concentration, $c_{NH_4F} = 0.05$ mol/l [from Miethe (2004)].

with ν_{cap} being the number of captured holes, and ν_{inj} being the number of injected electrons during the oxidation of one silicon atom. The dissolution valency, $\nu = 2$, being the sum of ν_{cap} and ν_{inj}, is a measure for the number of charges contributing to the current density per dissolving silicon atom.

The subsequent reaction steps with HF take place in solution (Memming and Schwandt, 1966):

$$SiF_2 + 2HF \longrightarrow SiF_4 + H_2 \tag{2.9}$$

$$SiF_4 + 2HF \longrightarrow H_2SiF_6 \tag{2.10}$$

The oxidation step (2.8) is rate determining and takes place at the silicon|electrolyte interface. The dissolution of silicon involving fluoride species leads to the formation of a porous silicon film, so-called porous silicon, on the electrode surface (*e.g.* Zhang *et al.*, 1989), because silicon is non-uniformly oxidized. The value of J_1 depends on the fluoride concentration.

At current densities larger than J_1, *i.e.* at higher U, silicon is oxidized involving hydroxide ions in a tetravalent mechanism (domain **II**):

$$Si + 4OH^- + \nu_{cap}h^+ \longrightarrow Si(OH)_4 + \nu_{inj}e^- \tag{2.11}$$

$$Si(OH)_4 \longrightarrow SiO_2 + H_2O \tag{2.12}$$

with $\nu = 4$.

A thin layer of so-called 'wet' oxide, is formed on the electrode containing a high percentage of silicon hydroxide (Ozanam and Chazalviel, 1993). This can presumably be attributed to an etch rate slower than reaction (2.11) and faster than reaction (2.12). Beneath the 'wet' oxide layer the surface is electropolished. The 'wet' oxide layer serves as a means to limit the mass transport to the silicon surface, which is a prerequisite for electropolishing (Landolt, 1987).

According to Cattarin *et al.* (2000) the following minimum set of etch reactions can be formulated:

$$SiO_2 + 6HF \longrightarrow SiF_6{}^{2-} + 2H^+ + 2H_2O \tag{2.13}$$

$$SiO_2 + 3HF_2{}^- + H^+ \longrightarrow SiF_6{}^{2-} + 2H_2O \tag{2.14}$$

$$SiO_2 + 2HF + 2HF_2{}^- \longrightarrow SiF_6{}^{2-} + 2H_2O \tag{2.15}$$

with the etch rate of HF_2^- being four times higher than that of HF (Judge, 1971).

At applied voltages higher than $U(J_3)$ a passivating 'dry' oxide layer forms on the surface that contains a considerably lower silicon hydroxide percentage than 'wet' oxide (Ozanam and Chazalviel, 1993). It can be assumed that as the overall oxidation rate increases, also more silicon oxide is formed (reaction (2.12)). According to Schmidt and Ashner (1971), the etch rate depends on the concentration of the hydroxyl ions in the oxide layer. A passivating oxide layer is formed on the electrode surface (Eddowes, 1990), because the hydroxyl ion concentration decreases with increasing oxide layer thickness. In this domain (**III**) oscillations are observed.

In the description of the mechanism above, $\nu = 4$ was assumed, however Eddowes (1990) showed that ν is actually lower than 4, even for high U. In the case of p-type silicon, ν is approximately 3.6 and in the case of n-type silicon, ν is even smaller, namely 2.2. This is due to the reaction of a partially oxidized silicon species with protons, leading to hydrogen evolution (Blackwood *et al.*, 1992):

$$Si(OH)_2 + 2H_2O \longrightarrow Si(OH)_4 + H_2 \tag{2.16}$$

In summary, the $J - U$ characteristic reflects the oxidation chemistry for different anodic applied voltages. In domain **0**, the surface is hydrogen terminated, because the overpotential necessary for anodic oxidation has not been reached. In domain **I**, silicon is divalently dissolved according to reaction (2.8). At the first characteristic peak, J_1, the fluoride concentration becomes too small to support divalent silicon dissolution. Subsequently, in domain **II**, a 'wet' oxide layer is tetravalently formed according to reaction (2.11).

At the second characteristic peak, J_3, the high oxidation rate leads to the formation of a passivating oxide layer, *i.e.* 'dry' oxide. The ion conductivity of this oxide, more precisely its conductivity for hydroxide ions and oxygen ions, O^{2-}, is low. Hence, in domain **III** most of the applied voltage drops across the oxide and the migration of ions through the silicon oxide layer becomes rate determining. Therefore, the current density attains a plateau, J_4.

Chazalviel *et al.* (1992) showed that in the case of p-type silicon without an additional series resistor no sustained current density oscillations are observed. Time series at a constant applied voltage exhibited oscillatory transients, but eventually the current density became stationary. This suggests that the steady state is a focus. Adding a series resistance of at least 8.25 kΩ led to time series of sustained current density oscillations upon a small perturbation of the system (Fig. 2.7).

As can be seen in Fig. 2.5, current density oscillations are observed also in the $J - U$ characteristic. They are prominent during the backward scan, where the current density is lower than on the forward scan. Furthermore, the characteristic peaks, J_{-1} and J_{-3}, appear at voltages 1 V lower than their equivalent peaks during the forward scan.

In this thesis, the focus is on understanding the origin of the current density oscillations, therefore the oxidation of silicon in domain **III** is discussed in the following in more detail. Part of the oxidation current results from hole capture of silicon atoms in a low oxidation state, and the remaining part from electron injection of partly oxidized silicon species. The rate of hole capture, in turn, depends on the existence of holes in the valence band of the semiconductor. The first oxidation step consists of a silicon atom capturing a hole:

$$Si + h^+ + OH^- \longrightarrow Si(OH) \tag{2.17}$$

with hydroxide ions migrating through the oxide layer to the silicon|oxide interface (Matsumura and Morrison, 1983). The first hole capture step is assumed to be followed by electron injection from the partially oxidized species, Si(OH), into the conduction band of the

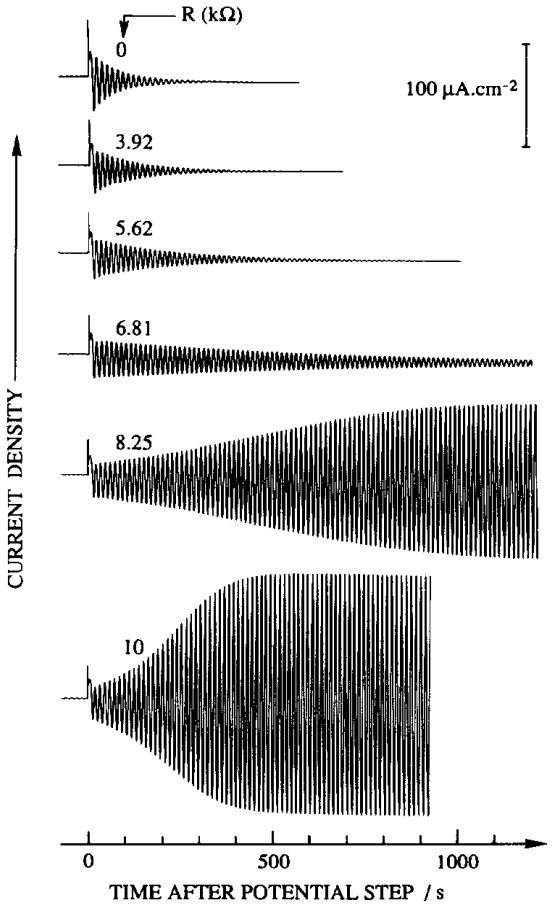

Figure 2.7: Current transients observed after a +100 mV perturbation to a steady state at $U - JAR_{\text{ser}} = 3\,\text{V}$. The value of R_{ser} [kΩ] is indicated next to the different curves. As R_{ser} is increased, damped oscillations change to sustained oscillations [from Chazalviel *et al.* (1992)]

semiconductor:

$$\text{Si(OH)} + \text{OH}^- \longrightarrow \text{Si(OH)}_2 + e^- \tag{2.18}$$

The partially oxidized species, Si(OH)_2, either reacts with water causing the formation of hydrogen according to reaction (2.16), or injects two further electrons according to:

$$\text{Si(OH)}_2 + \text{OH}^- \longrightarrow \text{Si(OH)}_3 + e^- \tag{2.19}$$

$$\text{Si(OH)}_3 + \text{OH}^- \longrightarrow \text{Si(OH)}_4 + e^- \tag{2.20}$$

However, it is also possible that more than one hole capture step is involved in the anodic oxidation of silicon. The exact mechanisms of electron injection and hole capture are not yet known.

If p-type silicon is used, holes are readily available at sufficiently high anodic bias, because they constitute the majority charge carriers. In contrast, n-type silicon samples require illumination. Upon illumination, a photon, γ, with an energy larger than the band gap of silicon is absorbed generating a pair of free charge carriers:

$$\gamma \longrightarrow h^+ + e^- \tag{2.21}$$

In summary, the four charges necessary to oxidize one silicon atom are split up between electrochemical oxidation and chemical oxidation, the latter being accompanied by hydrogen evolution. The charges necessary for electrochemical oxidation result from either hole capture or electron injection. This is reflected in the overall oxidation reaction:

$$\mathrm{Si} + \nu_{\mathrm{cap}} h^+ + \nu \mathrm{OH}^- + (4-\nu)\mathrm{H_2O} \longrightarrow \mathrm{Si(OH)_4} + \nu_{\mathrm{inj}} e^- + \frac{1}{2}(4-\nu)\mathrm{H_2} \tag{2.22}$$

In the case of n-type silicon the anodic oxidation is only possible under illumination, therefore the quantum efficiency, Y, is important. The estimation of Y makes it possible to discern captured holes from injected electrons in the current density. Assuming that each photon that hits the electrode surface generates an electron-hole pair and that each hole generated by a photon is used for silicon oxidation:

$$Y = \frac{N_{\mathrm{anod}}}{N_\gamma} \tag{2.23}$$

$$= \frac{\nu}{\nu_{\mathrm{cap}}} \tag{2.24}$$

with N_{anod} being the number of charge carriers contributing to the current density and N_γ being the number of photons hitting the electrode surface in the same time interval.

The hydrogen evolution efficiency, η_{H}, is the ratio of the number of protons reacting to give hydrogen, $N_{\mathrm{H^+}}$, to N_{anod}:

$$\eta_{\mathrm{H}} = \frac{N_{\mathrm{H^+}}}{N_{\mathrm{anod}}} \tag{2.25}$$

$$= \frac{4-\nu}{\nu} \tag{2.26}$$

In the case of p-type silicon, the dissolution valency corresponds to $\eta_{\mathrm{H}} = 11\%$ (Blackwood *et al.*, 1992). To oxidize one atom of p-type silicon, 0.2 molecules hydrogen are formed. In the case of n-type silicon, the dissolution valency corresponds to $\eta_{\mathrm{H}} = 82\%$ (Blackwood *et al.*, 1992). To oxidize one atom of p-type silicon, 0.9 molecules hydrogen are formed.

Chapter 3

Experimental Setup

The measurement of the spatio-temporal dynamics during the electrodissolution of silicon requires custom-built instrumentation. On the one hand, the experimental setup has to be air-tight and resistant to ammonium fluoride. On the other hand, the oxide layer on the electrode (1 to 50 nm) has to be imaged, data-processed and displayed together with the measured electrochemical quantities. In this chapter, the custom-made experimental setup and on-line data processing are described and explained.

An overview of the setup, consisting of the electrochemical cell and the ellipso-microscope, is depicted in Figs. 3.1a, 3.1b and Fig. 3.1c, respectively. The cell and the electrochemical setup are discussed in detail in Sec. 3.1. Ellipso-microscopy and the optical setup are described in Sec. 3.2. In Sec. 3.3, the pretreatment of the silicon samples and the cell are discussed. The synchronized acquisition of the electrochemical and optical data, and their display are described in Sec. 3.4.

3.1 Electrochemical Setup

The electrochemical cell has to meet the diverse demands of the experiment. It has to withstand the electrolyte containing hydrofluoric acid, allow for sample illumination, enable imaging of the sample, accommodate a three-electrode electrochemical setup, permit the removal and exclusion of oxygen from the electrolyte during the experiment and allow for precise positioning of the sample. In the following, the details of the electrochemical cell are discussed.

Fig. 3.1a shows an illustration of the entire cell including the silicon working electrode, the platinum counter electrode and the argon inlets for purging oxygen with argon from the electrolyte solution. In Fig. 3.1b, the interior of the cell is depicted, further including the reference electrode.

Most commercial and custom made electrochemical cells are made from glass. However, glass is not fluoride resistant. Teflon is fluoride resistant and is therefore used as the cell material. By comparison, Teflon can be easily handled in a workshop.

Optical glass windows are needed to permit undisturbed sample illumination and imaging. The cell was built in such a way that the optical glass windows could be exchanged upon damage from the electrolyte. Experiments were carried out in diluted ($0.05 - 0.2$ mol/l) solutions of ammonium fluoride. In some of the experiments, borosilicate glass (Linos) and for the remaining experiments, synthetic sapphire (Linos), are used. Fig. 3.2a shows a 3D image of the cell and holders for the optical glass windows.

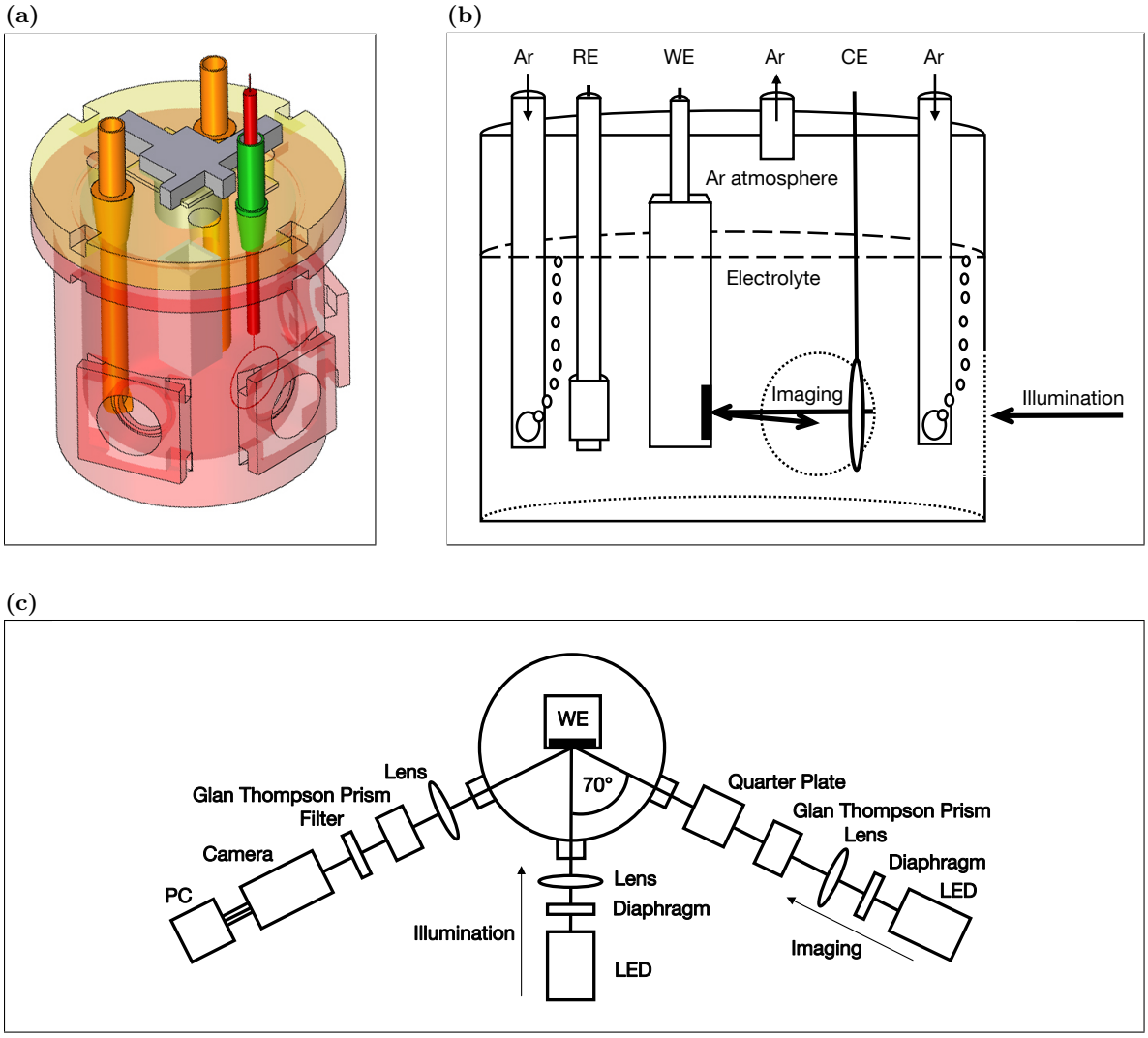

Figure 3.1: Custom-built instrumentation for the measurement of spatio-temporal dynamics during the electrodissolution of silicon. **(a)** The electrochemical cell with the silicon working electrode (white), the platinum counter electrode (red), and the argon inlets for purging oxygen from the electrolyte solution (orange). **(b)** Cross-section of the electrochemical cell including working electrode (WE), counter electrode (CE), reference electrode (RE) and argon inlets (Ar). The imaging and the illumination light paths are indicated with arrows. **(c)** The optical setup depicting the imaging light path at an angle of incidence, $\alpha_i = 70°$, and the sample illumination path at $\alpha_i = 0°$, both with light emitting diodes (LED).

A construction made of two o-rings and a holder is used to keep the optical glass window leak proof in each of the three bore in the Teflon cell (Fig. 3.2b). Four braces are used to keep each holder in place.

Cell Body

The angle between the first and middle, as well as between the middle and third optical window, is 70°. The middle window is used for perpendicular sample illumination. The other two windows are used for the imaging of the sample at an angle of incidence, $\alpha_i = 70°$.

The cell holds an electrolyte volume of 400 ml. The inside diameter and height are chosen

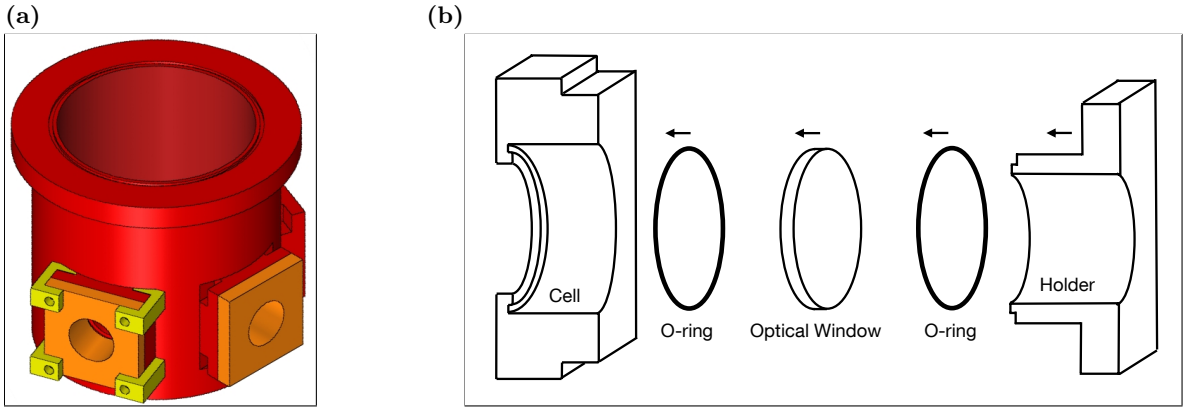

Figure 3.2: Integration of the optical glass windows into the cell body. **(a)** The Teflon cell body (red) with the optical windows held in place by holders (orange) and braces (yellow). **(b)** Two o-rings prevent the optical windows from leaking.

in such a way that all other parts of the electrochemical setup can be accommodated economically. A groove at the top of the cell contains a large o-ring to ensure air-tightness of the closed cell. The cell was cut from a block of Teflon (workshop of E19 in cooperation with the central workshop, Physik Department, Technische Universität München).

The Teflon cell is fixed inside a holder attached to a large z-table (lab jack) in the experimental setup. A magnetic Teflon coated stirrer can be introduced at the bottom of the cell. The continuously variable stirring device is embedded in the cell holder on the z-table.

Working Electrode

The silicon working electrode is constructed in such a way that a defined area of silicon is in contact with the electrolyte. Silicon with a single crystal surface (111) and a charge carrier density of 10^{15} cm^{-3}, *i.e.* a resistivity of 10-20 Ω cm in the case of p-type silicon (doped with phosphor) and of 1-2 Ω cm in the case of n-type silicon (doped with boron), is used.

It is important to ensure an ohmic contact at the back of the silicon wafer. A nonlinear and asymmetric behavior of the resistance, *i.e.* a Schottky contact, would lead to a loss of control over the system. The Fermi energy of the back contact metal has to be smaller than the Fermi energy of the n-type semiconductor and larger than the Fermi energy of the p-type semiconductor. The energy barrier, Φ_B, for the charge carriers at the contact is minimized by using an aluminum back contact in the case of n-type silicon ($\Phi_B = 0.50\,\text{eV}$) and a gold back contact in the case of p-type silicon ($\Phi_B = 0.34\,\text{eV}$) (Ruge, 1975). Both contacts are tested for ohmic behavior using samples with two metal contacts at the front of the wafer. The back contact metals were vapor phase deposited at the Helmholtz-Zentrum Berlin by first dipping the wafers into a solution of 2% hydrofluoric acid, then sputtering it with 400 nm aluminium (n-type silicon) or 330 nm gold (p-type silicon), and finally cutting it into small pieces with approximate areas of 30 to 50 mm^2.

During the experiments, the working electrode is attached to a holder on the multi-functional Plexiglas lid. It enables fine adjustment of the sample position and electrical contact to the potentiostat (Fig. 3.3a). Fig. 3.3c shows how the working electrode is assembled from a Teflon blank, a piece of wafer and epoxy sealing. A banana jack and gold wire are fitted to ensure electrical contact. A piece of wafer is glued to the gold wire that protrudes 0.1 mm from the hole on the front surface of the Teflon blank, with conducting silver epoxy glue (Plano

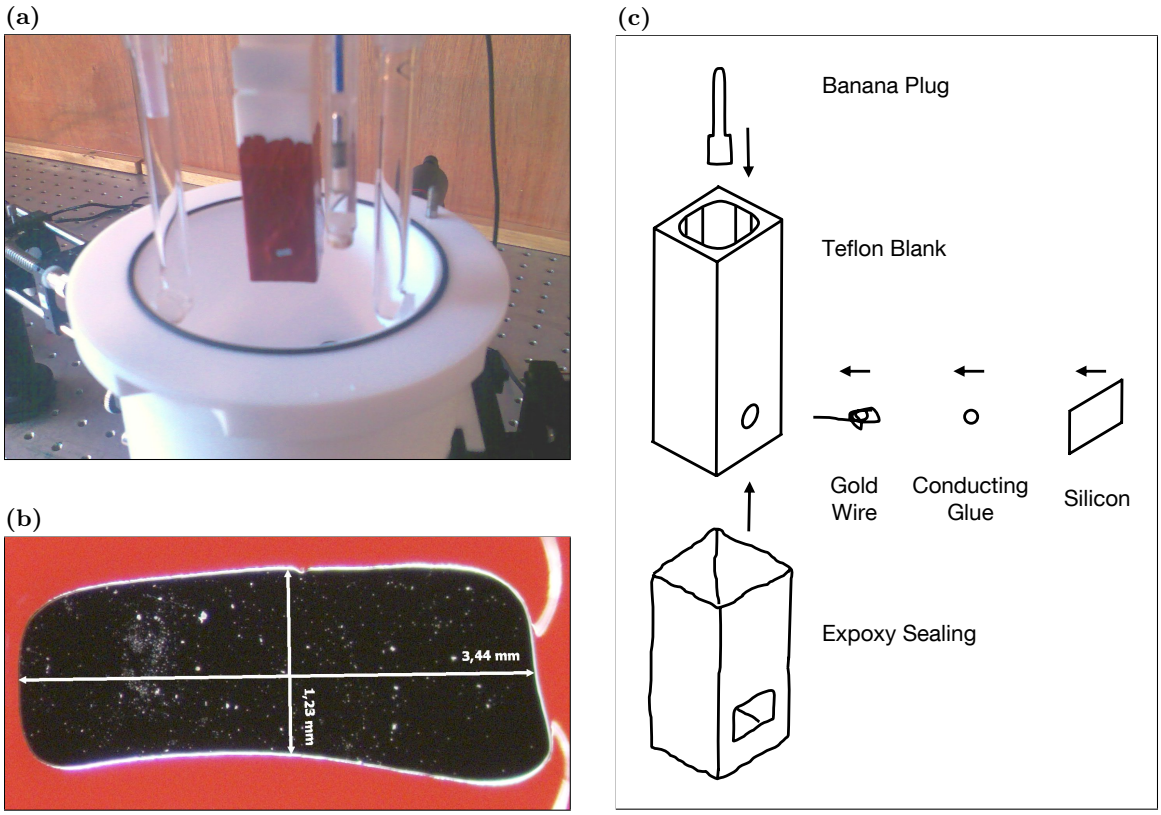

Figure 3.3: Construction of the working electrode. **(a)** Photograph of the working electrode attached to its holder on the Plexiglas lid. The lid with gas inlets, reference electrode and working electrode held above the cell. **(b)** Enlargement of the sealed sample area. **(c)** Illustration of the assembly of the working electrode. A banana jack and gold wire are fitted into the Teflon blank to ensure electrical contact. The wafer is glued to the gold wire with conducting silver epoxy glue. Finally, a layer of silicone rubber is applied with a brush.

GmbH). The wafer is thus positioned flat on the front surface of the Teflon blank. Silicone rubber, Scrintex 901 (Ralicks GmbH), seals the surface area of the electrode except what is intended to be in contact with the electrolyte. The sealing is applied with a small size, regular painting brush and is left for 4 to 6 h at room temperature to cross-link. A sample area of 4 to 10 mm^2 is left without sealing. Fig. 3.3b shows an enlargement of the sealed sample area. An overview of the electrode sizes used in the experiments can be found in Tab. A.1 (Appendix A).

Plexiglas Lid

The Plexiglas lid (Figs. 3.4a and 3.4c) fits air-tight onto the Teflon cell and is fastened to the cell with braces similar to those used to fix the optical glass windows. The electrolyte solution is degassed using argon entering the electrolyte through glass frits. During the experiment, the gas enters the cell above the electrolyte to avoid argon bubbles obstructing the camera image and ensuring a small argon overpressure to prevent air from entering the cell. A "bubbler" filled with water is used as gas outlet. The glassware was made by J. Höhn (Glasbläserei, Garching). One of the braces includes a holder for fastening a charge-coupled device (CCD) sensor on top of the Plexiglas lid. This CCD sensor monitors the sample illumination during the experiments.

The working electrode holder on the underside of the Plexiglas lid is connected to a vernier adjustment unit on top of the lid. With this unit, the sample can be tilted and rotated (Fig. 3.4b). The tilt angle is adjusted with a bolt pressing against the vertical metal rod in the center of the lid. This rod is fitted into a rubber septum and fixed at a point just above the lid. The working electrode at the bottom of the rod can be tilted towards and away from the middle window. The tilt adjustment rotates the working electrode around the vertical axis. The vernier adjustment unit enables the adjustment of the sample position from the outside of the cell during the experiments. The mechanics of the vernier adjustment unit were designed in cooperation with M. Haß and J. Dörbecker (E19 workshop). The technical drawings were prepared by G. Roth. The entire cell can be moved in the horizontal direction by moving the z-table, adjusting the sample position in the z-direction.

A banana connection is used to keep the electrode from sliding from the holder and to ensure an electrical connection. The banana plug is installed in the working electrode and a banana jack in the holder. An electrical cable passing through the hollow axis to the BNC connector at the top of the vernier adjustment allows for its connection to the potentiostat.

Vernier adjustment necessary to focus the imaging light beam on the camera enables tilting, rotating, and vertical movement of the sample, as shown in Fig. 3.4a.

Potential Control

A standard three electrode setup is used consisting of the working electrode, a counter electrode and a reference electrode. All three electrodes are attached to the multi-functional Plexiglas lid (Figs. 3.3a and 3.4c). A saturated $Hg|Hg_2SO_4$ reference electrode is inserted through the lid into the electrolyte.

The counter electrode is made from 0.5mm thick, 50cm long, 99.99% platinum wire (Chempur) fused into a hollow glass rod. A short piece of platinum is left at one end of the rod for connection to the potentiostat. The long piece at the other side is woven into a ring electrode with a diameter a little larger than the windows in the electrochemical cell. The glass rod is fitted into a holder that is attached to the lid via ground glass joints. The counter electrode ring is positioned between illumination window and sample.

The anodic potential is applied using a FHI-2740 potentiostat that was built by the electronic laboratory of the Fritz-Haber-Institut in Berlin by M. Dinzel-Graef, P. Zilske and G. Heyne. The potentiostat regulates the current between working electrode and counter electrode in such a way that the voltage between working electrode and reference electrode is kept constant or changes with time according to a voltage ramp.

3.2 Optical Setup

Fig. 3.1c shows an overview of the ellipso-microscopic optical setup, consisting of two light paths. The working electrode is positioned vertically in the middle of the cell facing the middle window. This window is used for the illumination light path. The other two windows are used for imaging. In this imaging light path at an angle of incidence of 70°, the temporal variations of the spatial distribution of the oxide thickness on the silicon are monitored by analyzing the change of the ellipse of the light upon reflection from the sample.

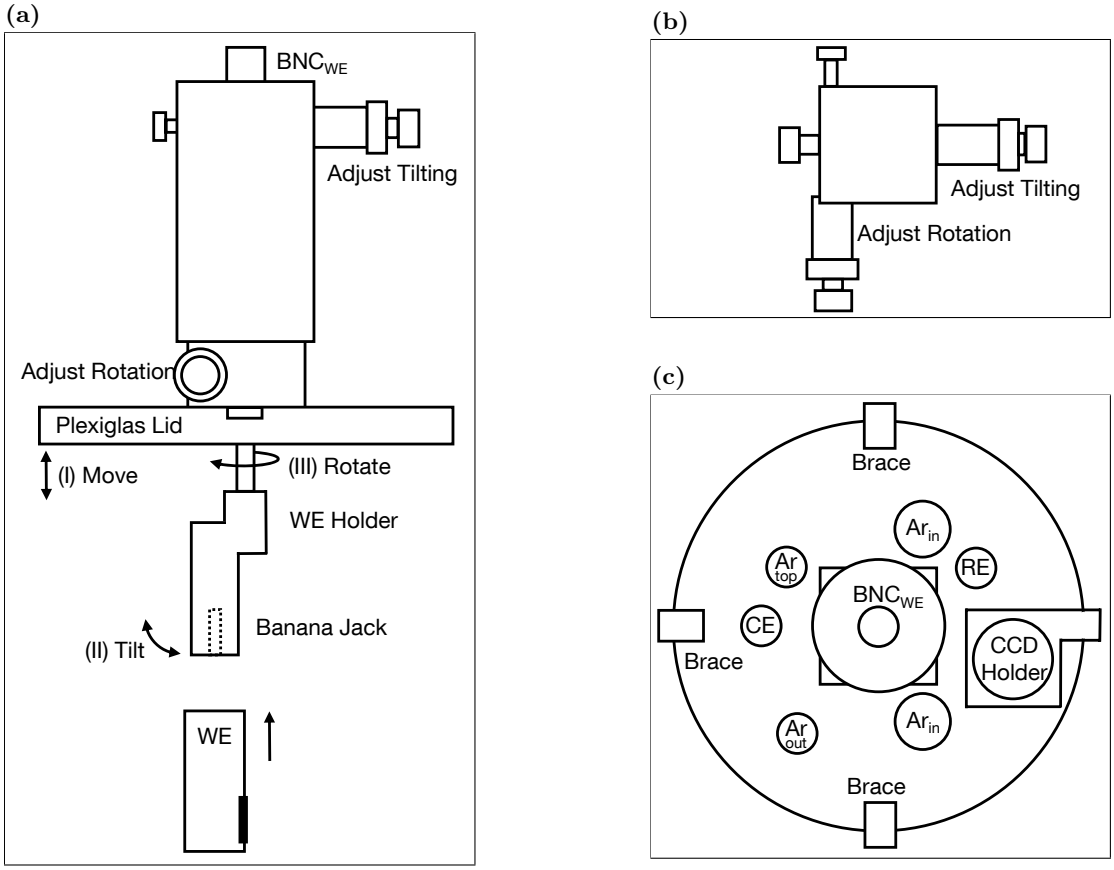

Figure 3.4: Multi-functional Plexiglas lid and vernier adjustment unit. **(a)** Side view of the multi-functional Plexiglas lid with the vernier adjustment on top with set screws for tilting and rotation adjustment. The working electrode is attached to its holder via a banana jack-plug connection. The sample can be moved vertically, (I), in the z-direction with a z-table (not depicted), tilted out of a position perpendicular to the lid, (II), and rotated around the vertical axis, (III). **(b)** Top view of the vernier adjustment unit. **(c)** Top view of the Plexiglas lid with braces to fit the lid air-tight on the cell. One of the braces is exchanged for a bracing device that is used for fastening a CCD sensor on top of the lid. Bore holes in the lid are used for the ground glass joints of reference electrode (RE), counter electrode (CE), argon inlets into the electrolyte (Ar_{in}), argon inlet on top of the electrolyte (Ar_{top}) and an argon outlet (Ar_{out}).

Illumination

Sample illumination is necessary in the case of n-type silicon, since holes, which are the minority charge carriers, are necessary for the anodic oxidation of silicon. A diaphragm and a lens with a focal length of 50 mm are used to homogeneously focus light from a red (typical wavelength $\lambda_{illu} = 630$ nm) light emitting diode, LED (Linos), onto the electrode. The LED is fixed in a micro bank holder (Linos).

The intensity of the sample illumination is measured with a CCD sensor fastened to the top of the Plexiglas. An amplification circuit with a defined output resistance provides a defined load to the CCD sensor. The circuit diagram of the amplification circuit is described in more detail by Heinrich (2009). Thus the sensor is supplied with a stable voltage proportional to the sample illumination. A linear dependency of the light power density, L, on the voltage of the CCD sensor, U_{ccd}, is assumed. L is calculated from the difference between the maximum,

$U_{\mathrm{ccd}}^{\mathrm{max}}$, and the minimum, $U_{\mathrm{ccd}}^{\mathrm{min}}$, of the photo detector voltage:

$$L = L^{\mathrm{max}} \frac{U_{\mathrm{ccd}} - U_{\mathrm{ccd}}^{\mathrm{min}}}{U_{\mathrm{ccd}}^{\mathrm{max}} - U_{\mathrm{ccd}}^{\mathrm{min}}} \tag{3.1}$$

The maximum light power density of the red LED, L^{max}, was measured with a calibrated Watt-meter, LaserCheck (Coherent). The measurement was conducted inside the cell without electrolyte. $L^{\mathrm{max}} = 1.53\,\mathrm{mW/cm^2}$ with an estimated error of 5%. $U_{\mathrm{ccd}}^{\mathrm{max}}$ and $U_{\mathrm{ccd}}^{\mathrm{min}}$ are measured again for each experiment to account for the influence of light pollution from the surroundings.

During the experiments, a blue LED is used to image the electrode as will be discussed below. The contribution of the blue LED to L is negligibly small. It has less power than the red LED by specification. Its intensity is further reduced by several factors: by being operated at only 40% of maximum power; by the polarizer and the quarter plate in its light path; by the light approaching the sample at an angle of incidence of 70° (66% reduction). The total light power intensity from the blue LED does not exceed $10\,\mu\mathrm{W/cm^2}$, which is small compared to the estimated error of L, $\Delta L = 76\,\mu\mathrm{W/cm^2}$.

Ellipso-microscopic Imaging

The optical components in the imaging and the illumination light path are depicted in Fig. 3.1c. Elliptically polarized light approaches the silicon electrode at an angle of incidence close to the Brewster angle. The ellipticity of the light is changed upon reflection at the working electrode, whereby the change of polarization sensitively depends on the thickness of the oxide layer. The reflected light is passed through an analyzer and an imaging lens, finally reaching the camera. The intensity image on the camera mirrors local changes of oxide thickness and refractive indices at the interface. A similar setup has been used by Rotermund *et al.* (1995) in a different system.

The ellipso-microscopic light path is built with optical components assembled in a microbench system from Linos. Light with a typical wavelength of $\lambda_{\mathrm{imag}} = 470\,\mathrm{nm}$ from a blue LED (HighLED, Linos) is homogeneously focused on the electrode using a lens with a focal length of 50 mm and a diaphragm. Before reaching the sample, it is linearly polarized with a Glan Thompson prism positioned at an angle between the transmission axis and the plane of incidence, α_{P}. Circularly polarized light is obtained with a zeroth order quarter plate ($\lambda = 488\mathrm{nm}$) positioned at an angle between the fast axis and the plane of incidence, $\alpha_{\mathrm{C}} = 45°$.

After being reflected from the electrode surface, the light is imaged onto the camera (JAI CV-A50) with an imaging lens (100 mm). The enlargement thus obtained is 2.5. The resolution is limited by the pixel size of the camera and amounts to $25\,\mu\mathrm{m}$ in the x-direction and $10\,\mu\mathrm{m}$ in the y-direction. Before reaching the camera, the light passes the analyzer, a Glan Thompson prism, positioned at an angle between the transmission axis and the plane of incident, α_{A}. In this way, differences in the polarization state are converted to intensity differences. The red filter, DCRed (Linos), prevents stray light from the red LED reaching the camera. Polarizer, quarter plate and analyzer were bought from B. Halle Nachfl. GmbH, Berlin.

Brewster Angle

To obtain the largest possible contrast when imaging the oxide thickness, the angle of incidence, α_{i}, is chosen close to the Brewster angle, α_{B}, where the ratio of the absolute values of parallel to perpendicular component of the reflection coefficient, $|\hat{r}_{\mathrm{p}}|/|\hat{r}_{\mathrm{s}}|$, is minimal and the contrast maximal.

For a two-layer system, $\hat{r}_\mathrm{p}$, vanishes at $\alpha_\mathrm{i} = \alpha_\mathrm{B}$. All light is transmitted and none is reflected, because it cannot be radiated by the oscillating electric dipoles at the interface. Electromagnetic radiation emitted from the oscillating dipoles in the second medium is responsible for reflection. Emission is not possible in the direction of the dipole oscillation, which would be the direction of reflection in the case of p-polarized light at α_B. Light with perpendicular polarization, *i.e.* s-polarized light, is reflected at all angles of incidence, because it oscillates parallel to the interface. For a one-interface system, α_B can thus be calculated with Snell's law (Hecht, 2002):

$$\alpha_\mathrm{B} = \frac{n_2}{n_1} \tag{3.2}$$

with n_1 and n_2 being the refractive indices for the two domains separated by the interface.

For a film covered surface, such as silicon oxide on silicon in a water based electrolyte, $\hat{r}_\mathrm{p}$ does not reach zero except for very thin oxide layers. This is due to several reflections and transmissions at the two interfaces. α_B is defined as the minimum of $|\hat{r}_\mathrm{p}|/|\hat{r}_\mathrm{s}|$. The reflection coefficients in a two-interface system are calculated with the Drude equation (Born and Wolf, 1964) representing the phase delay due to the film on the surface (Muller, 1991):

$$\hat{r}_\mathrm{p} = \frac{\hat{r}_{\mathrm{p-H_2O|SiO_2}} + \hat{r}_{\mathrm{p-SiO_2|Si}}\ \exp(-iD)}{1 + \hat{r}_{\mathrm{p-H_2O|SiO_2}}\ \hat{r}_{\mathrm{p-SiO_2|Si}}\ \exp(-iD)} \tag{3.3}$$

$$\hat{r}_\mathrm{s} = \frac{\hat{r}_{\mathrm{s-H_2O|SiO_2}} + \hat{r}_{\mathrm{s-SiO_2|Si}}\ \exp(-iD)}{1 + \hat{r}_{\mathrm{s-H_2O|SiO_2}}\ \hat{r}_{\mathrm{s-SiO_2|Si}}\ \exp(-iD)} \tag{3.4}$$

$$\tag{3.5}$$

with

$$D = \frac{4\pi}{\lambda_\mathrm{imag}} z_\mathrm{L} \hat{n}_{\mathrm{SiO_2}} \cos\alpha_\mathrm{t} \tag{3.6}$$

using the wavelength of the reflected light in vacuum, λ_imag, the thickness of the oxide layer, z_L, the refractive index of silicon oxide, $\hat{n}_{\mathrm{SiO_2}}$, and the angle of transmission at the first interface α_t. The Fresnel coefficients for the interface between the electrolyte and silicon oxide, $\hat{r}_{\mathrm{p-H_2O|SiO_2}}$ and $\hat{r}_{\mathrm{s-H_2O|SiO_2}}$, and for the interface between silicon and its oxide $\hat{r}_{\mathrm{p-SiO_2|Si}}$ and $\hat{r}_{\mathrm{s-SiO_2|Si}}$, are obtained from the Fresnel equations (Muller, 1991):

$$\hat{r}_{\mathrm{p-H_2O|SiO_2}} = \frac{\hat{n}_{\mathrm{SiO_2}} \cos\alpha_\mathrm{i} - \hat{n}_{\mathrm{H_2O}} \cos\alpha_\mathrm{t}}{\hat{n}_{\mathrm{H_2O}} \cos\alpha_\mathrm{t} + \hat{n}_{\mathrm{SiO_2}} \cos\alpha_\mathrm{i}} \tag{3.7}$$

$$\hat{r}_{\mathrm{p-SiO_2|Si}} = \frac{\hat{n}_{\mathrm{Si}} \cos\alpha_{\mathrm{i}*} - \hat{n}_{\mathrm{SiO_2}} \cos\alpha_{\mathrm{t}*}}{\hat{n}_{\mathrm{SiO_2}} \cos\alpha_{\mathrm{t}*} + \hat{n}_{\mathrm{Si}} \cos\alpha_{\mathrm{i}*}} \tag{3.8}$$

$$\hat{r}_{\mathrm{s-H_2O|SiO_2}} = \frac{\hat{n}_{\mathrm{H_2O}} \cos\alpha_\mathrm{i} - \hat{n}_{\mathrm{SiO_2}} \cos\alpha_\mathrm{t}}{\hat{n}_{\mathrm{H_2O}} \cos\alpha_\mathrm{i} + \hat{n}_{\mathrm{SiO_2}} \cos\alpha_\mathrm{t}} \tag{3.9}$$

$$\hat{r}_{\mathrm{s-SiO_2|Si}} = \frac{\hat{n}_{\mathrm{SiO_2}} \cos\alpha_{\mathrm{i}*} - \hat{n}_{\mathrm{Si}} \cos\alpha_{\mathrm{t}*}}{\hat{n}_{\mathrm{SiO_2}} \cos\alpha_{\mathrm{i}*} + \hat{n}_{\mathrm{Si}} \cos\alpha_{\mathrm{t}*}} \tag{3.10}$$

with $\hat{n}_{\mathrm{Si}}$ being the refractive index of silicon and $\hat{n}_{\mathrm{H_2O}}$ being the refractive index of water used for the electrolyte solution. α_i is the angle of incidence on the silicon oxide covered electrode. $\alpha_\mathrm{t} = \alpha_{\mathrm{i}*}$ is the first angle of transmission and therefore the angle of incidence at the silicon|oxide interface. $\alpha_{\mathrm{t}*}$ is the second angle of transmission. The latter two are calculated with Snell's law.

α_B is estimated by calculating and plotting $|\hat{r}_\mathrm{p}(\alpha_\mathrm{i})|$, $|\hat{r}_\mathrm{s}(\alpha_\mathrm{i})|$ and $|\hat{r}_\mathrm{p}(\alpha_\mathrm{i})|/|\hat{r}_\mathrm{s}(\alpha_\mathrm{i})|$ versus α_i, respectively. The reflective coefficients are calculated using Eqs. (3.3) and (3.10) and plotted in Fig. 3.5. An angle of incidence, $\alpha_\mathrm{i} = 70°$, is used for the optical setup, because it is the position of the minimum of the ratio of the reflection coefficients.

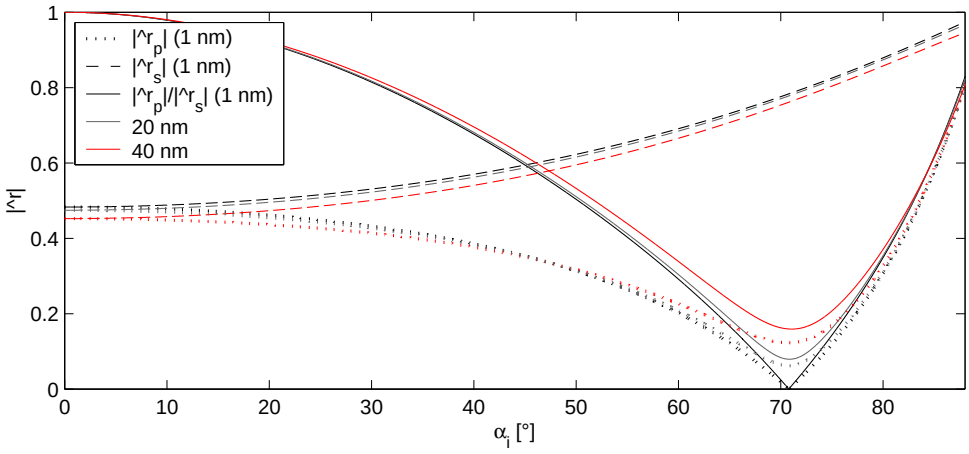

Figure 3.5: The Fresnel coefficients for a reflection of electromagnetic radiation with $\lambda_{\mathrm{imag}} = 470\,\mathrm{nm}$ at the silicon|oxide|silicon double interface as a function of the angle of incidence, α_{i}, for three different layer thicknesses of the oxide: 1 nm (black), 20 nm (gray) and 40 nm (red). Fresnel coefficients in p-direction are dotted, in s-direction are dashed and their quotient is drawn as a solid line. The following refractive indices were used for the calculations: $\hat{n}_{\mathrm{SiO_2}} = 1.46$, $\hat{n}_{\mathrm{Si}} = 3.85{+}0.02i$, $\hat{n}_{\mathrm{H_2O}} = 1.34$ Lewerenz *et al.* (1989).

3.3 Chemical Pretreatment and Experimental Preparations

All glassware used for the chemical pretreatment and during the experiment is cleaned with refluxing nitric acid (65%, Merck, extra pure). After 20 hours of steaming, all organic contaminations are oxidized and the glassware is rinsed with water. Ultra-pure water is produced with a combination of a Millipore Elix 5 and a Millipore Milli-Q Gradient A10 system.

The optical glass windows of the Teflon cell are exchanged for Teflon discs during the cleaning process. The cell is filled with 600 ml Caroic acid, consisting of one part 30% hydrogen peroxide (Merck, p.a.) and one part 95 – 97% sulfuric acid (Merck, p.a.). The cleaning solution is stirred in the cell for 10 hours and discarded. The cell is rinsed with water. In the meantime the optical windows are cleaned with n-isopropanol (Merck, p.a.). Finally, the windows are re-installed in the cell.

The working electrode is immersed in organic solvents and then in an etching solution prepared from 14 g ammonium fluoride (Merck, p.a) and 35 ml water. The whole procedure, including rinsing steps, is outlined in Tab. 3.1. The preparation method was adapted from the one used by Jakubowicz (2003). The chemical oxidation with Caroic acid is omitted to avoid undercutting under the epoxy sealing. No extra care is taken to purge oxygen from the water, used to prepare solutions. This is not necessary because the sample stays in the etching electrolyte solution for at least 60 minutes prior to starting the experiment, which removes a possible native oxide film on the sample.

The counter electrode is immersed in Caroic acid for 2 to 3 hours and subsequently rinsed with water. The reference electrode is rinsed with water immediately before inserting it into the electrolyte solution for the experiments.

The electrolyte solution is freshly prepared on the day of the experiment. For the standard solution, 0.927 g ammonium fluoride and 0.7 ml 96% sulfuric acid (Merck, ultra-pure) are dissolved in water to 500 ml. This leads to an ammonium fluoride solution with a concentration of 0.05 mol/l and a pH of 2.3. Solutions with higher concentrations and higher pH were prepared for some of the experiments (Tab. A.1 in Appendix A).

Duration [min]	Treatment
10.0	Immersed in acetone (100%, Merck p.a.)
0.1	Rinsed with ethanol (100%, Merck p.a.)
10.0	Immersed in ethanol
1.0	Rinsed with water
1.0	Dried with argon
10.0	Immersed in ammonium fluoride etching solution
1.0	Rinsed with water
1.0	Dried with argon

Table 3.1: Chemical pretreatment steps for the working electrode.

The pH is measured with pH testing strips (Lyphan): L653-8 (pH $1.8 - 3.2$) and L656-8 (pH $3.0 - 4.4$). They allow for a resolution of 0.2 units of the pH. Other solutions are prepared in the same way adjusting the concentration by adjusting the amount of ammonium fluoride, and adjusting the pH by adjusting the amount of sulfuric acid.

The Teflon cell is filled with the electrolyte solution to a level just above the optical windows. After assembling the cell, oxygen is purged from the electrolyte solution with argon for at least 60 minutes.

3.4 Data Acquisition and Online Processing

Different kinds of data are synchronously digitized, processed and ultimately saved. Fig. 3.6 shows an overview of the data flow. The camera images are digitized with the frame grabber, PCI-1405 (National Instruments). The signal for the current, a voltage from the potentiostat, the signal for the applied voltage, a voltage from the potentiostat, and the signal for the illumination light power density, a voltage from the CCD sensor, are digitized with the data acquisition board, PCI-6221 (National Instruments). An amplification circuit is used between CCD sensor and acquisition board, because a defined load for the CCD sensor is needed to prevent interference with the other signals.

A control code written in LabView 8.2 (National Instruments) manages the synchronized acquisition of all four signals. It also processes, displays and ultimately saves the data. The processed data is displayed on-line during data acquisition in the graphic user interface (GUI).

The camera can operate at a speed of 25 Hz. During each control loop, the chosen region of interest, ROI, of one frame is grabbed, loaded to the image buffer, processed and, when in recording mode, saved to the disc. Currently, processing and saving limit the maximum sampling rate to 5 Hz. Long time series of oscillations with long periods are recorded at lower sampling rates. A trigger signal from the frame grabber is used to initiate data acquisition at the acquisition board.

An image of the GUI of the acquisition software is displayed in Fig. 3.7. The parameter tab panel is used to adjust a variety of parameters for the display of the experimental data, including background subtraction and the representation of the camera image.

The image tab panel displays the camera image. Light is reflected from the electrode at $\alpha_\mathrm{i} = 70°$ and the camera is positioned perpendicular to the light beam. Due to this positioning, the image of the camera is compressed in the direction perpendicular to the plane of incident,

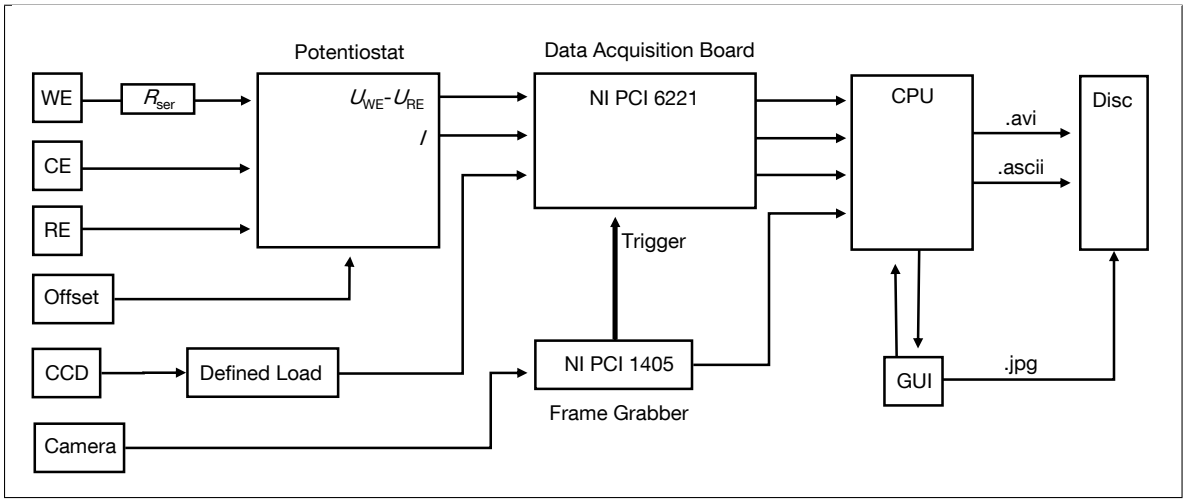

Figure 3.6: Overview of data production, acquisition and processing.

i.e. in the y-direction. The compression factor is $\cos\alpha_{\mathrm{i}} = 0.342$. Thus the size of the pixel in the y-direction was multiplied by an expansion factor of 3.

The data tab panel displays the time series of averaged quantities. Fig. 3.8a shows another tab that gives more insight into the spatio-temporal dynamics by displaying the temporal evolution of a cross section of the electrode. It is displayed together with the time series of the current, I, the applied voltage, U, the illumination signal, U_{ccd} and the averaged ellipsometric signal, $\overline{\xi}$. Other tabs display $I(U)$ and $\overline{\xi}(U)$ in a representation useful for cyclic voltammograms (Fig. 3.8b) or a phase space representation of $\overline{\xi}(I)$ and $U(I)$ in one plot (Fig. 3.8c). Additionally, the numerical values of all monitored signals, *i.e.* I, U, time, t, U_{ccd}, and $\overline{\xi}$, are displayed at the top text to the image tab panel.

Image data, $\overline{\xi}(t, x, y)$, are saved to an .avi file frame by frame during each acquisition loop in the record mode. The frame number, t, I, U, U_{ccd} and $\overline{\xi}$ are saved to an .ascii file when leaving the record mode. Snapshots of the GUI are saved to .jpg files for documentation purposes.

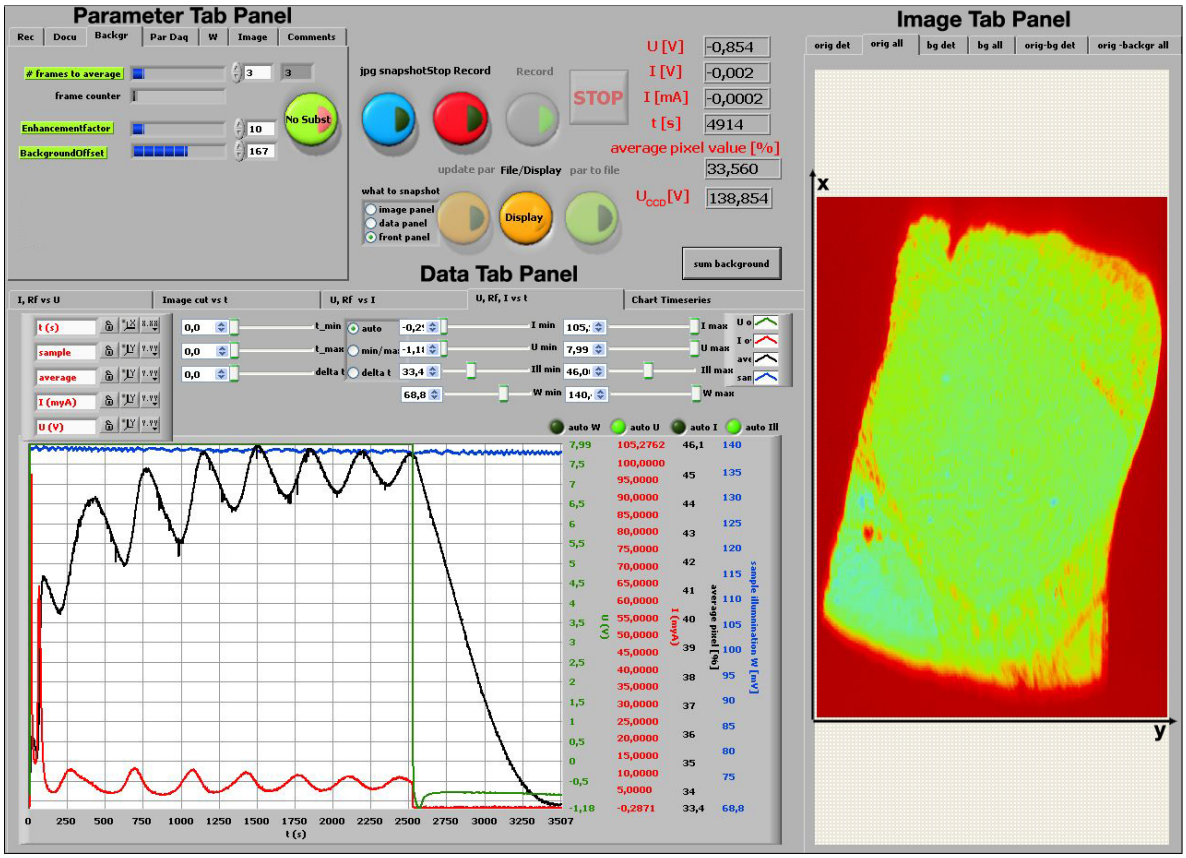

Figure 3.7: Screen shot of the graphic user interface, GUI, used for data acquisition, processing and saving.

(a)

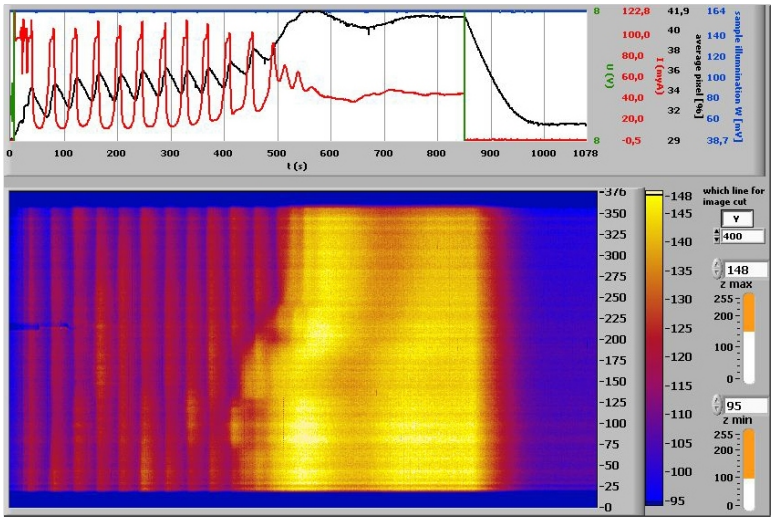

(b)

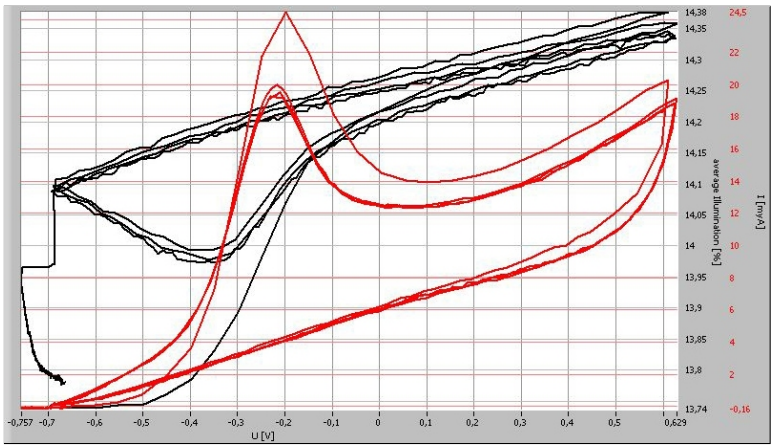

(c)

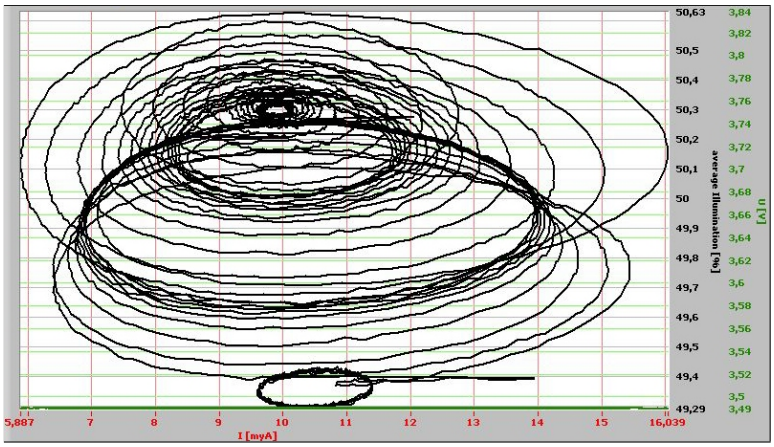

Figure 3.8: Additional tabs from the data tab panel. **(a)** Time series of averaged quantities and the time evolution of a cross section of the camera image. **(b)** Voltammogram representation with $I(U)$ and $\overline{\xi}(U)$. **(c)** Phase space representation, $\overline{\xi}(I)$.

Chapter 4

Correlations between Current Density and Ellipso-microscopic Signal

Understanding the correlations between current density, J, and averaged ellipso-microscopic signal, $\overline{\xi}$, is vital to understanding the chemical, electrochemical and dynamical features of this oscillatory electrochemical system.

In this chapter, the spatially averaged signals, J and $\overline{\xi}$, from experiments with p-type silicon are analyzed. In Sec. 4.1, a general overview of the dynamics when scanning the applied potential, U, is given. In different anodic domains, the $J-U$ and the $\overline{\xi}-U$ characteristics are compared. In Sec. 4.2, the oscillatory domain is investigated using voltage step experiments. In Sec. 4.3, the etch back of the passivating oxide layer at open-circuit potential is analyzed. Finally, a functional relationship between J and $\overline{\xi}$ during oscillations (Sec. 4.4) is discussed.

4.1 Voltage Characteristics of Current Density and Ellipso-microscopic Signal

The typical $J-U$ characteristic of the electrooxidation of silicon, providing an overview of the different dynamical domains, was discussed in Sec. 2.2. The $J-U$ characteristic and the $\overline{\xi}-U$ characteristic depicted in Fig. 4.1a were obtained with a series resistance, $R_{\mathrm{ser}} = 100\,\mathrm{k}\Omega$, because this guaranteed a stable limit cycle, *i.e.* sustained oscillations (Chazalviel *et al.*, 1992). Because of the ohmic voltage, $\Phi_{\mathrm{ohm}} = JAR_{\mathrm{ser}}$, only part of U contributes to the effective voltage across the silicon|oxide|electrolyte interface, Φ_{eff}:

$$\Phi_{\mathrm{eff}} = U - \Phi_{\mathrm{ohm}} \tag{4.1}$$

with the other ohmic resistances being neglected. Φ_{eff} is relevant for the electrochemical processes at the silicon|electrolyte interface (at low applied U) and at the silicon|oxide|electrolyte interface at more positive values of U. In Fig. 4.1b, both voltage characteristics are corrected for the ohmic voltage drop by plotting J and $\overline{\xi}$ versus Φ_{eff}.

The forward scan starts at open-circuit potential with a hydrogen terminated surface. J and $\overline{\xi}$ are constant. This domain **0** ends at $\Phi_{\mathrm{eff}} = -0.45\,\mathrm{V}$, where J starts increasing as silicon is dissolved and porous silicon is formed with a divalent mechanism (domain **I**). A porous silicon layer is formed on silicon with a different refractive index, leading to a change in $\overline{\xi}$. ξ_1

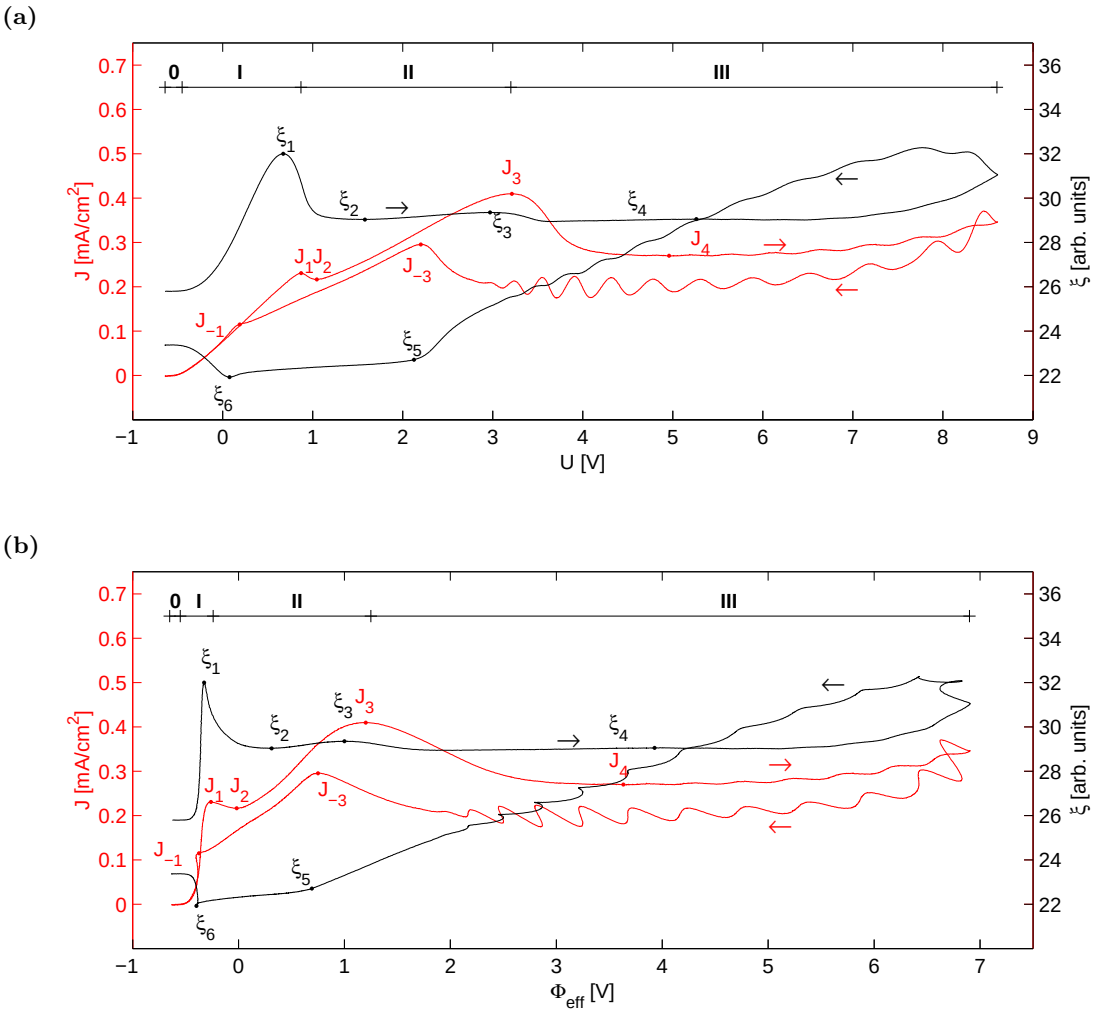

Figure 4.1: Typical voltage characteristics for p-type silicon. **(a)** The $J-U$ characteristic (red) and the $\overline{\xi}-U$ characteristic (black). **(b)** The $J-\Phi_{\text{eff}}$ characteristic (red) and the $\overline{\xi}-\Phi_{\text{eff}}$ characteristic (black). Experimental conditions: $R_{\text{ext}} = 100\,\text{k}\Omega$, $A = 4.91\,\text{mm}^2$, $c_{\text{NH}_4\text{F}} = 0.05\,\text{M}$, and pH = 2.4.

marks the maximum thickness of the porous silicon layer. At J_1 ($\Phi_{\text{eff}} = -0.28\,\text{V}$), divalent oxidation starts leading to the formation of 'wet' oxide and electro-polishing of the surface (domain **II**). $\overline{\xi}$ first decreases as the porous silicon is dissolved and the 'wet' oxide is formed. The minimum of the current density, J_2, is observed at lower values of U than the minimum of $\overline{\xi}$, ξ_2.

Beyond the second characteristic peak, J_3, at $\Phi_{\text{eff}} = 1.2\,\text{V}$, tetravalent oxidation leads to the formation of a 'dry' oxide layer (domain **III**). The transition from 'wet' to 'dry' oxide is accompanied by a very shallow peak of $\overline{\xi}$, ξ_3. In domain **III**, J and $\overline{\xi}$ reach their plateau values, J_4 and ξ_4, respectively. Here, current density oscillations are accompanied by oscillations of $\overline{\xi}$, both showing a small amplitude with respect to their average value. At $\Phi_{\text{eff}} = 5.5\,\text{V}$, $\overline{\xi}$ increases above its plateau value. This suggests an increase in the thickness of the 'dry' oxide layer, because a change of the refractive index of the oxide or the formation of another layer is not to be expected in this region.

During the backward scan, both signals deviate considerably from the forward scan at respective voltages leading to pronounced hysteresis in the $J-U$ and $\overline{\xi}-U$ characteristics. The oscillations of J are more prominent in the backward scan, *i.e.* the oscillation amplitude is

large, but the absolute value is smaller than on the forward scan. The lower value of J results in a decrease of $\overline{\xi}$, because the oxide formation rate falls below the etch rate.

As the 'dry' oxide layer thickness, z_{L}, decreases, R_{ox} decreases, which in turn leads to a decrease in Φ_{ox}. This results in an increase of Φ_{sc} and a growing J. This growth ends at J_{-3}, because the applied voltage is continuously reduced. Between J_{-3} (ξ_5) and J_{-1} (ξ_6), the oxidation switches back to a divalent mechanism and 'wet' oxide is formed. Beyond this domain, oxide formation is replaced by silicon dissolution in combination with porous silicon formation. At open-circuit potential, $\overline{\xi}$ after the voltage scan differs from $\overline{\xi}$ before the scan, because a layer of porous silicon is present beneath the hydrogen terminated surface.

The $\overline{\xi} - U$ and the $\overline{\xi} - \Phi_{\mathrm{eff}}$ characteristics illustrate that $\overline{\xi}$ is very sensitive to the properties of the interface region, *i.e.* the layer thicknesses and their refractive indices.

4.2 The Domain of Dry Oxide

In the following, a closer look is taken at the oscillatory dynamics in domain **III**. The correlation between J and $\overline{\xi}$ is investigated at constant applied voltages. Firstly, voltage step experiments from open-circuit potential into the oscillatory domain are discussed, providing insights in the phase relationship between J and $\overline{\xi}$. This is a widely used technique to initiate sustained oscillations (Chazalviel *et al.*, 1992). Secondly, the etch back of 'dry' oxide at open-circuit potential is analyzed, further elucidating the contrast of the ellipso-microscopic setup.

U is stepped from open-circuit potential to a constant value of U that lies in domain **III**. Fig. 4.2a depicts simple oscillations that result from the excitation due to the increase of the voltage. Upon raising the voltage to $U = 5.35\,\mathrm{V}$, the current density increases rapidly to $J = 0.7\,\mathrm{mA/cm^2}$ and then decreases again. During this initial peak, $\overline{\xi}$ grows close to its long-time mean value. This indicates the initial formation of the passivating oxide layer. After this transient, oscillations with a time average of $J = 0.25\,\mathrm{mA/cm^2}$ are established. As discussed in detail in Sec. 2.2, sustained oscillation are only obtained in the presence of a series resistance. Here $R_{\mathrm{ext}} = 100\,\mathrm{k\Omega}$ is used. As can be seen in the magnification of two oscillation cycles in Fig. 4.2d, J and $\overline{\xi}$ oscillate with a constant phase difference. The extrema of J coincide with the points of inflection of $\overline{\xi}$, and the extrema of $\overline{\xi}$ coincide with the points of inflection of J.

At higher R_{ext}, high-amplitude oscillations (Fig. 4.2b) with double the oscillation amplitude of low-amplitude oscillations are observed. The high-amplitude current density oscillations stabilize after 100 s, with minima at $0.1\,\mathrm{mA/cm^2}$ and maxima at $0.6\,\mathrm{mA/cm^2}$. $\overline{\xi}$ stops drifting after 300 s and oscillates around a constant mean value. The character of these oscillations is more relaxational compared to the nearly sinusoidal character of the low-amplitude oscillations. At the same R_{ext} and a higher U, complex modulated low-amplitude oscillations (Fig. 4.2c) are established. High-amplitude and complex low-amplitude oscillations also show that the extrema of $\overline{\xi}$ coincide with the points of inflection of J, and vice versa (Figs. 4.2e and 4.2f).

In conclusion, the analysis of the times series shows that during oscillations J and $\overline{\xi}$ have a fixed phase relationship to each other. The agreement of the extrema of one with points of inflection of the other suggests that one behaves like a derivative of the other. The case of complex low-amplitude oscillations illustrates the fact that even small details in one time quantity are matched by equivalent details in the other (Fig. 4.2f).

At this point, two hypotheses are established. Firstly, it is assumed that $\overline{\xi}$ in domain **III**,

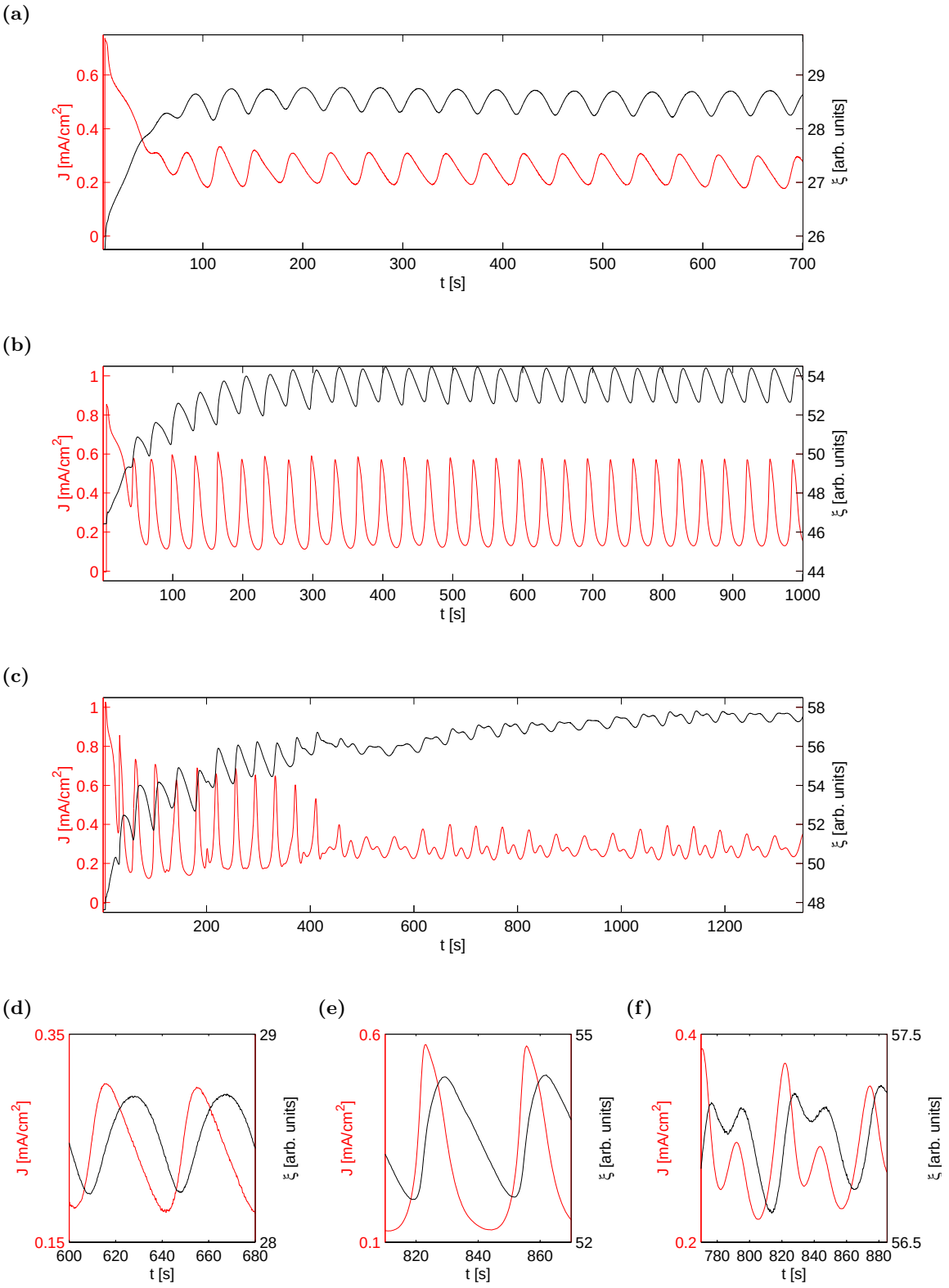

Figure 4.2: Typical time series following upon stepping the voltage from open-circuit potential to a voltage inside domain **III**. **(a,d)** Stable simple low-amplitude oscillations for $U = 5.35\,\mathrm{V}$ and $R_{\mathrm{ext}} = 100\,\mathrm{k\Omega}$. **(b,e)** Stable simple high-amplitude oscillations for $U = 7\,\mathrm{V}$ and $R_{\mathrm{ext}} = 200\,\mathrm{k\Omega}$. **(c,f)** Damped high-amplitude oscillations followed by complex low-amplitude oscillations for $U = 8.5\,\mathrm{V}$ and $R_{\mathrm{ext}} = 200\,\mathrm{k\Omega}$. Experimental conditions: **(a,d)** $c_{\mathrm{NH_4F}} = 0.05\,\mathrm{M}$, pH = 2.4, and $A = 7.65\,\mathrm{mm^2}$. **(b,e)** $c_{\mathrm{NH_4F}} = 0.05\,\mathrm{M}$, pH = 2.4, and $A = 4.26\,\mathrm{mm^2}$. **(c,f)** $c_{\mathrm{NH_4F}} = 0.05\,\mathrm{M}$, pH = 2.4, and $A = 7.65\,\mathrm{mm^2}$.

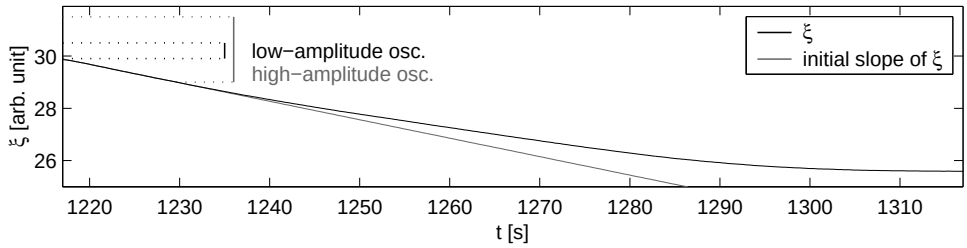

Figure 4.3: Etch back at open-circuit potential after sustained low-amplitude oscillations. The initial slope of 0.07 s^{-1} of the etch back is indicated in gray. The vertical lines in the upper part indicate typical values of $\overline{\xi}$ during damped high-amplitude oscillations (gray) and stable low-amplitude oscillations (black).

i.e. for effective voltages $\Phi_{\text{eff}} > 3\,\text{V}$, is solely attributed to changes in the thickness of the 'dry' silicon oxide layer. Secondly, it is proposed that the relationship between the oxide layer thickness, z_{L}, and ξ is linear. This approach is tested in the following, analyzing the etch back of anodically formed 'dry' oxide.

4.3 Etch Back

Every experiment starts at open-circuit potential, at which the electrode is kept for several minutes. Therefore, all oxide on the surface is etched and the surface is hydrogen terminated. During the experiment, oxide is formed when a voltage corresponding to a value inside domain **III** is applied. Since the electrolyte contains ammonium fluoride, the oxide is continuously chemically removed. Hence in this domain, oxide is continuously formed and etched with an oxide layer being present on the electrode. At the end of the experiment, the potential is switched back to open-circuit potential. No current flows and the oxide layer thickness depends solely on the etch rate, which is controlled by the diffusion of the etching fluoride species. Therefore, the relaxation of an oxide covered surface to an hydrogen terminated surface at open-circuit potential is called etch back.

After returning to open-circuit conditions, $\overline{\xi}$ at first decreases linearly. The etch rate decreases until all oxide is etched. The ellipso-microscopic signal is linear for those values of $\overline{\xi}$ where oscillations take place. This is depicted in Fig. 4.3. $\overline{\xi}$ is at least linear during the first 15 s. $\overline{\xi}$ depends linearly on the oxide layer thickness, z_{L}, suggesting a constant etch rate.

The dependency of ξ on z_{L} can be calculated theoretically assuming a layer of oxide on silicon in a water-based electrolyte. The ratio of the light intensity at the camera, ξ_{calc}, to the light intensity of the light source is defined (Azzam and Bashara, 1977) according to:

$$\xi_{\text{calc}} = \frac{\hat{\mathbf{E}}^{\dagger}\,\hat{\mathbf{E}}}{(E_{\text{P}})^2} \tag{4.2}$$

with E_{P} being the electrical field strength transmitted by the polarizer, $\hat{\mathbf{E}}$ being the electrical field strength at the detector, and $\hat{\mathbf{E}}^{\dagger}$ being its Hermitian adjoint, *i.e.* the complex conjugate of the transpose of $\hat{\mathbf{E}}$.

$\hat{\mathbf{E}}$ results from the interaction of the light, emitted from the light source, with the optical components (Fig. 3.1c) and with the sample interface. The light intensity that reaches the camera depends on the positions of the optical components, the properties of the sample, and the angle of incidence. During a single experiment the properties of the optical setup are kept constant, but the optical properties of the sample interface change.

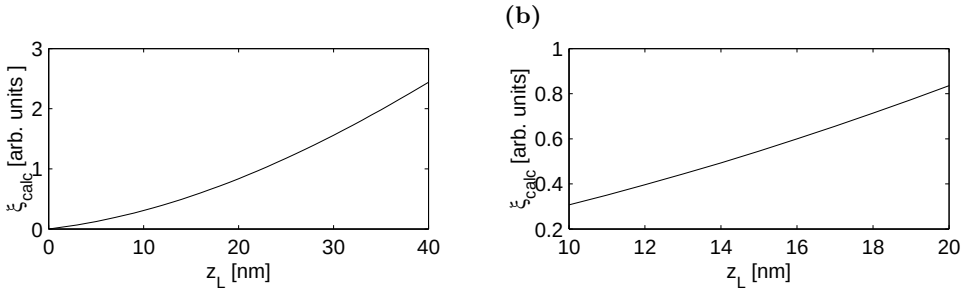

Figure 4.4: $\xi_{\mathrm{calc}}(z_{\mathrm{L}})$ calculated with Eq. (4.5) with $\alpha_{\mathrm{P}} = 175\,^{\circ}$, $\alpha_{\mathrm{C}} = 45\,^{\circ}$, and $\alpha_{\mathrm{A}} = 20\,^{\circ}$. **(a)** For the entire range of expected oxide thicknesses. **(b)** For oxide thicknesses expected in the oscillatory domain **III**.

Assuming a constant refractive index, the intensity of the reflected light can be calculated from the oxide layer thickness, only. The derivation of an explicit equation to calculate the ellipso-microscopic signal, ξ_{calc}, is described by Linke and Merkel (2005). The electromagnetic wave is represented by the complex Jones vector, and the effect of the optical components on light is represented by their respective Jones matrices:

$$\hat{\mathbf{E}} = \mathbf{R}_{-\alpha_{\mathrm{A}}}\mathbf{T}_{\alpha_{\mathrm{A}}}\mathbf{R}_{\alpha_{\mathrm{A}}}\mathbf{T}_{\hat{r}}\mathbf{R}_{-\alpha_{\mathrm{C}}}\mathbf{T}_{\lambda/4}\mathbf{R}_{\alpha_{\mathrm{C}}-\alpha_{\mathrm{P}}}\begin{pmatrix} E_{\mathrm{P}} \\ 0 \end{pmatrix} \tag{4.3}$$

with:

$$\mathbf{T}_{\alpha_{\mathrm{A}}} = \begin{pmatrix} 1 & 0 \\ 0 & 0 \end{pmatrix} \qquad \mathbf{T}_{\hat{r}} = \begin{pmatrix} \hat{r}_{\mathrm{p}} & 0 \\ 0 & \hat{r}_{\mathrm{s}} \end{pmatrix} \qquad \mathbf{T}_{\lambda/4} = \begin{pmatrix} 1 & 0 \\ 0 & i \end{pmatrix} \qquad \mathbf{R}_{\alpha} = \begin{pmatrix} \cos\alpha & \sin\alpha \\ -\sin\alpha & \cos\alpha \end{pmatrix} \tag{4.4}$$

with α being the angle between the fast axis of the optical component and the plane of incidence, $\mathbf{T}_{\alpha_{\mathrm{A}}}$ being the Jones matrix for polarization, $\mathbf{T}_{\hat{r}}$ being the Jones matrix for reflection, $\mathbf{T}_{\lambda/4}$ being the Jones matrix for retardation, and $\mathbf{R}_{\alpha}$ being a matrix for rotation. Expanding the Jones matrices leads to:

$$\xi_{\mathrm{calc}} = \cos(2\alpha_{\mathrm{A}})\left(f_1\hat{r}_{\mathrm{p}}^{*}\hat{r}_{\mathrm{p}} - f_2\hat{r}_{\mathrm{s}}^{*}\hat{r}_{\mathrm{s}}\right) + 2\sin(2\alpha_{\mathrm{A}})\,\mathrm{Re}\left(f_3\hat{r}_{\mathrm{p}}^{*}\hat{r}_{\mathrm{s}}\right) + \left(f_1\hat{r}_{\mathrm{p}}^{*}\hat{r}_{\mathrm{p}} + f_2\hat{r}_{\mathrm{s}}^{*}\hat{r}_{\mathrm{s}}\right) \tag{4.5}$$

with the following abbreviations:

$$\begin{aligned} f_1 &= \cos^2(\alpha_{\mathrm{C}} - \alpha_{\mathrm{P}})\cos^2\alpha_{\mathrm{C}} + \sin^2(\alpha_{\mathrm{C}} - \alpha_{\mathrm{P}})\sin^2\alpha_{\mathrm{C}} \\ f_2 &= \cos^2(\alpha_{\mathrm{C}} - \alpha_{\mathrm{P}})\sin^2\alpha_{\mathrm{C}} + \sin^2(\alpha_{\mathrm{C}} - \alpha_{\mathrm{P}})\cos^2\alpha_{\mathrm{C}} \\ f_3 &= \sin\alpha_{\mathrm{C}}\cos\alpha_{\mathrm{C}}\Big(\cos^2(\alpha_{\mathrm{C}} - \alpha_{\mathrm{P}}) - \sin^2(\alpha_{\mathrm{C}} - \alpha_{\mathrm{P}})\Big) - i\sin(\alpha_{\mathrm{C}} - \alpha_{\mathrm{P}})\cos(\alpha_{\mathrm{C}} - \alpha_{\mathrm{P}}) \end{aligned} \tag{4.6}$$

The Fresnel coefficients calculated with Eqs. (3.3) to (3.10) are used with the constants listed in Tab. B.3. The plot of ξ_{calc} in Fig. 4.4a shows a monotonous increase for experimentally relevant values of z_{L}. For oxide layer thicknesses between 10 nm and 20 nm, where current density oscillations take place (Chazalviel *et al.*, 1998; Yahyaoui *et al.*, 2003; Lehmann, 1996), $\xi(z_{\mathrm{L}})$ is, to a very good approximation, linear (Fig. 4.4b).

To convert the measured intensity $\overline{\xi}$ to an absolute value of the oxide layer thickness on the electrode a linear functional relation between the two is assumed. The imaged area is larger than the electrode area. Therefore, the spatial average, $\overline{\xi}(t)$, contains contributions from the electrode area, $\overline{\xi}_{\mathrm{elec}}(t)$, and from the inactive surroundings $\overline{\xi}_{\mathrm{sur}}$:

$$\overline{\xi}(t) = \overline{\xi}_{\mathrm{elec}}(t) + \overline{\xi}_{\mathrm{sur}} \tag{4.7}$$

In the case of an oxide free hydrogen terminated electrode, the notations $\overline{\xi}^{\mathrm{ref}}(t)$ and $\overline{\xi}^{\mathrm{ref}}_{\mathrm{elec}}(t)$ are used for the average of the entire camera image and the average of the electrode area, respectively:

$$\overline{\xi}^{\mathrm{ref}}(t) = \overline{\xi}^{\mathrm{ref}}_{\mathrm{elec}}(t) + \overline{\xi}_{\mathrm{sur}} \tag{4.8}$$

For reference, the value $\overline{\xi}$ before the experiment, *i.e.* of the hydrogen terminated electrode, is used. The average oxide layer thickness, $\overline{z}_{\mathrm{L}}$, is a function of the difference between $\overline{\xi}$ of the electrode, with and without oxide:

$$f(\overline{z}_{\mathrm{L}}(t)) = \overline{\xi}_{\mathrm{elec}}(t) - \overline{\xi}^{\mathrm{ref}}_{\mathrm{elec}}(t) \tag{4.9}$$

Using Eqs. (4.7) and (4.8) one obtains:

$$f(\overline{z}_{\mathrm{L}}(t)) = \overline{\xi}(t) - \overline{\xi}^{\mathrm{ref}}(t) \tag{4.10}$$

Under the assumption of the linearity of this functional relation, it is extended to:

$$\overline{z}_{\mathrm{L}}(t) = c_{\mathrm{opt}}(\overline{\xi}(t) - \overline{\xi}^{\mathrm{ref}}) \tag{4.11}$$

with the proportionality constant, c_{opt}. Aggour *et al.* (2007) measured the oxide layer thickness variations with FTIR. The form of the oscillations of the oxide thickness and the phase shift with respect to J closely resemble the measurements depicted in Fig 4.2e. This is a further indication that the the initial assumption of linearity is valid. Hence, the experimental observations during etch back and the ellipsometric calculations are indications for the suggested linearity. A quantitative interpretation of the ellipso-microscopic signal seems possible. Such a quantitative approach is investigated in the next section.

4.4 Analytic Relationship between Ellipso-microscopic Signal and Current Density

Assuming that a capacitive current density can be neglected, J stems only from the electrochemical oxidation of silicon. Furthermore, assuming that the etch rate of the oxide, $\dot{\overline{z}}_{\mathrm{E}}$, is constant, J is a linear function of the time derivative of $\overline{\xi}$, $\dot{\overline{\xi}}(t)$, as changes of $\overline{\xi}$ depend solely on the oxide formation rate. Therefore J can be calculated from $\dot{\overline{\xi}}(t)$ and correspondingly, $\overline{\xi}$ is a linear function of the integral of J thus it can be calculated from the measured J.

To discriminate between the directly measured current density and the one calculated from $\overline{\xi}$, the latter is denoted by $J_{\overline{\xi}}$. Correspondingly, the notation $\overline{\xi}_J$ is used for the ellipso-microscopic signal obtained from J. For the following discussion it is useful to introduce a number of other quantities. The oxide layer thickness on the electrode is denoted by $z_{\mathrm{L}}(t)$, the oxide thickness etched between t_0 and t by $z_{\mathrm{E}}(t)$, and the oxide thickness that is produced by the anodic current density between t_0 and t by $z(t)$. As above, the spatially averaged oxide thicknesses are indicated by vertical bars. The averaged oxide formed by the anodic current density on silicon is the sum of the increase of average oxide on the electrode and the decrease that results from etching:

$$\overline{z}_{\mathrm{L}}(t) + \overline{z}_{\mathrm{E}}(t) = \overline{z}(t) \tag{4.12}$$

with the time derivative:

$$\dot{\overline{z}}_{\mathrm{L}}(t) + \dot{\overline{z}}_{\mathrm{E}}(t) = \dot{\overline{z}}(t) \tag{4.13}$$

and $\dot{\overline{z}}$ being the oxide layer continuously produced by electrochemical oxidation, which is calculated from the overall quantity of formed silicon oxide:

$$\overline{z}(t) = \frac{M}{\rho A} n_{\mathrm{SiO_2}}(t) \tag{4.14}$$

A being the electrode area, $M = 60.2\,\mathrm{g/mol}$ the molar mass of silicon oxide, ρ the density of silicon oxide, and $n_{\mathrm{SiO_2}}$ the amount of moles of silicon oxide formed anodically. The density, ρ, of anodic oxide formed in a water-based electrolyte differs from that of thermal oxide. ρ is estimated with the Lorentz-Lorens equation (Pliskin, 1977) using the refractive index of silicon oxide, $\hat{n}_{\mathrm{SiO_2}}$ (Tab. B.3), and the constant $K = 8.0461$ (Hung *et al.*, 1991):

$$\begin{aligned} \rho &= K \frac{(\hat{n}_{\mathrm{SiO_2}})^2 - 1}{(\hat{n}_{\mathrm{SiO_2}})^2 + 2} \\ &= 1.69\,\mathrm{g/cm^3} \end{aligned} \tag{4.15}$$

The Anodic Charge

The time derivative of the amount of moles of silicon oxide, $\dot{n}_{\mathrm{SiO_2}}$, is directly related to the current density, J:

$$J(t) = \frac{1}{A}\,\dot{q}(t) \tag{4.16}$$

$$= \frac{F\nu}{A}\,\dot{n}_{\mathrm{SiO_2}}(t) \tag{4.17}$$

with $F = 96485.3\,\mathrm{As/mol}$ being the Faraday constant, ν being the oxidation valency, and q being the amount of charges necessary to electrochemically oxidize silicon. In the case of p-type silicon in the oscillatory voltage domain **III**, the oxidation valency is $\nu = 3.6$ (Eddowes, 1990). From Eqs. (4.17) and (4.14) it follows that:

$$J(t) = \frac{F\nu\rho}{M}\,\dot{\overline{z}}(t) \tag{4.18}$$

using the time derivative of $\dot{\overline{z}}$ from Eq. (4.13) yields to:

$$J(t) = \frac{F\nu\rho}{M}\left(\dot{\overline{z}}_{\mathrm{L}}(t) + \dot{\overline{z}}_{\mathrm{E}}(t)\right) \tag{4.19}$$

Thereafter the time derivative of Eq. (4.11) is inserted:

$$\boxed{J_{\overline{\xi}}(t) = \frac{F\nu\rho}{M}\left(c_{\mathrm{opt}}\dot{\overline{\xi}}(t) + \dot{\overline{z}}_{\mathrm{E}}(t)\right)} \tag{4.20}$$

Knowing the values for the etch rate, $\dot{\overline{z}}_{\mathrm{E}}$, and c_{opt}, the current density calculated from $\overline{\xi}$, $J_{\overline{\xi}}$, can be compared to J.

Period Averaged Etch Rate

J and $\overline{\xi}$ can also be related to each other via the integral of J. Integrating Eq. (4.20) results in the following expression:

$$\int_{t'}^{t} J(\tau)d\tau = \frac{F\nu\rho}{M}\left(c_{\mathrm{opt}}\int_{t'}^{t}\dot{\overline{\xi}}(\tau)d\tau + \int_{t'}^{t}\dot{\overline{z}}_{\mathrm{E}}(\tau)\right) \tag{4.21}$$

$$= \frac{F\nu\rho}{M}\left(c_{\mathrm{opt}}\overline{\xi}(t) - c_{\mathrm{opt}}\overline{\xi}(t') + \overline{z}_{\mathrm{E}}(t) - \overline{z}_{\mathrm{E}}(t')\right) \tag{4.22}$$

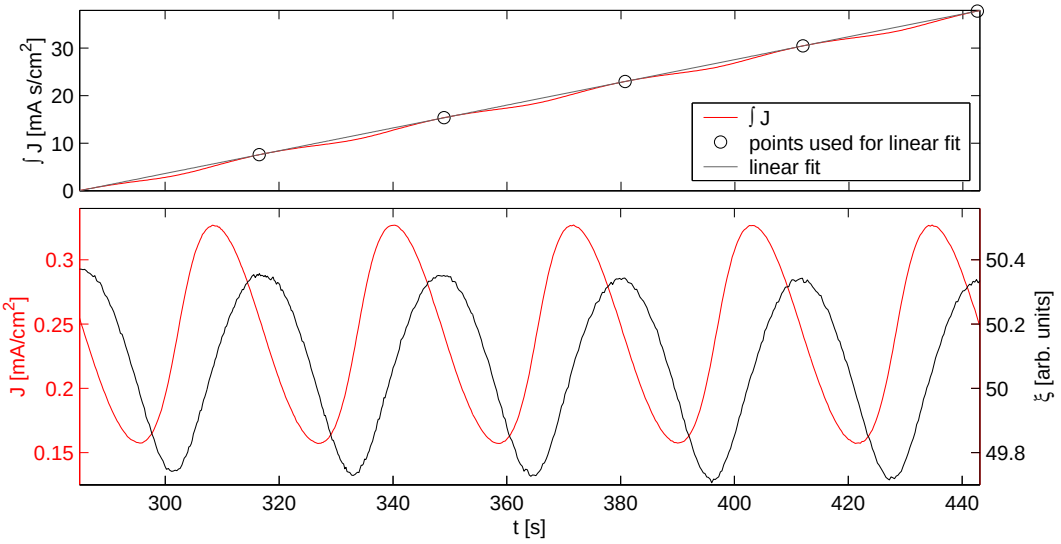

Figure 4.5: The integral of the current density, $\int J$ (top panel), the current density, J, and the averaged ellipso-microscopic signal, $\overline{\xi}$, (both bottom panel), displayed between two maxima of $\overline{\xi}$. The period averaged etch rate, $\dot{\overline{z}}_{\mathrm{E}} = 0.25\,\mathrm{nm/s}$, is obtained from the slope of the linear fit of $\int J$ (top panel) and calculated at the maxima of $\overline{\xi}$. Experimental conditions: $U = 4\mathrm{V}$, $R_{\mathrm{ser}} = 100\,\mathrm{k\Omega}$, $c_{\mathrm{NH_4F}} = 0.05\,\mathrm{M}$, pH = 2.3, and $A = 4.26\,\mathrm{mm}^2$.

In the case of sustained oscillations, the etch rate averaged over one oscillation period is constant and equal to the oxide formation rate averaged over one period. In Fig. 4.2a, it can be observed that the extrema of $\overline{\xi}$ in the oscillatory time series have the same value. During one oscillation period, equal amounts of charge, q, flow in the circuit, q being equal to the time integral of J, which is displayed in the top panel of Fig. 4.5. The integral resembles a "staircase" in shape, which results from the oscillatory formation rate. This integral of J evaluated at the maxima of $\overline{\xi}$ lie on a straight line. In fact, all sets of points separated in time by multiples of one oscillation period, P, form a straight line.

A variation of the etch rate, $\dot{\overline{z}}_{\mathrm{E}}(t)$, during one oscillation period cannot be ruled out. Instead, the period averaged etch rate, $\dot{\overline{z}}_{\mathrm{E}}$, which is constant, will be used in the following. The last term in Eq. (4.22) can be rewritten, integrating between two time instances which are separated by $t - t'$, a multiple of the oscillation period:

$$\int_{t'}^{t} J(\tau)d\tau = \frac{F\nu\rho}{M}\left(c_{\mathrm{opt}}\overline{\xi}(t) - c_{\mathrm{opt}}\overline{\xi}(t') + (t-t')\dot{\overline{z}}_{\mathrm{E}}\right) \tag{4.23}$$

The equation can be rearranged as a function of J:

$$\boxed{\overline{\xi}_J(t) = \frac{M}{F\nu\rho c_{\mathrm{opt}}}\int_{t'}^{t} J(\tau)d\tau + \overline{\xi}(t') - \frac{t-t'}{c_{\mathrm{opt}}}\dot{\overline{z}}_{\mathrm{E}}} \tag{4.24}$$

with $\overline{\xi}_J$ being $\overline{\xi}$ calculated from J, once $\dot{\overline{z}}_{\mathrm{E}}$, c_{opt}, and $\overline{\xi}(t')$ are determined from experimental data.

The objective is to extract $\dot{\overline{z}}_{\mathrm{E}}$ from the integration of J. Therefore the time derivative of Eq. (4.22) is considered:

$$\frac{d}{dt}\int_{t'}^{t} J(\tau)d\tau = \frac{F\nu\rho}{M}\left(c_{\mathrm{opt}}\dot{\overline{\xi}}(t) + \dot{\overline{z}}_{\mathrm{E}}\right) \tag{4.25}$$

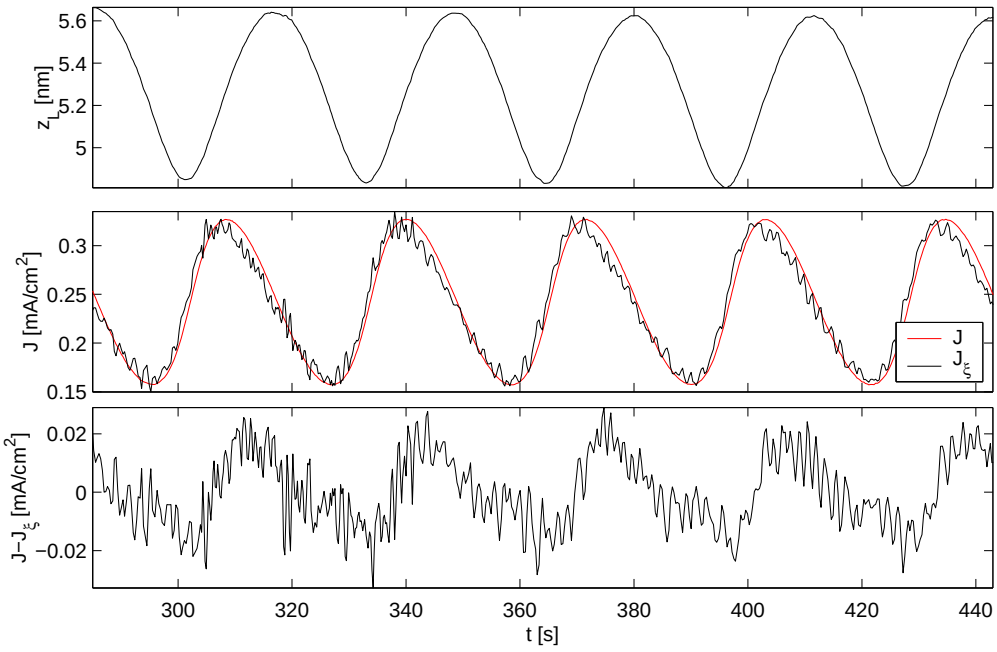

Figure 4.6: Low-amplitude current density oscillations: the oxide layer thickness, z_L (top panel), the measured current density, J, the calculated current density, $J_{\overline{\xi}}$, (both middle panel), and the difference, $J - J_{\overline{\xi}}$ (bottom panel). Experimental conditions: $R_\mathrm{ext} = 100\,\mathrm{k\Omega}$, $U = 4\,\mathrm{V}$, $\dot{\overline{z}}_\mathrm{E} = 0.25\,\mathrm{nm/s}$, $A = 4.26\,\mathrm{mm}^2$, $c_{\mathrm{NH_4F}} = 0.05\,\mathrm{mol/l}$, and pH = 2.4. Smoothing: $k = 1$. Fitting: $c_\mathrm{opt} = 1.30$.

The time derivative of $\overline{\xi}$ at the maxima $t = t_\mathrm{max}$ is zero:

$$\left.\frac{d}{dt}\right|_{t_\mathrm{max}} \int_{t'_\mathrm{max}}^{t_\mathrm{max}} J(\tau)d\tau = \frac{F\nu\rho}{M}\,\dot{\overline{z}}_\mathrm{E} \tag{4.26}$$

Hence, $\dot{\overline{z}}_\mathrm{E}$ is proportional to the slope of the integral of J evaluated at the maxima of $\overline{\xi}$ (Fig. 4.5):

$$\dot{\overline{z}}_\mathrm{E} = \frac{M}{F\nu\rho}\,\left.\frac{d}{dt}\right|_{t_\mathrm{max}} \int_{t'_\mathrm{max}}^{t_\mathrm{max}} J(\tau)d\tau \tag{4.27}$$

Fitting

By fitting J to $J_{\overline{\xi}}$, c_opt is obtained using Eq. (4.20):

$$c_\mathrm{opt} = \frac{\dfrac{M}{F\nu\rho}J(t) - \dot{\overline{z}}_\mathrm{E}}{\dot{\overline{\xi}}(t)} \tag{4.28}$$

This equation indicates that c_opt is determined by ν and $\dot{\overline{z}}_\mathrm{E}$. If there are discrepancies between the values of these quantities and the values used, they are contained in c_opt. Temporal variations of the values are not contained in c_opt and therefore visible in $J_{\overline{\xi}}(t)$ and $\overline{\xi}_J(t)$.

$\overline{\xi}$ is smoothed before differentiation to reduce the noise level. A central moving average over $2k + 1$ points is used according to:

$$\overline{\xi}(t)_\mathrm{smooth} = \sum_{i=-k}^{k} \frac{\overline{\xi}(t + i\Delta t)}{2k + 1} \tag{4.29}$$

For $k = 0$, no smoothing is applied. For most of the calculations, $k = 1$ or $k = 2$ are used.

In Fig. 4.6, $\overline{z}_{\mathrm{L}}(t)$, $J(t)$ and $J_{\overline{\xi}}(t)$ are displayed. The agreement of $J_{\overline{\xi}}(t)$ with $J(t)$ is very good and the oxide thickness oscillates in a similar range as found by Böhm *et al.* (2001). Thus, the assumptions and the approach itself are justified. A good fit is also obtained for complex low amplitude oscillations in Fig. 4.7.

There is, however, a small systematic discrepancy. The maxima of $J_{\overline{\xi}}$ are ahead of the maxima of $J(t)$ by approximately 1 s. The difference $J - J_{\overline{\xi}}(t)$ is of the order of 50 μA/cm^2, *i.e.* 12% of J.

In contrast, in the case of the high-amplitude current density oscillations, the difference between J and $J_{\overline{\xi}}$ is significant (Fig. 4.8). This creates problems fitting c_{opt}. Consequently, c_{opt} fitted for low-amplitude oscillations under the same optical conditions, *i.e.* positions of the polarizer, analyzer and quarter plate, and the light intensity of the LED, is also used for high-amplitude oscillations.

4.5 Discussion and Outlook

The analysis of oxide etch back experiments at open-circuit potential strongly suggest that $\overline{\xi}$ depends linearly on the oxide layer thickness. The good fit of the data based on that assumption further supports this ansatz. In the oscillatory domain **III**, two types of oscillations are observed in the case of p-type silicon, low-amplitude and high-amplitude. The fit is excellent in the case of low-amplitude oscillations, but shows significant deviations in the case of high-amplitude oscillations. The values for the oxide thickness range and the etch rate calculated during the fitting procedure reproduce what is known from IR measurements of the oxide layer dynamics in the literature (Yahyaoui *et al.*, 2003). This further supports the assumption that changes in the refractive index of silicon oxide can be neglected.

The discrepancies in the fit point to, so far, undiscovered elements in the oscillatory mechanism. They possibly arise from a non-negligible charging current density, variations in the valency, ν, the etch rate, $\dot{\overline{z}}_{\mathrm{E}}$, or in the amount of partially oxidized silicon in the oxide layer. One of these sources may serve as the sole explanation for the discrepancies, but a mixture of two or more also has to be considered.

Capacitive Current Density

The difference, $J - J_{\overline{\xi}}$, may be interpreted as capacitive current density responsible for charging the interfacial region. This would imply that the charge stored in this region changes periodically during the oscillations. The interfacial capacity has to be sufficiently high to give rise to the observed current density discrepancy. As can be seen in the top panels of Figs. 4.9a and 4.9b, positive charge is released from the interface during the ascending flanks of J, while it is stored again during the descending flanks. This is indicated by the shaded areas in Fig. 4.9b. This effect is observed to a smaller extent in the case of low-amplitude oscillations and to a larger extent in the case of high-amplitude oscillations.

The charge density, $\Delta\sigma$, transported back and forth can be calculated by integrating $J - J_{\overline{\xi}}$:

$$\Delta\sigma(t) = \int_{t'}^{t} \left(J(\tau) - J_{\overline{\xi}}(\tau) \right) d\tau \tag{4.30}$$

$\Delta\sigma$ is displayed in the bottom panels of Fig. 4.9. In the case of low- and high-amplitude oscillations, 0.15 mC/cm^2 and 0.9 mC/cm^2 have to be stored and released, respectively.

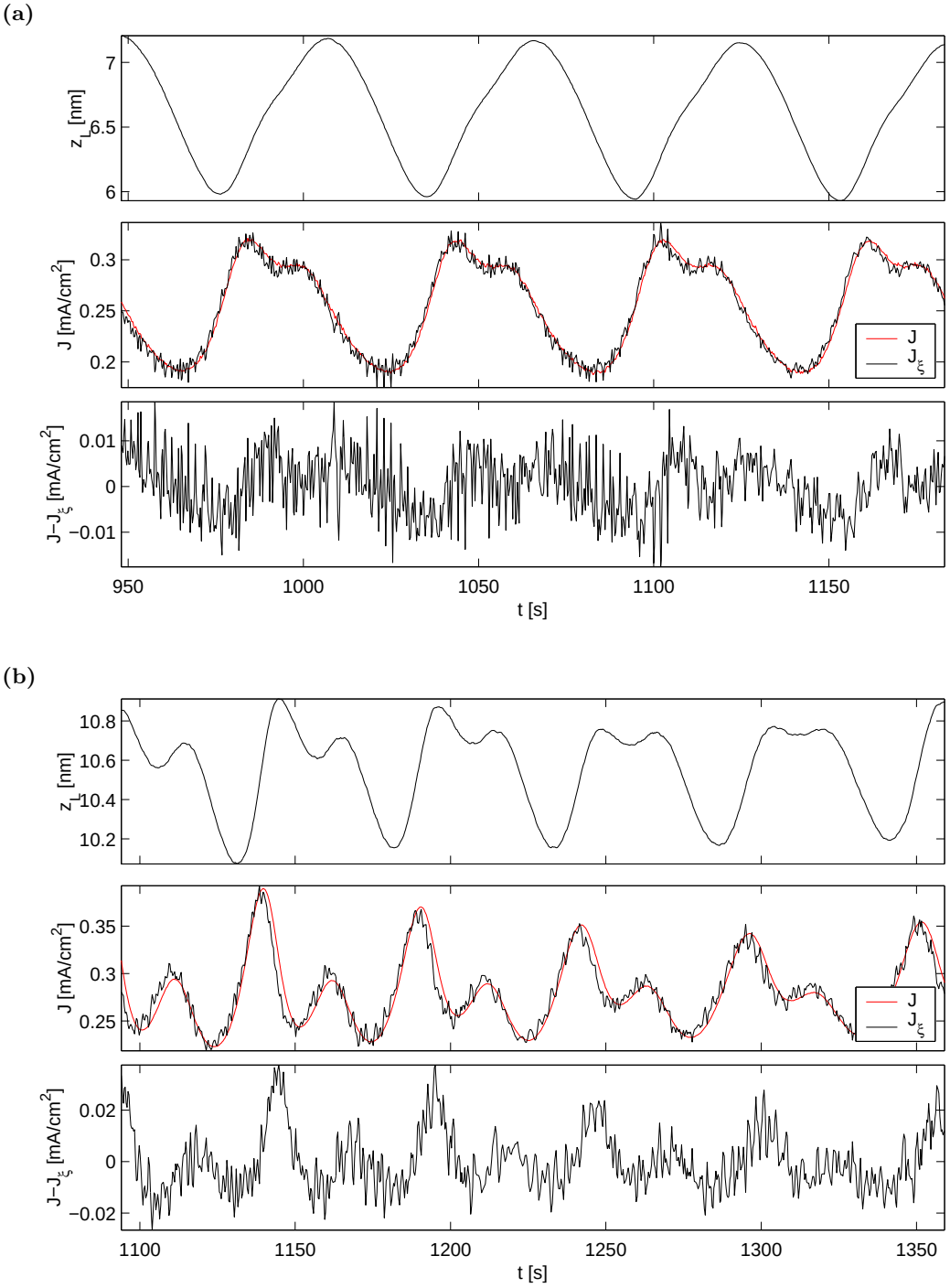

Figure 4.7: Complex low-amplitude current density oscillations: the oxide layer thickness, z_{L} (top panel), the measured current density, J, the calculated current density, $J_{\overline{\xi}}$, (both middle panel), and the difference, $J - J_{\overline{\xi}}$ (bottom panel). **(a)** Experimental conditions: $R_{\mathrm{ext}} = 100\,\mathrm{k\Omega}$, $U = 7.35\,\mathrm{V}$, $\dot{\bar{z}}_{\mathrm{E}} = 0.26\,\mathrm{nm/s}$, $A = 7.65\,\mathrm{mm}^2$, $c_{\mathrm{NH_4F}} = 0.05\,\mathrm{mol/l}$, and pH = 2.4. Smoothing: $k = 2$. Fitting: $c_{\mathrm{opt}} = 1.89$. **(b)** Experimental conditions: in Fig. 4.2c. Smoothing: $k = 1$. Fitting: $c_{\mathrm{opt}} = 1.30$.

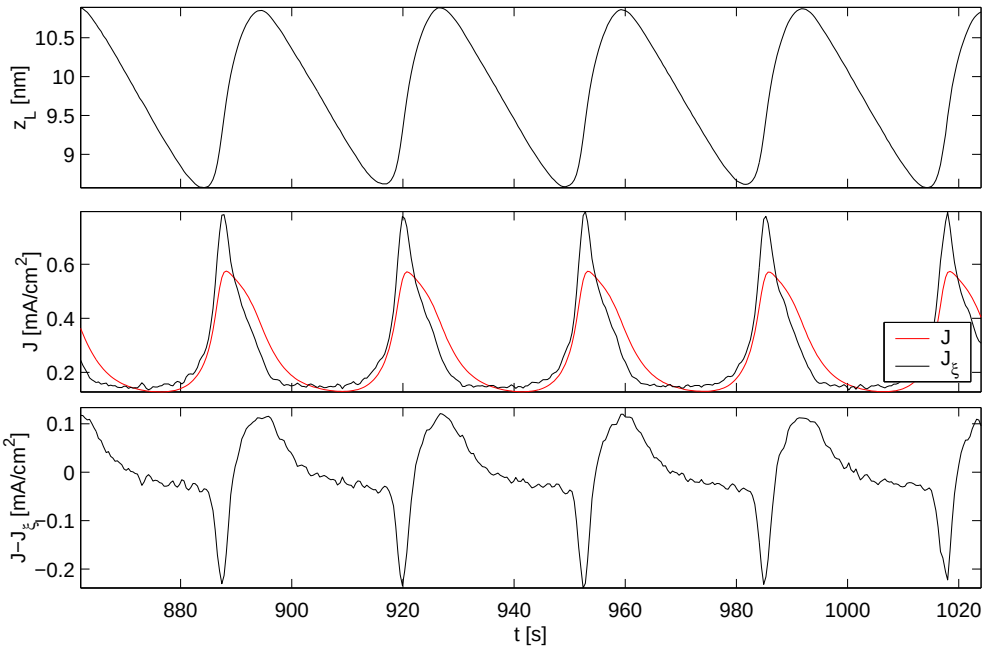

Figure 4.8: High-amplitude current oscillations: the oxide layer thickness, z_{L}, (top panel), the measured current density, J, and the calculated current density, $J_{\bar{\xi}}$, (both middle panel), and the difference, $J - J_{\bar{\xi}}$, (bottom panel). Experimental conditions: in Fig. 4.2b. Smoothing: $k = 1$. Fitting: $c_{\mathrm{opt}} = 1.30$.

The charge could be either stored in the space charge layer of silicon or in the oxide layer where positive charges are stabilized in the lattice of partially oxidized silicon oxide. In both cases, the counter charges would be expected in the electrolyte near the interface. The latter hypothesis is supported by the measurement of the free carrier absorption in the oxide layer using electro-modulated *in situ* IR spectroscopy (Chazalviel *et al.*, 1998). The absorption is at a maximum directly before and at a minimum directly after the current density peak. Negatively charged species are the charge carriers in the oxide as illustrated in Fig. 4.9.

The estimation of the capacity responsible for the charge storage is not simple, because the capacity of the oxide layer is expected to depend on the oxide layer thickness. Values for the capacity of the oxide, $C_{\mathrm{ox}} = 1\ \mu\mathrm{F/cm^2}$ and for the capacity of the space charge layer, $C_{\mathrm{sc}} = 0.1\ \mu\mathrm{F/cm^2}$, were estimated in impedance experiments by Kim *et al.* (1999), much too low to explain the difference between J and $J_{\bar{\xi}}$.

Partially Oxidized Silicon

As described in Chapter 2, the anodic oxidation of silicon results from a combination of hole capture and electron injection steps. The first oxidation step could be shown to be always a hole capture step and to be rate determining. This suggests a very low concentration of partially oxidized silicon, because the ratio of the hole capture reaction rate to the reaction rates for the following electron injection is large. However, the hole capture rate depends on the band bending. As it changes in the course of one oscillation cycle, the reaction rate ratio changes as well.

Assuming that the refractive index of partially and fully oxidized species are similar, the discrepancy between J and $J_{\bar{\xi}}$ would indicate that the amount of partially oxidized silicon in the interfacial region changes during one oscillation cycle. The lower the oxidation number of a silicon species, the lower the amount of charge necessary for its formation. Irrespective

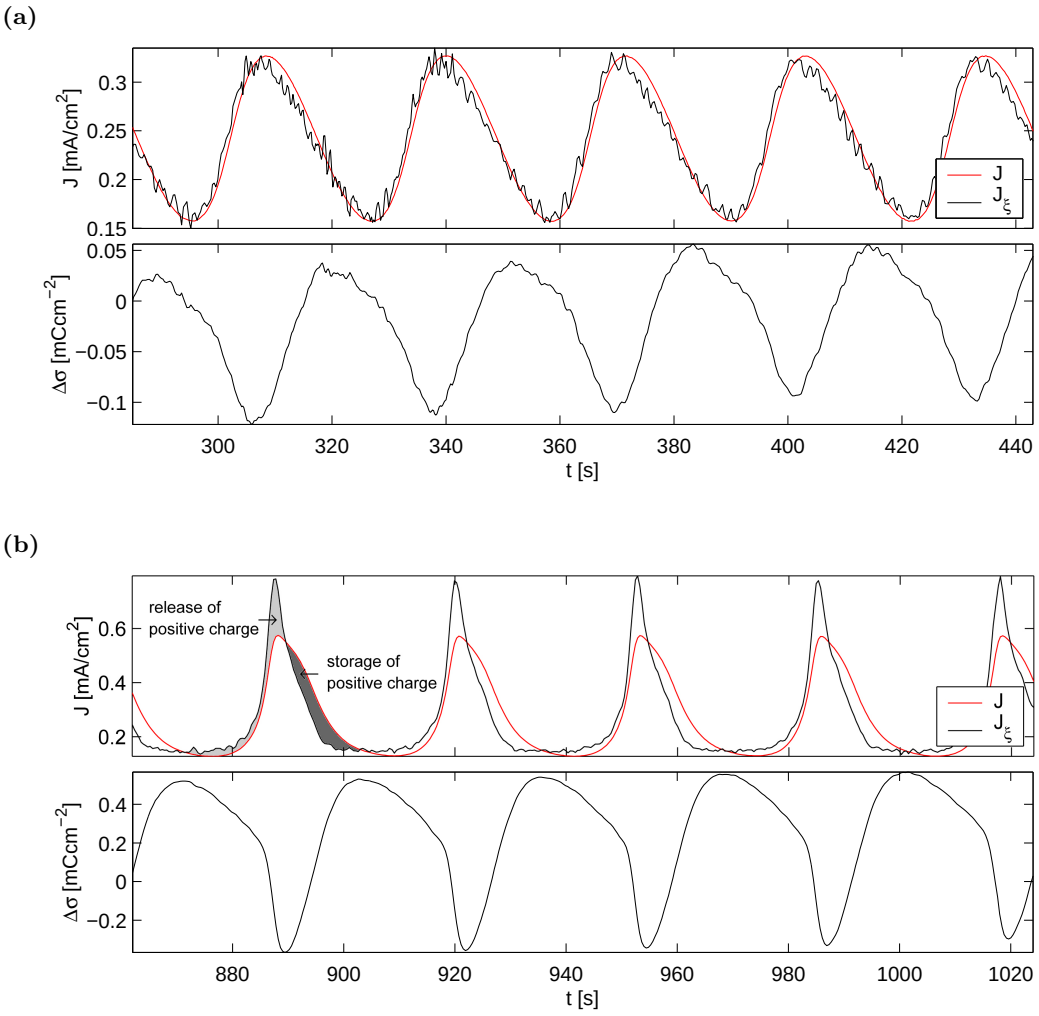

Figure 4.9: Discrepancy fitting the current density, $J - J_{\overline{\xi}}$ (top panel), and the corresponding charge density variations, $\Delta\sigma(t)$ (bottom panel). **(a)** Low-amplitude current density oscillations. Conditions: in Fig. 4.6. **(b)** High-amplitude current density oscillations. Conditions: in Fig. 4.2b.

of its oxidation number, the oxide species is always part of a the oxide layer measured with ellipso-microscopy. Hence, additional current density, not reflected in $\overline{\xi}$, could result from the completion of the oxidation of partially oxidized species.

This suggests that while J is increasing, the concentration of partially oxidized silicon increases, due to an increase in the hole capture rate or a decrease in the electron injection rate. The opposite is the case while J is decreasing, *i.e.* the concentration of partially oxidized species decreases.

Matsumura and Morrison (1983) proposed an abrupt change from silicon to silicon oxide, with partially oxidized species being present only at the interface, but the roughness of this interface can extend to several monolayers. A silicon (111) surface has a surface atom density of $8 \cdot 10^{14}\,\mathrm{cm}^{-2}$ (Allen and Gobeli, 1962). One monolayer of Si(OH) corresponds to a stored charge of $0.38\,\mathrm{mC/cm}^2$. The observed charge density variations have the same order of magnitude. The first and second panel of Fig. 4.10 illustrate the variations of the thickness of the layer of partially oxidized silicon in the case of high-amplitude oscillations. The effect is smaller in the case of low-amplitude oscillations (Fig. 4.11). Due to the smaller amplitude of

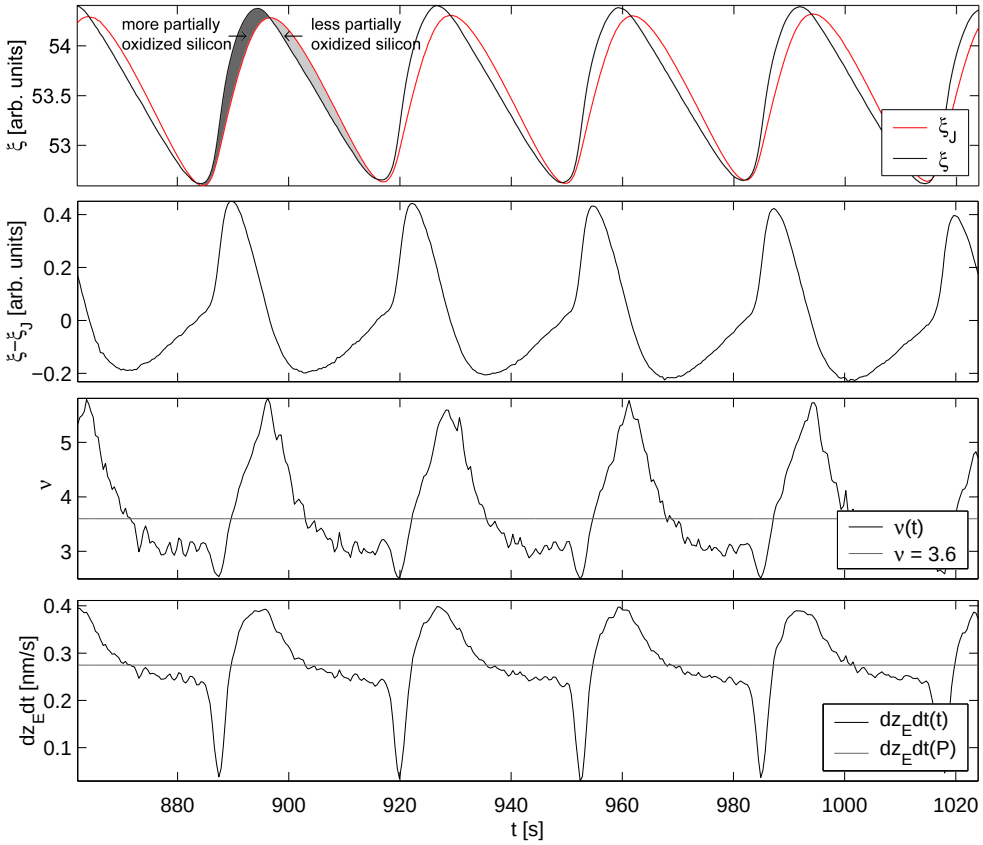

Figure 4.10: High-amplitude current density oscillations: time series of $\overline{\xi}$ and $\overline{\xi}_J$ (both top panel), the difference, $\overline{\xi} - \overline{\xi}_J$ (second panel), the time dependent dissolution valency, $\nu(t)$ (third panel), and time dependent etch rate, $\dot{\bar{z}}_{\mathrm{E}}(t)$ (bottom panel). Conditions: in Fig 4.8.

the current density oscillations, a smaller amplitude of Φ_{sc}, and therefore a smaller variation in the reaction rate ratio, is expected.

Valency Variation

Variations in the oxidation valency, ν, are connected to variations in the hydrogen evolution rate (Sec. 2.2). Blackwood *et al.* (1992) investigated hydrogen evolution *in situ* during current density oscillations. They observed maxima in the hydrogen evolution and minima in the oxide layer thickness simultaneously during the increasing flanks of J. The larger the contribution of hydrogen evolution to the overall oxidation, the lower the oxidation valency, ν.

In the fitting approach of this chapter, ν was assumed to be constant. To estimate how the discrepancy between the calculated and the measured time series translates into a variation of ν, the latter was calculated from Eq. (4.20):

$$\nu(t) = \frac{M}{F\rho} \frac{J(t)}{c_{\mathrm{opt}} \dot{\overline{\xi}}(t) + \dot{\bar{z}}_{\mathrm{E}}} \tag{4.31}$$

$\nu(t)$ being displayed in the third panel of Figs. 4.10 and 4.11 for high and low-amplitude oscillations, respectively. In the case of high-amplitude oscillations, $\nu(t)$ takes on values larger than 4, which cannot be physically explained. Instead, this either results from the fitting of c_{opt}, or it stems from other effects described in this discussion. However, the overall

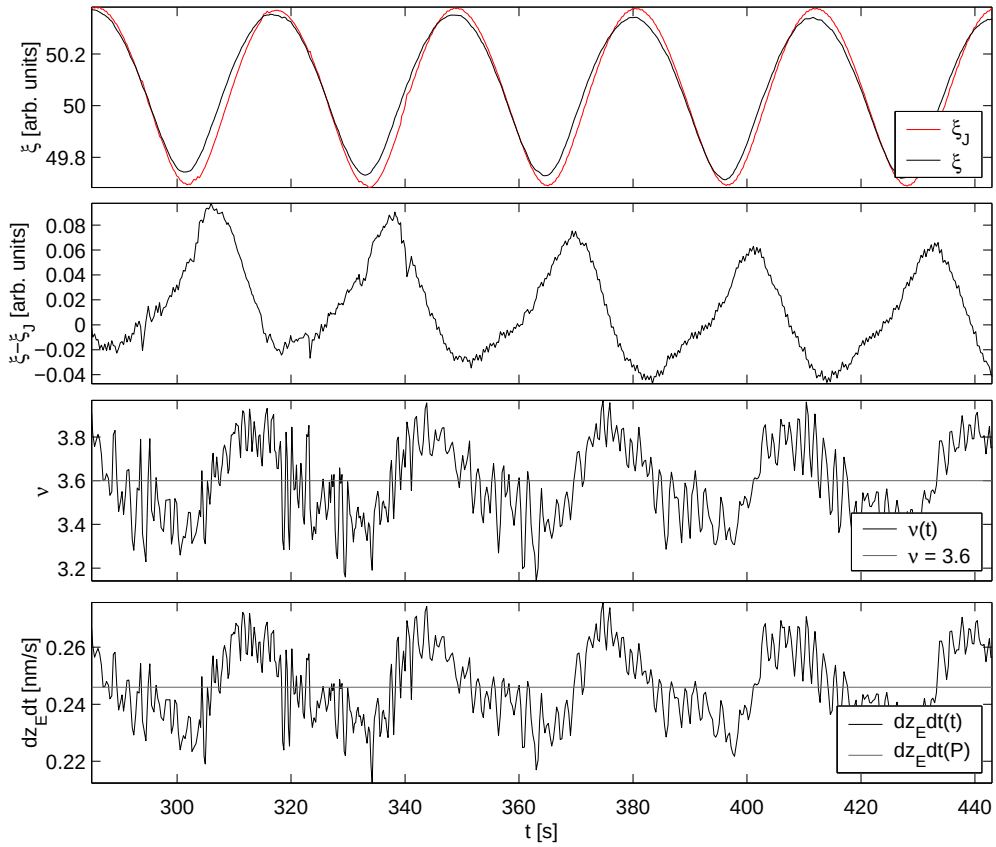

Figure 4.11: Low-amplitude current density oscillations: time series of $\overline{\xi}$ and $\overline{\xi}_J$ (both top panel), the difference, $\overline{\xi} - \overline{\xi}_J$ (second panel), the time dependent dissolution valency, $\nu(t)$ (third panel), and time dependent etch rate, $\dot{\bar{z}}_{\mathrm{E}}(t)$ (bottom panel). Conditions: in Fig 4.6.

trend observed by Blackwood *et al.* (1992) is observed with hydrogen evolution being larger when the oxide layer is thinner.

Etch Rate Variation

It is also possible that the discrepancy between J and $J_{\overline{\xi}}$ results from periodic changes in the etch rate. A negative current density discrepancy, *i.e.* $J - J_{\overline{\xi}} < 0$, would indicate an etch rate smaller than the period-averaged etch rate and *vice versa*. The variation of the etch rate resulting from the discrepancy between the calculated and the measured time series, $\dot{\bar{z}}_{\mathrm{E}}(t)$, is also calculated using Eq. (4.20):

$$\dot{\bar{z}}_{\mathrm{E}}(t) = \frac{M}{F\nu\rho} J(t) - c_{\mathrm{opt}} \dot{\overline{\xi}}(t) \tag{4.32}$$

The time series of $\dot{\bar{z}}_{\mathrm{E}}(t)$ compared to the period averaged values, $\dot{\bar{z}}_{\mathrm{E}}(P)$, are displayed in the last panel of each of Figs. 4.10 and 4.11. The temporal evolution of the etch rate is discussed in more detail in the next chapter.

Summary and Outlook

In this chapter it could be shown that the ellipso-microscopic signal is sensitive to the properties of the interface between silicon and the electrolyte, with and without an extra oxide

layer on top of the silicon surface. The domains of porous silicon formation (**I**), 'wet' oxide formation (**II**), and 'dry' oxide formation (**III**), can be distinguished, because of changes in the refractive index and layer thickness.

Furthermore, a linear dependency between the spatially averaged ellipso-microscopic signal and the spatially averaged oxide layer thickness could be established during the current density oscillations in domain **III**. A period averaged etch rate is assumed and the proportionality constant for the ratio of the oxide layer thickness to the ellipso-microscopic signal, c_{opt}, is obtained from fitting $J_{\overline{\xi}}$ to J.

At the end of this chapter several questions remain unsolved. On the one hand, the proportionality factor has to be evaluated quantitatively. On the other hand, the possible origins for the discrepancy between J and $J_{\overline{\xi}}$ have to be tested in order to ascertain which of them is responsible for the discrepancy. Several experimental routes for obtaining information to help answer these questions are proposed in the following. Furthermore, the role of etch rate variations is discussed in more detail in Chapter 5, with regard to experiments and to the setup of a mathematical model

It has been shown above that in domain **III** the data can be evaluated quantitatively, provided the proportionality factor is known. c_{opt} was estimated by fitting $J_{\overline{\xi}}$ to J, but it would be desirable to measure c_{opt} independently. This can be achieved by the inclusion of standard ellipsometry in the setup. The oxide thickness and refractive index of the oxide layer could be obtained with long exposure times when the system is in a steady state and be compared to the measured values of $\overline{\xi}$.

Combining the ellipso-microscopic setup with an infrared setup measuring the absorption of the silicon oxide bonds would provide a possibility to estimate the amount of partially oxidized silicon in the oxide layer. The simultaneous use of both methods using total reflection infrared spectroscopy at the back of a silicon prism would provide insights into phase relations between the amount of partially oxidized silicon, the oxide layer thickness and the current density.

To obtain insights into the phase relations between hydrogen evolution and current density, the hydrogen concentration could be measured *in situ* in the vicinity of the electrode to elucidate a possible correlation with the discrepancy between $J_{\overline{\xi}}$ and J.

As more than a single effect might be at work, further investigations to gain insight into their interplay have to be undertaken.

Chapter 5

Spatially Averaged Dynamics on p-type silicon

Understanding the spatially averaged dynamics of p-type silicon is the first step towards an understanding the dynamics of the electrodissolution of silicon. The analysis of the complication of spatial phenomena is postponed to Chapter 7. The necessity of illumination in the case of n-type silicon, also brings additional complications that are addressed in a later chapter (Chapter 6).

In Sec. 5.1, the dependency of the anodic electrodissolution on experimental parameters, such as external resistance, applied voltage and electrolyte concentration, is investigated.

In Sec. 5.2, a model consisting of ordinary differential equations is proposed, which is numerically simulated and compared to the experimental findings.

5.1 Parameter Dependency

In Sec. 4.2, it was shown that different types of oscillations establish depending on the final voltage in potential-step experiments. In particular, low-amplitude oscillations with and without complex dynamics, and high-amplitude oscillations were distinguished. Fig. 5.1 gives examples of non-oscillatory dynamics, where the system attains a steady states after a transient time. Two different kinds of steady states are observed, namely nodes (Fig. 5.1a) and foci (Fig. 5.1b), which show monotonous and oscillatory behavior, respectively, when the trajectory approaches the steady state. The character of the steady state depends on the applied voltage and the series resistance. Nodes are observed for low voltages, more specifically for low effective voltages, $\Phi_{\mathrm{eff}} < 2\,\mathrm{V}$, independently of the value of the series resistance. Foci are observed at an effective voltage larger than 2 V and low series resistances, $R_{\mathrm{ser}} < 30\,\mathrm{k\Omega}$.

A semilogarithmic parameter space plot giving an overview of the different dynamical states and their dependency on the applied voltage and the applied resistance is shown in Fig. 5.2. In addition to steady states, the parameter space plot includes oscillatory dynamics. For simplification, R_{ext} is assumed to be the sum of the R_{ser} and R_{cont}, all other contributions considered in Eq. 2.3 are neglected. From sheet resistance measurements R_{cont} could be estimated to be approximately $15.5\,\Omega$.

Sustained low-amplitude oscillations are observed for a sufficiently high resistance. High-amplitude oscillations are stable only at a very high resistance and a large applied voltage. They are damped in other regions of the parameter space. Damped high-amplitude oscilla-

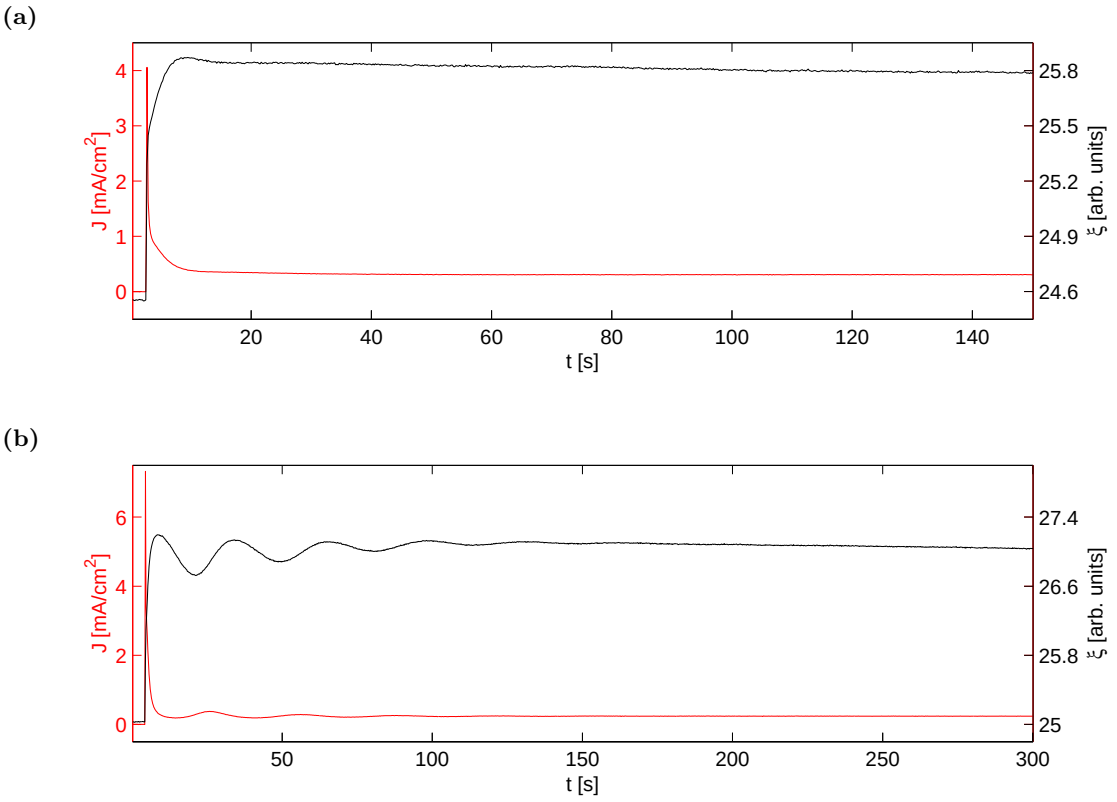

Figure 5.1: Typical transients in the steady state region. **(a)** Stable node at $U = 1.35$ V. **(b)** Stable focus at $U = 2.35$ V. Experimental conditions: $R_{\text{ext}} = 0\,\Omega$, $c_{\text{NH}_4\text{F}} = 0.05$ mol/l, pH = 2.4, and $A = 7.65\,\text{mm}^2$.

tions can be part of the transient leading to stable low-amplitude oscillations (Fig. 4.2c).

The damped current oscillations are accompanied by an overall drift of $\overline{\xi}$ to larger values. It is important to note that $\overline{\xi}$ is a sensitive indicator for the stationarity of the dynamics. Even if J has settled to a constant value, in the case of steady states, or to a constant average value, in the case of oscillatory dynamics, $\overline{\xi}$ is often still changing which indicates that the dynamical system is still drifting.

Fig. 5.3 shows phase space presentations of part of the data from the parameter space presentations (Fig. 5.2). In Fig. 5.3a, $\overline{\xi}$ is plotted versus J. The phase space trajectories all appear in a similar range of J, but $\overline{\xi}$ changes significantly. Trajectories of foci, high-amplitude oscillations (larger limit cycles) and low-amplitude oscillations (smaller limit cycles) are interspersed. The plot of $\overline{\xi}$ versus Φ_{eff} (Fig. 5.3b) reveals that $\overline{\xi}$ monotonously increases with Φ_{eff}. This increase is nearly linear for small and intermediate Φ_{eff}.

Assuming that the potential drop across the space charge layer is much smaller than the potential drop across the oxide layer, *i.e.* $\Phi_{\text{eff}} \approx \Phi_{\text{ox}}$, Fig. 5.3b suggests that the electric field within the oxide layer, E, is independent of the applied voltage and the external resistance. In Fig 5.3a, the constant current density is consistent with the presumption that the current density is limited by the migration of charge carriers through the oxide layer.

In the following, the interference of selected parameters, *i.e.* applied voltage, resistance and ammonium fluoride concentration, with the dynamics is discussed in detail. The experiments are conducted slightly differently from the ones discussed so far. After an initial potential-step from open-circuit potential to the operating voltage at a specific external resistance, the

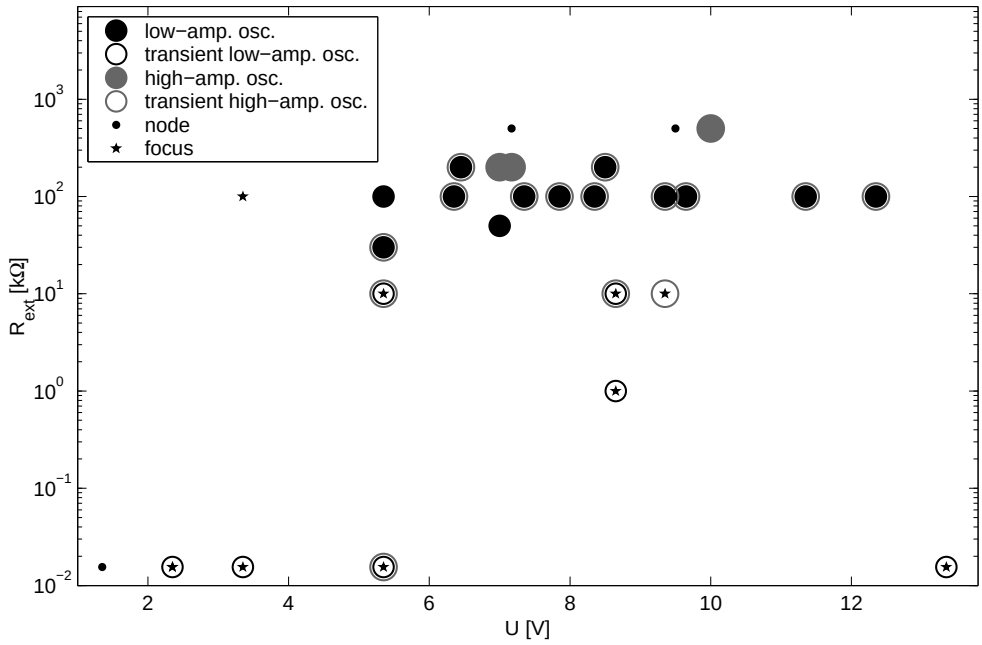

Figure 5.2: Resistance-voltage parameter plane obtained from voltage step experiments on p-type silicon at $c_{NH_4F} = 0.05$ mol/l.

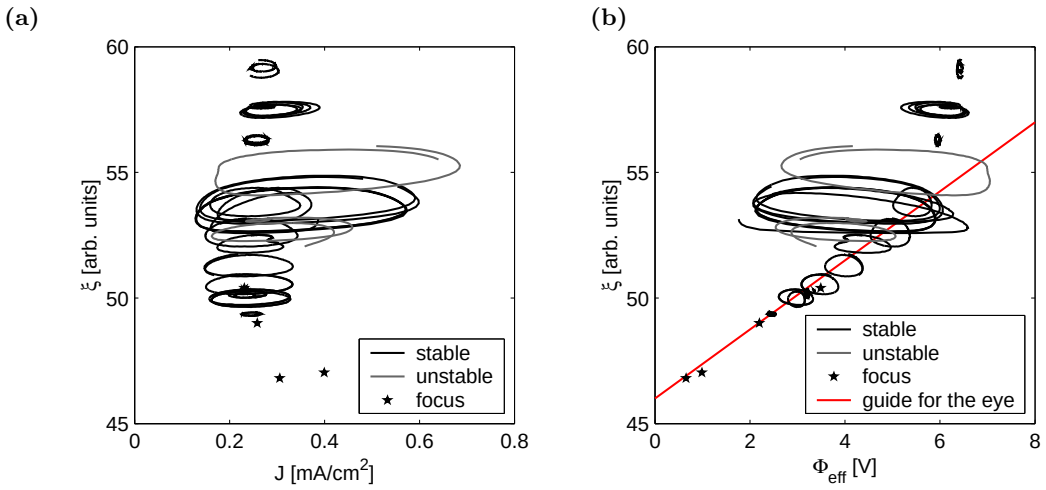

Figure 5.3: Phase space plots of data at different values of U and R_{ext} (for one sample electrode with $A = 4.26\,\mathrm{mm}^2$) for p-type silicon with $c_{NH_4F} = 0.05$ mol/l. **(a)** $\overline{\xi}$ versus J. **(b)** $\overline{\xi}$ versus Φ_{eff}.

parameters are adjusted step by step without returning to open-circuit potential in between the experiments. This reduces the transition time before the system has reached a stationary behavior.

Influence of the Effective Voltage

To get a better understanding of the influence of Φ_{eff}, phase space trajectories with a constant series resistance are compared. In contrast to Fig. 5.3, in Fig. 5.4 the $\overline{\xi} - \Phi_{eff}$ plot and the $\overline{\xi} - J$ plot show only data at $R_{ext} = 100\,\mathrm{k}\Omega$ for different values of U. Fig. 5.4a shows a linear dependency of $\overline{\xi}$ on Φ_{eff}. Fig. 5.4b shows that all trajectories are centered around the

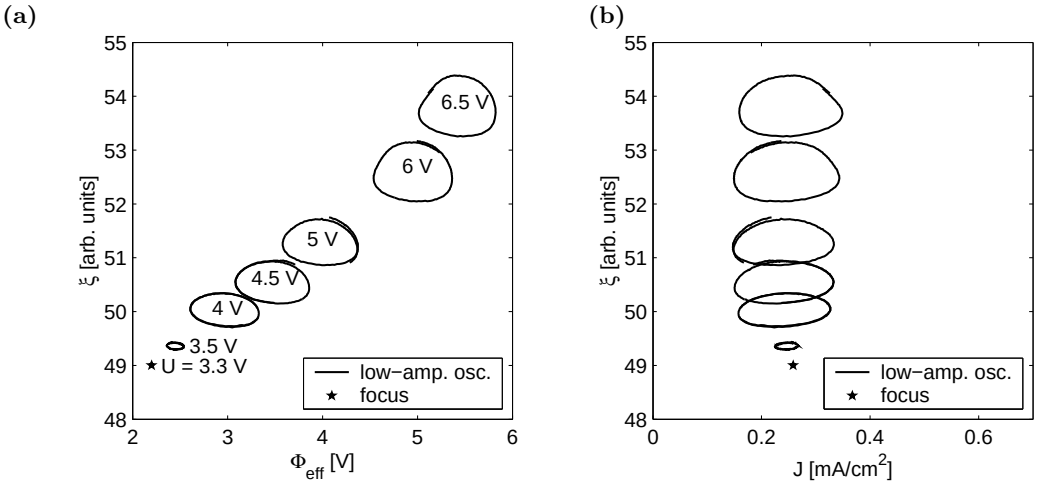

Figure 5.4: Hopf bifurcation upon changing the applied voltage, U. **(a)** $\overline{\xi}$ versus Φ_{eff}. **(b)** $\overline{\xi}$ versus J. Experimental conditions: $R_{\text{ser}} = 100\,\text{k}\Omega$, $A = 4.26\,\text{mm}^2$, and $c_{\text{NH}_4\text{F}} = 0.05\,\text{mol/l}$.

same current density value, $J \approx 0.24\,\text{mA/cm}^2$. With increasing applied voltage the dynamics changes from a stable fixed point (focus) to stable oscillations. As U is further increased, the limit cycle grows in size. This behavior indicates a supercritical Hopf bifurcation.

A Hopf bifurcation, *i.e.* a small amplitude limit cycle bifurcating from a fixed point branch, is the bifurcation through which oscillations most frequently arise. The amplitude of the limit cycle grows as the bifurcation parameter departs from the bifurcation point into the oscillatory region. The bifurcation is called supercritical when a stable fixed point becomes an unstable fixed point and a stable limit cycle emerges. Fig. 5.4 shows exactly the behavior indicative of a super-critical Hopf bifurcation. The bifurcation point for the Hopf bifurcation at $R_{\text{ser}} = 100\,\text{k}\Omega$ lies between $U = 3.3\,\text{V}$ and $U = 3.5\,\text{V}$.

Effective Voltage and Etch Rate

The effective voltage has an influence on the dynamics of the system, as seen in the previous section, where it was established that with increasing Φ_{eff} the oxide layer thickness increases. In this section it is investigated, whether it also affects the etch rate. The latter can be calculated in different ways, depending on the experimental conditions. A different calculation method is used for oscillations, for etch back at open-circuit potential, and for steady states. Two of the methods are introduced in Chapter 4. The period-averaged etch rate during oscillations, $\left(\dot{\overline{z}}_{\text{E}}\right)_{\text{osc}}$, is obtained from the integral of the current density with Eq. (4.27). When the system is at a steady state (ss), $\overline{\xi}$ is constant. It follows that the oxide formation rate equals the oxide etch rate:

$$\left(\dot{\overline{z}}_{\text{E}}\right)_{\text{ss}} = \left(\dot{\overline{z}}\right)_{\text{ss}} \tag{5.1}$$

with the formation rate given by Eq. (4.18):

$$\left(\dot{\overline{z}}_{\text{E}}\right)_{\text{ss}} = \frac{M}{F\nu\rho}\,J \tag{5.2}$$

The etch rate at open-circuit potential, $\left(\dot{\overline{z}}_{\text{E}}\right)_{\text{ocp}}$, is calculated by multiplying the initial rate

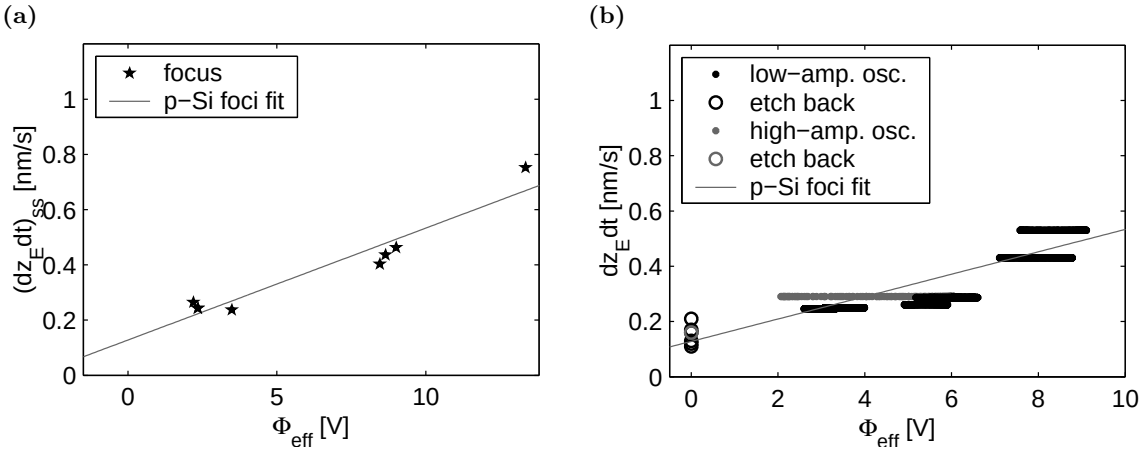

Figure 5.5: Dependency of the etch rate, $\dot{\bar{z}}_{\mathrm{E}}$, on the effective voltage, Φ_{eff}, for p-type silicon with $c_{\mathrm{NH_4F}} = 0.05\,\mathrm{mol/l}$. **(a)** $(\dot{\bar{z}}_{\mathrm{E}})_{\mathrm{ss}}$ is linearly fitted with a slope, $c_{\mathrm{inc}} = 0.041\,\mathrm{nm/sV}$, and an axis intercept, $\left(\dot{\bar{z}}_{\mathrm{E}}\right)_0 = 0.13\,\mathrm{nm/s}$. **(b)** The values for $(\dot{\bar{z}}_{\mathrm{E}})_{\mathrm{osc}}$ and $(\dot{\bar{z}}_{\mathrm{E}})_{\mathrm{ocp}}$ from Tab. 5.1 in comparison to the fit from (a).

U_{osc} [V]	$\left(\dot{\bar{z}}_{\mathrm{E}}\right)_{\mathrm{osc}}$ [nm/s]	c_{opt} [nm]	$\left(\dot{\bar{\xi}}\right)$ [1/s]	$\left(\dot{\bar{z}}_{\mathrm{E}}\right)_{\mathrm{ocp}}$ [nm/s]	U_{ocp} [V]
7.35	**0.26**	1.89	0.07	**0.13**	-0.60
5.35	**0.25**	1.54	0.07	**0.11**	0.10
7.17	**0.29**	1.33	0.12	**0.16**	-1.20
8.50	**0.29**	1.30	0.12	**0.16**	-1.00
3.50	**0.25**	1.30	0.09	**0.12**	-0.60
12.35	**0.53**	1.78	0.12	**0.21**	-0.54
11.35	**0.43**	1.99	0.09	**0.17**	-0.49

Table 5.1: Comparison of etch rates during oscillations, $\left(\dot{\bar{z}}_{\mathrm{E}}\right)_{\mathrm{osc}}$, and at open-circuit potential, $\left(\dot{\bar{z}}_{\mathrm{E}}\right)_{\mathrm{ocp}}$.

of change of the averaged ellipso-microscopic signal, $\left(\dot{\bar{\xi}}\right)_{\mathrm{init}}$, with c_{opt} estimated from independent experiments in the oscillatory domain according to Eq. (4.28):

$$\left(\dot{\bar{z}}_{\mathrm{E}}\right)_{\mathrm{ocp}} = c_{\mathrm{opt}} \left(\dot{\bar{\xi}}\right)_{\mathrm{init}} \tag{5.3}$$

In Fig. 5.5a, the etch rates of the steady states as obtained from Eq. 5.2 are plotted versus the effective voltage, Φ_{eff}. Only steady states that lie in domain **III** of passivating oxide, which are all foci, are plotted (Fig. 5.2). They show a linear dependency on Φ_{eff} according to:

$$\left(\dot{\bar{z}}_{\mathrm{E}}\right)_{\mathrm{ss}} = c_{\mathrm{inc}} \Phi_{\mathrm{eff}} + \left(\dot{\bar{z}}_{\mathrm{E}}\right)_0 \tag{5.4}$$

$c_{\mathrm{inc}} = 0.41\,\mathrm{nm/sV}$ being the etch rate increment and $\left(\dot{\bar{z}}_{\mathrm{E}}\right)_0 = 0.13\,\mathrm{nm/s}$ being the etch rate at $\Phi_{\mathrm{eff}} = 0\,\mathrm{V}$.

$\left(\dot{\bar{z}}_{\mathrm{E}}\right)_{\mathrm{osc}}$ and $\left(\dot{\bar{z}}_{\mathrm{E}}\right)_{\mathrm{ocp}}$ are obtained in pairs for the same experimental conditions, and are therefore directly comparable (Tab. 5.1). $\left(\dot{\bar{z}}_{\mathrm{E}}\right)_{\mathrm{osc}}$ is one to three times larger than $\left(\dot{\bar{z}}_{\mathrm{E}}\right)_{\mathrm{ocp}}$.

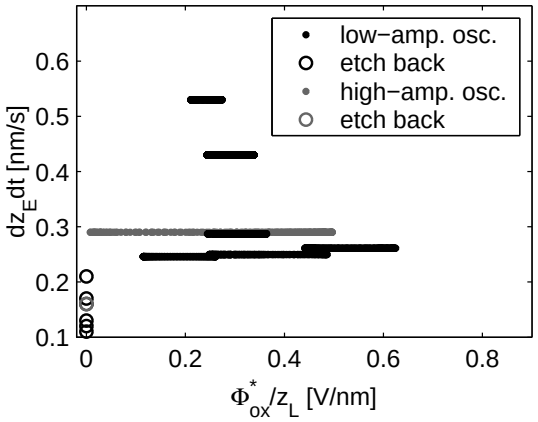

Figure 5.6: Dependency of the etch rate, $(\dot{\tilde{z}}_{\mathrm{E}})_{\mathrm{osc}}$, on the electric field, $\Phi^*_{\mathrm{ox}}/z_{\mathrm{L}}$, for p-type silicon. Experimental conditions: in Fig. 5.5b.

Their voltage dependency is similar to that observed in the case of the steady states. The etch rates during oscillations and during the subsequent etch back are displayed in Fig. 5.5b together with the linear fit of the steady states (Eq. 5.4). They agree well with each other.

In summary, the etch rates of steady states and of oscillations show a distinct linear dependency on Φ_{eff}. This dependency could be responsible for a feedback in the oscillation mechanism. It also explains the stability of steady states at a variety of applied voltages, because the increase in the etch rate can balance an increases in the oxide formation rate.

In Fig. 5.6, the etch rate is plotted versus the electric field in the oxide layer. The latter is approximated by assuming that $\Phi_{\mathrm{sc}} - \Delta E_{\mathrm{F}}/e_0 \approx 2\,\mathrm{V}$ and:

$$\Phi^*_{\mathrm{ox}} = U - JAR - 2\,\mathrm{V} \tag{5.5}$$

with z_{L} being obtained with the method described in Sec. 4.4.

Fig. 5.6 shows that under different conditions, the trajectories oscillate around a values of the approximated field, $\Phi^*_{\mathrm{ox}}/z_{\mathrm{L}} = 0.3\,\mathrm{V/nm}$.

Influence of the External Resistance

A resistor in series with the working electrode is essential to obtain sustained current density oscillations. Upon increasing R_{ser}, a supercritical Hopf bifurcation is observed at constant U (Fig. 5.7a), as it was found for increasing U at constant R_{ser}. A stable focus changes to an unstable one and a stable limit cycle emerges. The size of the limit cycle initially increases when increasing R_{ser}. The system moves out of the oscillatory regime through a second Hopf bifurcation at very high values of R_{ser}. This can be seen from the small limit cycle at $R_{\mathrm{ser}} = 100\,\mathrm{k\Omega}$. Fig. 5.7b shows that again all phase space trajectories are centered around an average current density value, $J \approx 0.24\,\mathrm{mA/cm^2}$. At $U = 3.5\,\mathrm{V}$, the critical value of the bifurcation parameter R_{ser} lies between $5\,\mathrm{k\Omega}$ and $15\,\mathrm{k\Omega}$. The Hopf bifurcation is supercritical.

Influence of the Concentration of Ammonium Fluoride

The concentration of ammonium fluoride has a large influence on the dynamics, because, in combination with the pH, it changes the concentration of the etching species (Sec. 2.2). Figs. 5.8b and 5.8a show data from experiments conducted under similar conditions. The

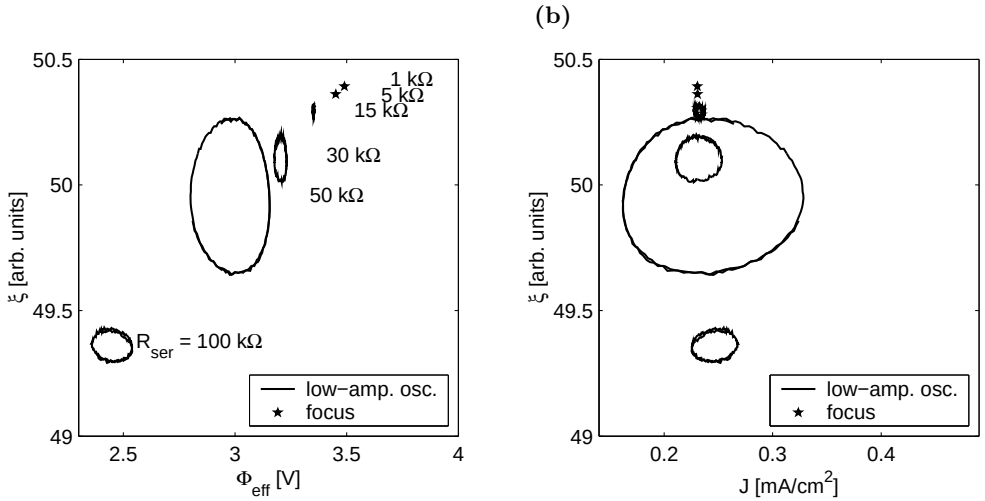

Figure 5.7: Hopf bifurcation upon changing the series resistance, R_{ser}. **(a)** $\overline{\xi}$ versus Φ_{eff}. **(b)** $\overline{\xi}$ versus J. Experimental conditions: $U = 3.5\,\mathrm{V}$, $A = 4.26\,\mathrm{mm}^2$, and $c_{\mathrm{NH_4F}} = 0.05\,\mathrm{mol/l}$.

former is conducted at a four times higher ammonium fluoride concentration leading to a current density that is four times larger than in the former case.

During one oscillation period, the average etch rate balances the average formation rate. It is thus not surprising that the latter increases to the same degree as the former: In the case of a higher electrolyte concentration, more oxide is etched. As more oxide is etched, the current density is higher, because more oxide can be formed, as oxide formation is limited by the thickness of the oxide layer on the electrode. At the same time the oxide formation rate is limited by the current density, because the effective voltage, Φ_{eff} decreases due to the increase of the ohmic potential drop. It decreases as the current density increases. The rate of oxide formation depends on Φ_{eff} and below a critical value, the oxide formation falls below the etch rate and z_{L} decreases. At high currents, Φ_{eff} is lower, therefore shorter oscillation periods, P, are anticipated and indeed observed. $P = 4.2\,\mathrm{s}$ ($c_{\mathrm{NH_4F}} = 0.2\,\mathrm{mol/l}$) is considerably smaller than $P = 56.4\,\mathrm{s}$ ($c_{\mathrm{NH_4F}} = 0.05\,\mathrm{mol/l}$).

$\overline{\xi}$ is also affected by the increase in $c_{\mathrm{NH_4F}}$. At $c_{\mathrm{NH_4F}} = 0.2\,\mathrm{mol/l}$, the amplitude of $\overline{\xi}$, $\overline{\xi}^{\mathrm{max}} - \overline{\xi}^{\mathrm{min}} = 0.34$, is three times smaller than at $c_{\mathrm{NH_4F}} = 0.05\,\mathrm{mol/l}$. The increase of the oxide formation compensates the increase in oxide etching, but the shorter periods lead to a much smaller amplitude of $\overline{\xi}$. The averaged signal, $\overline{\xi}$, can still be resolved, but the resolution of the local dynamics, which is important for investigations of spatial pattern formation, is problematic. In the case of $c_{\mathrm{NH_4F}} = 0.2\,\mathrm{mol/l}$, the local oscillation amplitude of ξ is close to the amplitude of the noise. In Fig. 5.9, the local dynamics of ξ for both concentrations are compared.

Furthermore, hydrogen blisters are observed during oscillations at $c_{\mathrm{NH_4F}} = 0.2\,\mathrm{mol/l}$. The blisters increase their size over the course of the experiments, as can be seen in Fig. 5.10. The increased concentration leads to a higher current density and therefore to a higher hydrogen evolution rate. Instead of dissolving into the electrolyte solution, as in the case of the lower concentration, the hydrogen forms gas bubbles at the edges of the electrode surface.

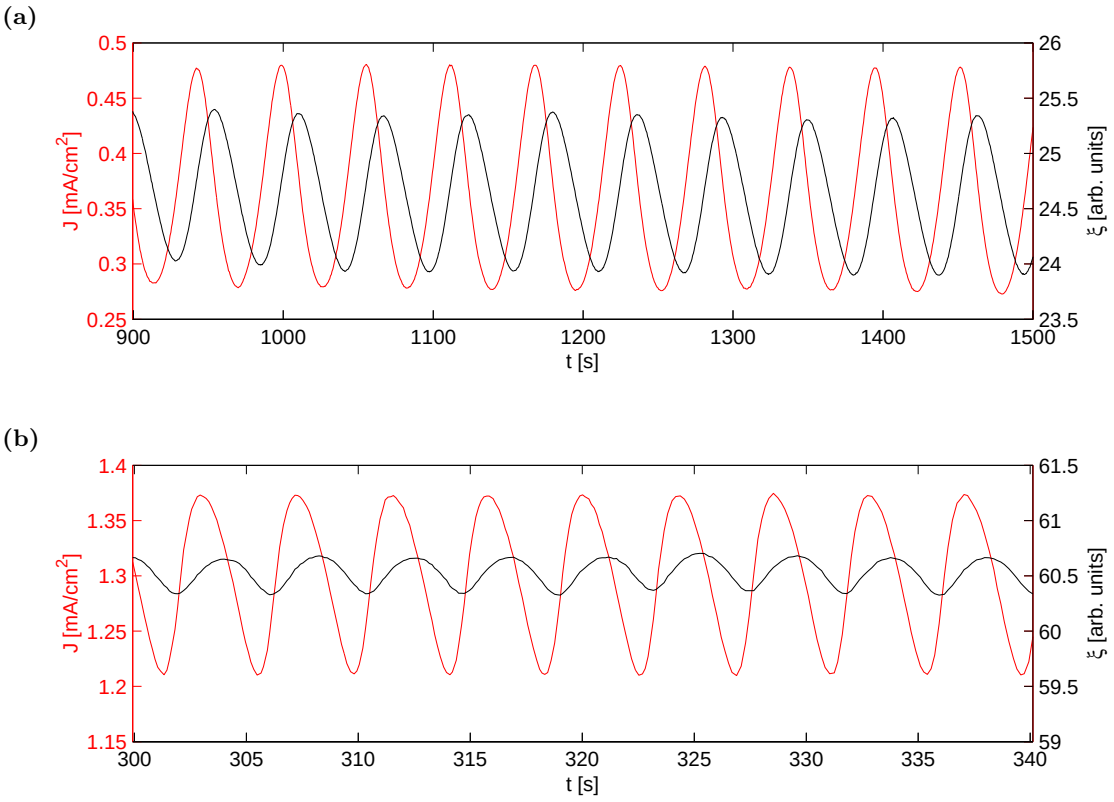

Figure 5.8: Influence of the ammonium fluoride concentration on the oscillations. At **(a)** c_{NH_4F} = 0.05 mol/l the oscillation period is P = 56.4 s, and at **(b)** c_{NH_4F} = 0.2 mol/l the oscillation period is P = 4.2 s. The ranges of J and $\overline{\xi}$ are equal in both panels. The time axes are scaled differently. Experimental conditions: **(a)** U = 9.65 V, R_{ser} = 100 kΩ, c_{NH_4F} = 0.05 mol/l, pH = 2.3, and A = 4.91 mm²; **(b)** U = 8.65 V, R_{ser} = 100 kΩ, c_{NH_4F} = 0.2 mol/l, pH = 3.5, and A = 4.66 mm².

Concentration and Complex Dynamics

The concentration also has a strong influence on the complexity of the dynamics. At the lower concentration, *i.e.* c_{NH_4F} = 0.05mol/l, period-1 and complex period-2 oscillations are observed (Fig. 4.2). A time series exhibiting simple period-2 oscillations is displayed in Fig. 5.11a. In addition, at the higher concentration, *i.e.* c_{NH_4F} = 0.2mol/l, period-3 oscillations (Fig. 5.11b) and irregular oscillations (Figs. 5.11c and 5.11d) are observed.

Fig. 5.12 displays the $J - \overline{\xi}$ phase space plots of oscillations with differing periodicity. In the case of period-1 oscillations, only one loop is observed (Fig. 5.12a). The phase space plot of the period-2 oscillations from Fig. 5.11a in Fig. 5.12b exhibits also only one loop, which is however deformed. Thus the minimal phase space dimension of these period-2 oscillations is still two. In contrast, the trajectory of the time series in Fig. 4.2c intersects itself in the $J - \overline{\xi}$ phase plane (Fig. 5.12c). Thus, the minimal phase-space dimension is three.

The phase space trajectory for the period-3 oscillations shows two distinct loops and a broad band of low amplitude (Fig. 5.12d). Fig. 5.12e shows no more separate loops but a broad band structure. The phase space trajectory in Fig. 5.12f shows a very high degree of irregularity.

Next-maximum mapping (Fig. 5.13) is used to investigate the periodicity more closely and to elucidate the existence of chaos. In a next-maximum map, one maximum, $J^{max}(n+1)$, is plotted versus the previous maximum, $J^{max}(n)$, which reduces the continuous dynamics to a two-dimensional time-discrete map. The next-maximum map of period-1 oscillations is a

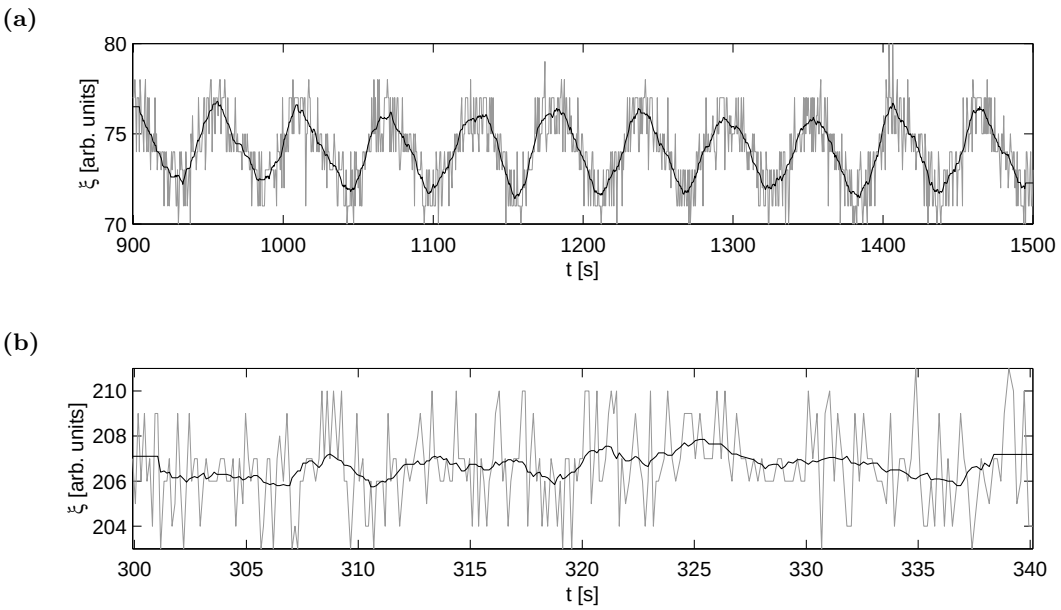

Figure 5.9: Local time series of the ellipso-microscopic signal, ξ (gray) smoothed with a central moving average with $k = 10$ (black) for **(a)** $c_{\mathrm{NH_4F}} = 0.05\,\mathrm{mol/l}$ and **(b)** $c_{\mathrm{NH_4F}} = 0.2\,\mathrm{mol/l}$. Conditions: Fig. 5.8.

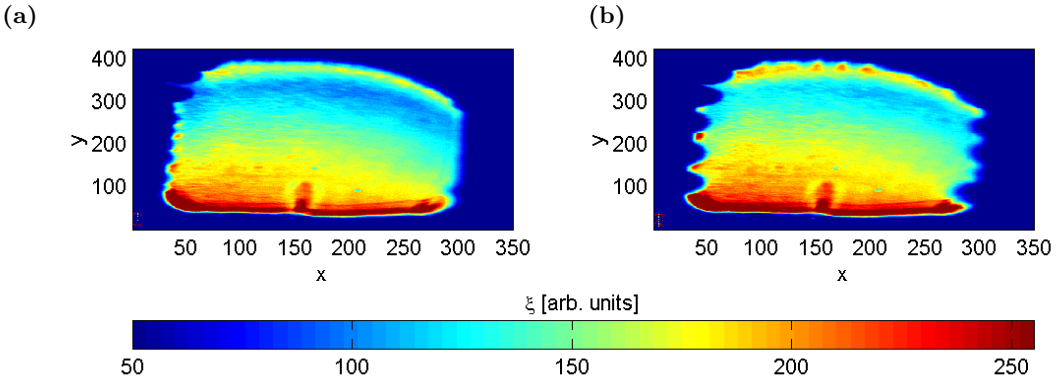

Figure 5.10: Hydrogen blisters at the edge of the electrode area in the plot of ξ for the whole electrode at two maxima of $\overline{\xi}$ at **(a)** $t = 460\,\mathrm{s}$. **(b)** At $t = 775\,\mathrm{s}$, the size of the blisters has increased. Experimental conditions: $U = 12.49\,\mathrm{V}$, $R_{\mathrm{ser}} = 10\,\mathrm{k\Omega}$, $c_{\mathrm{NH_4F}} = 0.02\,\mathrm{mol/l}$, pH = 3.5, and $A = 4.66\,\mathrm{mm^2}$.

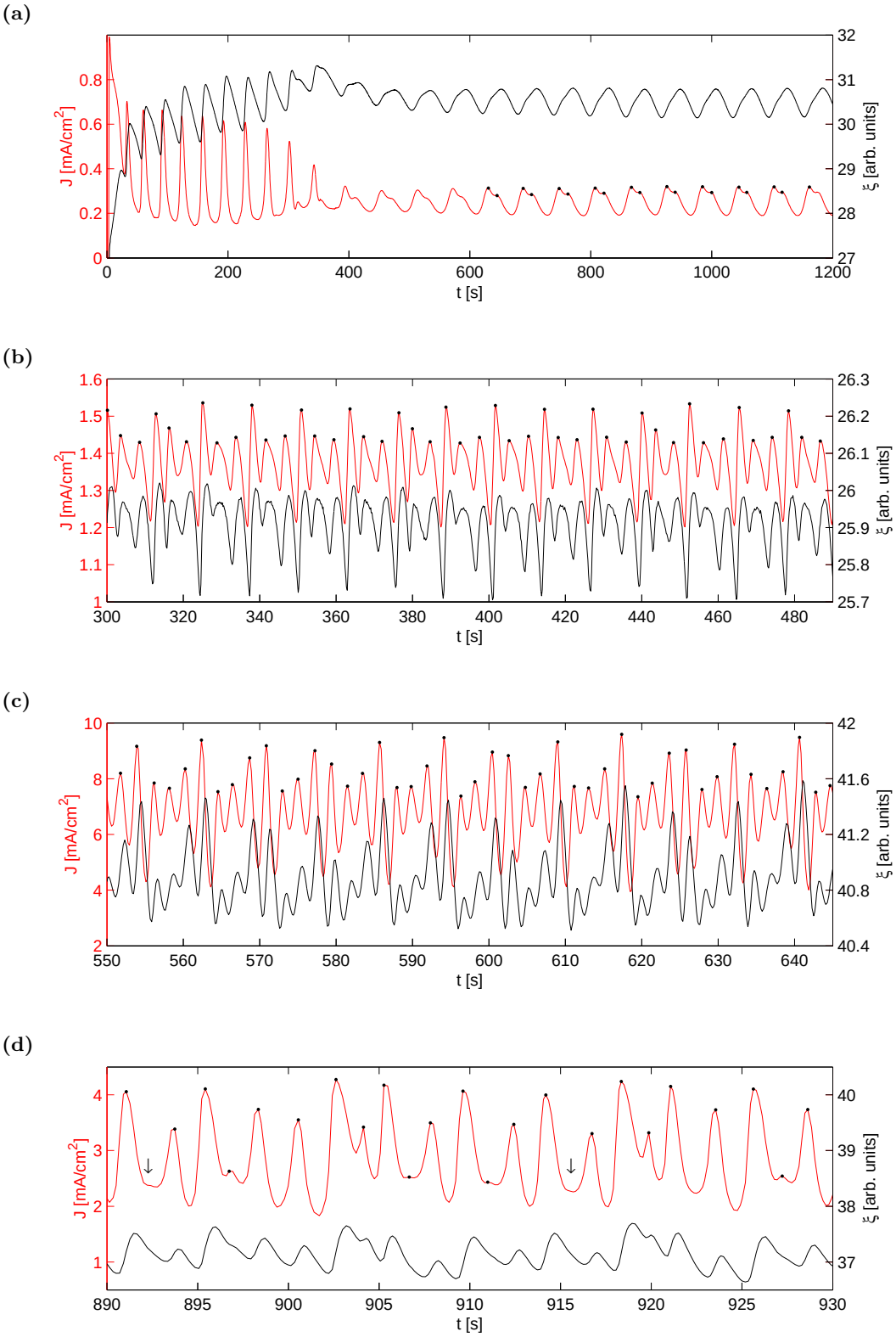

Figure 5.11: Complex dynamics at low (a) and high (b-d) ammonium fluoride concentrations. Dots indicate the maxima of the current density oscillations. Maxima that are not resolved are indicated by ↓. **(a)** Damped high-amplitude oscillations followed by low-amplitude period-2 oscillations. **(b)** Period-3 oscillations. **(c,d)** Irregular oscillations. Experimental conditions: **(a)** $R_{\mathrm{ext}} = 100\,\mathrm{k\Omega}$, $U = 7.35\,\mathrm{V}$, $c_{\mathrm{NH_4F}} = 0.05\,\mathrm{mol/l}$, pH = 2.4, and $A = 7.65\,\mathrm{mm^2}$. **(b-d)**: $c_{\mathrm{NH_4F}} = 0.2\,\mathrm{mol/l}$, pH = 3.5, and $A = 4.66\,\mathrm{mm^2}$. **(b)** $U = 12.49\,\mathrm{V}$, $R_{\mathrm{ser}} = 150\,\mathrm{k\Omega}$. **(c)** $U = 12.49\,\mathrm{V}$, $R_{\mathrm{ser}} = 10\,\mathrm{k\Omega}$ **(d)** $U = 10\,\mathrm{V}$, $R_{\mathrm{ser}} = 40\,\mathrm{k\Omega}$.

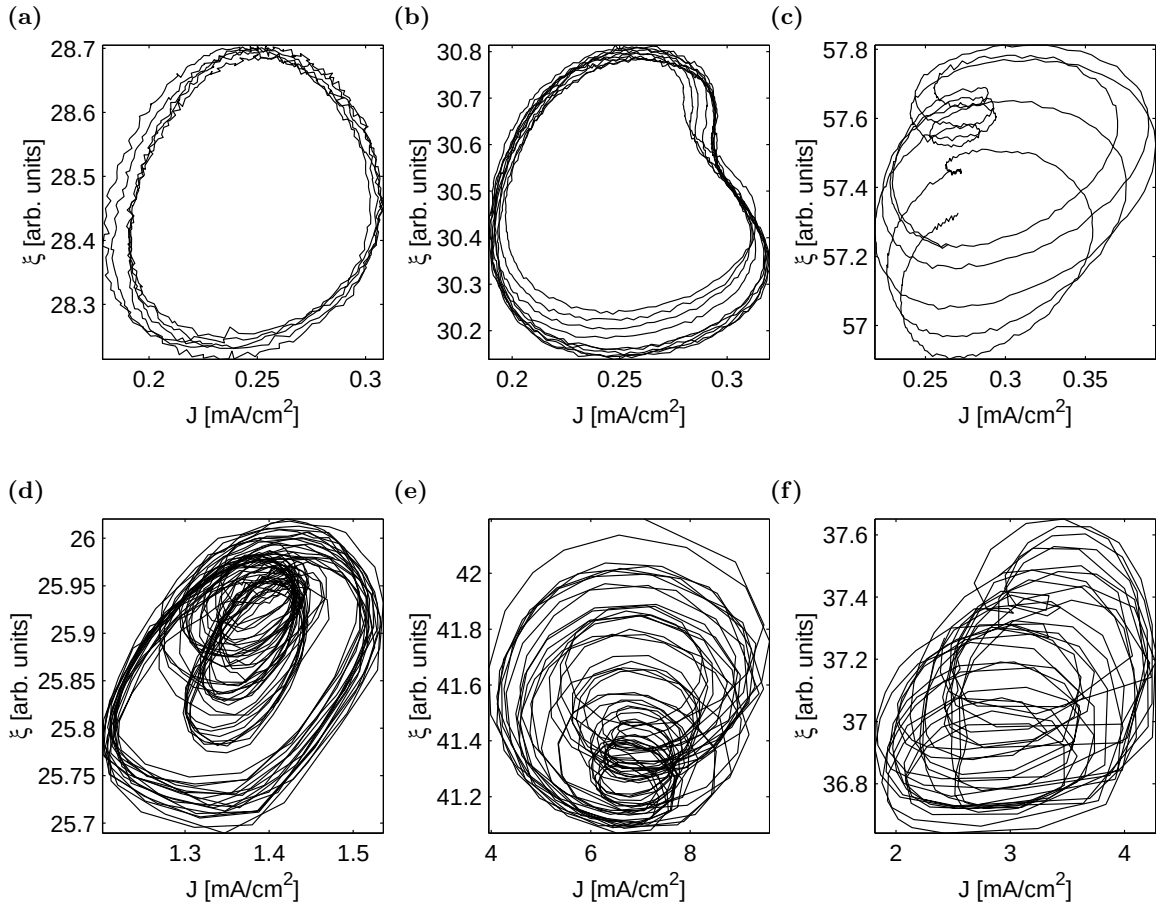

Figure 5.12: $J - \overline{\xi}$ phase space for different oscillation dynamics. **(a)** Period-1 oscillations. Experimental conditions in Fig. 4.2a. **(b)** Period-2 oscillations. Experimental conditions in Fig. 5.11a. **(c)** Period-2 oscillations. Experimental conditions in Fig. 4.2c. **(d)** Period-3 oscillations. Experimental conditions in Fig. 5.11b. **(e)** Quasi-periodic oscillations. Experimental conditions in Fig. 5.11c. **(f)** Chaotic oscillations. Experimental conditions in Fig. 5.11d.

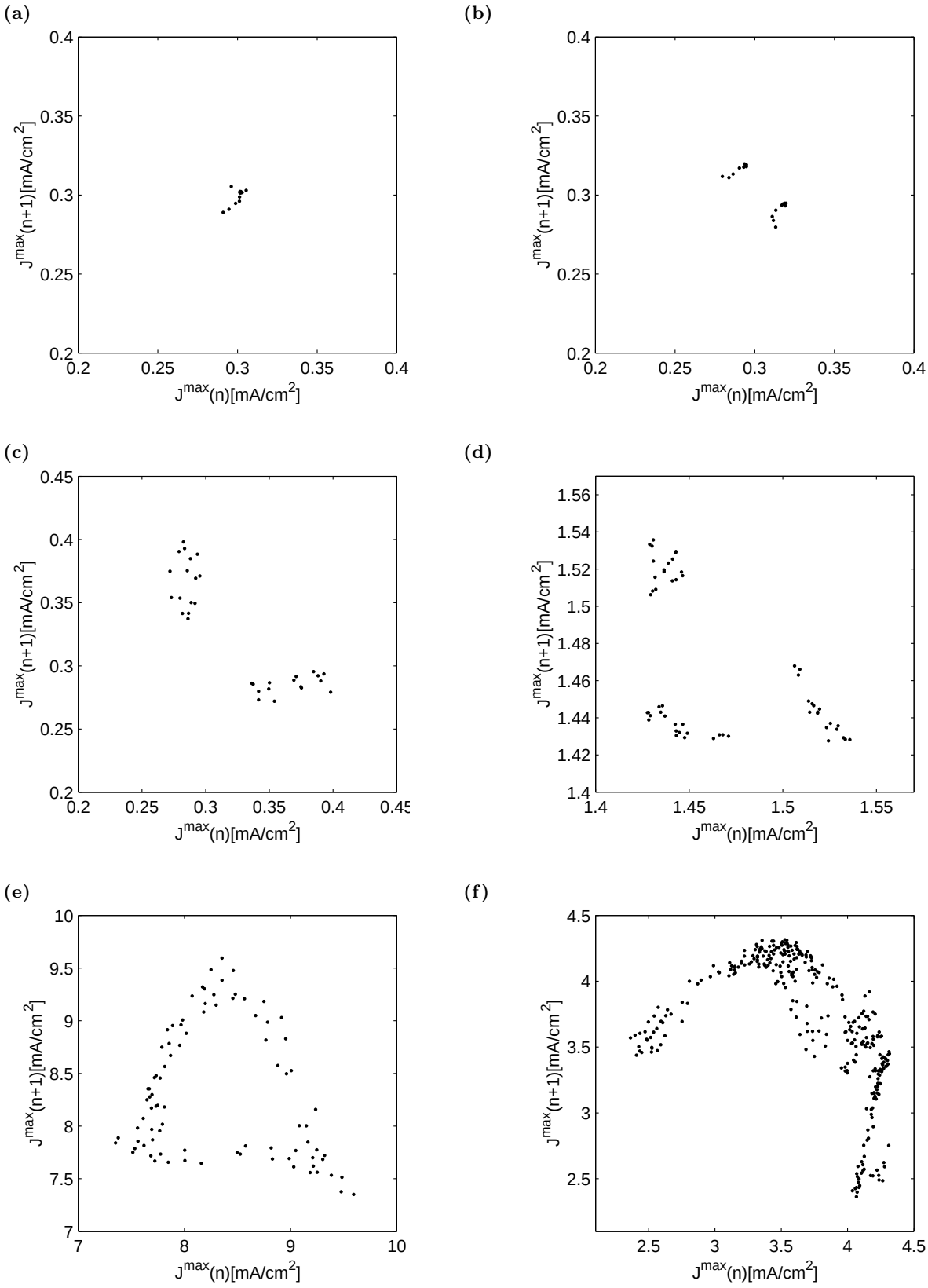

Figure 5.13: Next-maximum maps for the different oscillations in Fig. 5.12. **(a)** Period-1 oscillations. **(b)** Period-2 oscillations. **(c)** Period-2 oscillations. **(d)** Period-3 oscillations. **(e)** Quasi-periodic oscillations. **(f)** Chaotic oscillations.

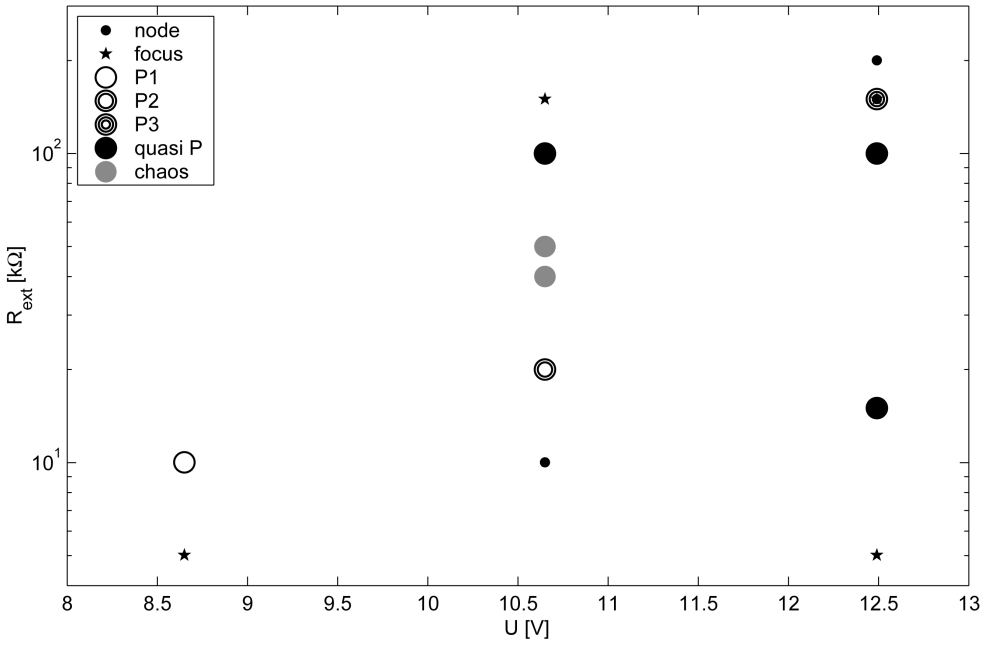

Figure 5.14: $R_{\mathrm{ext}} - U$ parameter space. Experimental conditions: $c_{\mathrm{NH_4F}} = 0.02\,\mathrm{mol/l}$, pH = 3.5, $A = 4.66\,\mathrm{mm}^2$.

single point, because the trajectory returns to the same point at each maximum (Fig. 5.13a). The next-maximum map of the period-2 oscillations displays two distinct areas of recurrence (Figs. 5.13b and 5.13c). In the case of the period-3 oscillations, three loops in phase space are represented by three areas of recurrence (Fig. 5.13d). The areas of recurrence discussed in these four examples are not points but rather clusters of points. The spreading out of the points results most probably from noise in the signals. Quasi-periodicity manifest itself as closed curve in the next-maximum map (Fig. 5.13e). Accordingly, the time series in Fig. 5.12e shows a certain amount of periodicity, but no repetitive pattern can be observed.

In contrast, the next-maximum map of the data in Fig. 5.12f can to a first approximation be described by a one-dimensional curve exhibiting two maxima, one at $J^{\max}(n) = 3.5\,\mathrm{mA/cm}^2$ and one at $J^{\max}(n) = 4\,\mathrm{mA/cm}^2$ (Fig. 5.13f). Obviously, the curve is significantly broadened, which most likely stems from noise. The quasi one-dimensional map therefore suggests that the dynamics is deterministically chaotic and thus lives in a low dimensional phase space.

An overview of the dynamics at a concentration, $c_{\mathrm{NH_4F}} = 0.2\,\mathrm{mol/l}$, is given in Fig. 5.14. The experimental data show a large diversity of dynamics. No obvious scenario for the onset of complex oscillations can be observed. Nevertheless, complex dynamics at intermediate R_{ext} are enclosed by steady states at higher and lower resistances. Chaotic dynamics are enclosed by less complex dynamics.

5.2 Oscillation Mechanism

In this section, the experimental results described in the previous section and literature data are used to derive a mathematical model that captures the oscillatory behavior and enables the essential feedback loops that cause the oscillatory instability to be determined. As described in the first section of this chapter, during the electrodissolution of silicon oscillations emerge

from a Hopf bifurcation when either the applied voltage or the resistance in series with the silicon working electrode is changed. Furthermore, oscillatory dynamics always requires a nonzero value of $R_{\mathrm{ser}} > 0$. This shows that electrical quantities are important for the oscillatory instability, *i.e.* that a purely chemical mechanism cannot be sufficient to describe the system.

Therefore, first the evolution equations for the potential drops across the oxide layer, Φ_{ox}, and the space charge layer of silicon, Φ_{sc}, are derived. Then a mass balance equation for the oxide layer thickness is set up.

The pH at the oxide|electrolyte interface is assumed to be constant, because of the buffer capacity of the ammonium fluoride electrolyte. Simulations showed that concentration of the etching species never deviate considerably from their bulk values. Therefore, they are kept constant in the further expansions of the model.

Derivation of the Mathematical Model

The evolution equations for Φ_{sc} and Φ_{ox} follow from the simplified equivalent circuit (Fig. 2.3b). Φ_{ox} can be expressed through the specific capacitance of the oxide, C_{ox}:

$$\Phi_{\mathrm{ox}} = \frac{q}{C_{\mathrm{ox}} A} \tag{5.6}$$

$$= \frac{q\ z_{\mathrm{L}}}{A\ \epsilon\ \epsilon_0} \tag{5.7}$$

assuming that C_{ox} can be described by the capacitance of a plate capacitor, $\epsilon = 3.75$ being the relative permittivity of silicon oxide (Demierry *et al.*, 1994), and $\epsilon_0 = 8.85418\ 10^{-14}\,\mathrm{F/cm}$ being the vacuum permittivity. q is the charge in the oxide layer located at the two interfaces. z_{L} and q are both time dependent during current density oscillations. Accordingly, the time derivative of Φ_{ox} is given by:

$$\dot{\Phi}_{\mathrm{ox}} = \frac{1}{A\ \epsilon\ \epsilon_0} \left(z_{\mathrm{L}} \dot{q} + q\ \dot{z}_{\mathrm{L}}\right) \tag{5.8}$$

The time derivative of the charge, $\dot{q}$, results from the difference between the total current density, J, and the migration current density through the oxide, J_{mig}. With Eq. (5.7) this can be rewritten as:

$$\boxed{\dot{\Phi}_{\mathrm{ox}} = \frac{z_{\mathrm{L}}}{\epsilon\ \epsilon_0}(J - J_{\mathrm{mig}}) + \frac{\Phi_{\mathrm{ox}}}{z_{\mathrm{L}}}\dot{z}_{\mathrm{L}}} \tag{5.9}$$

J_{mig} depends on the electrical field, E, which is assumed to be constant across the oxide layer, *i.e.* Φ_{ox} is assumed to drop linearly over z_{L}:

$$J_{\mathrm{mig}} = \kappa\ E \tag{5.10}$$

$$\boxed{J_{\mathrm{mig}} = \kappa \frac{\Phi_{\mathrm{ox}}}{z_{\mathrm{L}}}} \tag{5.11}$$

with κ being the conductivity of the oxide layer.

When the surface states at the silicon|oxide interface are neglected, charge balance results in the following equation for the time derivative of the voltage drop across the space charge layer in silicon, $\dot{\Phi}_{\mathrm{sc}}$:

$$\boxed{\dot{\Phi}_{\mathrm{sc}} = \frac{1}{C_{\mathrm{sc}}}(J - J_{\mathrm{F}})} \tag{5.12}$$

with J_{F} being the Faradaic current density. In the simplest case, J_{F} can be expressed as exponentially dependent on Φ_{sc} (Gellings and Bouwmeester, 1997):

$$\boxed{J_{\mathrm{F}} = \nu \; e_0 \; k_{\mathrm{sc}} \; \exp\left(f\Phi_{\mathrm{sc}}\right)} \tag{5.13}$$

with $e_0 = 1.60219 \; 10^{-19}$ C being the elementary charge, k_{sc} being the rate constant of the oxidation reaction and $f = 19.5 \; \mathrm{V}^{-1}$ being the usual exponential coefficient.

The overall current density can be expressed through the voltage drop across the resistor combining Eq. (2.4) with Eq. (2.5) and assuming a negligible small potential drop across the Helmholtz layer:

$$\boxed{J = \frac{U - \Phi_{\mathrm{sc}} - \dfrac{\Delta E_{\mathrm{F}}}{e_0} - \Phi_{\mathrm{ox}}}{AR_{\mathrm{ext}}}} \tag{5.14}$$

After having defined the time derivatives of the electrical variables in the system, the time derivative of the chemical variable z_{L}, $\dot{z}_{\mathrm{L}}(t)$, is derived. A change in the oxide layer thickness is given by the difference between the oxide formation rate and the etch rate as discussed in Sec. 4.4:

$$\dot{z}_{\mathrm{L}} = \dot{z} - \dot{z}_{\mathrm{E}} \tag{5.15}$$

$$\boxed{\dot{z}_{\mathrm{L}} = \frac{M}{F\nu\rho}J_{\mathrm{F}} - \dot{z}_{\mathrm{E}}} \tag{5.16}$$

Furthermore, a dependency of the etch rate on the potential drop across the oxide layer was found in the experiments (Fig. 5.5). Parkhutik (2001) pointed out that an accumulation of stress in the oxide layer increases its conductivity. If this stress is reduced, possibly at higher fields, the conductivity decreases.

Since no functional dependency of κ on E is known from experimental data, some function has to be assumed. Therefore, a sigmoidal dependency of the conductivity, κ, on the electric field in the oxide layer, E, is postulated:

$$\boxed{\kappa_E = \kappa_0 + \kappa_\Delta \left[\frac{1}{2} - \frac{1}{\pi}\arctan\left(\frac{4(E - E_0)}{E_\Delta}\right)\right]} \tag{5.17}$$

with κ_E being the equilibrium conductivity at a specific electric field, κ_Δ being the difference between the two sigmoidal branches, and κ_0 being an offset value accounting for the minimum possible value of κ_E. Furthermore, E_0 is the inflection point of the function and E_Δ is the range of values for E where the inflection takes place. This field dependency of κ_{E} is displayed in the upper panel of Fig. 5.15. It results in a field dependent migration current density, J_{mig},

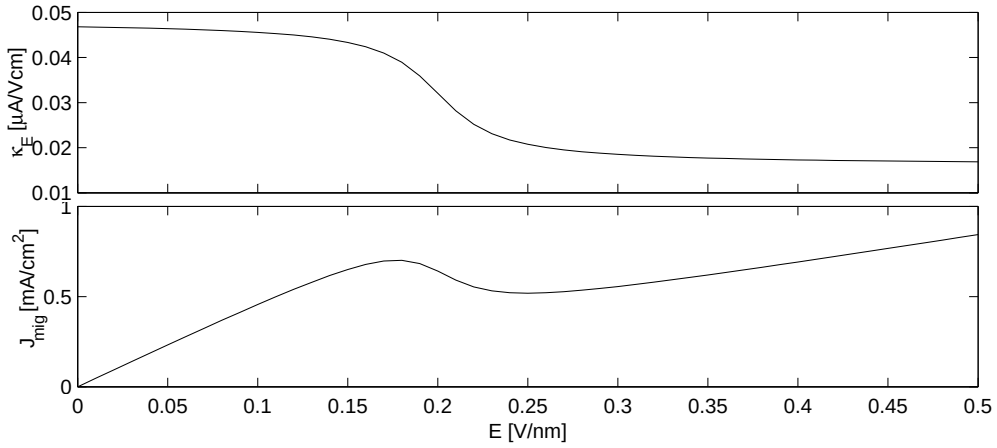

Figure 5.15: Dependency of the conductivity, κ_{E} **(upper panel)**, and the migration current density, J_{mig} **(lower panel)**, on the electrical field, E. Simulation conditions: Tab. 5.2.

of the hydroxide anions through the oxide layer (Eq. (5.10)), which is nonlinear (Fig. 5.15). The conductivity adjusts to the field with the rate constant k_κ:

$$\boxed{\dot{\kappa} = k_\kappa \left(\kappa_E - \kappa\right)} \tag{5.18}$$

An increase in E is connected to a decrease in κ, which in turn results in an N-shaped $J_{\mathrm{mig}}-E$ characteristic with a negative differential conductivity branch. This is reminiscent of a negative differential resistance which is part of an N-shaped dependency of the current density on the electrode potential which is observed in many oscillatory electrochemical systems. It may also induce bistability, which is not observed in the system at hand.

It is important to note that the dependency of κ on E induces autocatalysis in the model (upper loop in Fig. 5.16). An increase of κ leads to an increase of J_{mig}, which causes a higher potential drop across the external resistor. This decreases the potential drop across the oxide layer also decreasing E, which in turn increases κ.

Finally, a last feedback has to be considered. Silicon oxide with a high concentration of hydroxide ions is etched faster, because hydroxide functions as a nonbridging oxide in the silicon oxide network which enables the attack of the etchants (Schmidt and Ashner, 1971). This is supported by the experiments discussed in Sec. 5.1, which relate the etch rate to the electrical field. Diggle (1973) explained that the dependency of the etch rate on the electrical field results from the polarizing force applied to the oxide by the field which enhances the dissolution. For simplicity, a linear dependency between the etch rate and the conductivity is assumed:

$$\boxed{\dot{z}_{\mathrm{E}} = \dot{z}_{\mathrm{E0}} + \frac{\dot{z}_{\mathrm{E}\Delta}}{\kappa_\Delta}\kappa} \tag{5.19}$$

with $\dot{z}_{\mathrm{E}\Delta}$ regulating the difference between minimal and maximal $\dot{z}_{\mathrm{E}}$, and $\dot{z}_{\mathrm{E0}}$ being an offset value accounting for the minimum possible value of $\dot{z}_{\mathrm{E}}$. This function is plotted versus E in Fig. 5.17.

The field dependency of the etch rate induces a negative feedback loop that is indicated in the lower loop in Fig. 5.16. An increase in the conductivity leads to an increase in the etch rate, which in turn reduces the oxide layer thickness and therefore increasing the electrical field across the oxide which reduces the conductivity. This loop has an inhibiting effect on κ.

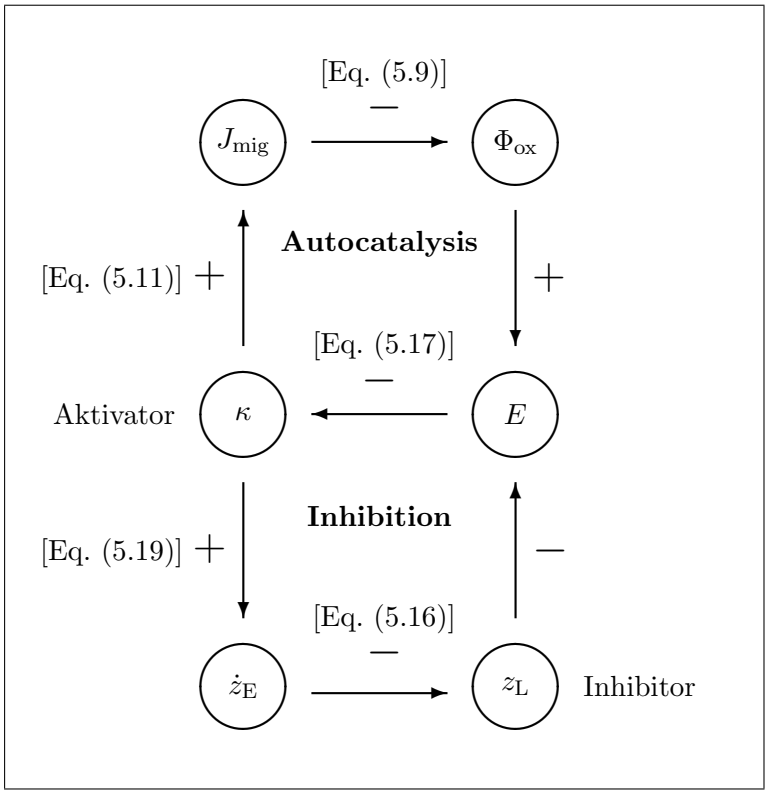

Figure 5.16: Positive and negative feedback loops in the mechanism. The autocatalytic feedback loop is fast. The inhibitory feedback loop is slow.

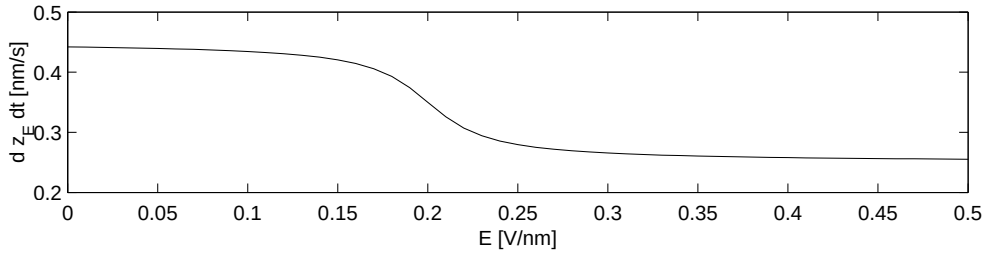

Figure 5.17: Sigmoidal $\dot{z}_{\mathrm{E}} - E$ characteristic resulting from a linear dependency of $\dot{z}_{\mathrm{E}}$ on κ.

This mechanism essentially describes a kind of activator-inhibitor system, which is known to exhibit oscillations when the activator variable, here κ, is fast and the inhibitor variable, here z_{L}, is slow.

Numerical Simulations

The model described in the preceding section consists of four ordinary differential equations, indicated by double frames. Other essential equations are indicated by single frames. In the following, the results of the numerical simulations with SCIGMA are discussed and compared to the experimental results from Sec. 5.1. The parameters used for the simulations are displayed in Tab. 5.2.

Numerical simulations were performed using the integration software SCIGMA, which was first developed by Taylor *et al.* (1989). The name stands for Stability Computations and

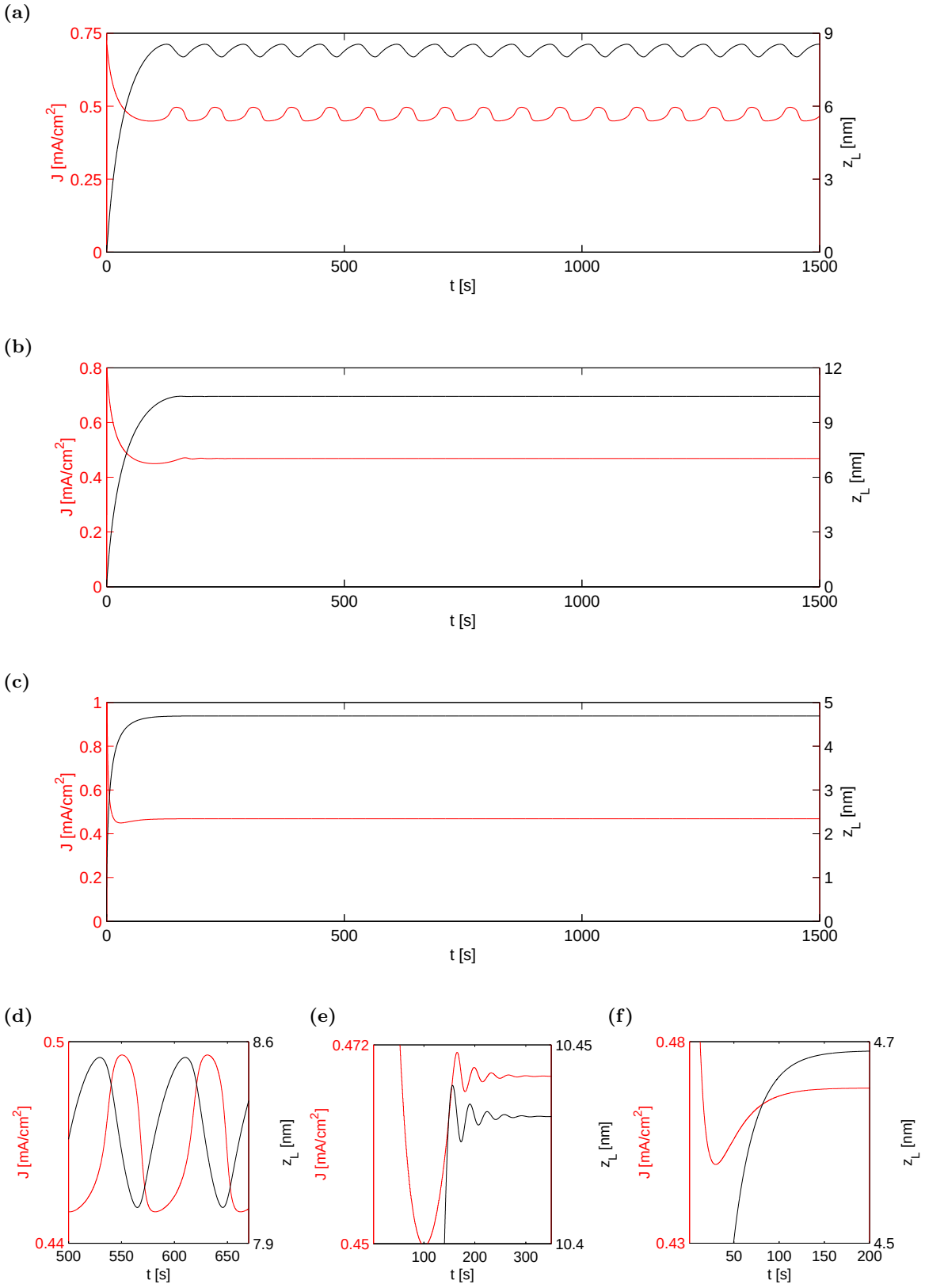

Figure 5.18: Typical time series following upon starting the simulations at $z_{\mathrm{L}} = 0.1$. **(a,d)** Stable oscillations for $U = 8\,\mathrm{V}$ and $R_{\mathrm{ext}} = 70\,\mathrm{k\Omega}$. **(b,e)** Focus for $U = 8\,\mathrm{V}$ and $R_{\mathrm{ext}} = 61\,\mathrm{k\Omega}$. **(c,f)** Node for $U = 4\,\mathrm{V}$ and $R_{\mathrm{ext}} = 1\,\mathrm{k\Omega}$. Simulation conditions: in Tab. 5.2.

Interactive Graphics for Invariant Manifold Analysis. The bifurcation package AUTO, a software for continuation and bifurcation problems in ordinary differential equations, by Eusebius Doedel [http://indy.cs.concordia.ca/auto] is part of the functionality of SCIGMA, which was adapted for usage on a PC by R. Hölzel (Krischer group).

The typical time series of the potential step experiments are mimicked by starting the simulations at an initial oxide layer thickness $z_\mathrm{L} = 0.1\,\mathrm{nm}$ applying different values of U and R_ext. In Fig. 5.18a, oscillations reminiscent of experimental high-amplitude oscillations (Fig. 4.2b) are observed under comparable conditions. The experimental current density oscillations and the oxide layer thickness oscillations from the top panel of Fig. 4.6 are well reproduced by the simulations. The oscillation period and the absolute values of current density and oxide layer thickness are very similar to the experiment, even though the amplitudes of the latter two are smaller in the experiments.

Comparing the enlarged experimental time series of J and $\overline{\xi}$ in Fig. 4.2e with J and z_L from the numerical simulations (Fig. 5.18d), however, reveals a phase-shift disparity between the current density and the respective signal related to the oxide thickness. In the case of the experiment, the maxima of the current density precede the maxima of the oxide layer thickness at a fraction of the oscillation period. The maxima of J coincide with the inflection point of the increasing slope of the oxide layer thickness. In contrast, the maxima of the current density oscillations obtained from numerical simulations coincide with the inflection points of the decreasing slopes of the oxide thickness oscillations.

The time series in Figs. 5.18b and 5.18e reproduce experimental time series of foci, *e.g.* Fig. 5.1b. As with the experimental system (Fig. 5.1a), the model system shows nodes (Figs. 5.18c and 5.18f). In Fig. 5.19, the dependency of the dynamics of the proposed mechanism on the external resistance and on the applied voltage is shown in a semilogarithmic parameter space plot. As in the experimental parameter plot (Fig. 5.2), a significant external resistance is necessary for the appearance of sustained oscillations, which are observed in a smaller region of the parameter plane compared to the experiments. At low R_ext, the system relaxes to a steady state. In this region of the experimental parameter space, only foci were observed. The numerical simulations show foci at intermediate R_ext and nodes at low R_ext. At high R_ext, the numerically simulated values for z_L go below zero. The proposed mechanism does not provide physical results in this region, because the assumption of an oxide layer on the electrode cannot be fulfilled anymore. This corresponds well to the observed nodes at high R_ext in the experiments. The system moves out of domain **III** and settles to a steady state in another reaction regime without a passivating oxide layer.

Hopf bifurcations are observed in the model system upon changing the parameters U or R_ext. In Fig. 5.20, trajectories in the $\Phi_\mathrm{eff} - z_\mathrm{L}$ phase space show how a limit cycle emerges from a focus as the external resistance is increased above the critical value $R_\mathrm{ext} = 61\,\mathrm{k\Omega}$. Fig. 5.20a shows that the simulations reproduce the trend from the experiment, meaning that z_L increases with decreasing R_ext.

The corresponding bifurcation was observed in the experimental system in Fig. 5.7. Furthermore, the experimental system showed a Hopf bifurcation upon changing U (Fig. 5.4). This is also observed in the simulations, except that here the limit cycle emerges from a focus upon decreasing the bifurcation parameter instead of increasing it (Fig. 5.21). However, the average oxide layer thickness increases with increasing U (Fig. 5.21a).

Two more aspects of the experimental oscillatory dynamics are reproduced. Firstly, the average current density is the same for all values in the $U - R_\mathrm{ext}$ parameter plane. Secondly, the average oxide layer thickness grows linearly with the effective voltage.

Fig. 5.22 gives an overview of several time series of the numerically simulated model system

Parameter	Value
A	$0.1\,\mathrm{cm}^2$
C_{sc}	$5\ 10^{-3}\,\mathrm{mF/cm}^2$
E_0	$0.2\,\mathrm{V/nm}$
$\Delta E_{\mathrm{F}}/e_0$	$0.4\,\mathrm{V}$
E_Δ	$0.1\,\mathrm{V/nm}$
k_{sc}	$1\ 10^{-7}\,1/\mathrm{cm}^2\mathrm{s}$
k_κ	$1\,\mathrm{s}^{-1}$
$\dot{z}_{\mathrm{E}\Delta}$	$0.2\,\mathrm{nm/s}$
$\dot{z}_{\mathrm{E}0}$	$0.15\,\mathrm{nm/s}$
ϵ	3.75
κ_0	$1.6\ 10^{-8}\,\mathrm{cm/Vs}$
κ_Δ	$1.6\ 10^{-8}\,\mathrm{cm/Vs}$

Table 5.2: Parameters used in the numerical simulations of the mechanism

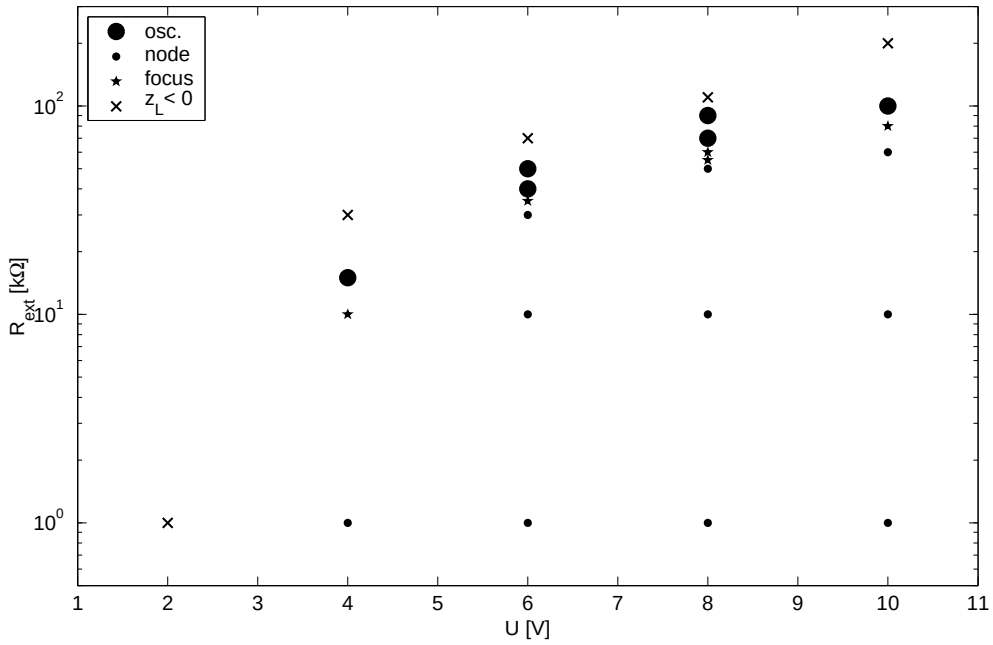

Figure 5.19: Resistance-voltage parameter space obtained from numerical simulations.

and their dependency on the electrical field. Fig. 5.22a, shows that one period of the time series of the electrical field can be divided into two fast branches ($\mathbf{F_1}$ and $\mathbf{F_2}$) and two slow branches ($\mathbf{S_1}$ and $\mathbf{S_2}$). When the system is on the branches $\mathbf{F_1}$ and $\mathbf{S_1}$, the electrical field is high and as long as it stays above a threshold value, the oxide layer is increasing in thickness (Fig. 5.22c). While the system is on the branches $\mathbf{F_2}$ and $\mathbf{S_2}$, the electrical field is low and z_{L} decreases. z_{L}, the slow inhibitor variable, exhibits no fast changes. In Fig. 5.22d, the slow and fast dynamics are indicated in the $z_{\mathrm{L}} - E$ phase space.

While the system is on the slow branches, the value of E, J and κ change slowly. Hence, the system follows the curves of the equilibrium conductivity, κ_{E} (Fig. 5.22f), and of the equilibrium migration current density, $J_{\mathrm{mig}} = \kappa_{\mathrm{E}} E$ (Fig. 5.22h), both indicated as red lines. During branch $\mathbf{S_2}$, E is slowly increasing. In the subsequent branch $\mathbf{F_1}$, E decreases fast until

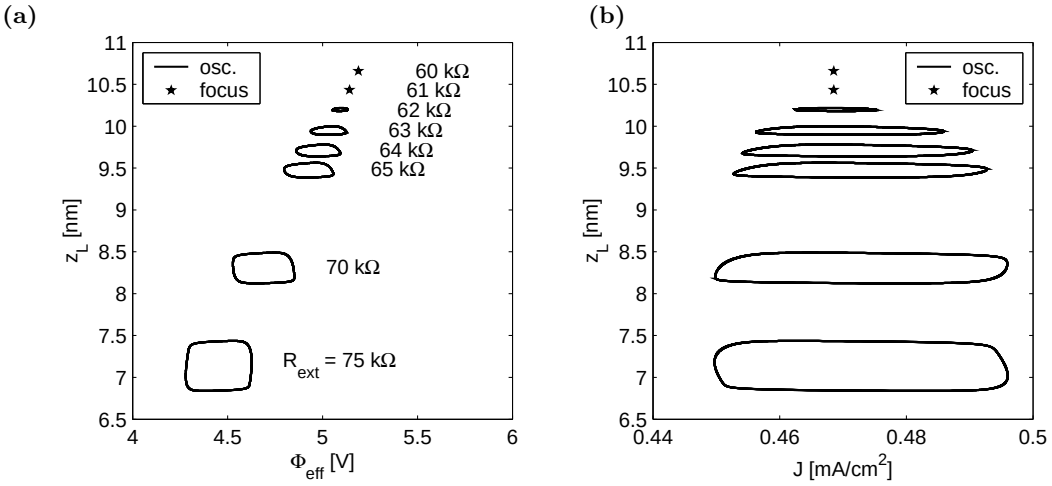

Figure 5.20: Hopf bifurcation upon changing the series resistance R_{ext} at constant $U = 8\,\mathrm{V}$. **(a)** z_{L} versus Φ_{eff}. **(b)** z_{L} versus J.

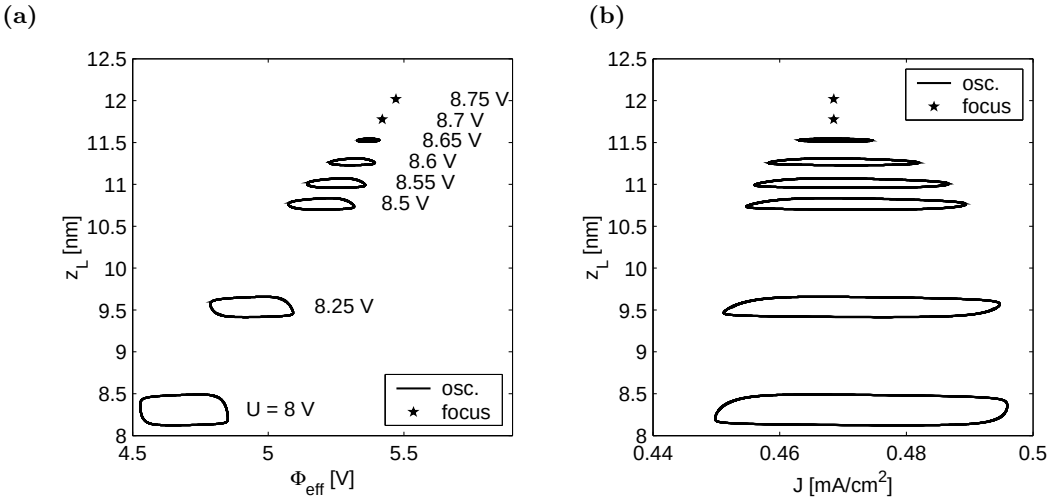

Figure 5.21: Hopf bifurcation upon changing the applied voltage U at constant $R_{\mathrm{ext}} = 70\,\mathrm{k\Omega}$. **(a)** z_{L} versus Φ_{eff}. **(b)** z_{L} versus J.

the end of the region with a negative differential conductivity, because autocatalysis dominates the dynamics. Then E is slowly decreasing during branch $\mathbf{S_1}$, and fast decreasing during branch $\mathbf{F_2}$. The switch between fast and slow changes of E is responsible for the oscillatory instability that results, because the trajectory is driven from the systems equilibrium curves.

Fig. 5.22b shows that Φ_{sc} changes only insignificantly during an oscillation cycle. It does not constitute a degree of freedom of this system, because the current density is migration-limited and not kinetically limited. Furthermore, Φ_{ox} is also not a true degree of freedom. It drives the autocatalytic feedback loop as depicted in Fig. 5.16, but because Φ_{sc} is constant it follows J.

Hence, the ansatz of temporal variations of the amount of partial oxidized silicon due to variations of the potential drop across the space charge layer (Sec. 4.5) is not included in this mechanism.

A second ansatz from Sec. 4.5 pertaining to etch rate variations is used to estimate the applicability of the mechanism. Fig. 5.23a shows the experimental time series of J and $\dot{z}_\mathrm{E}$ calculated from the discrepancy $J - J_{\overline{\xi}}$. These time series are phase shifted with respect to each other, J slightly preceding $\dot{z}_\mathrm{E}$. In the case of the simulations, the phase shift is equally small, but here J lags behind $\dot{z}_\mathrm{E}$ (Fig. 5.23b).

5.3 Summary and Outlook

Studies of the parameter dependency of current density oscillations have revealed insights into nonlinear dynamics and mechanistic aspects of the system. Nonlinear dynamical aspects of the system include a Hopf bifurcation and the observation of complex oscillatory dynamics, *e.g.* chaos at higher ammonium fluoride concentrations. Moreover, the observed dependency of the etch rate on Φ_eff has mechanistic implications.

Thus, the etch rate dependency on the potential drop across the double interface of the system also has to be included into any mechanistic approach. The observation of a significant discrepancy between the etch rates during oscillations and during etch back at open-circuit potential prompted a study of the dependency of the etch rate on the effective voltage drop. Indeed, the much lower rates observed at open-circuit potential indicate a dependency of the etch rate on the effective potential drop. In Sec. 5.1 it was shown that the etch rates of steady states increases linearly with Φ_eff. The period averaged etch rates of oscillations obtained from integrating J also lie on this line. This relationship results from a weakening of the silicon-oxygen bonds in the oxide by the electric field in the oxide layer.

As either the external resistance or the applied voltage are varied, a supercritical Hopf bifurcation, *i.e.* a transition of the dynamics from a steady state to oscillations, is observed. This suggests the existence of a negative differential resistance destabilized by a the resistance in series with the working electrode. This hypothesis is supported by the model system presented in this chapter. It offers an explanation for the origin of the oscillatory instability, which differs considerably from existing modeling approaches. The current density is a global variable that affects the potential distribution in the system via the negative differential resistance, resulting in global oscillations.

This supersedes the postulation of a next-neighbor synchronization of local oscillators with a local coupling mechanism. Only nearest neighbors are affected by local changes in the system. In the example of the current burst model (Carstensen *et al.*, 1998), neighboring sites synchronize their phases, because the current flow stops earlier at sites that have other oxide producing sites in their vicinity. Local synchronization can spread across the entire system when all oscillating sites synchronize locally.

The Hopf bifurcation observed in the experiments and the simulated model, explains also the existence of damped oscillations, which are the result of a perturbation relaxing back onto a focus, *i.e.* a steady state with a spiral characteristic in its vicinity in phase space. Thus damped oscillations are not a result of one synchronized domain splitting up into smaller desynchronized domains as described by all previous models. At the Hopf bifurcation, a stable limit cycle emerges as the fix point becomes unstable.

In addition, complex oscillation dynamics are observed at higher electrolyte concentrations. The concentration has a large influence on the dynamics of the oscillations. A high concentration leads to a high oscillation frequency, to a small amplitude of $\overline{\xi}$, and to a large current density. At an ammonium fluoride concentration of $c_{\mathrm{NH_4F}} = 0.2\,\mathrm{mol/l}$, a wide range of complex dynamics is observed. The $J - \overline{\xi}$ phase space plot of time series at different parameters

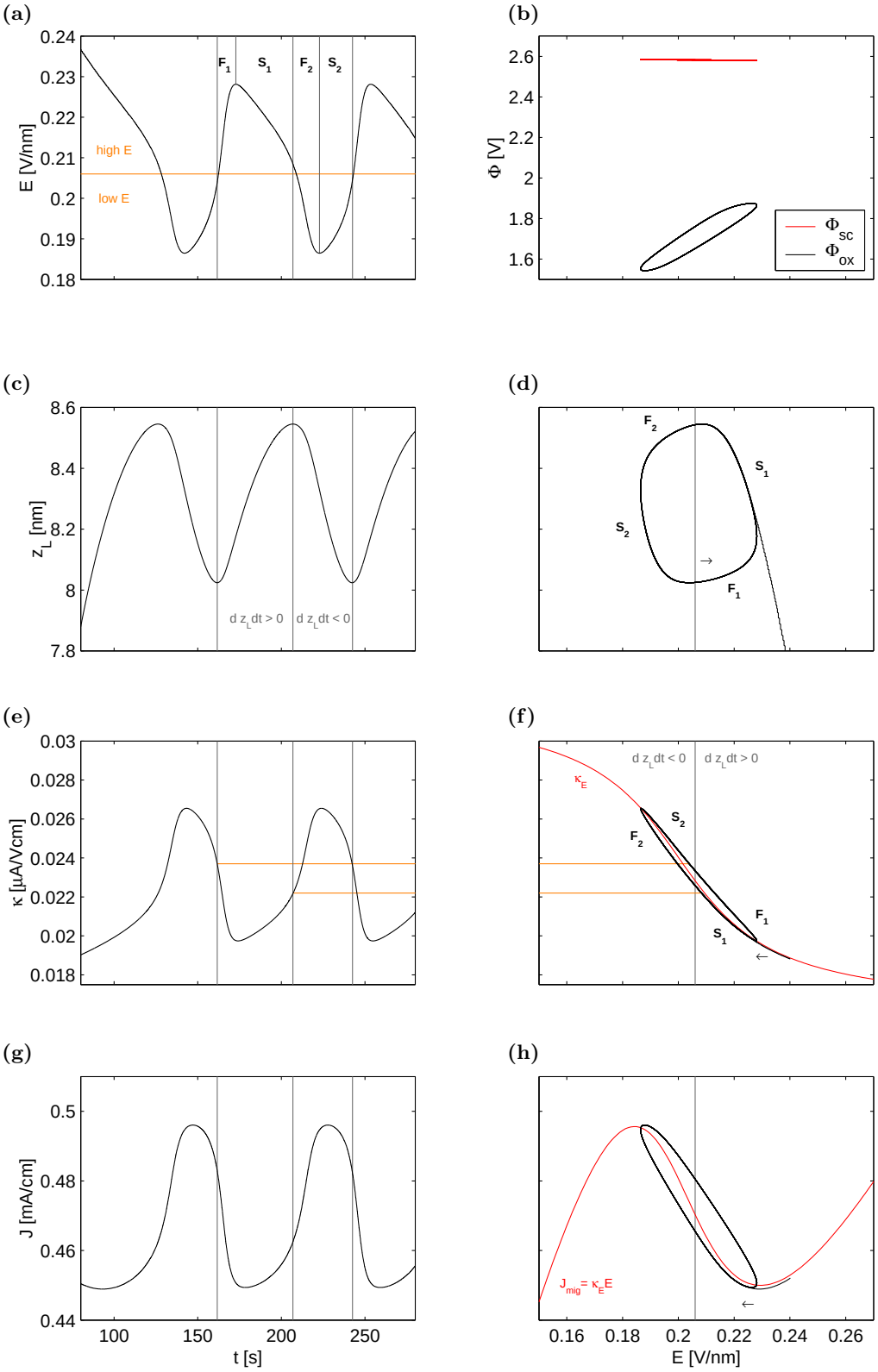

Figure 5.22: Overview of the oscillatory dynamics from the numerical simulations. **(a,c,e,g)** Time series of the electrical field, E, the oxide layer thickness, z_L, the conductivity, κ, and the current density, J, respectively. **(b)** The potential drop in the space charge layer of silicon, Φ_sc remains nearly constant during the oscillatory dynamics of the system. **(d)** $z_\mathrm{L} - E$ phase space. **(f)** $\kappa - E$ phase space. **(h)** $J - E$ phase space.

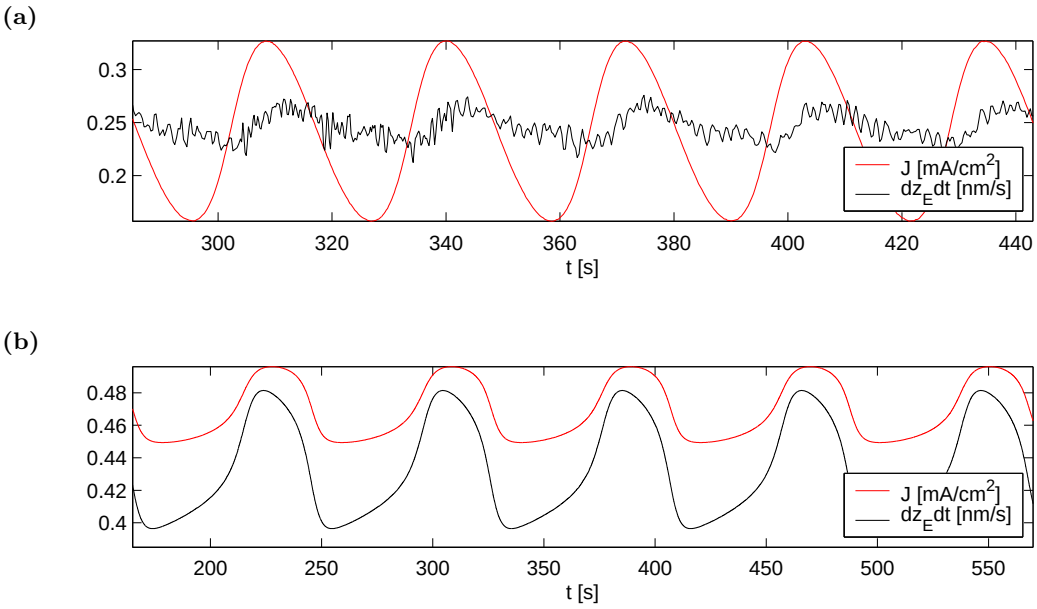

Figure 5.23: Comparison of the etch rate variations, $\dot{z}_E$, to the current density, J, for **(a)** experiment and **(b)** simulations. Experimental conditions: Fig. 4.6. Simulation conditions: in Tab. 5.2.

reveals the existence of period-1, period-2, period-3, and quasi-periodic oscillations. The next-maximum map of the latter suggests the existence of deterministic chaos in connection with a bimodal map. Complex dynamics, *i.e.* higher periodicity, quasi-periodicity and chaos, live in a phase space with more than two dimensions. As the model approach possesses only two degrees of freedom, it is not capable to model complex temporal dynamics.

The proposed oscillation mechanism reproduces the essential features of the oscillations during the anodic electrodissolution of silicon, except for the phase relation between current density and oxide layer thickness oscillations. The oscillations result from the interaction of the autocatalysis of the conductivity, which is fast, and the slow inhibition caused by a feedback via the etch rate. From the scheme in Fig. 5.16, it can be seen that a higher conductivity enhances the growth of the oxide layer, which in turn, leads to an increase of the conductivity. At the same time the etch rate is increased, which inhibits the growth of the oxide layer.

Outlook

The mathematical model is based on a sigmoidal functional dependency of the conductivity on the electrical field. Independent, direct measurements should be undertaken to measure the correlation between these two quantities.

Hiesgen *et al.* (2009) succeeded in nanoscopically resolving the conductivity of a Nafion membrane with electrochemical atomic force microscopy. This novel method could be used to further prove the absence of desynchronized domains in the case of damped oscillations.

Furthermore the dependency of the etch rate on the electrical field could be tested more sensitively by preparing defined oxide layer thicknesses in the absence of etchants in solution and consecutively adding ammonium fluoride to monitor the etching at different electrical fields.

Chapter 6

Spatially Averaged Dynamics on n-type silicon

In the case of p-type silicon, holes, which are necessary for anodic oxidation, are the majority charge carriers. The amount of holes is high enough to allow for an appreciable oxidation current density. In contrast, the anodic oxidation of n-type silicon is only possible under illumination, as holes necessary for the electrooxidation of silicon are minority charge carriers. They are formed as photons with sufficiently high energy interact with silicon. At high illumination intensities, n-type silicon behaves similarly to p-type silicon. In Sec. 6.1, the system is studied at different illumination intensities. The effect of stirring is discused in Sec. 6.2. Stirring can affect the dynamics of the system by influencing the concentration of etching species at the oxide|electrolyte interface.

6.1 Impact of Illumination

Illumination is especially important to the electrodissolution of n-type silicon. It was shown, that at a sufficiently high light intensity, the current-voltage characteristic, and therefore the dynamics, become indistinguishable from those of p-type silicon (Lewerenz *et al.*, 2000). However, the oxidation valency, ν, is different (Eddowes, 1990). Furthermore, there are hints in the literature that the oscillatory behavior significantly changes as the light intensity of the illumination is reduced (Rauscher, 2000). In the following, the impact of L is investigated in a range between 0 and 2 $\mathrm{mW/cm^2}$.

Typical Time Series under Illumination Limitation

Firstly, typical time series resulting from a potential step from open-circuit potential to more positive potentials is discussed. These time series illustrating the influence of L on the shape of the current density oscillations are displayed in Fig. 6.1. Even without an external resistance, R_{ext}, stable oscillations can be obtained at an appropriate L, whereas in the case of p-type silicon, only nodes and foci, but no sustained oscillations can be observed.

At low illumination intensity, $L = 0.23\,\mathrm{mW/cm^2}$, after an initial current density peak the system relaxes to a constant current density (Fig. 6.1a). Hence, the steady state is a stable node, even though a high voltage of $U = 8\,\mathrm{V}$ is applied, and no series resistor is inserted in the electrical circuit. In the case of p-type silicon, nodes are observed only at effective voltages well below $\Phi_{\mathrm{eff}} = 8\,\mathrm{V}$ (Fig. 5.2.

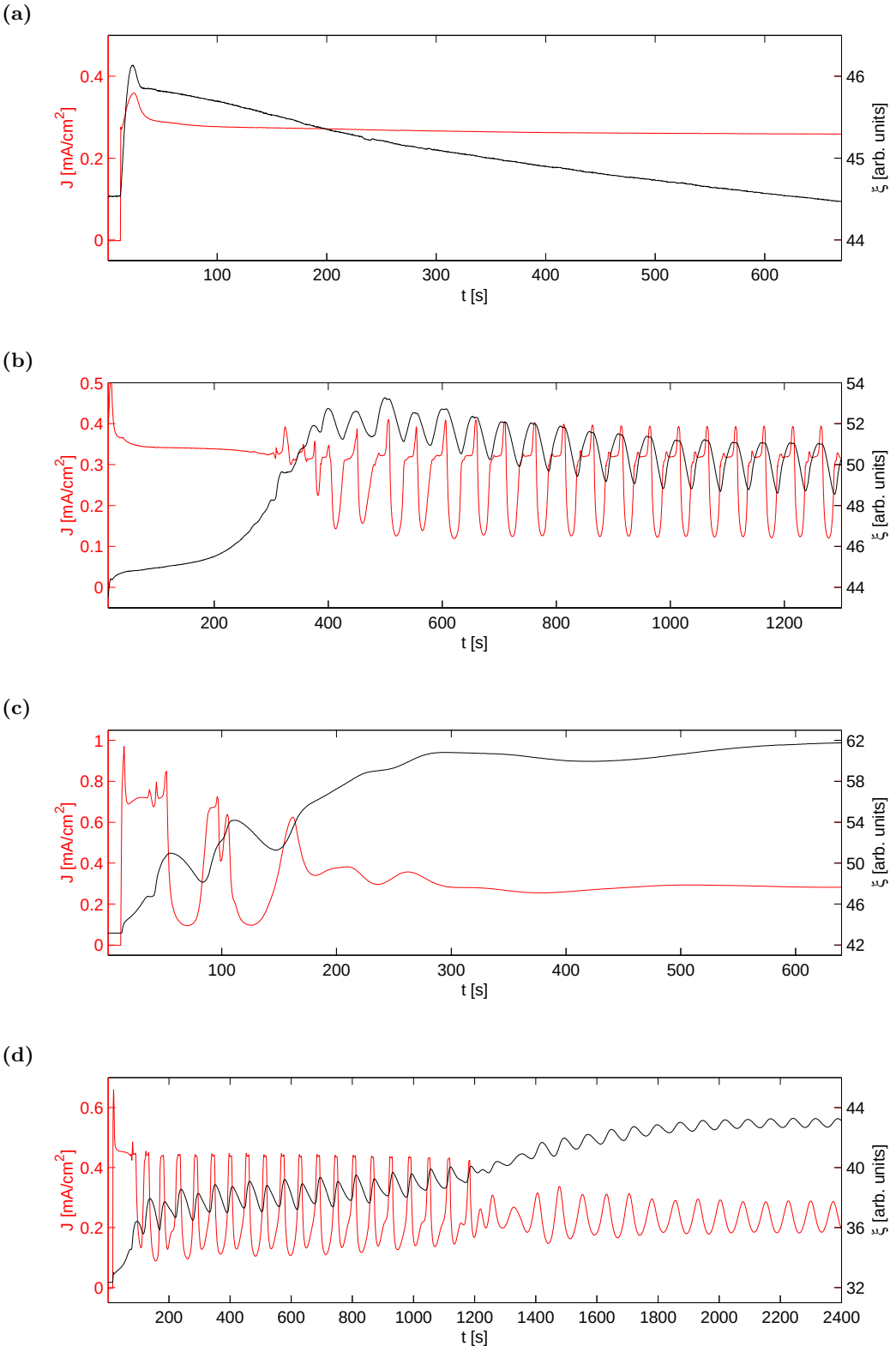

Figure 6.1: Typical time series of n-type silicon at different values of the illumination intensity. **(a)** Stable node with $L = 0.23\,\mathrm{mW/cm^2}$. **(b)** Stable high-amplitude oscillations with $L = 0.37\,\mathrm{mW/cm^2}$. **(c)** Stable focus with $L = 0.81\,\mathrm{mW/cm^2}$. **(d)** Damped high-amplitude oscillations followed by stable low-amplitude oscillations with $L = 0.64\,\mathrm{mW/cm^2}$. Experimental conditions: **(a-c)** $c_{\mathrm{NH_4F}} = 0.05$ mol/l, pH = 2.3, $U = 8\,\mathrm{V}$, $R_{\mathrm{ser}} = 0\,\mathrm{k\Omega}$, and $A = 8.11\,\mathrm{mm^2}$; **(d)** $c_{\mathrm{NH_4F}} = 0.05$ mol/l, pH = 2.3, $U = 8\,\mathrm{V}$, $R_{\mathrm{ser}} = 100\,\mathrm{k\Omega}$, and $A = 5.27\,\mathrm{mm^2}$.

In the case of n-type silicon at low illumination intensities, the rate of oxide formation is below the rate of oxide etching and no passivating oxide layer is formed, because of the current limiting effect of the small L. This is revealed in the times series of $\overline{\xi}$, which shows a monotonous decline after a transient of 40 s, even though the current density is constant.

At higher illumination intensity, $L = 0.37\ \mathrm{mW/cm^2}$, a larger initial peak current density is observed. During the subsequent 150 seconds, J remains at a constant value while $\overline{\xi}$ is growing (Fig. 6.1b). When $\overline{\xi}$ exceeds a threshold value several irregular oscillations appear, followed by a new type of high-amplitude oscillation. Their characteristic shape results from the current density limiting effect of L. This new type of high-amplitude oscillation shows a broad plateau preceding the spike-like oscillation maximum, which is not observed in the case of p-type silicon. The value of the plateau current density is similar to the value of the constant current density in the transition region following the initial peak. The connection between the plateau current and the illumination limitation will be discussed in a later part of this section.

A few hints of this new type of oscillation at intermediate L can be found in the literature, for example in the thesis by Rauscher (Fig. 6.2 in Rauscher (1993)), in the thesis by Aggour (Fig. 4.7 in Aggour (1994)), and on very close inspection in Fig. 3 in a paper in Aggour *et al.* (1995). However, a discussion of the phenomenon is missing.

It is striking that this type of high-amplitude oscillation is stable at zero external resistance. In fact, high-amplitude oscillations on p-type silicon are stable only in a very small region of the $R_{\mathrm{ext}} - \Phi_{\mathrm{eff}}$ parameter space (Fig. 5.2). In the case of p-type silicon, the current density is limited by the ohmic voltage drop, $\Phi_{\mathrm{ext}} = JAR_{\mathrm{ext}}$. In the case of n-type silicon, the current density can also be limited by the illumination, which results in stable high-amplitude oscillations in a larger region of parameter space.

On increasing the illumination intensity to $L = 0.81\ \mathrm{mW/cm^2}$, the oscillations lose stability and the system relaxes to a stable focus (Fig. 6.1c). This behavior is similar to that observed in the case of p-type silicon at $U = 8\ \mathrm{V}$ and $R_{\mathrm{ser}} = 0$. In Fig. 6.1d, damped high-amplitude oscillations are followed by stable low-amplitude oscillations when $R_{\mathrm{ext}} = 100\ \mathrm{k\Omega}$. The bifurcation of a stable focus to sustained low-amplitude oscillations is thoroughly discussed for p-type silicon in Sec. 5.1, where a careful investigation of the $R_{\mathrm{ext}} - \Phi_{\mathrm{eff}}$ parameter space reveals a Hopf bifurcation. A Hopf bifurcation is assumed also in the case of n-type silicon under sufficient illumination.

Fine Structure of New Type of High-amplitude Oscillation

The new type of oscillation (Fig. 6.1b) shows a characteristic fine structure. Fig. 6.2 shows an enlargement of two oscillation cycles. The shape of the high-amplitude current density oscillations on n-type silicon differs greatly from those on p-type silicon (Fig. 4.2e). The smooth oscillation minimum, a broad valley **0**, is not followed by a smooth oscillation maximum, but rather by a plateau **III**, and a large spike **IV**.

Between the increasing flank of J and the plateau, small steps **I** and a first spike **II** are observed. The depth of the valley **0**, and the height of the spikes and steps are sensitive to the value of L. The second spike **IV** and the plateau are observed under most conditions, whereas the first spike and the steps are observed only when the illumination intensity is sufficiently high.

The phase shift between J and $\overline{\xi}$ is similar to the phase shift observed in the case of p-type silicon. The minima of J coincide with the inflection points of the decreasing flank of $\overline{\xi}$. The minima of $\overline{\xi}$ coincide with the increasing flank of J following valleys. While J is on a plateau,

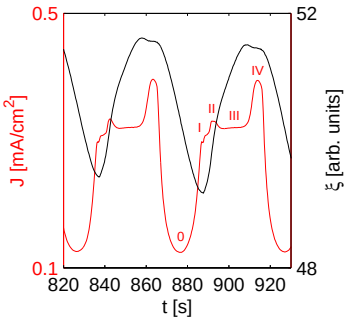

Figure 6.2: Characteristic shape of the current density of high-amplitude oscillations on n-type silicon under the conditions described in Fig. 6.1b. The shape of the current oscillations consists of a valley **0**, an increasing flank, small steps **I**, a first characteristic spike **II**, a current plateau **III**, a second spike **IV**, and a decreasing flank.

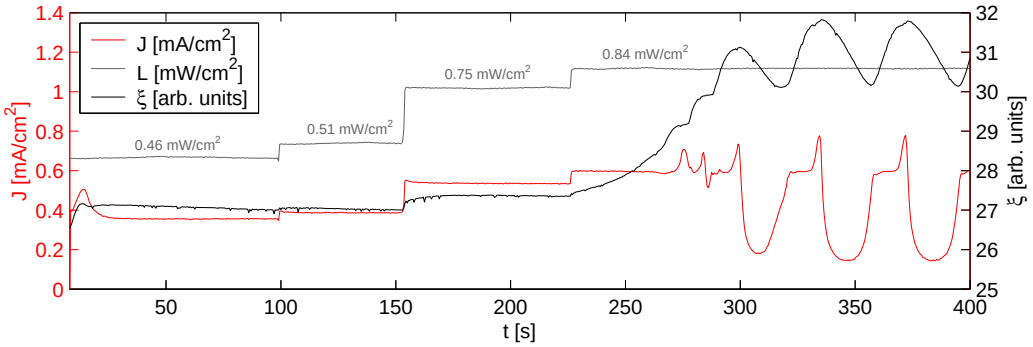

Figure 6.3: Increasing the light density, L, until high-amplitude oscillations are observed in the current density, J, and in the ellipso-microscopic signal, $\overline{\xi}$. Experimental conditions: $U = 8$ V, $R_{\mathrm{ser}} = 0\,\mathrm{k\Omega}$, $c_{\mathrm{NH_4F}} = 0.05$ mol/l, pH = 2.3, and $A = 8.91\,\mathrm{mm}^2$.

$\overline{\xi}$ increases. The maxima of $\overline{\xi}$ show a small flat region before decreasing again.

Illumination Intensity as Bifurcation Parameter

In Fig. 6.3, L is increased until the system exhibits high-amplitude current oscillations. L is changed stepwise and the response of J and $\overline{\xi}$ is analyzed.

Increasing the voltage from open-circuit potential to $U = 8\,\mathrm{V}$ at $L = 0.46\,\mathrm{mW/cm^2}$, an initial current peak and a subsequent constant value of J are observed. $\overline{\xi}$ shows the same behavior. The system relaxes to a node. On increasing L to $0.51\,\mathrm{mW/cm^2}$ and $0.75\,\mathrm{mW/cm^2}$, the node prevails at higher values of J and $\overline{\xi}$. Upon increasing L to $0.84\,\mathrm{mW/cm^2}$, $\overline{\xi}$ increases initially, while J is constant. Here obviously, the oxide layer thickness increases because the oxide formation rate is larger than the etch rate. Current density oscillations start as $\overline{\xi}$ exceeds a threshold value. They are accompanied by oscillations of $\overline{\xi}$.

Fig. 6.4 displays short time series of J and $\overline{\xi}$ for two (Figs. 6.4a to 6.4d) and four (Fig. 6.4e) oscillation periods while decreasing L stepwise in a range from 0.65 to $0.25\,\mathrm{mW/cm^2}$. Fig. 6.4f gives an overview of the dynamics of the preceding plots in the $J - \overline{\xi}$ phase space plane. As L is lowered, it can be observed that the oscillation frequency grows and the oscillation shape changes. The limit cycle in phase space shrinks. Additionally, the width of the valley decreases as the width of the plateau increases. The first spike grows and its height exceeds that of the second spike in Fig. 6.4e. The valley of the oscillation disappears and the oscillations are

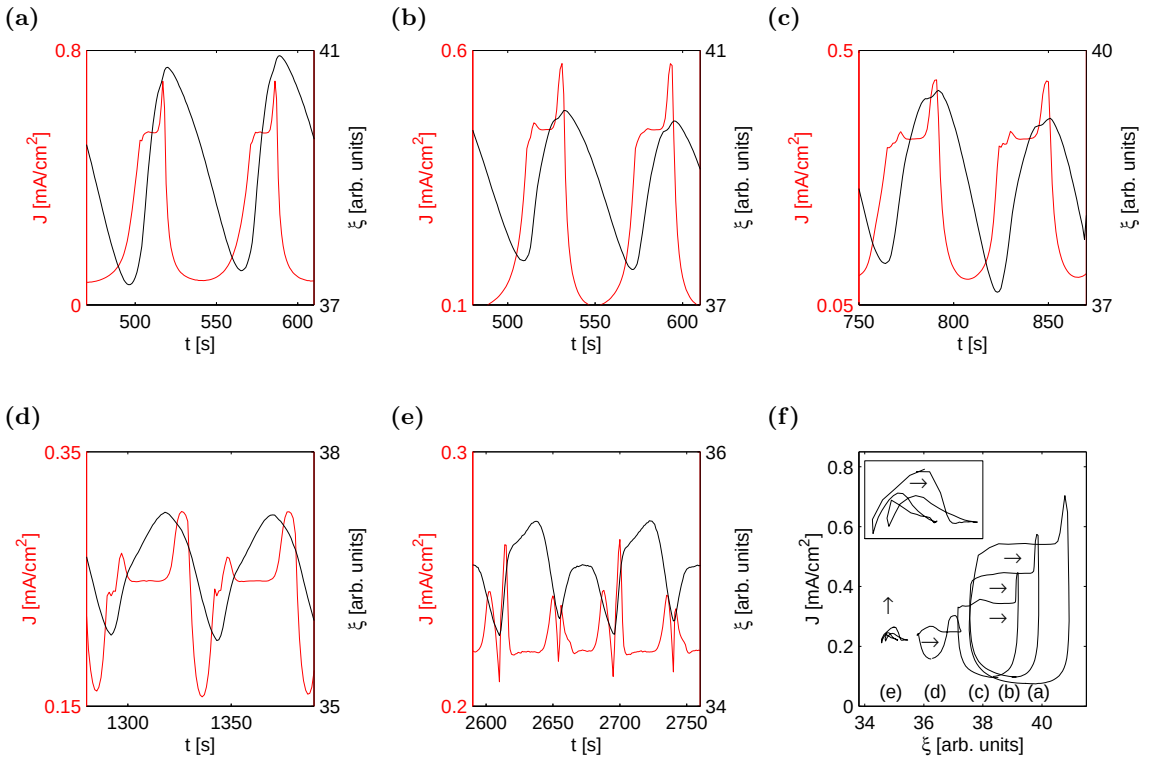

Figure 6.4: Short time series of J and $\overline{\xi}$ illustrating the influence of the illumination intensity, L, on the shape of the oscillations on n-type silicon. **(a)** $L = 0.65\,\mathrm{mW/cm^2}$. **(b)** $L = 0.52\,\mathrm{mW/cm^2}$. **(c)** $L = 0.41\,\mathrm{mW/cm^2}$. **(d)** $L = 0.30\,\mathrm{mW/cm^2}$. **(e)** $L = 0.25\,\mathrm{mW/cm^2}$. **(f)** $J - \overline{\xi}$ phase space plot of the limit cycles of the oscillations from **(a-e)**. The phase space plot of **(e)** is enlarged in the inset of **(f)**. Experimental conditions: $U = 8\,\mathrm{V}$, $R_{\mathrm{ser}} = 0\,\mathrm{k\Omega}$, $c_{\mathrm{NH_4F}} = 0.05\,\mathrm{mol/l}$, pH = 2.3, and $A = 5.27\,\mathrm{mm^2}$.

dominated by spikes. Further increasing L leads to a steady state.

Starting at a steady state and increasing L, $\overline{\xi}$ does not change considerably up to $L = 0.75\,\mathrm{mW/cm^2}$ (Fig. 6.3). For $L \geq 0.84\,\mathrm{mW/cm^2}$, the steady state is replaced by high-amplitude oscillations at much higher $\overline{\xi}$. First increasing and then decreasing L, hysteresis of $\overline{\xi}$ is observed (Fig. 6.5a). The system displays high-amplitude oscillations for values of L where steady states are observed on the increasing scan. In contrast, Fig. 6.5b illustrates that no hysteresis is observed in J. The plateau current density, J_{plat}, and the current densities of the steady state depend linearly on L, *i.e.* lie on a straight line.

Spike Dominated Oscillations

In order to obtain a better understanding of the spike dominated oscillations (Fig. 6.4e), a transient leading toward these oscillations and a transient leading away from these oscillations are studied in the following. During the transients, changes in the phenomenology of the spikes can be tracked.

Fig. 6.6 displays the emergence of spike dominated oscillations. At $L = 0.40\,\mathrm{mW/cm^2}$ and $R_{\mathrm{ser}} = 30\,\mathrm{k\Omega}$, the system is at a steady state. At $t = 155\,\mathrm{s}$, L is reduced to $0.25\,\mathrm{mW/cm^2}$. Due to the sudden parameter change, high amplitude oscillations are initiated. They are damped to spike dominated oscillations. At $t = 480\,\mathrm{s}$, R_{ser} is decreased to zero. This parameter change

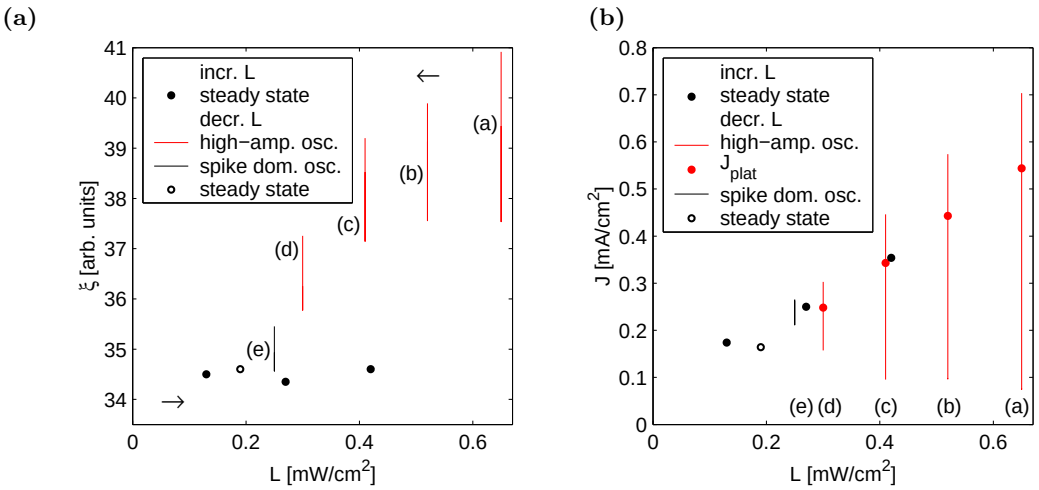

Figure 6.5: Plot of J and $\overline{\xi}$ upon increasing and decreasing L. The data from Fig. 6.4 are marked with respective letters. **(a)** Hysteresis in $\overline{\xi}$ between $L = 0.25\,\mathrm{mW/cm^2}$ and $L = 0.41\,\mathrm{mW/cm^2}$. **(b)** Linear dependency of the current density, J, on the light intensity, L. Experimental conditions: $U = 8\,\mathrm{V}$, $R_{\mathrm{ser}} = 0\,\mathrm{k\Omega}$, $c_{\mathrm{NH_4F}} = 0.05\,\mathrm{mol/l}$, pH = 2.3, and $A = 5.27\,\mathrm{mm^2}$.

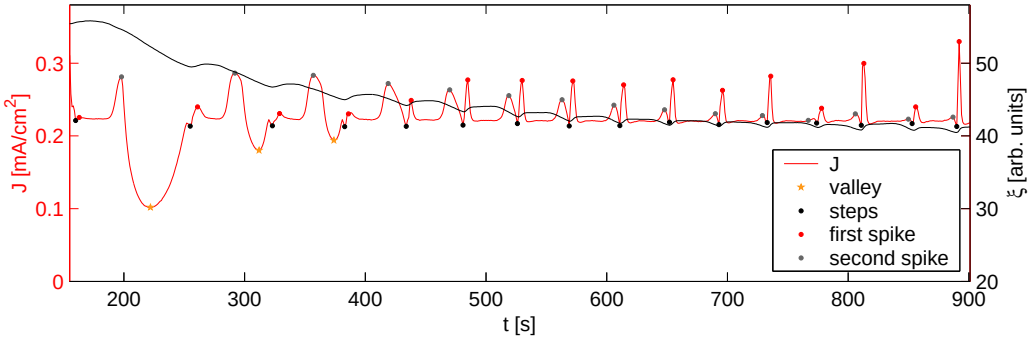

Figure 6.6: The emergence of spike dominated oscillations upon changing first L and then R_{ser}. The evolution of different features of the oscillations can be followed with colored spots. At $t = 155\,\mathrm{s}$, L is decreased from $0.40\,\mathrm{mW/cm^2}$ to $0.25\,\mathrm{mW/cm^2}$ and at $t = 480\,\mathrm{s}$ R_{ser} is decreased from $30\,\mathrm{k\Omega}$ to zero. Experimental conditions: $U = 8\,\mathrm{V}$, $c_{\mathrm{NH_4F}} = 0.05\,\mathrm{mol/l}$, pH = 2.3, and $A = 5.27\,\mathrm{mm^2}$.

is negligible and does not show up in the shape of the spike dominated oscillations.

This transition can shed light on the origin of the spikes. At constant L, $\overline{\xi}$ changes from 56 to 40. The system passes through changes similar to those discussed in Fig 6.4, which shows the behavior of the system at different values of L with ξ decreasing as the value of L is lowered. In the case of the transient, the oscillation form changes as $\overline{\xi}$ decreases. This suggests that the form of the oscillations is strongly influenced by $\overline{\xi}$, which reflects the oxide layer thickness.

The different characteristic features of the spike dominated oscillations are marked with dots of different color in Fig. 6.6 to make it easy to follow the changes of the time series. During the transition, the first spike of the high-amplitude oscillations increases until it dominates the dynamics, eventually showing period-2 oscillations. In contrast, the second spike of the high-amplitude oscillations disappears. Furthermore, the valley, *i.e.* the minimum of the high-amplitude oscillations, disappears fast and the width of the plateau slowly increases.

Fig. 6.7 shows a similar experiment of a sample with a slightly larger electrode size. At $L = 0.39\,\mathrm{mW/cm^2}$, the system exhibits sustained high-amplitude oscillations. Spike dominated

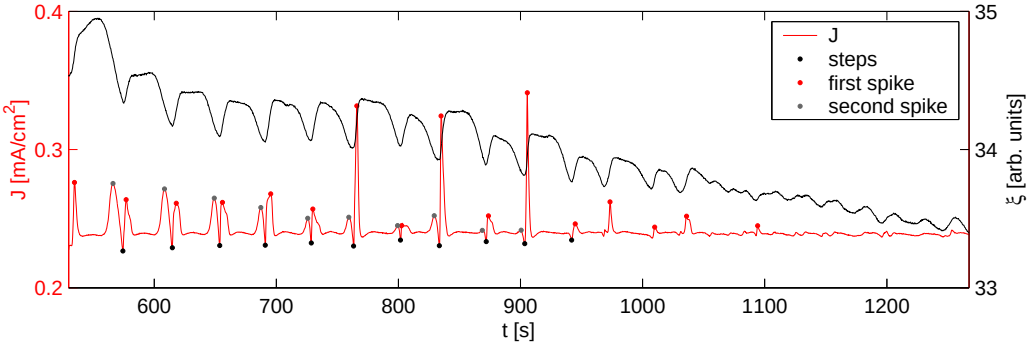

Figure 6.7: Transition from spike dominated oscillations to a steady state upon decreasing L from $0.39\,\mathrm{mW/cm^2}$ to $0.25\,\mathrm{mW/cm^2}$. Experimental conditions: $U = 8\,\mathrm{V}$, $R_{\mathrm{ser}} = 0\,\mathrm{k\Omega}$, $c_{\mathrm{NH_4F}} = 0.05\,\mathrm{mol/l}$, pH = 2.3, and $A = 5.66\,\mathrm{mm^2}$.

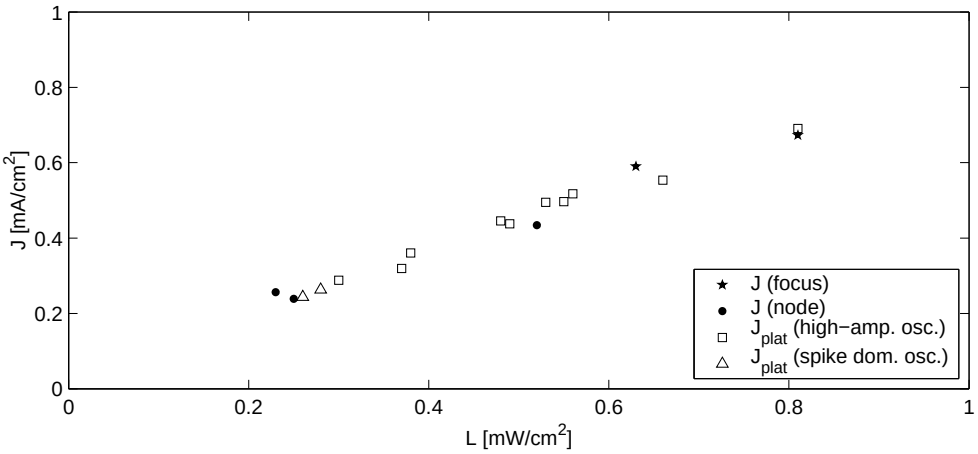

Figure 6.8: Linear dependency of the limited current density, J, on the illumination intensity, L, of high-amplitude oscillations, spike dominated oscillations, nodes and foci for three different n-type silicon electrodes. Experimental conditions: $U = 8\,\mathrm{V}$, $R_{\mathrm{ser}} = 0\,\mathrm{k\Omega}$, $c_{\mathrm{NH_4F}} = 0.05\,\mathrm{mol/l}$, and pH = 2.3.

oscillations first emerge and then relax to a steady state upon decreasing L to $0.25\,\mathrm{mW/cm^2}$. In this transition, $\overline{\xi}$ decreases continuously. The second spike decreases and eventually disappears. The first spike increases and settles to period-2 pattern of alternating high and low peaks starting at $t = 750\,\mathrm{s}$. It disappears at $t = 1100\,\mathrm{s}$, and therewith the oscillations.

Quantum Efficiency and Current Density Plateau

As is already apparent from Fig. 6.5b, J_{plat} and the current density at the steady state, J_{ss}, increase linearly with L. This is further examined by plotting more data points of J_{plat} and J_{ss} versus L (Fig. 6.8). There is indeed a linear dependency of J_{plat} on L for the entire measured interval of L.

The quantum efficiency, Y, indicates how many charges are transfered to the semiconductor for each generated electron-hole pair (Eq. (2.23)). Y is the ratio of the the particle flux according to anodic oxidation, $N_{\mathrm{anod}} = J_{\mathrm{plat}}/e$, to the flux of photo-induced electron-hole pairs, $N_{\mathrm{h}\gamma}$, obtained from the light intensity, L. E_{illu} being the energy of the light used for

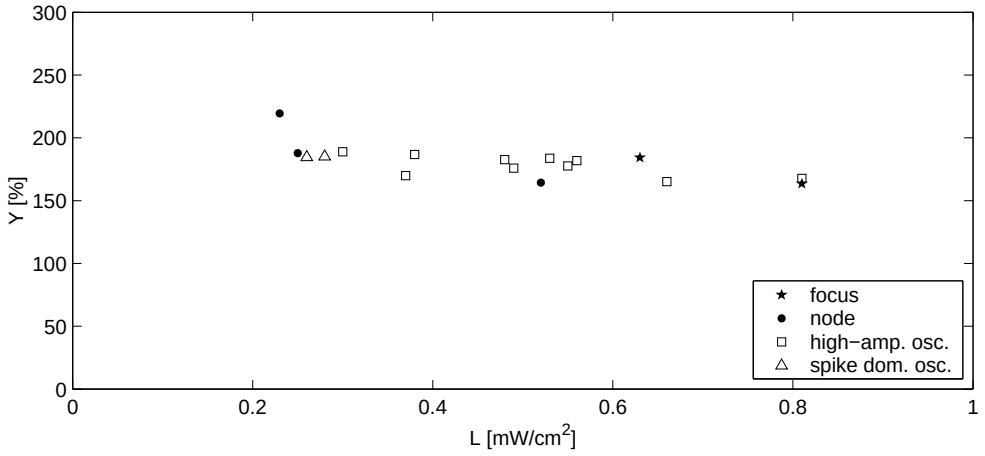

Figure 6.9: Quantum efficiency, Y, versus illumination intensity, L, for the data in Fig. 6.8.

illumination Eq. (2.23) is convert to:

$$Y = \frac{J_{\text{plat}} E_{\text{illu}}}{eL} \tag{6.1}$$

$$Y = \frac{hcJ_{\text{plat}}}{eL\lambda_{\text{illu}}} \tag{6.2}$$

with h being the Planck constant and c the speed of light.

Fig. 6.9 shows that Y is constant and therefore independent of L. This confirms again that the plateau current density results from the limited formation of electron-hole pairs. The value $Y \approx 200\%$ is close to the value $Y = 220\%$ obtained by Blackwood *et al.* (1992).

Eq. (2.24) can be rewritten in such a way as to obtain the ratio of captured holes to injected electrons.

$$Y = \frac{\nu_{\text{cap}} + \nu_{\text{inj}}}{\nu_{\text{cap}}} \tag{6.3}$$

$$\frac{\nu_{\text{inj}}}{\nu_{\text{cap}}} = Y - 1 \tag{6.4}$$

$$\tag{6.5}$$

The measured value of $Y \approx 2$ implies that $\nu_{\text{inj}}/\nu_{\text{cap}} \approx 1$. Furthermore the dissolution valency $\nu = 2.2$ (Eddowes, 1990) implies that the current doubling is due to the injection of 1.1 electrons into the conduction band for 1.1 holes that are captured. The ratio $\nu_{\text{inj}}/\nu_{\text{cap}}$ is equal to $J_{\text{inj}}/J_{\text{cap}}$. Accordingly, the ratio of J_{inj} to J_{cap} is constant within the plateau region, but may vary outside of this region. Changes in this ratio can be estimated by comparing J with $J_{\overline{\xi}}$.

Calculating the Current from the Ellipso-microscopic signal

Fig. 6.10 shows the current density, J, in comparison with the current density expected from the changes in $\overline{\xi}$, $J_{\overline{\xi}}$. While the current attains its plateau value, a large amount of partially oxidized silicon is generated from silicon via hole capture and $J_{\overline{\xi}}$ is much larger than J. During the second spike the amount of oxide species formed from partially oxidized silicon increases and $J_{\overline{\xi}}$ is smaller than J.

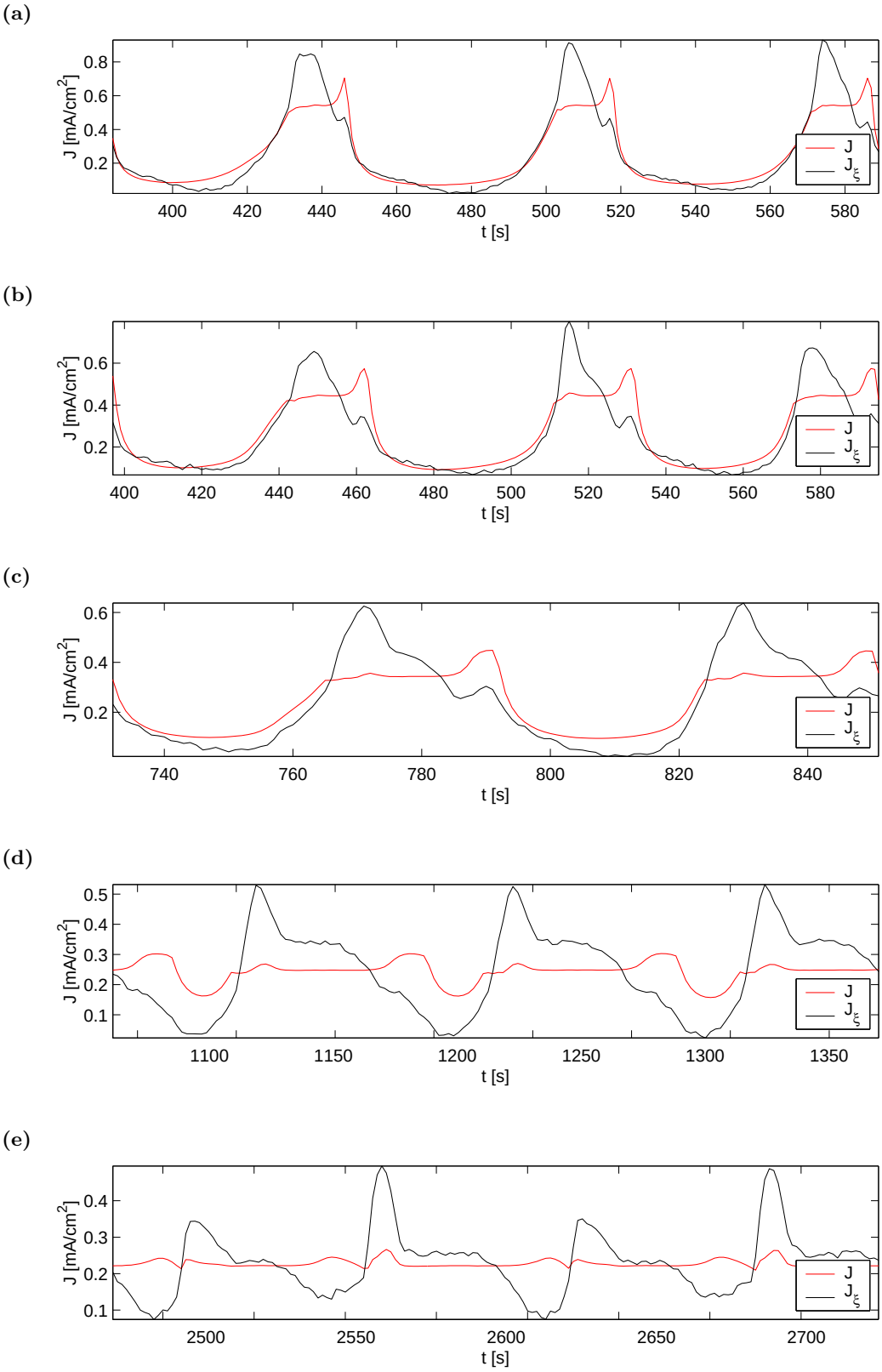

Figure 6.10: Current density time series, J, and $J_{\overline{\xi}}$, calculated from $\overline{\xi}$, illustrating the influence of the illumination intensity, L, on the shape of the oscillations on n-type silicon. Fit calculated with a dissolution valency, $\nu = 2.2$, and $c_{\mathrm{opt}} = 3.5744$ obtained from low-amplitude oscillations with $R_{\mathrm{ser}} = 100\,\mathrm{k\Omega}$. **(a)** $L = 0.65\,\mathrm{mW/cm^2}$. **(b)** $L = 0.52\,\mathrm{mW/cm^2}$. **(c)** $L = 0.41\,\mathrm{mW/cm^2}$. **(d)** $L = 0.30\,\mathrm{mW/cm^2}$. **(e)** $L = 0.25\,\mathrm{mW/cm^2}$. Experimental conditions: in Fig. 6.4.

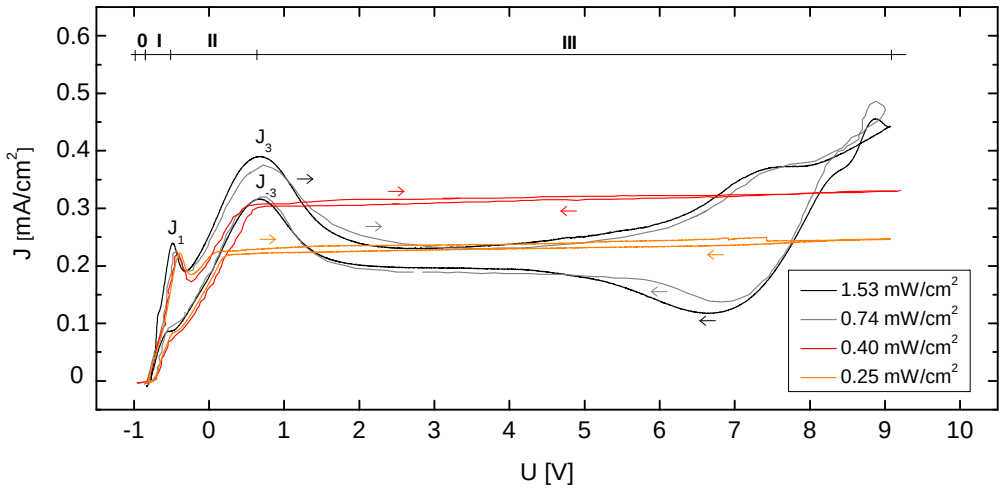

Figure 6.11: The $J-U$ characteristic at different illumination intensities, L. Experimental conditions: $R_{\text{ext}} = 0\,\text{k}\Omega$, $A = 3.19\,\text{mm}^2$, $c_{\text{NH}_4\text{F}} = 0.05\,\text{M}$, and pH = 2.2. [provided by K. Schönleber (Krischer group)]

Obviously the correlation approach from Sec. 4.4 can only be applied to illuminations high enough to cause formation of a passivating oxide layer on the electrode surface. Fig. 6.11 shows recently measured $J-U$ characteristics at different values of L by K. Schönleber (Krischer group). At $L = 0.74\,\text{mW/cm}^2$ and $L = 1.53\,\text{mW/cm}^2$ all three domains are resolved. At $L = 0.25\,\text{mW/cm}^2$ and $L = 0.40\,\text{mW/cm}^2$ a plateau is observed when the current density reaches a value inside domain **II**, where the electrode is covered with wet oxide. This plateau results from the limitation of charge carriers.

When there is no oxide present, the approach of calculating $J_{\bar{\xi}}$ is no longer applicable. This is illustrated by the significant difference between J and $J_{\bar{\xi}}$ in Fig. 6.10e. In summary, spike dominated oscillation are a phenomenon of domain **II** rather than domain **III**. From the overview of the etch rates determined by fitting J to $J_{\bar{\xi}}$ in Fig. 6.12a, it is obvious that the etch rate is independent of L in domain **III**.

The dependency of the etch rate of n-type silicon on the effectiv voltage is documented in Fig. 6.12b. The etch rates for various applied voltages are compared to the linear fit of etch rates at steady states for p-type silicon (Fig. 5.5). The silicon dissolution rates on n-type silicon fit the dissolution rates on p-type silicon (Fig. 5.5). A different oxidation valency was used in both cases. The largest divergence from the p-type silicon fit can be seen in the case of the etch back on n-type silicon.

6.2 Stirring

Stirring decreases the distance etchants have to diffuse from the bulk to the oxide layer. Therefore, stirring increases the concentration of etching fluoride species at the oxide|electrolyte interface. Stirring affects the system in the same way as a higher ammonium fluoride concentration. Its effect on the dynamics should be similar to increasing the electrolyte concentration in a stagnant electrolyte.

In the first part of this section, the stirring rate is changed during high-amplitude current oscillations. In the second part, two voltage step experiments at the same conditions, apart from the stirring rate, are compared.

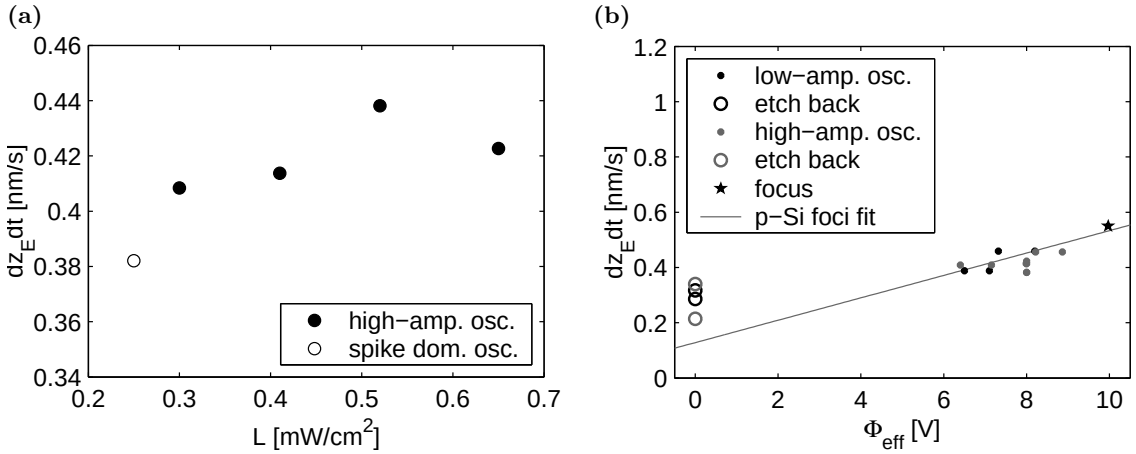

Figure 6.12: **(a)** Etch rates, $\dot{\bar{z}}_{\mathrm{E}}$, calculated for the time series in Figs. 6.4 and 6.10 by fitting J to $J_{\overline{\xi}}$. **(b)** Dependency of the etch rate, $\dot{\bar{z}}_{\mathrm{E}}$, on the effective voltage, Φ_{eff}, for n-type silicon with $c_{\mathrm{NH_4F}} = 0.05\,\mathrm{mol/l}$ and pH = 2.3 in comparison to the fit for the etch rates of the foci of p-type silicon (Fig. 5.5).

Stirring with Argon

The experimental conditions are changed by switching the argon flow from entering the cell above the electrolyte surface to entering below the surface. Argon agitates the solution and therefore has a stirring effect. Argon bubbles with a frequency of 0.15 Hz are produced in the bubbler outside the cell. Fig. 6.13 shows the time series upon turning the stirring on at $t = 650\,\mathrm{s}$ and off at $t = 1550\,\mathrm{s}$. The irregularities in $\overline{\xi}$ are due to argon bubbles crossing the light path of the optical imaging. The oscillation period decreases from $P = 58.5\,\mathrm{s}$ to $P = 34.9\,\mathrm{s}$. A higher oscillation frequency is expected when increasing the availability of etching fluoride species. In the magnification of the time series in Fig. 6.14, it can be observed that J_{plat} stays the same. This is not surprising, since the light intensity is kept constant at $L = 0.38\,\mathrm{mW/cm^2}$. In contrast, the current density values of the valleys and of the first spike increase, and the current value of the second spike decreases when the electrolyte is stirred.

Fig 6.14c displays both cases in the $J - \overline{\xi}$ phase space plane. The changes in the trajectories are comparable to those resulting from changing L. The trajectories (a) at $L - 0.65\,\mathrm{mW/cm^2}$ and (c) at $L = 0.41\,\mathrm{mW/cm^2}$ in Fig. 6.4f are similar to the trajectory of the stirred and the unstirred system at $L = 0.38\,\mathrm{mW/cm^2}$ in Fig. 6.14c except for the average current density level which is affected by the limitation of L. This indicates once more that the dynamics are influenced by the ratio of oxide formation rate to etch rate, whereby the former can be adjusted by L and the latter can be adjusted by the ammonium fluoride concentration in the electrolyte or by the striring rate.

Magnetic Stirring

Instead of adjusting the stirring rate with argon, it is now adjusted with a magnetic stirrer. The magnetically stirred experiment in Fig. 6.15, is conducted under the same conditions as the unstirred experiment in Fig. 6.1c. The stirring leads to stable high-amplitude oscillations, where otherwise a stable focus is observed. Indeed, high-amplitude oscillations are stable without stirring at lower L (Fig. 6.1b). At higher L, the higher concentration of etching fluoride species, obtained from stirring, is necessary for stable oscillations. In Fig. 6.1c, $\overline{\xi}$

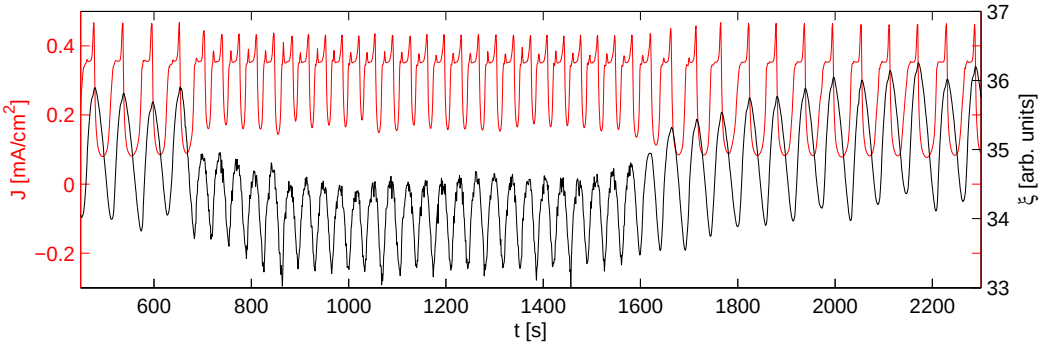

Figure 6.13: Influence of stirring of the solution between $t = 650\,\mathrm{s}$ and $t = 1550\,\mathrm{s}$ on high-amplitude oscillations on n-type silicon. Experimental conditions: $L = 0.38\,\mathrm{mW/cm^2}$, $U = 8\,\mathrm{V}$, $R_{\mathrm{ser}} = 1\,\mathrm{k\Omega}$, $c_{\mathrm{NH_4F}} = 0.05\,\mathrm{mol/l}$, pH = 2.3, and $A = 9.64\,\mathrm{mm^2}$.

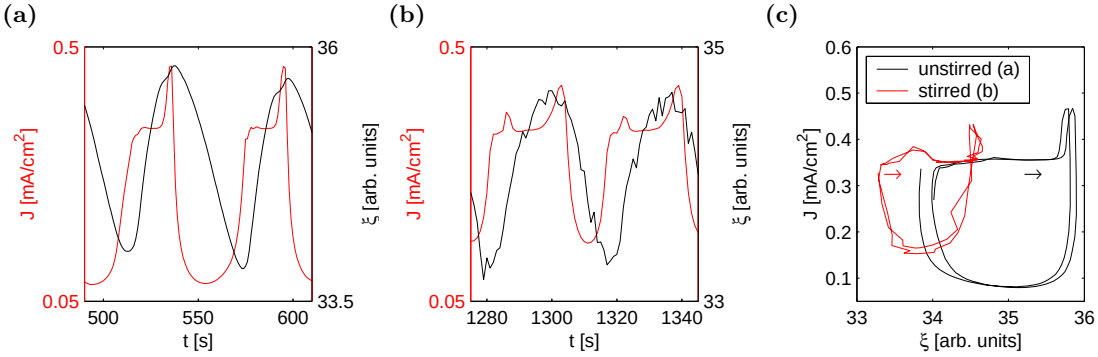

Figure 6.14: Enlargement of the time series in Fig. 6.13 **(a)** without and **(b)** with stirring. **(c)** $J - \overline{\xi}$ phase space plot of **(a-b)**. The ragged edges in $\overline{\xi}$ are a result of gas bubbles loosened by the stirring obstructing the optical path.

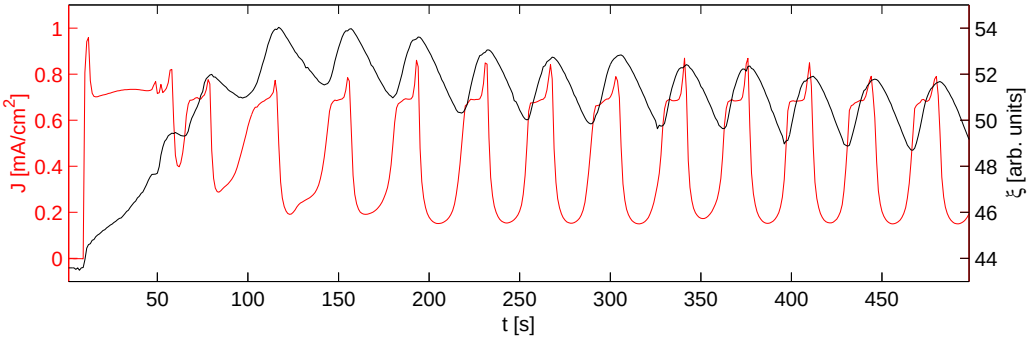

Figure 6.15: Stable high-amplitude oscillations on n-type silicon in an stirred electrolyte. Experimental conditions: $c_{\mathrm{NH_4F}} = 0.05\,\mathrm{mol/l}$, pH = 2.3, $R_{\mathrm{ser}} = 0\,\mathrm{k\Omega}$, $U = 8\,\mathrm{V}$, $L = 0.81\,\mathrm{mW/cm^2}$, and $A = 8.11\,\mathrm{mm^2}$.

increases to 62, where oscillations are not stable. At a higher etch rate under otherwise identical conditions, $\overline{\xi}$ does not rise above 54 and eventually oscillates around 50 (Fig. 6.15). This clearly suggests that a certain oxide layer thickness is necessary to enable oscillations. It has to be large enough to provide a limiting effect on the current in combination with the resistance of the system. The system is driven out of the oscillatory regime when the oxide layer thickness is too large.

6.3 Discussion and Outlook

Current density oscillations occur in a certain interval of oxide layer thickness. The oxide layer thickness can be adjusted by changing the oxide formation rate or by changing the etch rate. In the case of n-type silicon, the former can be easily adjusted by limiting the current density with the illumination intensity. The higher the value of L, the larger z_{L}. For very low values of L, the domain **III**, where a 'dry' oxide layer covers the electrode is not reached. Fig. 6.4e gives an example of such a case. At high values of L, the observed dynamics on n-type silicon are similar to those on p-type silicon and the oxide formation rate can be adjusted by changing the applied voltage or the size of the series resistance in the system. What can be considered a high value of L depends on the values for those two parameters.

An increase in the oxide formation rate at a constant etch rate leads to a thicker oxide layer. Conversely, an increase in the etch rate at a constant oxide formation rate leads to a thinner oxide layer. This can be seen in Fig. 6.13. Comparison of Fig.6.1c (unstirred) and Fig. 6.15 (stirred) indicates that a change in the oxide layer thickness as a result of changing the stirring rate affects the dynamics, as oscillations are stable only in the stirred case.

At intermediate values of L, *e.g.* $L = 0.40\,\mathrm{mW/cm^2}$, the $J - U$ characteristic in Fig. 6.11 shows that the limited current density is higher than the unlimited current density in the plateau region of domain **III**. At the same time it is smaller than the unlimited current density of the second characteristic peak. This constitutes the origin of hysteresis depicted in Fig. 6.5a. During potential scans and upon applying small potential steps one after the other, not enough oxide is formed and the system stays in domain **II** due to the current density limitation. In contrast, the system moves right to domain **III** when a large potential step is applied at the same parameters, or when L is lowered stepwise starting at a state with a sufficiently thick oxide layer. The system may exhibit sustained high-amplitude oscillations or be in a steady state under the same experimental conditions due differing kinds of oxide qualities, *i.e.* 'wet' or 'dry' oxide.

Understanding these parameters allows for fine tuning of the oscillations as low-amplitude oscillations occur at larger oxide thickness as high-amplitude oscillations. In the case of n-type silicon in contrast to p-type silicon, sustained oscillations, though only high-amplitude ones, are observed even in the absence of a series resistance in the circuit. Low-amplitude oscillations on n-type silicon are observed only under sufficient illumination and the same conditions as for p-type silicon, *i.e.* intermediate applied voltages and sufficiently high series resistances. Hence, it is likely that the oscillation mechanism is the same in both cases, except for the source of the limitation.

High-amplitude oscillations exhibit marked differences between p-type silicon and n-type silicon. They are clearly influenced by the illumination intensity in the case of an n-type silicon electrode. The most prominent feature is a plateau in the current density encompassed by two current spikes. The ratio of the size of one spike to the other depends on the value of L.

The behavior of high-amplitude oscillations on n-type silicon with the highest current density plateau at high values of L is the one most similar to high-amplitude oscillations on p-type silicon. An example is the transient high-amplitude oscillations depicted in Fig. 6.1d between 100 and 1100s. J shows a plateau, but no spikes. Fig. 6.16 shows z_{L}, J and $J_{\bar{\xi}}$, the discrepancy, $J - J_{\bar{\xi}}$, and the change in buffered charge, $\Delta\sigma$, resulting from the discrepancy. The optical proportionality constant, c_{opt}, was determined for sustained low-amplitude oscillations under the same experimental conditions. These time series are similar to the ones obtained for high-amplitude oscillations in the case of p-type silicon (Fig. 4.8 and Fig. 4.9). The different characteristics of $\Delta\sigma$ can be attributed to the existence of the plateau in the case of n-

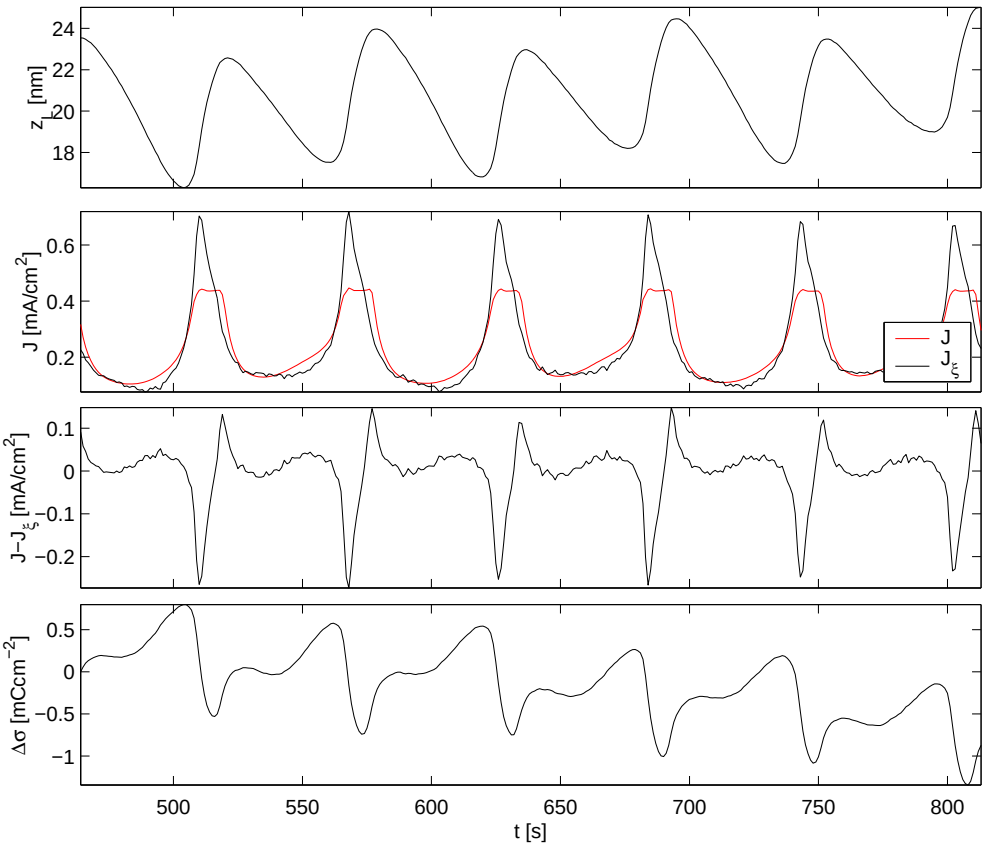

Figure 6.16: High-amplitude current oscillations: oxide layer thickness, z_{L} (top panel), the measured current density, J, and the calculated current density, $J_{\overline{\xi}}$ (both second panel), the difference, $J - J_{\overline{\xi}}$ (third panel), and the charge density variations, $\Delta\sigma$ (bottom panel). Experimental conditions: in Fig. 6.1d. Smoothing: $k = 0$. Fitting: $c_{\mathrm{opt}} = 3.57$.

type silicon. As L is decreased, the discrepancy between J and $J_{\overline{\xi}}$ increases and the spikes encompassing the plateau become more pronounced until only spikes survive. Presumably, the spike before and the spike after the plateau have different origins.

The current spike following the current density plateau results from electron injection. Only hole capture is affected by the limitation of charge carriers in the semiconductor. In contrast, electron injection depends mainly on the amount of partially oxidized silicon species that are able to inject electrons. Evidence for the connection of the spikes following the plateau to electron injection is that the quantum efficiency increases during these spikes. In addition, the time series from Fig. 6.4 show that the slope of $\overline{\xi}$ decreases during these spikes, even though the current density is increasing. This also indicates electron injection from partially oxidized species, because silicon species oxidized to different degrees cannot be distinguished from one another in $\overline{\xi}$.

The behavior of $\overline{\xi}$ results from the difference between the hole capture rate and the etch rate. The higher the ratio of electron injection to hole capture, the less 'visible' oxide is formed per charge flowing in the circuit. J is smaller than $J_{\overline{\xi}}$ in the plateau region in Fig. 6.10. During the decreasing flank, J is larger than $J_{\overline{\xi}}$, *i.e.* electron injection is above its average value and hole capture is below the value dictated by the limiting effect of L.

The spike preceding the current density plateau may result from the hole capture of excess holes not used during the increasing flank of J. Another possibility is changes in the recombination rate, which depends on the space charge voltage drop (Memming, 1964). Band

bending makes recombination possible as it increases the amount of holes at the surface. The spike before the plateau is accompanied by a high ohmic voltage drop, and a high hole capture rate. The high current density leads to a low expected recombination rate of electron-hole pairs.

In the present ellipso-microscopic setup, it is not possible to distinguish between changes of $\overline{\xi}$ stemming from 'dry' oxide from domain **III**, and 'wet' oxide or other interface layers from the domains **I** or **II**. However, it can be expected that a completely different oscillation mechanism is responsible for the spike dominated oscillations in the absence of a 'dry' oxide layer. The present results give valuable further insight into the adjustment of different oscillation types, as well as into the contribution of J_{cap} and J_{inj} to the current density.

The steady states at low values of L lie in a domain where silicon is not covered by passivating 'dry' oxide. Depending on the size of J, they either lie in domain **I** (divalent dissolution) or in domain **II** ('wet' oxide). Scanning the $J - L$ and the $\overline{\xi} - L$ characteristics could lead to more insight into the influence of L, especially when comparing them to the $J - \Phi_{\mathrm{eff}}$ and the $\overline{\xi} - \Phi_{\mathrm{eff}}$ characteristics. This could also elucidate the origin of the spike dominated oscillations. Furthermore, the application of *in situ* ellipsometry or another quantitative surface probing technique could enhance the understanding of the processes at the interface.

Quantitative stirring speeds are not available in the current setup. The study of a wide range of defined stirring speeds could also prove successful in advancing the understanding of the system.

Chapter 7

Spatial Pattern Formation

This chapter is concerned with the dynamics of the spatially extended system. By including an imaging lens in the optical setup, the ellipsometric signal can be monitored as a function of position. In this way it can be investigated if and how current density oscillations are accompanied by spatial patterns in oxide layer thickness.

Apart from the measurement of the time evolution of the current density distribution of a quasi-one dimensional ring electrode (Miethe, 2004), the spatio-temporal pattern formation at the silicon|oxide|electrolyte double interface was essentially unexplored, because satisfactory resolution, both in time and space, had never previously been achieved experimentally. However, an investigation of the electroluminescence during the anodic oxidation of silicon hinted at a variety of patterns dependent on doping level and illumination (Hasegawa *et al.*, 1988; Arimoto *et al.*, 1988). These experiments were conducted at voltages of 200 V. The oxide grew to a thickness of 100 nm, because it was not etched. Undoped and n-type silicon showed pattern formation at small oxide thicknesses around 20 nm. Localized oxidation of silicon in the form of concentric moving fronts, labyrinthine patterns, stripes and homogeneity at constant current densities were observed. The order of magnitude of the characteristic wavelength of the patterns is similar to the one presented in this chapter. Equally important, the oxide layer thickness of p-type silicon was always uniform apart from short transients.

In Sec. 5.1 it was shown that the temporal dynamics are greatly determined by the size of the series resistance R_{ser}. In the case of n-type silicon, the illumination intensity affects the temporal dynamics as well. Both parameters also play a decisive role in the formation of spatial patterns. An overview of the connection between temporal and spatial dynamics influenced by R_{ser} and L is given in Sec. 7.1. Both n-type silicon and p-type silicon, as well as states with sustained and transient dynamics are investigated.

Complex spatial patterns during high-amplitude current oscillations on n-type silicon are discussed in detail following the overview. In Sec. 7.2, a labyrinthine cluster pattern is described with regard to phase locking and the superposition of the base frequency and its subharmonics. Furthermore, the observed behavior is elucidated by means of a modified complex Ginzburg-Landau equation. The focus of Sec. 7.3 are coexisting domains oscillating at different frequencies, and the mobility of the walls between these domains.

7.1 Temporal Dynamics and Spatial Pattern Formation

In a typical experiment, the electrode is left at open-circuit potential for some time such that it is hydrogen terminated. Then a potential step to a desired applied voltage is applied and the temporal evolution of ξ is measured as a function of space and time. It turns out that this approach always leads to pronounced transient patterns for the first hundred seconds after the potential step and then to sustained patterns or spatial uniformity.

Transient Pattern Formation

In the first few seconds, an initial passivating oxide layer is formed. The oxide formation kinetics strongly depends on position. In the following, two representative examples are shown. Fig. 7.1 shows a series of snapshots of $\xi(x, y)$ an n-type silicon electrode where the initial oxide formation is accompanied by the evolution of concentric waves. The time series of J and $\overline{\xi}$ are plotted in the bottom plate with black dots indicating the particular times, t_i, of the snapshots.

The local value of ξ is coded by the coloring according to the color bar in the top panel. The first electrode image is taken at a time close to the voltage jump. It shows spatial homogeneity. The following image shows the initiation of two wave fronts, one at the top and one at the bottom of the electrode, which propagate to the center of the electrode. A second concentric wave front follows the one at the top of the electrode in the third snapshot. Another one is created at the bottom of the electrode in the fifth snapshot. The movement of these wave fronts is accompanied by an uniform increase of the oxide layer thickness across the entire electrode. The overall increase of ξ is reflected in the time series of $\overline{\xi}(t)$. As will be shown below, the superposition of a spatially heterogeneous pattern on spatial uniform oscillations is typical for the electrodissolution of silicon.

In Fig. 7.2, another typical transient pattern, this time on p-type silicon, is depicted, where plane wave fronts, parallel to the longer side of the electrode, propagate across the electrode. The visibility of the stripe pattern in the snapshot is enhanced by subtracting a background image, $\xi_{\mathrm{bg}}(x, y)$:

$$\xi_{\mathrm{enh}}(t, x, y) = \xi(t, x, y) - \xi_{\mathrm{bg}}(x, y) \tag{7.1}$$

$\xi_{\mathrm{bg}}(x, y)$ being the temporal average over the displayed time range. In the first image of the series of snapshots, the oxide thickness layer increases in a domain between $y = 100$ and $y = 200$. The third image is similar. In the second image, a different domain ($y = 300 - 400$) shows the highest oxide thickness, which is similar to the one in the fifth image. In the fourth image, the increase is observed between $y = 100$ and $y = 300$. The increase of ξ in a certain domain compared to the rest of the electrode, is a sign of increased activity in this domain. At the extrema of $\overline{\xi}$, the activity of the electrode alternates between the domain in the center and the domain at the fringes of the electrode.

More insight into the spatio-temporal dynamics of the electrode is obtained by plotting the temporal evolution of a cross section of ξ at position x_i or at position y_j:

$$\xi_{\mathrm{cross}}(t, y) = \xi(t, x_i, y) \tag{7.2}$$

or

$$\xi_{\mathrm{cross}}(t, x) = \xi(t, x, y_j) \tag{7.3}$$

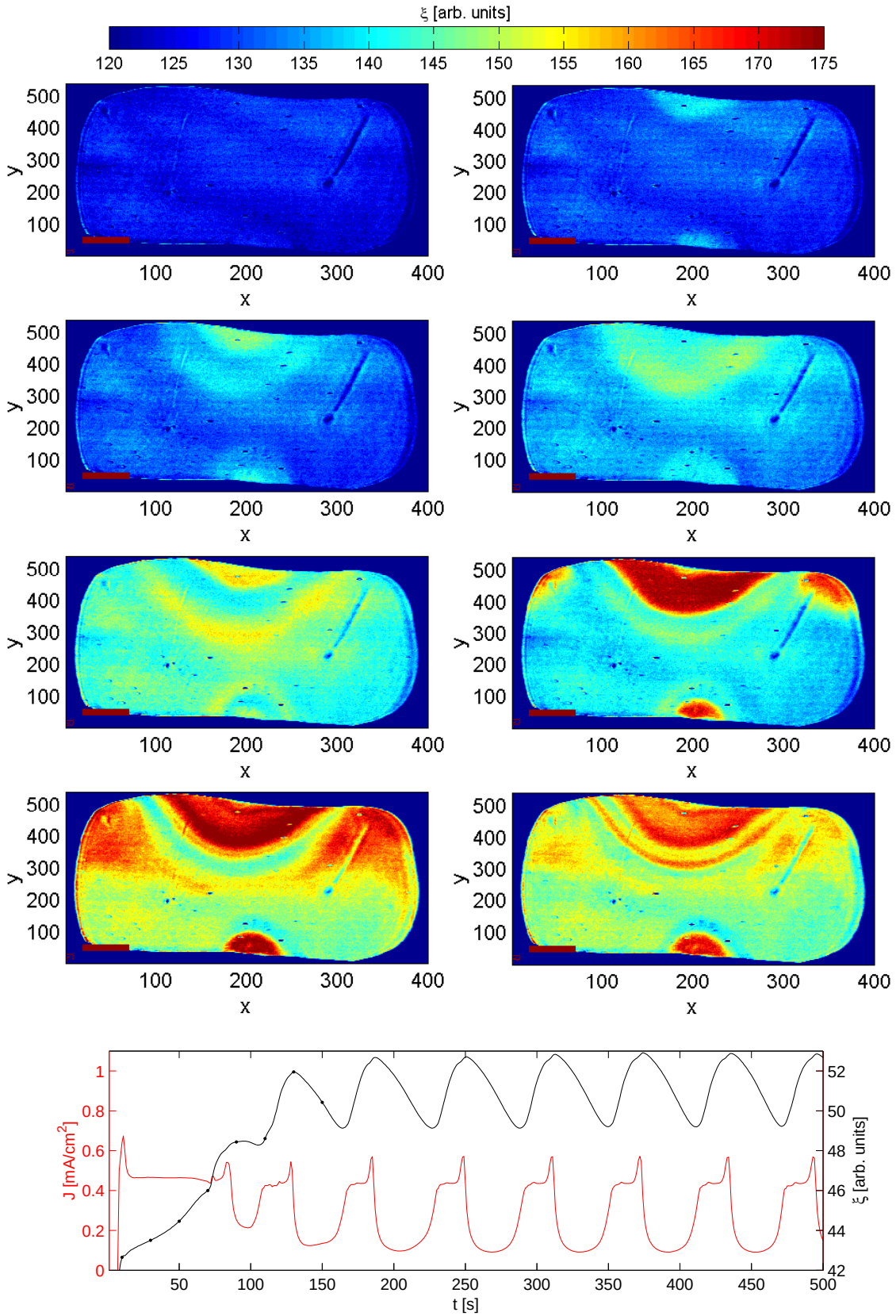

Figure 7.1: A series of snapshots of the spatial distribution of the ellipso-microscopic signal, ξ, of an n-type silicon electrode at the times indicated with • in the time series of $\overline{\xi}$, displayed together with the current density time series, J, (both bottom panel). The length of the horizontal red bar in the left hand bottom corner indicates a length of 1 mm. Experimental conditions: $c_{NH_4F} = 0.05$ mol/l, pH = 2.3, $A = 8.11\,\mathrm{mm}^2$, $R_{ser} = 0\,\mathrm{k}\Omega$, $U = 8\,\mathrm{V}$, $L = 0.52\,\mathrm{mW/cm}^2$, and n-type silicon.

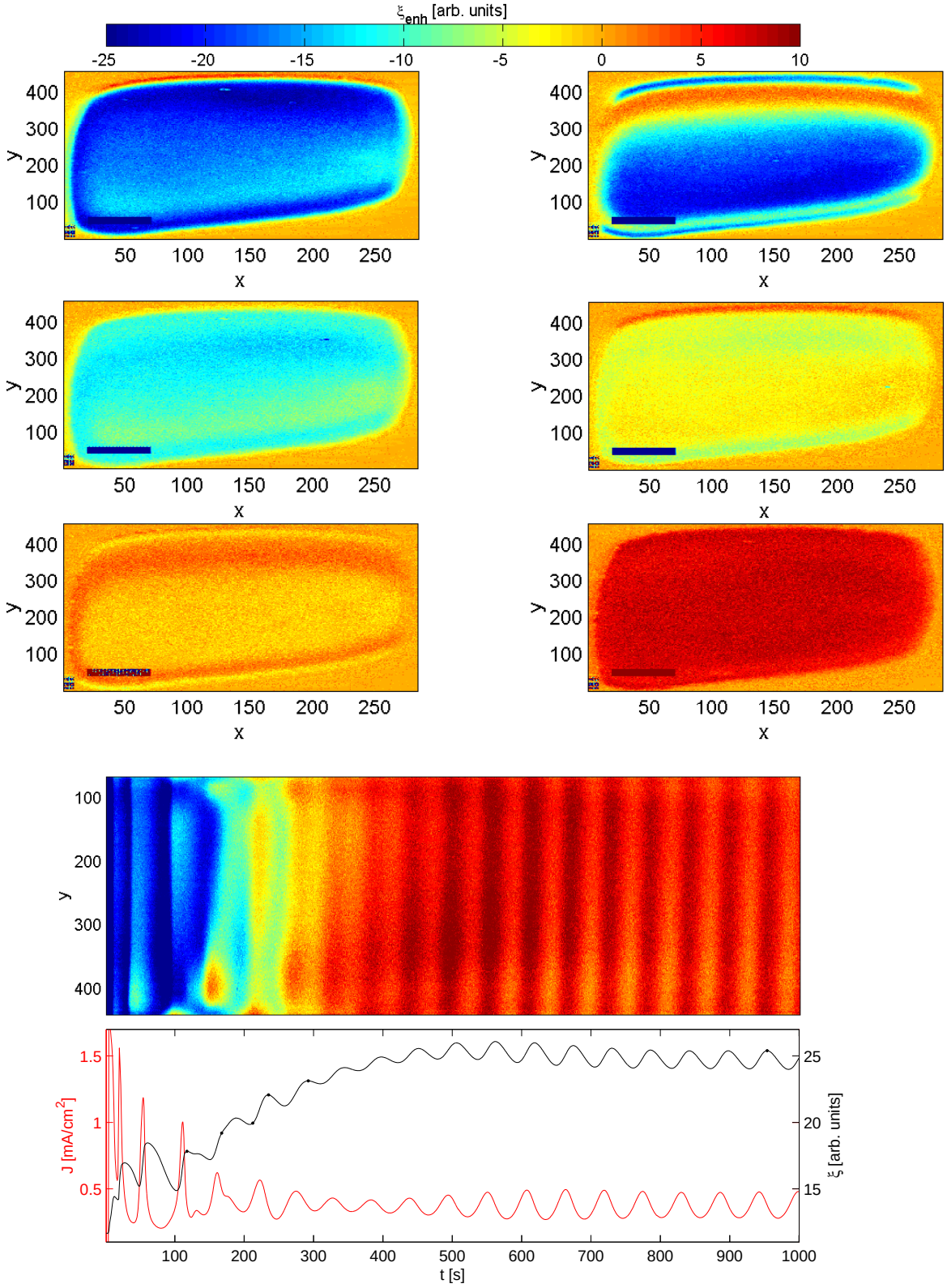

Figure 7.2: Transient cluster pattern followed by sustained spatially uniform oscillations. **(Upper plates)** Snapshots of $\xi(x, y)$ at six different times indicated by dots in the bottom panel. **(Second last panel)** Time evolution of a cross section of ξ at $x = 200$ enhanced by background subtraction. **(Bottom panel)** Time series of J and $\overline{\xi}$. The cross section is smoothed using a central moving average with $k = 2$. The length of the horizontal blue bar at the bottom indicates a length of 1 mm. Experimental conditions: $R_{\text{ext}} = 100\,\text{k}\Omega$, $U = 9.65\,\text{V}$, $c_{\text{NH}_4\text{F}} = 0.05\,\text{mol/l}$, pH = 2.4, $A = 4.91\,\text{mm}^2$, and p-type silicon.

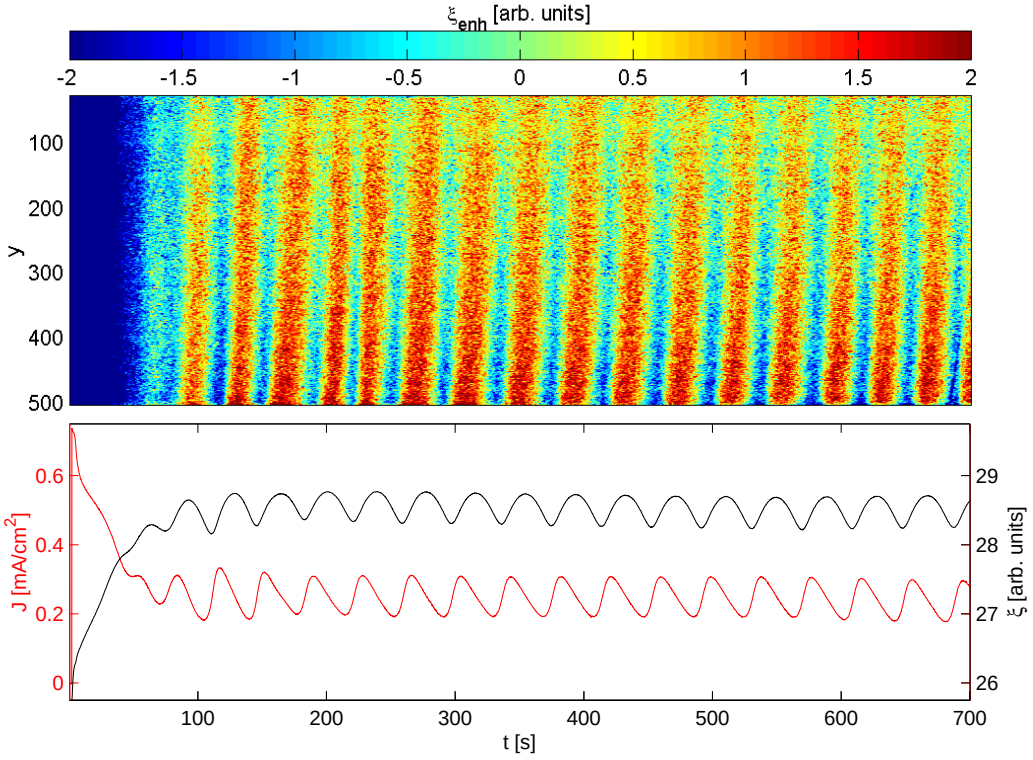

Figure 7.3: Spatial homogeneity of low-amplitude oscillations on p-type silicon. **(top panel)** Time evolution of a cross section of the local ellipso-microscopic signal, ξ, at $x = 200$ enhanced by background subtraction. **(bottom panel)** Time series of J and $\overline{\xi}$. Smoothing: $k = 5$. Experimental conditions: in Fig. 4.2a, and p-type silicon.

In Fig. 7.2 in the panel below the snapshots, $\xi(t, 200, y)$ and the time series of J and $\overline{\xi}$ are displayed. The data of the cross section are also enhanced via background subtraction. The time evolution of a cross section is particularly useful to obtain an overview of the dynamical behavior of the electrode in time, and thus allows for the easy elucidation of pattern formation.

In Fig. 7.2, the transient pattern exists for 400 seconds, after which spatially uniform oscillations are established across the entire electrode. The transient alternation of increased oxide layer thickness between the center and the fringes of the electrode at subsequent oscillation maxima is easy to see in the time evolution of the cross section between $t = 150$ s and $t = 300$ s. This spatial pattern accompanies the transient high-amplitude oscillations. They are followed by sustained low-amplitude oscillations which are associated with spatially uniform oscillations. The occurrence of uniformly oscillating states is further discussed in the next subsection.

Uniform Oscillations

In the case of p-type silicon, all spatial patterns are transient. Sustained current density oscillations are always accompanied by a practically, uniformly changing oxide layer thickness. Fig. 7.3 shows an example of quasi-uniform oscillation. The cross section reveals that the local oscillators are not fully synchronized. Instead, a very fast wave front moves across the electrode from $y = 500$ to $y = 1$. This is obvious at $t = 700$ s, where the local oscillators for large y have already reached their maximum, but the local oscillators for small y are still close to the preceding minimum. Because of the fast propagation velocity of the wave fronts, the oscillations are called quasi-uniform.

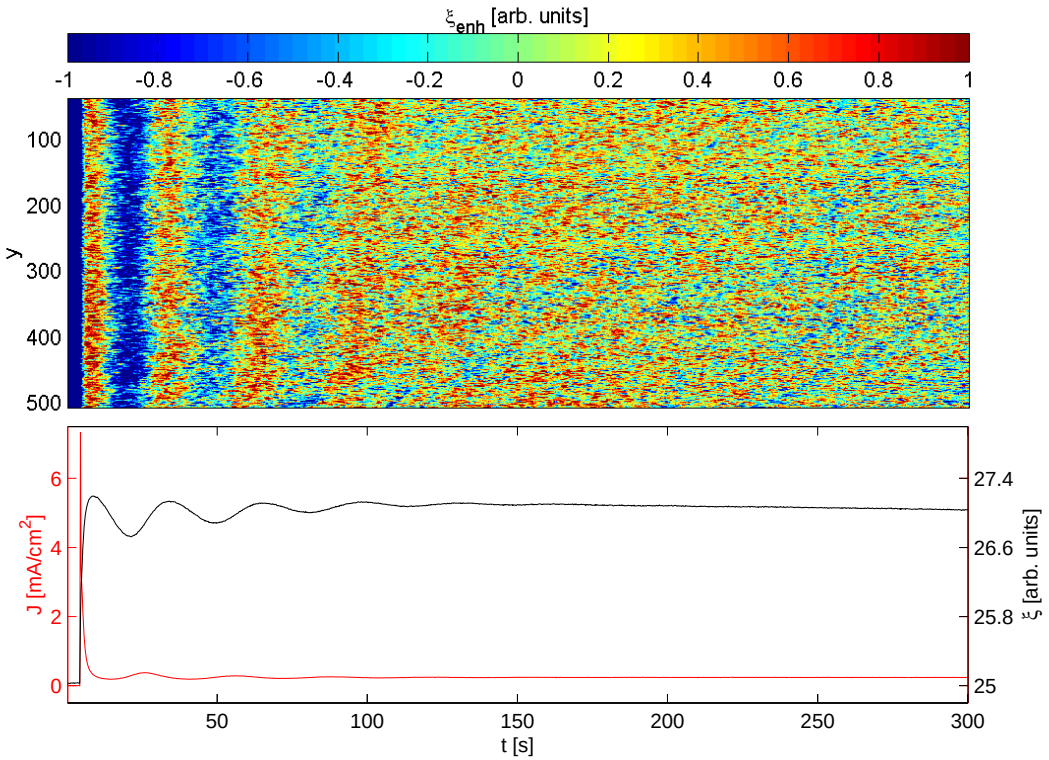

Figure 7.4: Spatially uniform damped oscillations on p-type silicon. **(top panel)** Time evolution of a cross section of the local ellipso-microscopic signal, ξ, at $x = 180$ enhanced by background subtraction. **(bottom panel)** Time series of J and $\overline{\xi}$. Smoothing: $k = 1$. Experimental conditions: in Fig. 5.1, and p-type silicon.

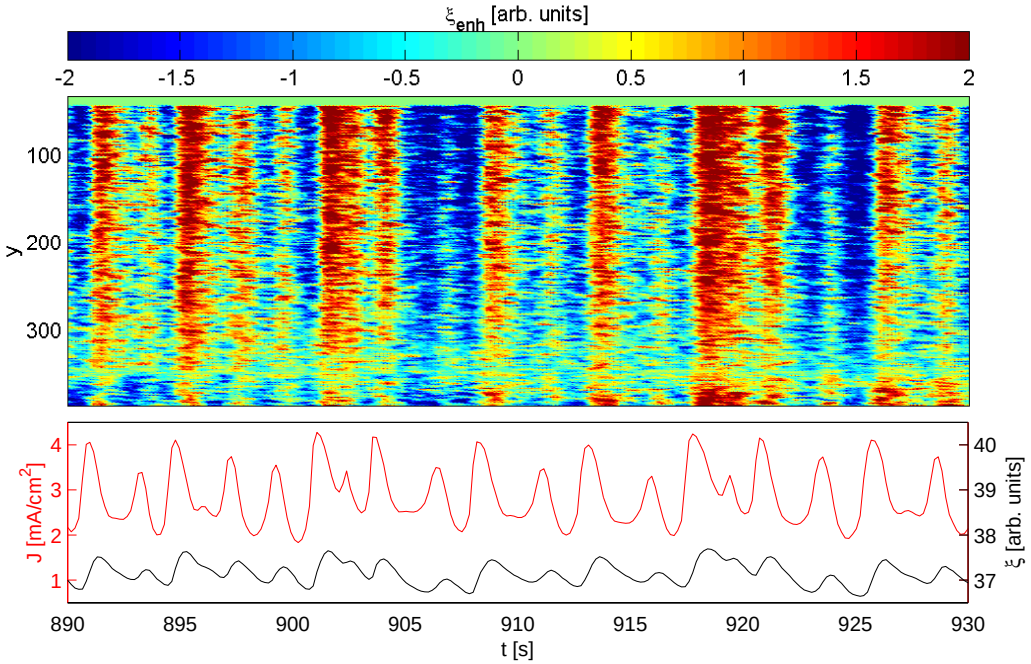

Figure 7.5: Temporally chaotic low-amplitude oscillations on p-type silicon. **(top panel)** Time evolution of the cross section of ξ at $x = 200$ enhanced by background subtraction. **(bottom panel)** Time series of J and $\overline{\xi}$. Smoothing $k = 2$. Experimental conditions: in Fig. 5.11d, and p-type silicon.

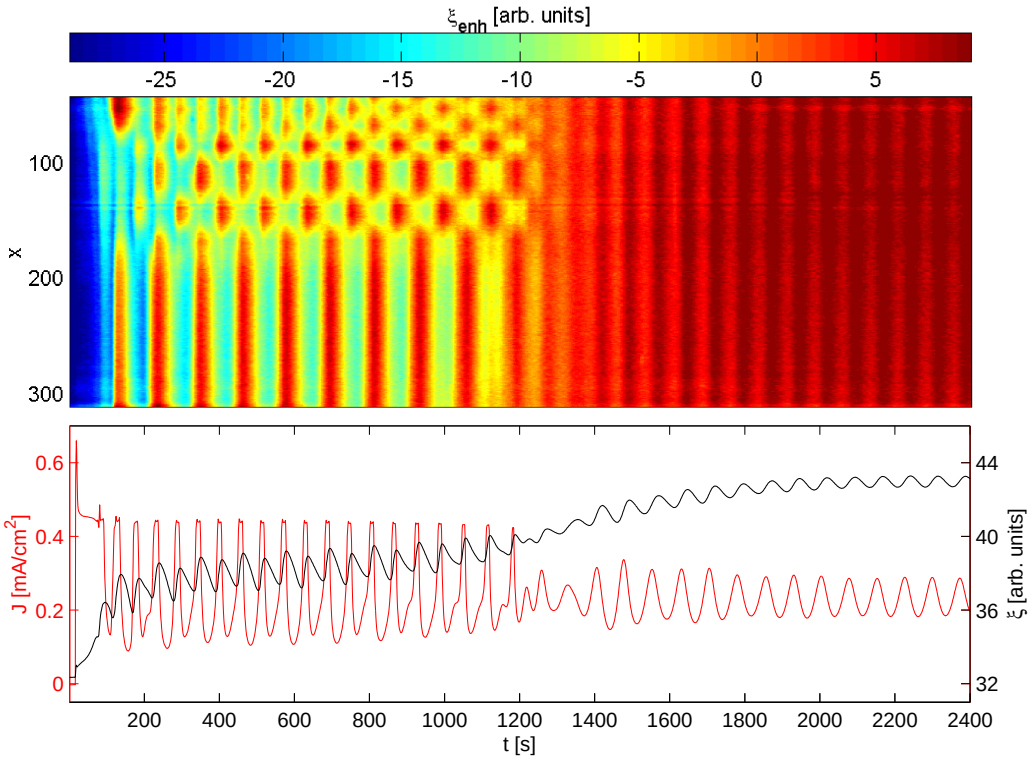

Figure 7.6: Emergence of spatial homogeneity from spatial clusters at the onset of low amplitude oscillations (n-type silicon). **(top panel)** Time evolution of the cross section of ξ at $y = 400$ enhanced by background subtraction. **(bottom panel)** Time series of J and $\overline{\xi}$. Smoothing $k = 5$. Experimental conditions: in Fig. 6.1d, and n-type silicon.

Similarly, damped current density oscillations are accompanied by uniformly damped oxide thickness oscillations (Fig. 7.4).

In Fig. 7.5, the chaotic oscillations from Fig. 5.11d also show spatial homogeneity. The amplitude of ξ is small, therefore the signal to noise ratio is poor.

On n-type silicon in contrast to p-type silicon, high-amplitude current density oscillations accompanied by spatial pattern formation were observed. However, the low-amplitude current density oscillations on n-type silicon, again go along with spatially uniform layer thicknesses. Fig. 7.6 shows that the transient spatial pattern disappears when the stable low-amplitude oscillations set in. Beyond $t = 1400$ s, all local oscillators of ξ oscillate synchronously and in phase with $\overline{\xi}$. A prominent feature of the cross section in Fig. 7.6 is the transient cluster pattern that forms initially when the time series shows high-amplitude current density oscillations. Sustained cluster patterns are discussed in the next subsection.

The spike dominated current density oscillations observed on n-type silicon at a low illumination intensity are also practically spatially uniform. The local oscillators in the cross section, depicted in Fig. 7.7 show a high degree of synchronization, but there are some variations across the electrode. The cross section and especially the two local time series of ξ, illustrate how the local dynamics change from period-1 to period-2 dynamics depending on the spatial position.

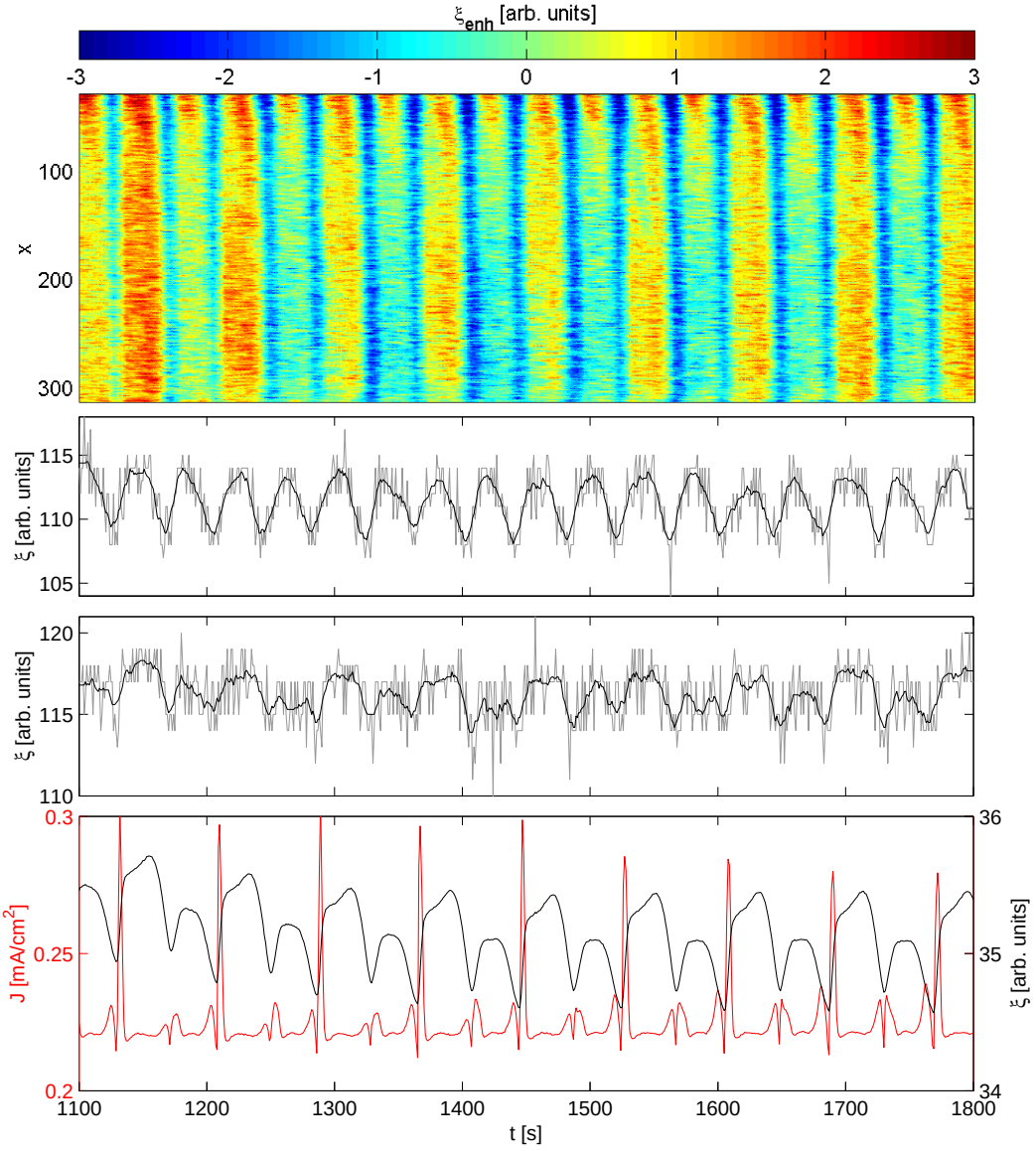

Figure 7.7: Spike dominated oscillations on n-type silicon. **(top panel)** Time evolution of the cross section of ξ at $y = 400$ enhanced by background subtraction. **(second panel)** Local time series at $y = 400$ and $x = 30$. **(third panel)** Local time series at $y = 400$ and $x = 200$. **(bottom panel)** Time series of J and $\overline{\xi}$. Smoothing $k = 5$. Experimental conditions: in Fig. 6.4e, and n-type silicon.

Cluster Pattern on n-type silicon

Cluster formation may occur in spatially extended oscillating systems or arrays of globally coupled oscillators where groups of synchronized states form. All oscillators within one group are fully synchronized. Oscillators belonging to different groups lie on different limit cycles in phase space (amplitude clusters), exhibit a phase shift (phase clusters) or a different frequency (frequency clusters). The difference between phase and frequency clusters is subtle and depends on the definition of phase. They are not distinguished here.

A non-transient cluster pattern develops on n-type silicon during high-amplitude current density oscillations only. Lower R_{ser} are necessary than in the case of low-amplitude oscillations. At intermediate R_{ser}, an immobile-cluster pattern evolves with a characteristic spatial wavelength between 200 and 500 μm. Fig. 7.8 shows four snapshots at consecutive extrema of $\overline{\xi}$.

A labyrinthine structure of the pattern is especially pronounced at the maxima of $\overline{\xi}$, *i.e.* in the first and third snapshot. Large parts of the electrode image appear inverted going from one maximum to the next. Formerly blue areas appear red and vice versa. The features of this cluster pattern are discussed in detail in Sec. 7.2.

At lower or zero R_{ser}, the cluster domains are mobile. As illustrated in the time evolution of the cross section in Fig. 7.9, domains with a larger characteristic wavelength move across the electrode. Some of the domains exhibit period-3 oscillations and others period-1 dynamics. This can be seen in the series of snapshots taken at consecutive maxima of $\overline{\xi}$ in the upper part of Fig. 7.9, *e.g.* the domain in the top left hand corner of the electrode is active in every third snapshot, *i.e.* in the third and the sixth. A detailed discussion of this moving-cluster pattern is given in Sec. 7.3.

Fig. 7.10 shows that the characteristic wavelength of the moving domains is affected by the stirring rate of the electrolyte solution. The solution is stirred between $t = 650$s and $t = 1550$s. In this time interval, the pattern of the oxide layer thickness clearly has another characteristic wavelength than the one in the stagnant electrolyte solution. Initially, the amplitude of the cluster domains decreases. Then, the domains appear at different positions in space with a smaller characteristic wavelength and a higher oscillation frequency. Upon switching off the argon again, the initial moving domain pattern is restored. However, even as the solution is stirred, the prominent period-3 character of the domains is maintained.

Lastly, an intermittent so-called plateau pattern is observed, that is not related to the change of a system parameter. A typical example is given in Fig. 7.11. The experimental conditions include no external series resistance, an applied voltage of $U = 8$ V and a high illumination intensity, $L = 1.21\ \mathrm{mW/cm^2}$. The plateau appears at $t = 450$ s and can be described as a domain with period-1 dynamics that shows a higher average oxide layer thickness than its surroundings which also have period-1 dynamics. This is reflected in the intermittent increase of $\overline{\xi}$. The edge of the plateau shows prominent period-2 dynamics. After 500 s, the plateau disappears. At later points in the time series, the plateau pattern reappears in different areas of the electrode.

In addition, the formation and disappearance of a plateau in the domain with period-1 dynamics is observed in coexistence with the moving domains.

High-dimensional Spatio-temporal Chaos

At a higher ammonium fluoride concentration, high-dimensional chaos is observed during high-amplitude oscillations (Fig. 7.12). The chaotic current oscillations are accompanied by chaotic local oscillations of ξ. The data are thus an example of spatio-temporal turbulence in an electrochemical system.

In contrast, the chaotic current oscillations observed during low-amplitude oscillations at a high R_{ser} in the case of p-type silicon show synchronized local oscillators (Fig. 7.5). In the next-maximum map of the spatially synchronized low-dimensional chaos (Fig. 5.13f), all data points lie in a small quasi one-dimensional band suggesting that the chaotic behavior lives in a low-dimensional phase space, *i.e.* that the chaos is low-dimensional.

A next-minimum map of the data from Fig. 7.12 is shown in Fig. 7.13. The data points form a cloud-like structure, which is a strong hint that the dynamics lives in a high-dimensional phase space. Fully developed spatio-temporal turbulence cannot be explained by a one or two dimensional map (Schuster, 1988).

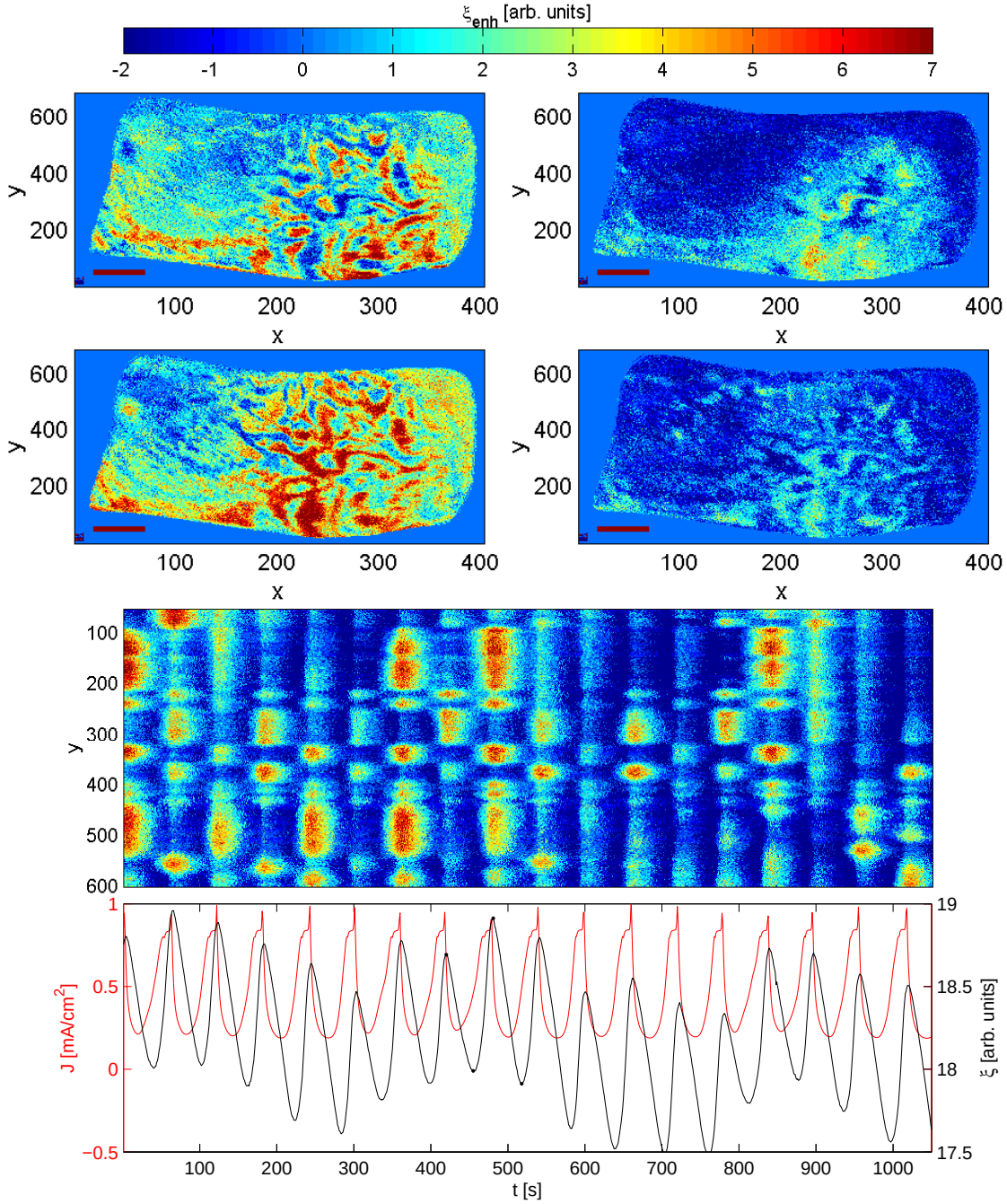

Figure 7.8: Labyrinthine cluster pattern on n-type silicon. **(upper plates)** Snapshots of the spatial distribution of the ellipso-microscopic signal, ξ, at the times indicated with dots in the bottom panel. **(second last panel)** Time evolution of the cross section of ξ at $x = 200$ enhanced by background subtraction. **(bottom panel)** Time series of $\overline{\xi}$, displayed together with the current density time series, J. The length of the horizontal red bar in the left hand bottom corner indicates a length of 1 mm. Experimental conditions: $c_{NH_4F} = 0.05$ mol/l, pH $= 2.3$, $A = 9.05$ mm^2, $R_{ser} = 30$ kΩ, $U = 11$ V, $L = 1.19$ mW/cm^2, and n-type silicon.

Overview of Spatio-temporal Pattern Formation

An overview of the spatial pattern formation is given in Tab. A.3 in the appendix. The character of the pattern depends, among other parameters, strongly on the doping of the silicon. In the case of p-type silicon, the oxide layer thickness shows a spatially uniform

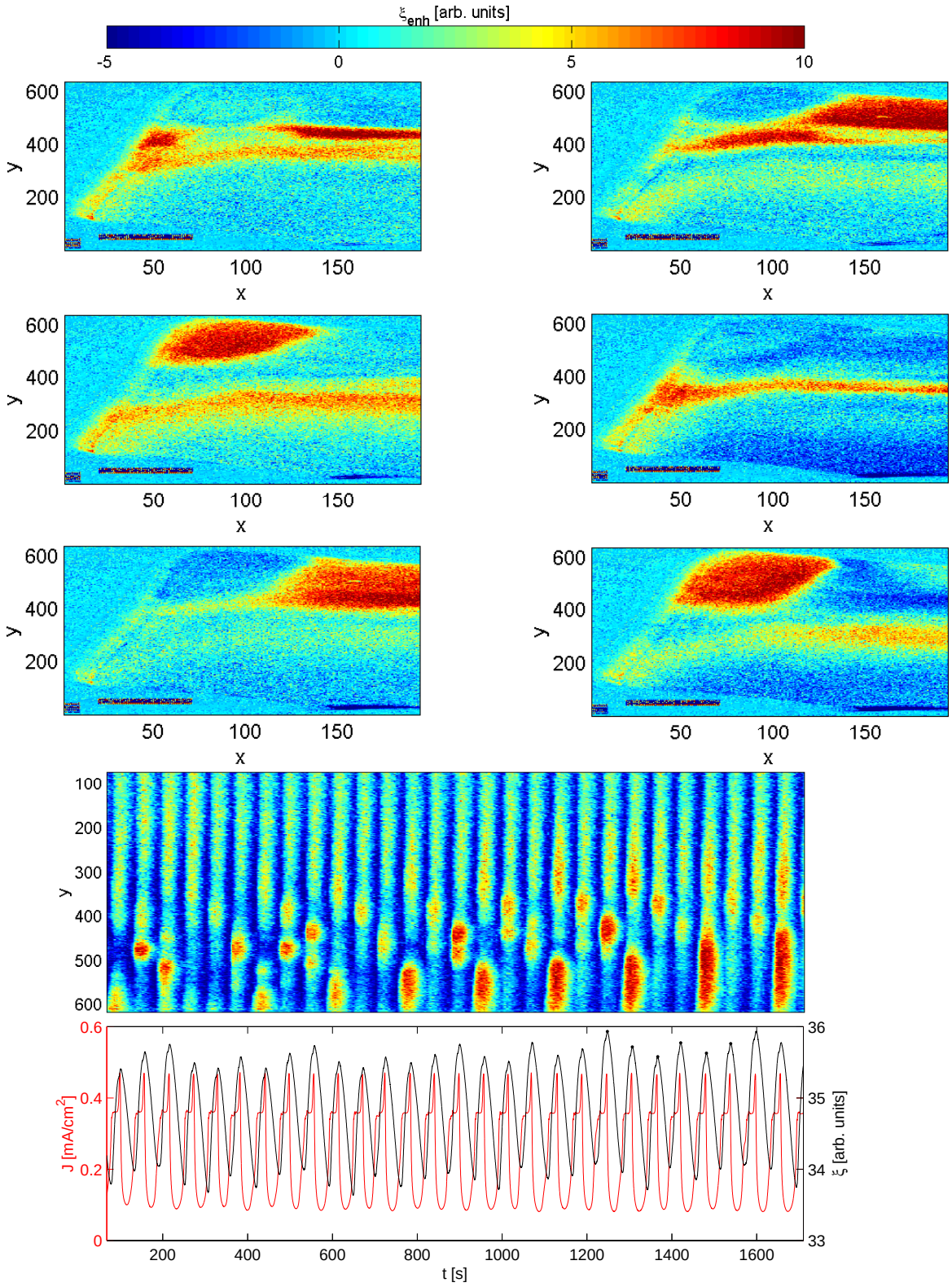

Figure 7.9: Moving domain pattern on n-type silicon. **(upper plates)** Snapshots of the spatial distribution of the ellipso-microscopic signal, ξ, at the times indicated with dots in the bottom panel. **(second last panel)** Time evolution of the cross section of ξ at $x = 100$ enhanced by background subtraction. **(bottom panel)** Time series of $\overline{\xi}$, displayed together with the current density time series, J. The length of the horizontal red bar in the left hand bottom corner indicates a length of 1 mm. Experimental conditions: $c_{NH_4F} = 0.05$ mol/l, pH = 2.3, $A = 9.64\,\mathrm{mm}^2$, $R_{ser} = 1\,\mathrm{k}\Omega$, $U = 8\,\mathrm{V}$, $L = 0.4\,\mathrm{mW/cm}^2$, and n-type silicon.

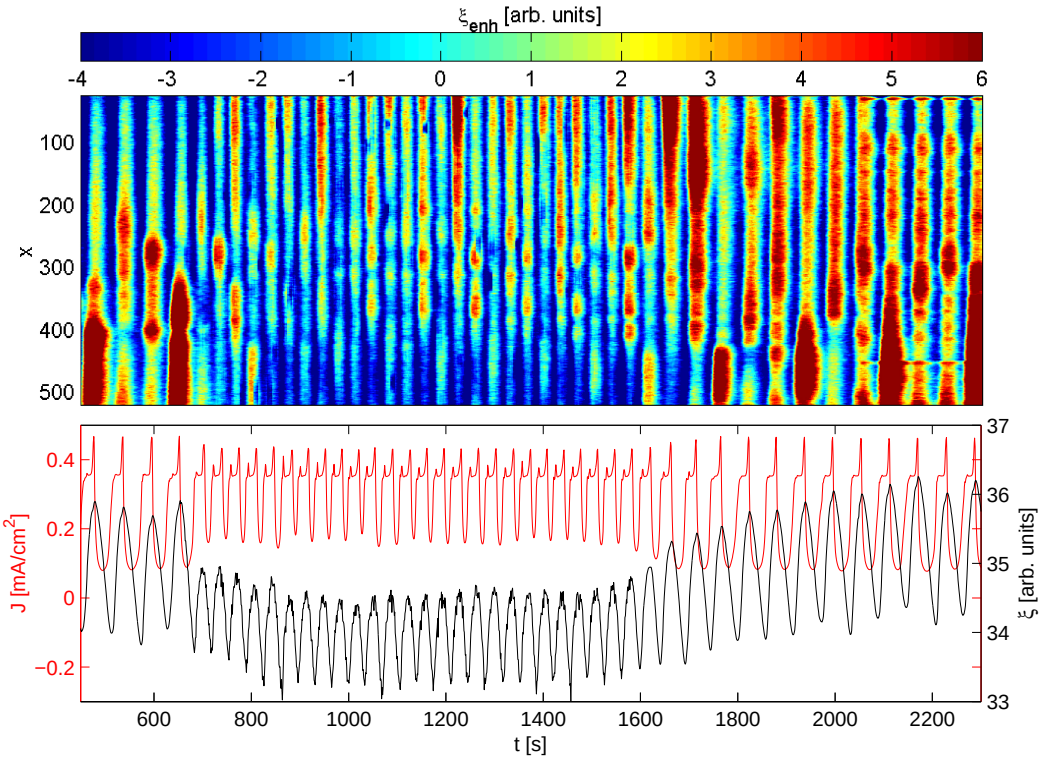

Figure 7.10: Influence of stirring between $t = 650\,\mathrm{s}$ and $t = 1550\,\mathrm{s}$ on the characteristic wavelength of a moving domain pattern (n-type silicon). **(top panel)** Time evolution of the cross section of ξ at $y = 290$ enhanced by background subtraction. **(bottom panel)** Time series of J and $\overline{\xi}$. Smoothing $k = 5$. Experimental conditions: in Fig. 6.13, and n-type silicon.

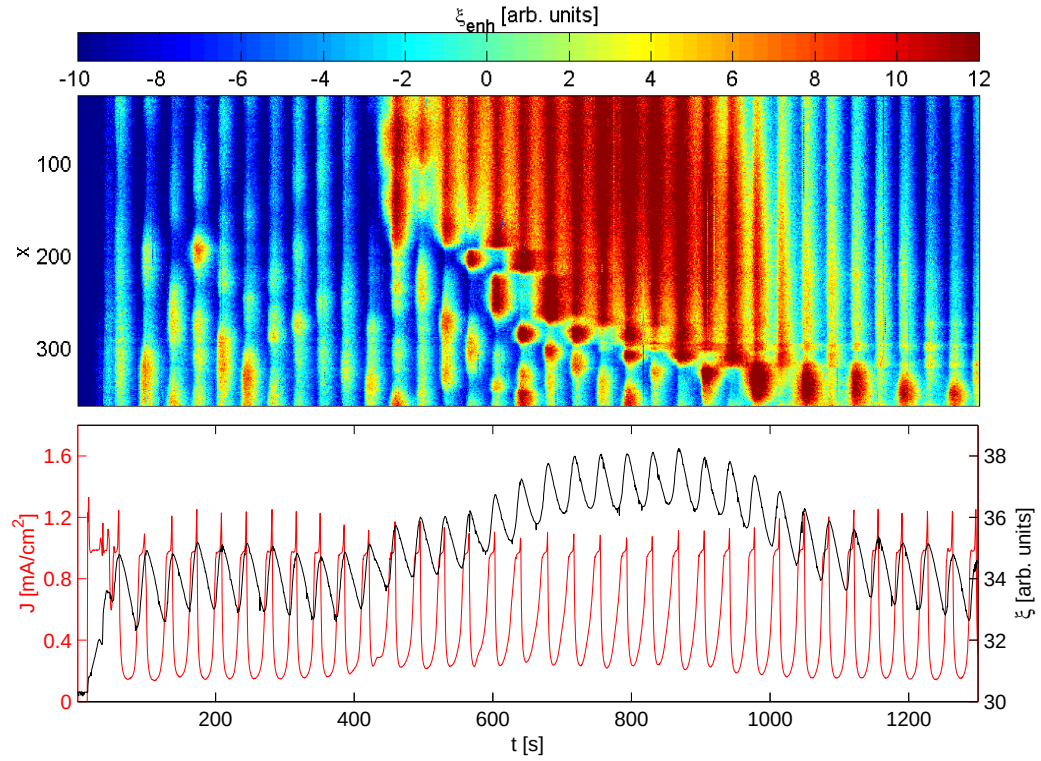

Figure 7.11: Plateau pattern on n-type silicon. **(top panel)** Time evolution of the cross section of ξ at $y = 400$ enhanced by background subtraction. **(bottom panel)** Time series of J and $\overline{\xi}$. Experimental conditions: $c_{\mathrm{NH_4F}} = 0.05\,\mathrm{mol/l}$, pH $= 2.3$, $A = 8.91\,\mathrm{mm^2}$, $R_{\mathrm{ser}} = 0\,\mathrm{k\Omega}$, $U = 8\,\mathrm{V}$, $L = 1.21\,\mathrm{mW/cm^2}$, and n-type silicon.

behavior, except for the transients that develop after applying a potential step from open-circuit potential to a potential that lies in domain **III**. In the case of n-type silicon, current density oscillations are accompanied by pattern formation in a certain region of parameter space. During low-amplitude oscillations and spike dominated oscillations of the current density the oxide layer thickness oscillates uniformly. In contrast, during high-amplitude oscillations cluster patterns form on the electrode surface. The features of these patterns depend on R_{ser}. A pattern of moving clusters is associated with low R_{ser}. This pattern is discussed in detail in Sec. 7.3. The moving clusters may be accompanied by the formation of plateaus. At intermediate R_{ser}, the clusters are immobile and show an intricate labyrinthine pattern, discussed in Sec. 7.2. Additionally, on n-type and p-type silicon, a variety of transient patterns may form after a potential step.

7.2 Immobile, Labyrinthine Cluster Pattern

Of all patterns discussed in this chapter, the cluster patterns are the most striking. They show phase clustering in the subharmonic mode that is superimposed on the spatially uniform base mode of the oscillations.

The labyrinthine pattern of spatially immobile clusters is most prominent during the oscillation maxima of $\overline{\xi}$. Snapshots of the electrode and the time evolution of a cross section illustrate this (Fig. 7.8). The pattern arises during high-amplitude current density oscillations on n-type silicon at intermediate R_{ser}. It appears inverted from one maximum to the next. From maximum to maximum, the bright and dark regions exchange their positions, suggesting that the overall dynamics is not simply periodic with the period of the total current.

From the cross section, one obtains the impression that a uniform oscillation with the base frequency, *i.e.* the frequency of the current density oscillations, is superimposed on an irregular pattern that changes with time. The irregular pattern has period-2 dynamics, *i.e.* the electrode pattern is restored at every other maximum. This impression becomes even stronger when looking at the local time series (Fig. 7.14). The local oscillation amplitude evolves irregularly with time and is different for each of the three oscillators shown, but an alternation between high and low maxima suggests underlying period-2 dynamics. However, the extrema of ξ of all individual oscillators are locked to the extrema of $\overline{\xi}$, though some of the extrema may disappear due to a large modulation of the local oscillation. The envelope of the complex dynamics of each individual oscillator contains harmonic contributions with half the base frequency.

This subharmonic contribution can be clearly seen in the power spectrum, $|a|^2(\nu)$, of the local time series along a cross section from Fig. 7.8. In Fig. 7.15, it is apparent that $|a|^2(\nu)$ exhibits two pronounced peaks. One peak lies at the base frequency, $f_1 = 17 \pm 1$ mHz, which is equivalent to the frequency of the current density oscillations. The second peak is subharmonic and lies at half the base frequency, $f_{1/2} = 9 \pm 1$ mHz. In contrast to the former peak, its intensity varies along the cross section.

In order to obtain an understanding of the two-dimensional spatial distribution of these modes, a frequency demodulation technique is used (Lin *et al.*, 2000). The dominant modes are extracted and the spatial distribution of amplitude, $|a|^2$, and phase, $\arg(a)$, are analyzed individually. In Fig. 7.16a, the spatial distributions of phase and amplitude are shown for the base frequency. The amplitude for the base mode is uniformly distributed and all local oscillators have the same phase.

This is also evident from Fig. 7.17a, where the distribution of the base mode is displayed in

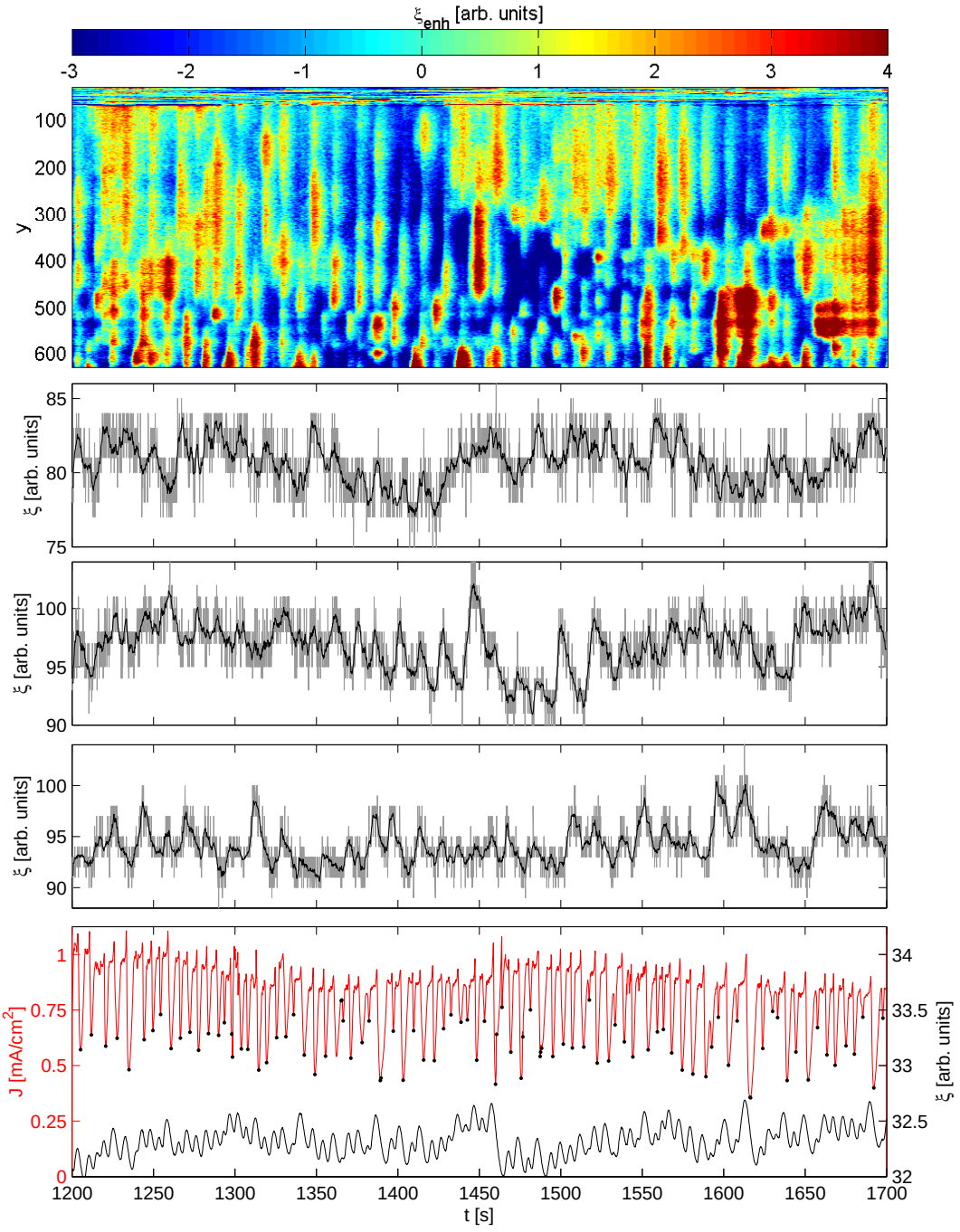

Figure 7.12: Spatio-temporal chaos on n-type silicon. **(top panel)** Time evolution of the cross section of ξ at $x = 200$ enhanced by background subtraction. **(second panel)** Local time series of ξ at $x = 200$ and $y = 250$. **(third panel)** Local time series of ξ at $x = 200$ and $y = 400$. **(fourth panel)** Local time series of ξ at $x = 200$ and $y = 560$. **(bottom panel)** Time series of J and $\overline{\xi}$. The minima of J are indicated by dots. Experimental conditions: $c_{\mathrm{NH_4F}} = 0.1$ mol/l, pH $= 3.1$, $A = 9.71\,\mathrm{mm}^2$, $R_{\mathrm{ser}} = 0\,\mathrm{k\Omega}$, $U = 8\,\mathrm{V}$, $L = 1.62\,\mathrm{mW/cm}^2$. Smoothing: $k = 5$.

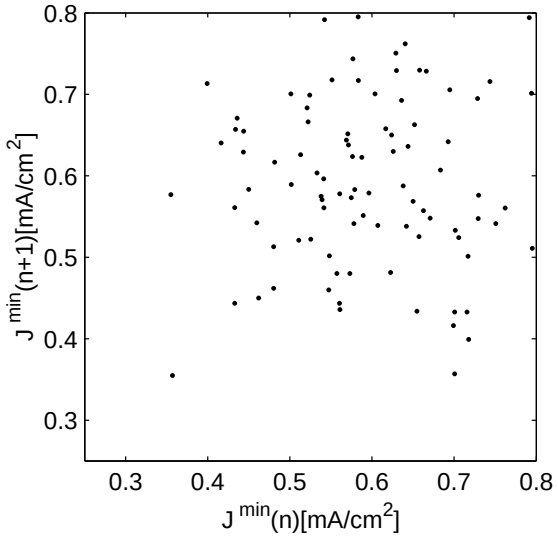

Figure 7.13: Next-minimum map of spatio-temporal turbulence. Due to the multi-dimensionality of the chaos, the chaotic dynamics cannot be represented by a simple mapping. Experimental conditions: in Fig. 7.12.

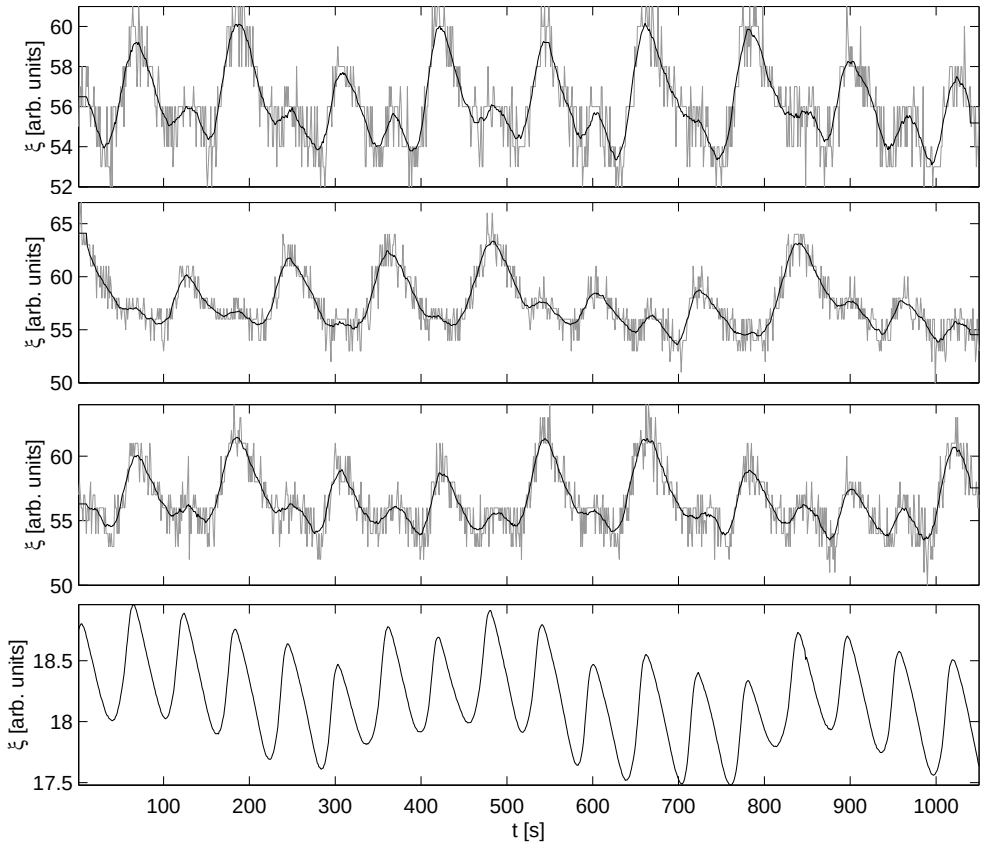

Figure 7.14: Local time series of ξ during labyrinthine clusters. **(top panel)** $x = 200$ and $y = 310$. **(second panel)** $x = 200$ and $y = 320$. **(third panel)** $x = 200$ and $y = 380$. **(bottom panel)** Time series of $\overline{\xi}$. Experimental conditions: in Fig. 7.8.

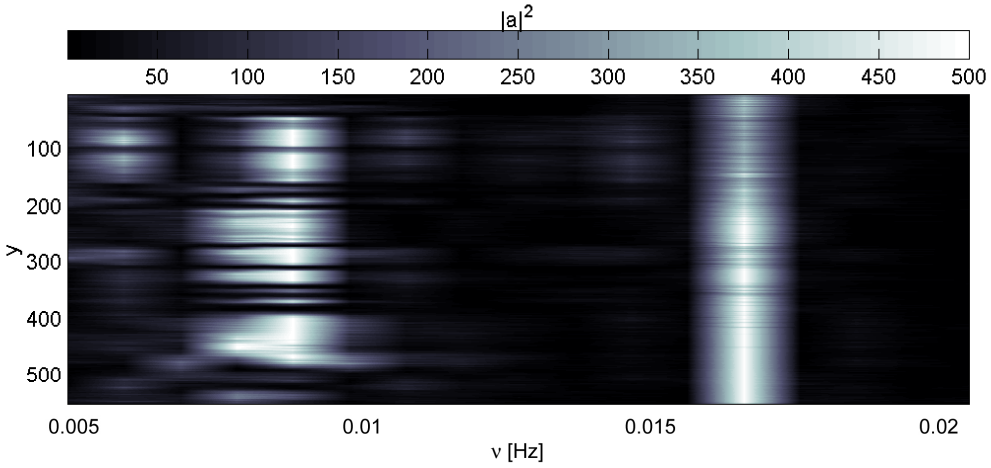

Figure 7.15: Power spectrum from the Fourier transform of the cross section, $\overline{\xi}(y,t)$, shown in Fig. 7.8. A spatially uniform peak is observed at the base frequency of the oscillation, $f_1 = 17 \pm 1$ mHz. The peak at $f_{1/2} = 9 \pm 1$ mHz, which corresponds to half the base frequency, is spatially non-uniform.

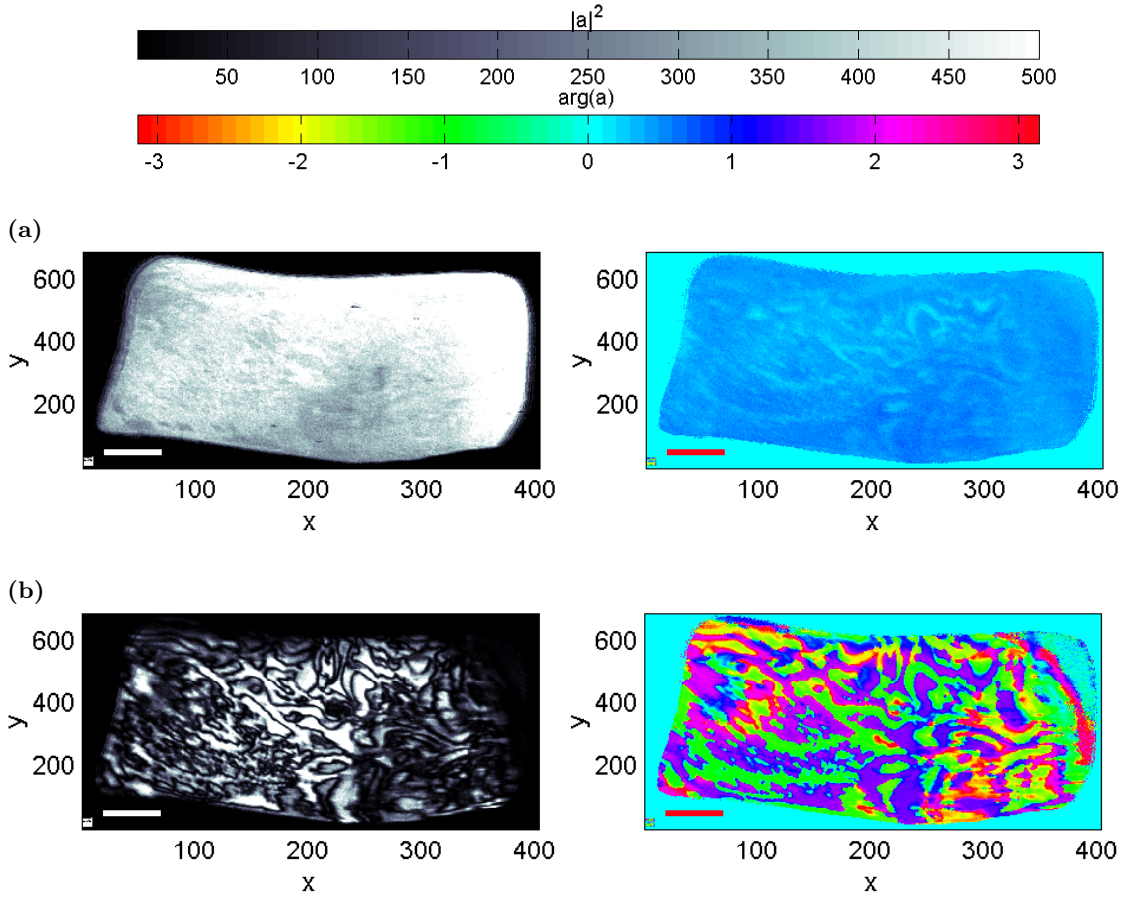

Figure 7.16: Spatial distribution of the amplitude and phase of the Fourier transformation for the two main modes. **(a)** Base mode. **(b)** Mode at half the base frequency. Experimental conditions in Fig. 7.8.

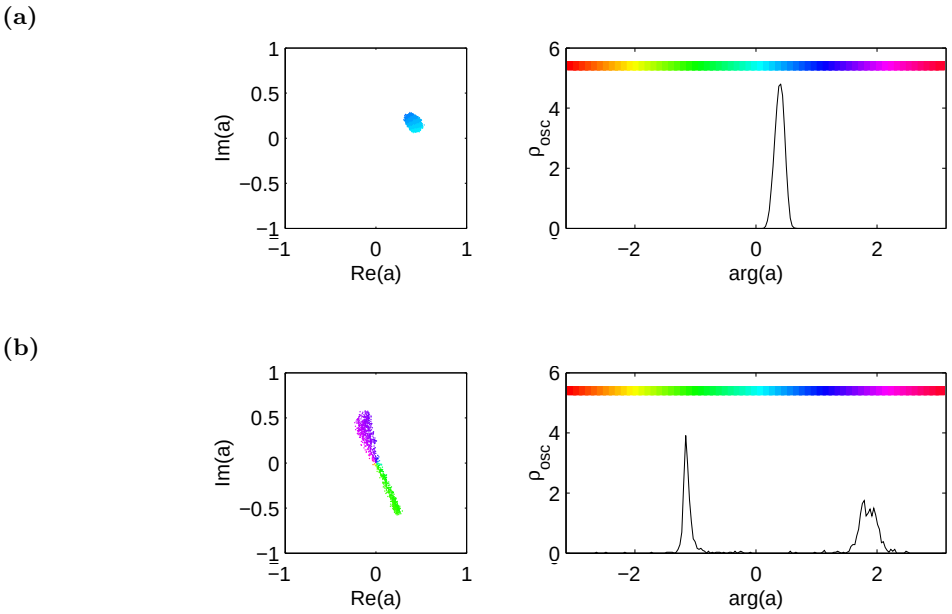

Figure 7.17: Complex Fourier coefficient in phase space with a normalization factor 1500, and phase histogram, *i.e.* histograms of the relative frequency density, ρ_{osc}, of the data in Fig. 7.16. **(a)** Base mode, evaluated in the region of interest: $x = 100 - 200$ and $y = 200 - 400$. **(b)** Mode at half the base frequency in the region of interest: $x = 110 - 130$ and $y = 270 - 320$.

the complex plane and in a phase histogram. In the phase histogram, the relative frequency density, ρ_{osc}, is plotted versus $\arg(a)$. The former is calculated from the ratio between the number of oscillators in a certain bin, N_{bin}, and the total number of oscillators, N_{tot}:

$$\rho_{\mathrm{osc}} = \frac{N_{\mathrm{bin}}}{N_{\mathrm{tot}} \Delta \arg(a)} \tag{7.4}$$

$\Delta \arg(a)$ being the width of the bin. The behavior of the base mode is related to the locking of the amplitude extrema of all local oscillators to the amplitude extrema of $\overline{\xi}$.

The spatial distribution of amplitude and phase of the subharmonic Fourier mode at half the base frequency is shown in Fig. 7.16b. Two domains having the same amplitude, but phase values differing by π, are entangled in a labyrinthine pattern. The complex plane and the phase histogram in Fig. 7.17b show that the local oscillators settle to one of two phase values. These 2-phase clusters are phase-balanced, *i.e.* there is the same number of oscillators in each phase. At the boundary between the domains, the amplitude drops down to zero as the phase switches. This indicates domains separated by Ising walls.

Ising walls are well known in the context of magnetic domains in ferro-magnets, where they form the boundary layer between domains of opposite magnetization neighboring domains having parallel spins of opposite direction. In the case of the spatially extended oscillatory system described in this thesis, neighboring domains are phase synchronized with regard to their main mode and show a phase shift of π in a subharmonic mode. An Ising wall is characterized by a sudden change in the phase (Fig. 7.18a). The amplitude drops to zero at the phase discontinuity. Ising walls are immobile. This is reflected in typical features of the phase space (Fig. 7.18b). In phase space, the oscillatory domains are positioned symmetrically with respect to the origin. They are connected by a line intersecting the origin, representing the domain wall with Ising character.

When maintaining a cluster pattern separated by Ising walls for several oscillation periods in an experiment, the labyrinthine pattern is imprinted into the electrode surface. This results

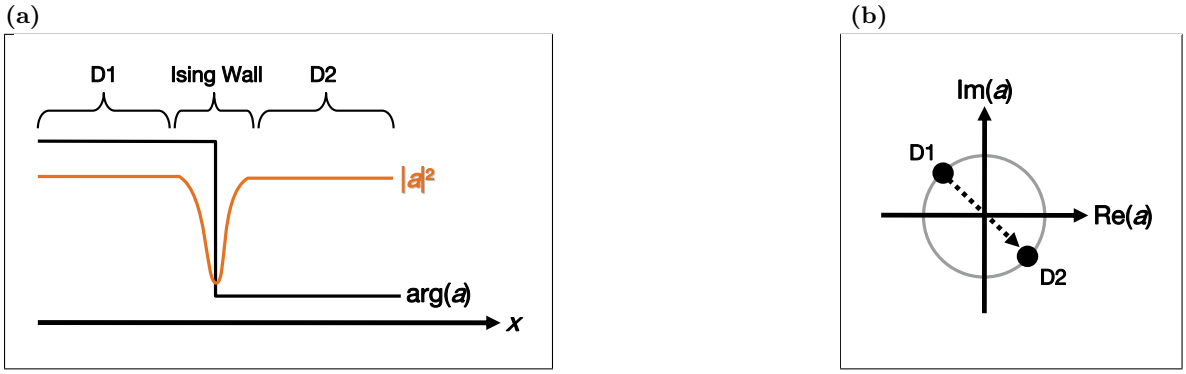

Figure 7.18: Clusters separated by Ising walls. **(a)** Variations of the modulus of the amplitude, $|a|^2$, and the phase, $\arg(a)$, along one spatial dimension. **(b)** Phase space plot of the complex Fourier coefficient.

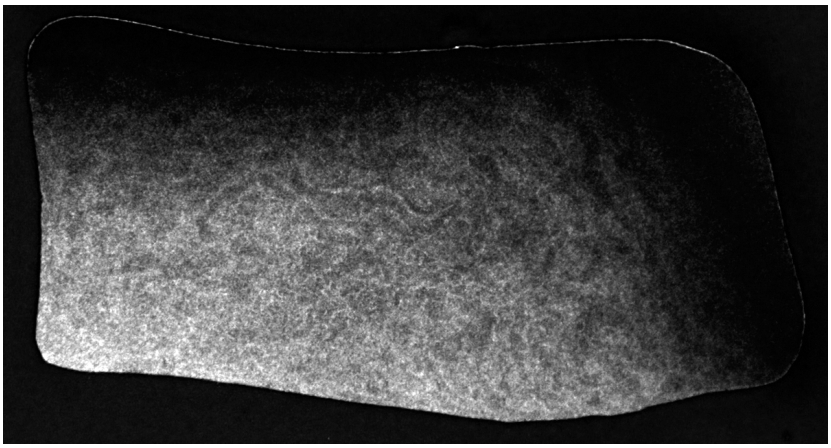

Figure 7.19: Microscope image of an n-type silicon electrode after 90 minutes of observing Ising walls. Experimental conditions: in Fig. 7.8.

from the immobility of the Ising walls and the decreased activity in the area of the walls. In the areas far from domain walls, a high oxide formation rate and a high etch rate can be observed. In Fig. 7.19, a microscope image of the electrode after keeping the electrode for some time at parameter values where immobile-cluster patterns are stable during current density oscillations, stepping back to open-circuit potential and removing the electrode from the solution after the oxide layer is etched. The electrode is covered with thin layer of native oxide that does not obscure the silicon structures. The image shows the remnants of the labyrinthine pattern.

Cluster Formation and the Modified Complex Ginzburg-Landau Equation

A cluster pattern resulting from the superposition of a spatially uniform main mode and a spatially clustered subharmonic mode was observed in simulations and experiments which include external forcing or feedback. Bertram and Mikhailov (2003) observed uniform oscillations, regular clusters with a subharmonic mode, and the coexistence of period-1 and period-2 dynamics in one-dimensional simulations of the oxidation of carbon monoxide on platinum under global delayed feedback. During periodic forcing of the oxidation of carbon

monoxide on platinum in two dimensions, the formation of a regular subharmonic intertwined labyrinthine cluster pattern was observed (Bertram, 2002; Bertram *et al.*, 2003). Irregular and regular clusters induced by subharmonic modes at one third and one quarter of the base frequency were observed in the photosensitive Belousov-Zhabotinsky reaction-diffusion system by applying a global photochemical feedback in simulations (Yang *et al.*, 2000) and experiments (Vanag *et al.*, 2000).

In contrast, Varela *et al.* (2005) described clusters in the electrooxidation of hydrogen on a quasi 1D platinum ring electrode in the absence of external feedback or external parametric forcing. Neither subharmonic phase clustering was discussed there, nor was a frequency demodulation applied, but the time evolution of the system show similar features to the ones discussed in this section. As in the case of the electrodissolution of silicon, the forcing or feedback is internal to the system.

In the case of the anodic oxidation of n-type silicon, no external feedback or forcing is applied. However, the concentration of holes at the silicon surface is oscillating in time. If it is assumed that this electrical quantity is always uniformly distributed, it can act as a harmonic forcing that is intrinsic to the system. The illumination strength limits the number of available holes, and thus poses a constraint on the maximum current.

Furthermore, it is known that a resistor in series to the working electrode introduces a global coupling (Krischer, 2003). In Sec. 5.1, the influence of R_{ser} on the temporal dynamics of the system is illustrated. The experiments discussed here reveal that R_{ser} has a considerable influence on the pattern formation on n-type silicon.

In cooperation with V. García-Morales (Krischer group), these aspects were integrated into the complex Ginzburg-Landau equation (CGLE) and numerically simulated. The CGLE is modified (MCGLE) in such a way that both types of global influence on the dynamics are captured. The CGLE is an amplitude equation valid for diffusively coupled oscillators near the Hopf bifurcation. The dynamics of the system are described in terms of the modulus of the amplitude and the phase in the frame work of normal form theory (Kuramoto, 1984). The observation of a Hopf bifurcation (Sec. 5.1) justifies the use of this approach. Even though the experimental system has anharmonic contributions and operates at some distance to the Hopf bifurcation point, the MCGLE can give valuable predictions that are qualitatively correct.

The modification incorporates the intrinsic self-forcing and the global coupling due to the external resistor into the normal form equation:

$$\partial_t W = W + (1 + ic_1)\partial_x^2 W - (1 + ic_2)|W|^2 W + B \tag{7.5}$$

with B constituting the modification term:

$$B = \gamma - (1 + i\omega_0)\langle W\rangle + (1 + ic_2)\langle |W|^2 W\rangle \tag{7.6}$$

W being a complex amplitude and $\langle ...\rangle$ denoting spatial averages. The real part of W, W_{r}, can be compared to the dynamics of the interfacial oxide thickness. $\langle W\rangle$ is a periodically oscillating function similar to $\overline{\xi}$ observed in the experiments.

The first summand in Eq. (7.5) accounts for a linear exponential growth, which has a destabilizing effect on the dynamics; the second summand contains the diffusive local next neighbor coupling; the third summand provides a nonlinear saturation of the limit cycle, *i.e.* a stabilizing effect on the dynamics.

The modification term, B, consists of γ, that describes a $1:1$ forcing, and an expression of the global coupling, where ω_0 specifies the frequency of the uniform oscillation. The latter represents an expansion of the negative global coupling to the third order. The cubic term is

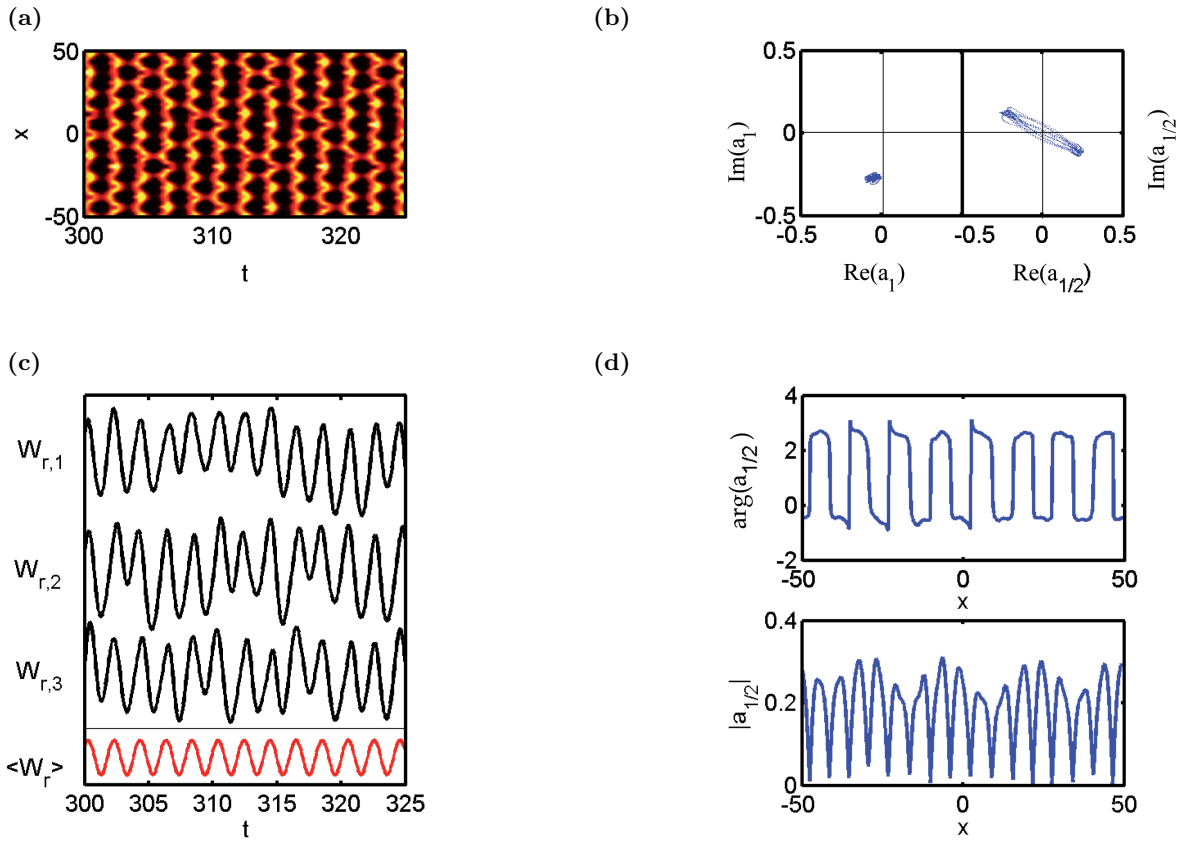

Figure 7.20: One dimensional simulations using the modified complex Ginzburg-Landau equation. **(a)** Spatio-temporal evolution of the real value of the complex amplitude, W_r, obtained from Eq. (7.5) for $c_1 = -10$, $c_2 = 1.5$, $\gamma = 1.55$ and $\omega_0 = 3.1$. **(b)** Representation of a in the complex plane, at base frequency, a_1 (left), and at half the base frequency, $a_{1/2}$ (right). **(c)** Local time series of W_r for three individual oscillators, $W_{r,1}$, $W_{r,2}$ and $W_{r,3}$, and the time series of the spatial average $\langle W_r \rangle$. **(e)** 1D distribution of the phase, $\arg(a_{1/2})$, and the amplitude, $|a_{1/2}|$, at the subharmonic mode at half the base frequency. [provided by V. García-Morales (Krischer group)]

motivated by analogous studies of phase ordering describing a global conservation law Conti *et al.* (2002). Neither the parametric force-like term nor the global-feedback-like ones in Eq. (7.6), correspond to an experimental time-dependent manipulation of the system, but rather arise intrinsically from its dynamics, *i.e.* these terms are self-induced in the system.

Simulations for this model are displayed in Fig. 7.20. The essential features of the experimental system in two dimensions are reflected in a cross section, such that a 1D model system can be considered for simplicity. x denotes the spatial direction.

The spatio-temporal evolution of W_r is depicted in Fig. 7.20a, which shows an irregular cluster pattern similar to the one in Fig. 7.8. Fig. 7.20c shows that any local oscillator has complicated modulations in the amplitude that render the spatial pattern irregular. Nonetheless, all extrema are locked to the ones of the average signal, $\langle W_r \rangle$, possessing the same base periodicity. In the simulation, the complexity of the spatial pattern results from the superposition of the subharmonic mode and the base mode. This kind of superposition is also observed in the local time series of the experimental data (Fig. 7.14).

Performing a Fourier analysis of the simulated time series for each oscillator, two main peaks are observed in the power spectrum, one for the base mode at the main frequency, f_1, and the other for the subharmonic mode at half the base frequency, $f_{1/2}$. In Fig. 7.20b, the phase

space plot for f_1 on the left hand side shows spatial homogeneity in amplitude and phase. The locking of all oscillators to the base frequency is also observed in the experiments (Fig. 7.17a). At $f_{1/2}$, a cluster pattern with Ising walls similar to the walls depicted in Figs. 7.16 and 7.17b is observed. Local oscillators in two different domains have a phase difference of π (Fig. 7.20d). At the walls separating the clusters from each other, the amplitude of the subharmonic mode drops to zero as the phase switches to the other value (Fig. 7.20d). The clustering is even more apparent in the phase space representation for $f_{1/2}$ on the right hand side of Fig. 7.20d. Phase balance is observed, with the same amount of oscillators in either phase (Fig. 7.20b). Phase balance in the subharmonic mode at half the base frequency results in the absence of a period-2 modulation of the averaged signals. The simulations reveal that the nonlinear global coupling is responsible for all oscillators being locked at their extrema, while the 1:1 resonance, γ, which is intrinsic to the silicon oxidation dynamics, contributes to the observed subharmonic 2-phase clustering.

7.3 Moving Clusters and Coexistence of Oscillations with Different Frequencies

Fig. 7.9 at the beginning of this chapter shows the evolution of a cluster pattern consisting of moving cluster domains with period-3 dynamics in the upper part of the electrode in coexistence with period-1 oscillations in the lower part of the electrode. The first panel of Fig. 7.21 depicts a respective local time series of ξ with period-1 oscillations. All local time series are phase locked to $\overline{\xi}$ at the maxima. Period-1 oscillations are similar in appearance to $\overline{\xi}$ displayed in the bottom panel. Period-3 oscillations can be distinguished by modulation of the amplitude. The period of this modulation amounts to three times the period of $\overline{\xi}$, *i.e.* the base period. The local times series in the second and third plate exhibit such a period-3 pattern. The phase shift between them corresponds to one period of the oscillations of $\overline{\xi}$. The oscillations in the fourth panel show period-3 oscillations during the last 600 seconds. The fifth plate displays a time series at another position on the electrode that exhibits more complicated dynamics, *e.g.* between $t = 0\,\mathrm{s}$ and $t = 1150\,\mathrm{s}$, a period-6 pattern is discernible.

From the series of snapshots in Fig. 7.9, two of the period-3 domains, both at the top of the electrode, can be easily distinguished. The domain on the right has its high maxima always one base period before the domain on the left. As for the labyrinthine pattern, a frequency demodulation technique is used to elucidate the characteristics of this mobile domain pattern. The use of the fast Fourier transform of the local time series is problematic in the case of moving domains, as the local dynamics close to the domain walls will be in different domains during different periods of time. As the domain walls move slowly, the Fourier transform may still be used to analyze short parts of the time series.

The local power spectra depicted in Fig. 7.22 for the data of the cross section shown in Fig. 7.9 displays three prominent peaks. The peak at the base frequency of the oscillation ($f_1 = 17.1 \pm 0.6\,\mathrm{mHz}$) stretches across the entire cross section, analogous to the base mode in the case of the Ising clusters. The subharmonic peaks at one half ($f_{1/2} = 8.5 \pm 0.6\,\mathrm{mHz}$) and at one third ($f_{1/3} = 5.5 \pm 0.6\,\mathrm{mHz}$) of the base frequency have a negligible amplitude in part of the cross section and exhibit a nearly spatially uniform distribution in the other part of the cross section.

Fig. 7.23 shows amplitude and phase distributions of the Fourier coefficients of the base mode, the second subharmonic mode and the third subharmonic mode of the entire electrode. As anticipated from Fig. 7.22, the distribution of amplitude and phase of the mode at the base frequency is uniform (Fig. 7.23a). A significant contribution of the second subharmonic mode

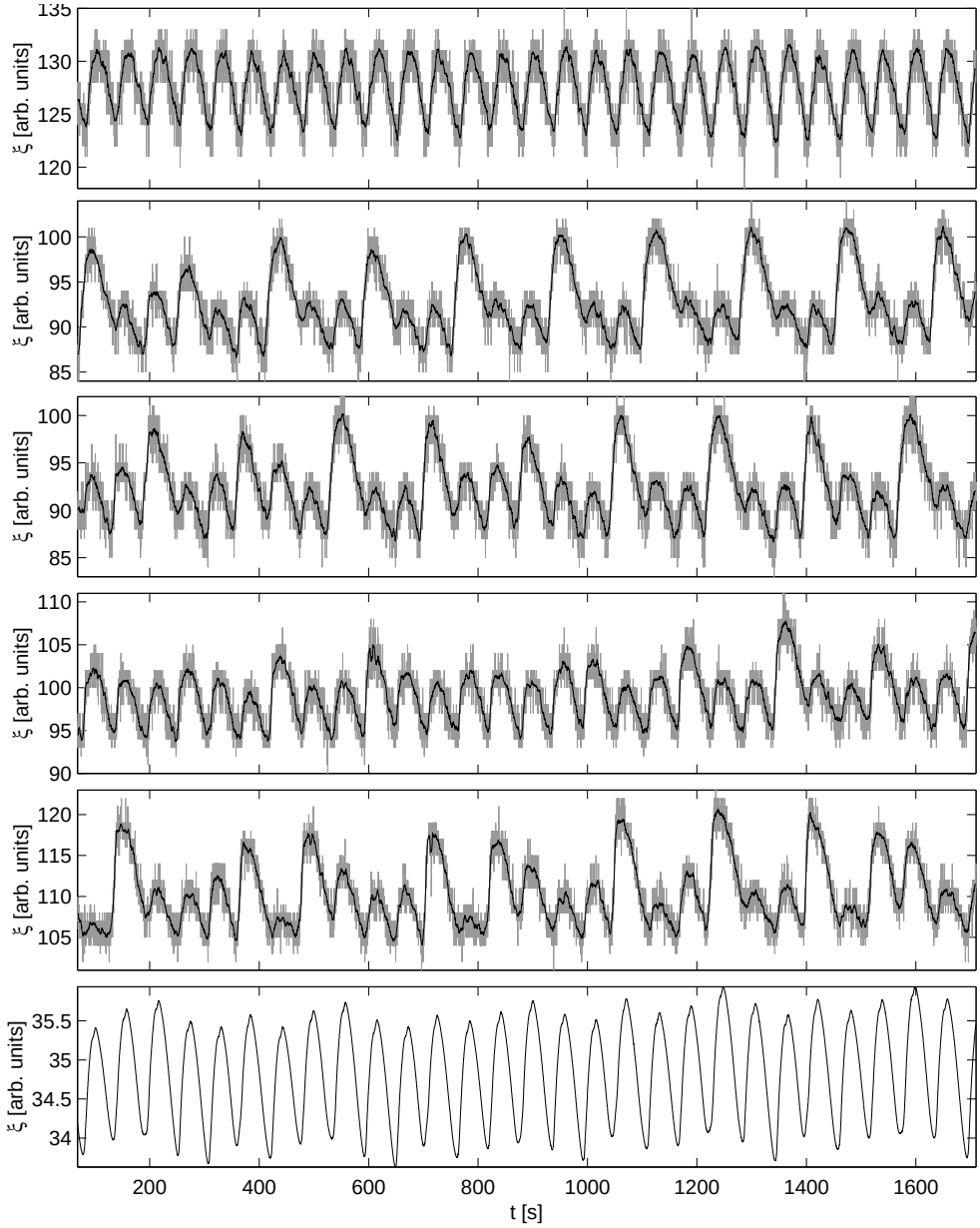

Figure 7.21: Local time series in different domains in the moving cluster pattern illustrating the coexistence of dynamics of different periodicity at different places on the electrode $[x, y]$: period-1 at $[100, 200]$, period-3 at $[120, 560]$, $[190, 550]$ and $[45, 340]$, and period-6 at $[190, 430]$. The last panel shows the times series of the space averaged ellipso-microscopy signal, $\overline{\xi}$. Experimental conditions: in Fig. 7.9.

(Fig. 7.23b) is restricted to a very small part of the electrode. In the case of the third subharmonic mode, a significant contribution is found in the upper half of the electrode (Fig. 7.23c). The distribution of the phase is only plotted for the regions where $|a|^2 > 1500$. Here, three large domains can be distinguished, one in the top left hand corner ($\arg(a) \approx 1.7$), one below and to the right hand ($\arg(a) \approx -0.4$), and another below ($\arg(a) \approx -2.5$). The phase changes by $2\pi/3$ when switching from one domain to another. The characteristics of the domain walls can be deduced from the complex Fourier coefficient in phase space and from the phase histogram (Fig. 7.24). As is the case with Ising clusters, the uniform distribution of amplitude and phase of the base mode manifests itself in a localized point cloud in the phase space representation (Fig. 7.24a). The cluster formation arises in a subharmonic mode.

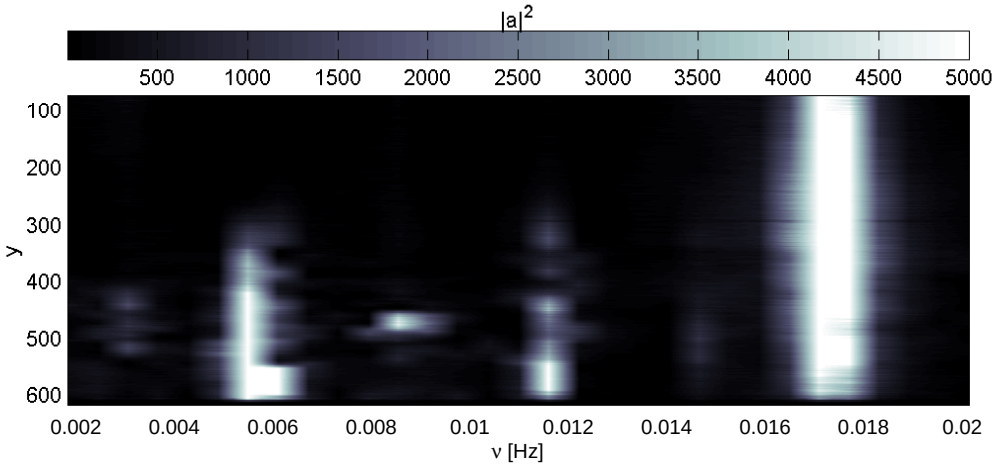

Figure 7.22: Power spectrum from the Fourier transform of the cross section, $\overline{\xi}(y,t)$, shown in Fig. 7.9. The three main peaks are observed at the base frequency of the oscillation, $f_1 = 17.1 \pm 0.6$ mHz, at half of the base frequency of the oscillation, $f_{1/2} = 8.5 \pm 0.6$ mHz, and at one third of the base frequency of the oscillation, $f_{1/3} = 5.5 \pm 0.6$ mHz, under the conditions described in Fig. 7.9. The peak at 11.6 ± 0.6 mHz is a higher harmonic of the one at one third of the base frequency.

In Fig. 7.24b the phase space representation and the histogramm are given for the third subharmonic mode. The histogram shows the clustering of the local oscillators at three different phases separated from each other by $2\pi/3$. In contrast to what is observed for Ising clusters, in the phase space representation in the left panel of Fig. 7.24b, the connection between the domains does not intersect the origin, but moves in a circle around the origin. This is a typical indicator for Bloch walls separating the domains.

A Bloch wall is, as an Ising wall, a boundary layer between two domains of different phase. However, in contrast to passing an Ising walls, when passing a Bloch wall the amplitude does not go through zero, but remains constant, and the phase changes continuously. Fig. 7.25 illustrates these characteristic features of Bloch walls. The phase space representation of the complex Fourier coefficient of the experimental data only show two domain connections in Fig. 7.24b, because the three domains are separated by only two domain walls, as can be seen in Fig. 7.23.

Another crucial difference between Ising and Bloch walls is the immobility of the former and the mobility of the latter. The motion of Bloch walls is surprising, because they separate symmetric states. Non-variational effects are responsible for chirality at the interface between the domains which induces the motion (Coullet *et al.*, 1990). Depending on the system parameters, the velocity of Bloch walls may be very small.

The behavior of the phase is a result of motion of the domain walls. In the case of moving domains, the Fourier transform of local domains can only give limited insight into the overall dynamics. This becomes obvious from the shape of the phase space plot and the phase histogram at the three characteristic frequencies discussed so far (Fig. 7.24).

The contribution to the dynamics of the mode at half the base frequency, $f_{1/2} = 0.0085$ Hz, is limited to a very small region on the electrode (Fig. 7.23b). Within this region the phase is uniformly distributed. The active region coincides with a region where the mode at one third of the base frequency is active as well. This superposition leads to period-6 oscillations, an example of which is displayed in the fifth plate of Fig. 7.21. The cross section in Fig. 7.9 suggests that this is the result of the movement of the domain walls.

Lin *et al.* (2000) investigated the features of domains separated by Bloch and Ising walls.

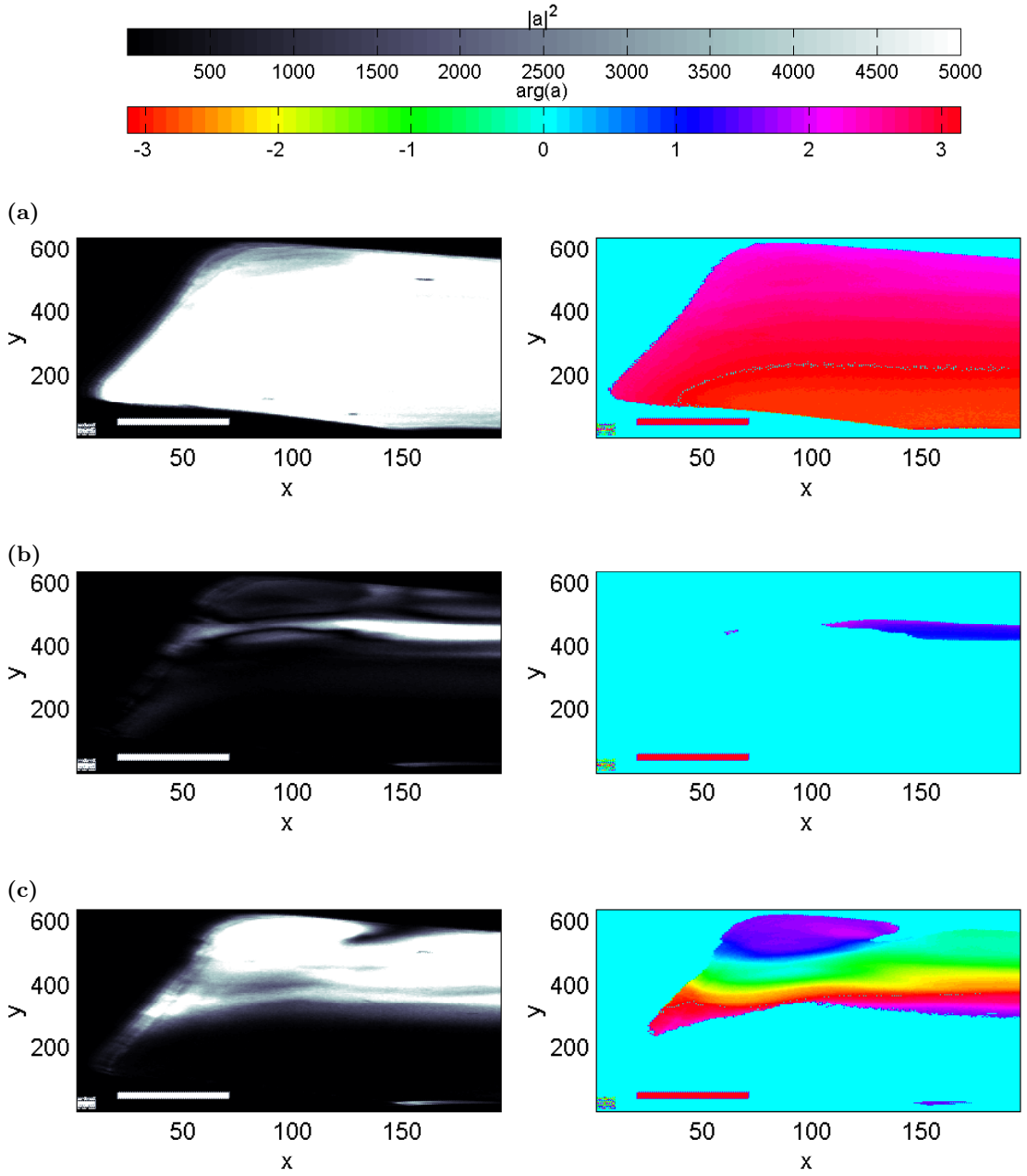

Figure 7.23: Spatial distribution of the amplitude and phase of the Fourier transformation for the three main modes. **(a)** Base mode. **(b)** Mode at half the base frequency. **(c)** Mode at one third of the base frequency. Experimental conditions: in Fig. 7.9.

In the case of the periodically forced Belousov-Zhabotinsky reaction, a labyrinthine pattern is connected to a 1:2 resonance with the forcing frequency. The forcing is twice as fast as the oscillation of the system, which locks to the forcing in two different phases. The patterning appears in the base mode of the system as the forcing is external. In the case of the electrodissolution of silicon, the subharmonic character of the pattern is a direct result of the intrinsic character of the forcing and the assignment of the self forcing to the base mode.

Reducing the light intensity of the parametric forcing changes the features of the standing wave pattern. Additionally, the character of the domain walls changes from Ising walls to Bloch walls. This qualitative change in the character of the walls is called non-equilibrium

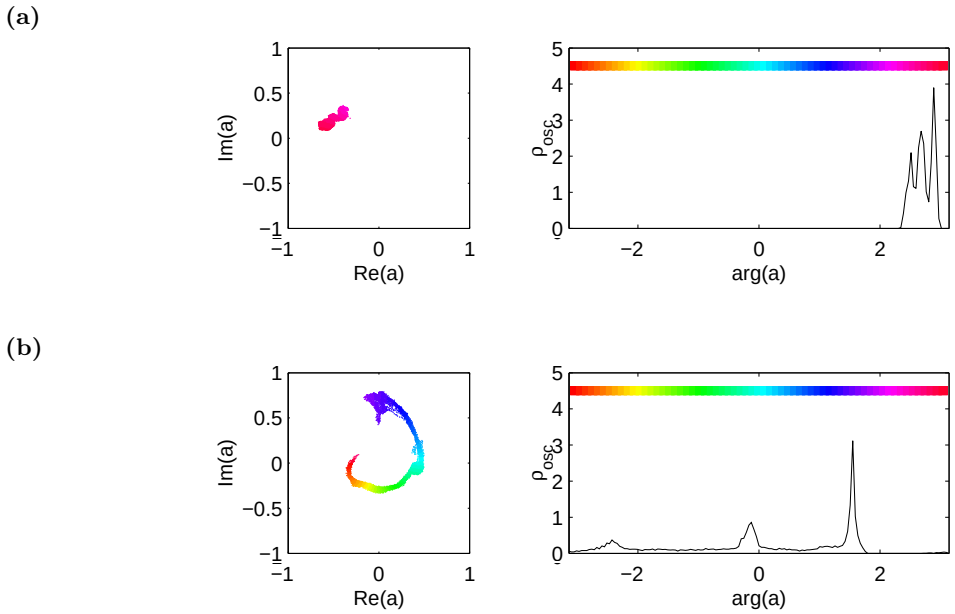

Figure 7.24: Complex Fourier coefficient in phase space with a phase space normalization factor 15000, and phase histogram, *i.e.* histograms of the relative frequency density, ρ_{osc}, of the data from Fig. 7.23. **(a)** Base mode, evaluated in the region of interest: $x = 70 - 150$ and $y = 300 - 500$. **(b)** Mode at one third of the base frequency in the region of interest: $x = 70 - 100$ and $y = 350 - 580$. Distribution of the Fourier transformation of the local oscillators in phase space for certain modes and the respective histograms of the relative frequency density, ρ_{osc}, under the conditions described in Fig. 7.9.

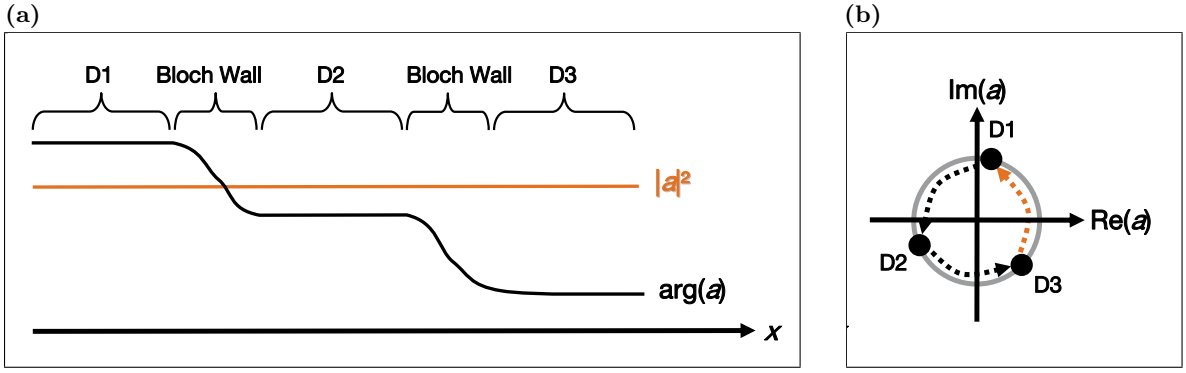

Figure 7.25: Clusters separated by Bloch walls. **(a)** Variations of the modulus of the amplitude, $|a|^2$, and the phase, $\arg(a)$, along one spatial dimension. **(b)** Phase space plot of the complex Fourier coefficient.

Ising-Bloch transition (NIB). It arises in oscillatory systems in 1:2 resonance with a parametric forcing (Esteban-Martin *et al.*, 2005). The name alludes to the equilibrium Ising-Bloch transition observed in the case of ferromagnets. In the NIB bifurcation, a immobile Ising front looses stability to two counterpropagating Bloch fronts as the forcing amplitude is decreased. This pitchfork bifurcation is illustrated in Fig. 7.26.

A NIB can be expected in the electrodissolution of silicon as well. The forcing amplitude in this system can be adjusted by experimentally changing the external resistance or by using different values of γ in the simulations of the MCGLE. The phase space diagrams of the subharmonic mode and the front velocities will prove the existence of such a bifurcation.

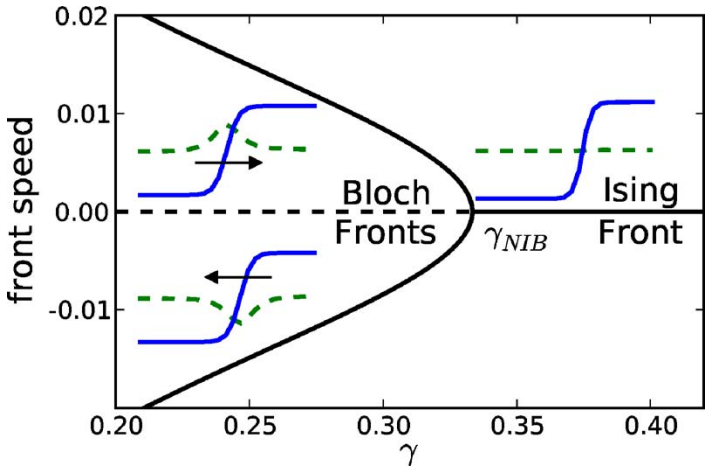

Figure 7.26: Illustration of the nonequilibrium Ising-Bloch (NIB) bifurcation, where a single stable Ising front becomes unstable at the bifurcation point, γ_{NIB}, and a pair of stable counterpropagating Bloch fronts emerges, whose front speeds increase as the forcing amplitude, γ, is decreased. The insets show the shape of the real part (blue curve) and the imaginary part (dashed green curve) of the complex valued amplitude [from (Marts *et al.*, 2006)].

7.4 Discussion and Outlook

Using imaging ellipsometry, it could be demonstrated that oscillations of the current density of the anodic oxidation of silicon may be accompanied by spatial pattern formation including stripes, concentric circles, clusters with subharmonic entrainment and spatio-temporal turbulence. The appearance of patterns strongly depends on the applied parameters. Most strikingly, sustained patterns are observed only on n-type silicon and never on p-type silicon. In fact, the existence of sustained spatial patterns is closely related to the limitation of the charge carriers generation by sample illumination, which seems to introduce interactions between different parts of the electrode that are essential for the emergence of the patterns.

If fluctuations or local heterogeneities locally introduce a higher reaction rate, holes are used up during the ensuing reaction. Making the plausible assumption that the characteristic time of lateral diffusion of the holes in the silicon is fast compared to the characteristic reaction time, the hole concentration remains spatially uniform at all times, because differences in the hole concentration are readily equalized. In this way the hole-concentration dynamics constitute a global coupling.

Cluster patterns characteristically develop in the presence of a global coupling. This is in accordance with the above interpretation. However, several questions still remain. Firstly, another global coupling is introduced by the resistor in series with the working electrode, both, on n-type silicon and p-type silicon. In this case the coupling results from a global reduction of applied potentials, because the sum of increases in the local current results in an increase of the ohmic voltage drop affecting the entire electrode. Why does the influence of the illumination result in pattern formation, whereas the influence of the series resistance is not sufficient? Understanding this seems to be the key to understanding the different dynamics of p-type and n-type silicon.

The discussions in the literature on the mechanistic origin of sustained current density oscillations revolves around the spatial synchronization of local oscillators. The basis for, both, the self-oscillating domain model (Chazalviel and Ozanam, 1992) and the current burst model

(Carstensen *et al.*, 1999) are self-oscillating domain that are either synchronized leading to sustained oscillations, or desynchronized leading to damped oscillations.

This synchronisation approach can be invalidated, specifically because spatially patterned sustained oscillations according to many figures in Sec. 7.1, and uniformly damped oscillations are observed. An example of the latter is displayed in Fig. 7.4, which shows that the local time series of a cross section are concertedly damped similar to the averaged signal $\overline{\xi}$. On a mesoscopic level, no splitting up into out of phase domains is observed.

Chapter 8

Summary

Electrochemical reactions usually proceed far from the thermodynamic equilibrium and have nonlinear reaction kinetics. These features constitute the basis for self-organized spatial and temporal phenomena, which are abundant in electrochemical systems. Hence, the elucidation of the nonlinear dynamics of these systems is essential for the understanding their behavior. This thesis focused on the electrified silicon|oxide|electrolyte interface and on two fundamental questions of its dynamics: (i) The physical origin of the oscillatory instability was studied combining tools of semiconductor electrochemistry and nonlinear dynamics. (ii) Synchronization between local sites on the spatially extended electrode was investigated. Closely related to this is the question whether the temporal oscillations are accompanied by spatial pattern formation.

An ellipso-microscopic imaging setup was built to study the spatio-temporal dynamics of the anodic electrodissolution of silicon. The first spatially and temporally resolved *in situ* measurements of the oxide layer thickness were presented here, demonstrating that the temporal oscillations can be indeed accompanied by spatial pattern formation. A theoretical and an experimental analysis of the ellipso-microscopic signal revealed that the measured light intensity relates linearly to the oxide layer thickness in the region of interest. This allowed for the correlation between oxide layer thickness and coulometrically determined current density. Concurrent measurements of these two quantities were carried out with n- and p-type silicon. Despite many similarities, the two types of electrodes also showed different behavior that was explored in detail.

The investigation of the parameter dependencies for p-type silicon was more straightforward than for n-type silicon, because illumination is not necessary for its anodic oxidation. Stable oscillations required a minimum voltage and series resistance and emerged in a Hopf bifurcation. This led to a new interpretation of the oscillatory instability from a dynamical point of view. In addition to these low-amplitude oscillations, which have a sinusoidal characteristic, relaxational high-amplitude oscillations were observed. At high ammonium fluoride concentrations, not only simple periodic, but also complex dynamics, such as quasi-periodicity or chaos were observed.

An increase of the applied voltage led to an increase of the oxide layer thickness and the voltage drop across the interface, while the ratio of the two remained constant or oscillated around a constant average value. Assuming a linear potential drop across the oxide layer, the electrical field is constant. This fact was also reflected in the constant or the constant average current density suggesting that the current density is limited by migration through the oxide layer. These results constitute one building block for the physical mechanism of the oscillations. A second building block was obtained from measurements of the etch rate under

various conditions. The difference between the etch rate at open-circuit potential and the one at applied anodic voltages indicated its dependency on the electrical field in the oxide layer.

Based on the above mentioned experimental results and literature data, a mathematical model was derived. It consists of four ordinary differential equations. The variables of the model are the potential drops across the oxide layer and across the space charge layer in the semiconductor, the conductivity and the oxide layer thickness. The latter two represent the activator and the inhibitor variable, respectively. Crucial for the existence of the oscillatory instability was is the dependency of the conductivity in the oxide layer on the electrical field. This ansatz is supported by literature data. Furthermore, the field dependency of the etch rate had to be accounted for. For lack of functional relationship between electrical field and etch rate in the literature, it was assumed to be a linear function of the conductivity.

The numerical simulation of the model reproduced sustained oscillations, foci and nodes in parameter regions comparable to the ones of the experiments and could even quantitatively capture the experimental values of the current density, the oxide layer thickness and the etch rate, while the phase relation between oxide layer thickness and current density of the numerical simulations does not match the experimentally measured one.

The analysis of the model system revealed the nature of the positive and negative feedback that are responsible for the oscillatory instability. The conductivity is the activator variable introducing a positive feedback loop that involves also the electrical quantities current density and potential drop across the oxide layer. The oxide layer thickness constitutes the inhibitory variable in this mechanism. The potential drop across the space charge layer does not change significantly, and the one across the oxide layer adjusts nearly instantaneously to changes in the current density. These two variables do not constitute true degrees of freedom. Therefore, the model system is quasi two-dimensional. One more degree of freedom is necessary to describe complex dynamics, such as quasi-periodicity and chaos, therefore these dynamical features are not captured by this model.

The electrodissolution of n-type silicon requires sample illumination and exhibited considerably different dynamical behavior. Sustained current density oscillations are observed also at zero series resistance at intermediate illumination intensities. This novel type of relaxational oscillations is characterized by clear current plateau arising from the illumination limitation superimposed by a fine structure with current density spikes, stemming from electron injection. It could be shown that this type of oscillation is connected to a bistability. Depending on the initial conditions, the system settles down to a steady state (‘wet’ oxide) or on a limit cycle (‘dry’ oxide). To capture this new type of oscillations the model has to be expanded taking into account the illumination intensity limiting the hole concentration at the surface of the semiconductor.

Spatially resolved experiments showed that this new type of relaxational oscillations on n-type silicon, and only this, is accompanied by sustained pattern formation. During the oscillations the oxide layer thickness forms unusual subharmonic cluster patterns. The base mode of the local oxide layer thickness oscillations being phase-locked to the current density oscillations is spatially uniform and superimposed with non-equilibrium Ising and Bloch clusters from the subharmonic modes. The former cluster show immobile labyrinthine patterns, and the latter cluster domains moving across the electrode.

The cluster patterns could be interpreted with the help of a modified complex Ginzburg-Landau equation. The combination of a 1:1 entrainment and a global coupling led to the reproduction of the Ising domains numerically simulated in one spatial dimension. It is feasible to assume that the entrainment results from the illumination and the global coupling from the series resistance. A mathematical model based on these physical ideas has yet to

be set up to verify this approach and provide a bridge between the experiments and the normal-form interpretation of the origin of this novel type of pattern.

In summary, this thesis combines the perspective of semiconductor electrochemistry with the one of nonlinear dynamics, thereby shedding new light on the mechanism and the dynamics of the electrodissolution of silicon.

Appendix A

Overview of Experiments

In the following two tables give an overview of the figures in this thesis. Tab. A.1 contains all samples used and Tab. A.2 recapitulates the experimental conditions presented in a figure. The experiment code in the last column indicates the sample in its first five digits (first column of Tab. A.1). In the third table (Tab. A.3), the figures are arranged according to the observed spatial phenomenon.

Preliminary experiments, not presented in this thesis, were essential for the setup and success of the presented experiments. Part of these experiments were conducted with M. Frigieri within the framework of his Master's thesis (Frigieri, 2007).

Part of the presented experiments on n-Si, were conducted in cooperation with A. Heinrich within the framework of his Bachelor's thesis (Heinrich, 2009).

Table A.1: Sample parameters and experimental conditions.

Sample	c_{NH_4F} [mol/l]	pH	A [mm^2]	Material	Back Contact	Fig.
ah002	0.05	2.3	5.27	n-Si(111)	Al	
ah003	0.05	2.3	8.11	n-Si(111)	Al	
ah005	0.05	2.3	4.31	n-Si(111)	Al	
ah006	0.05	2.3	5.66	n-Si(111)	Al	
im035	0.05	2.4	4.91	p-Si(111)	Au	5.2
im036	0.20	3.5	4.66	p-Si(111)	Au	5.14
im037	0.10	3.1	9.71	n-Si(111)	Al	
im039	0.05	2.3	9.64	n-Si(111)	Al	
im040	0.05	2.3	9.05	n-Si(111)	Al	7.19
im041	0.05	2.3	8.91	n-Si(111)	Al	
im042	0.05	2.3	7.65	p-Si(111)	Au	5.2
im045	0.05	2.3	4.26	p-Si(111)	Au	5.2, 5.3

Table A.2: Experiment parameters. In the fourth column the annotations indicate whether the solution was stirred (S), the experiment started with a potential step starting at open-circuit potential (O), or the applied voltage was scanned (V).

U [V]	R [kΩ]	L $\left[\frac{\mathrm{mW}}{\mathrm{cm}^2}\right]$	Annot.	Fig.	Experiment
p-Si					
0.63	0	0.00	V	3.8b	im035a00
1.35	0	0.00	O	5.1a	im042z03
2.35	0	0.00	O	5.1b	im042z02
3.30	100	0.00		5.4, 5.5, 5.6	im045h03d
3.50	1	0.00		5.5, 5.6, 5.7	im045h05c
3.50	5	0.00		5.7	im045h05b
3.50	15	0.00		3.8c, 5.7	im045h04d
3.50	30	0.00		3.8c, 5.7	im045h04c
3.50	50	0.00		3.8c, 5.7	im045h04b
3.50	100	0.00		5.4	im045h03c
3.50	100	0.00		3.8c, 5.7	im045h04a
4.00	100	0.00		4.5, 4.6, 4.9a, 4.11, 5.4, 5.5, 5.6	im045h03b
4.50	100	0.00		5.4	im045h02c
4.50	100	0.00		5.4	im045h03a
5.00	100	0.00		5.4	im045h02b
5.35	100	0.00	O	4.2a, 4.2d, 5.12a, 5.13a, 7.3	im042s00
6.00	100	0.00		5.4	im045h02a
6.50	100	0.00		5.4	im045h01b
7.00	200	0.00	O	4.2b, 4.2e, 4.8, 4.9b, 4.10	im045h00a
7.17	200	0.00	O	5.5, 5.6	im045c00
7.35	100	0.00	O	4.3, 4.7a, 5.11a, 5.12b, 5.13b	im042p00
8.50	200	0.00	O	4.2c, 4.2f, 4.7b, 5.5, 5.6, 5.12c, 5.13c	im045d00
8.60	100	0.00	V	2.5, 4.1	im035g00
8.65	0	0.00	O	5.5a	im035d01
8.65	10	0.00	O	5.5a	im035d02
8.65	100	0.00		5.8b, 5.9b	im036d01
9.65	100	0.00	O	5.8a, 5.9a, 7.2	im035d03
10.65	40	0.00		5.11d, 5.12f, 5.13f, 7.5	im036d06b
12.49	10	0.00		5.10, 5.11c, 5.12e, 5.13e	im036e00d
n-Si					
8.00	0	0.13		6.5	ah002b00b
8.00	0	0.19		6.5	ah002b00h
8.00	0	0.23	O	6.1a, 6.8, 6.9	ah003c00
8.00	0	0.25		6.4e, 6.4f, 6.5, 6.10e, 6.12a, 6.12b, 7.7	ah002d00c
8.00	0	0.25		6.7, 6.8, 6.9	ah006e00c
8.00	0	0.26		6.8, 6.9	ah006e01d

U [V]	R [kΩ]	L $\left[\frac{\text{mW}}{\text{cm}^2}\right]$	Annot.	Fig.	Experiment
8.00	0	0.27		6.5	ah002b00c
8.00	0	0.28		6.8, 6.9	ah006e01c
8.00	0	0.30		6.4d, 6.4f, 6.5, 6.10d, 6.12a, 6.12b	ah002b00g
8.00	0	0.31		6.8, 6.9	ah006e01b
8.00	0	0.37	O	6.1b, 6.2, 6.8, 6.9	ah003d00
8.00	0	0.39		6.8, 6.9	ah006e00b
8.00	0	0.41		6.4c, 6.4f, 6.5, 6.10c, 6.12a, 6.12b	ah002b00f
8.00	0	0.42		6.5	ah002b00d
8.00	0	0.46	O, S	6.3	im041e00a
8.00	0	0.49	O	6.8, 6.9	ah005b00
8.00	0	0.49	O	6.8, 6.9	ah003b00
8.00	0	0.51	S	6.3	im041e00b
8.00	0	0.52		6.4b, 6.4f, 6.5, 6.10b, 6.12a, 6.12b	ah002d00b
8.00	0	0.52	O	6.8, 6.9, 7.1	ah003f00
8.00	0	0.54	O	6.8, 6.9	ah006e00a
8.00	0	0.55		6.8, 6.9	ah006e01a
8.00	0	0.56	O	6.8, 6.9	ah005a00
8.00	0	0.64	O	6.8, 6.9	ah006b00
8.00	0	0.65		6.4a, 6.4f, 6.5, 6.10a, 6.12a, 6.12b	ah002b00e
8.00	0	0.67	O	6.8, 6.9	ah003g00
8.00	0	0.75	S	6.3	im041e00c
8.00	0	0.81	O	6.1c, 6.8, 6.9	ah003h00
8.00	0	0.81	O, S	6.8, 6.9, 6.15	ah003k00
8.00	0	0.84	S	6.3	im041e00d
8.00	0	1.16	O, S	2.5	im041h00
8.00	0	1.21	O, S	7.11	im041c00
8.00	0	1.30	O, S	3.8a	im041a00
8.00	0	1.62		7.12, 7.13	im037d01
8.00	1	0.40		7.9, 7.21, 7.22, 7.23, 7.24	im039f01
8.00	1	0.40		6.13, 6.14a, 6.14c	im039f02a
8.00	1	0.40	S	6.13, 6.14b, 6.14c, 7.10	im039f02b
8.00	1	0.40		6.13	im039f02c
8.00	100	0.64	O	6.1d, 6.12b, 7.6	ah002f00
9.00	30	0.25		6.6	ah005e01b
9.00	30	0.56	O	6.12b	ah005e00a
9.00	100	0.87		6.12b	ah005e01d
10.00	1	0.36	O	6.12b	im039e00
11.00	30	1.19	S	7.8, 7.14, 7.15, 7.16, 7.17	im040c02

Table A.3: Overview of spatial pattern formation during different temporal dynamics.

Temporal Pattern	Parameters	Spatial Pattern	Fig.
p-Si			
low-amp. osc.	high R_{ser}	uniform	7.3
chaotic low-amp. osc.	high $c_{\mathrm{NH_4F}}$	uniform	7.5
high-amp. osc.	low R_{ser}	uniform	
transient	changing U	stripes or uniform	7.2, 7.3
n-Si			
low-amp. osc.	high R_{ser}	uniform	7.6
high-amp. osc.	low R_{ser}	moving clusters	7.9, 7.10, 7.11
	intermediate R_{ser}	plateau pattern	7.11
	intermediate R_{ser}	immobile clusters	7.8
chaotic high-amp. osc.	high $c_{\mathrm{NH_4F}}$	turbulent	7.12
spike dom. osc.	low L	uniform	7.7
transient	changing U	clusters and concentric fronts	7.6, 7.1

Appendix B

Glossary

The glossary gives an overview of the acronyms (Tab. B.1), the physical constants (Tab. B.2), and the experimental parameters (Tab. B.3), and the symbols (Tab. B.4) used in this thesis.

Table B.1: Overview of acronyms used in this thesis.

Acronym	Explanation
AFM	Atomic force microscopy
CCD	Charge coupled device
CE	Counter electrode
CGLE	Complex Ginzburg Landau equation
e^-	Electron
GUI	Graphic user interface
h^+	Hole
LED	Light-emitting diode
MCGLE	Modified complex Ginzburg Landau equation
NIB	Nonequilibrium Ising Bloch bifurcation
OCP	Open circuit potential
RE	Reference electrode
TEM	Transmission electron microscopy
WE	Working electrode
γ	Photon

Table B.2: Overview of the physical constants used in this thesis.

Constant	Explanation
$c = 2.99792 \cdot 10^8$ m/s	Speed of light
$e_0 = 1.60218 \cdot 10^{-19}$ C	Elementary charge
$F = 9.64853 \cdot 10^4$ As/mol	Faraday constant
$h = 6.62607 \cdot 10^{-34}$ Js	Planck constant
$k = 1.38066 \cdot 10^{-23}$ J/K	Boltzmann constant
$K = 8.0461$	Constant for Lorentz-Lorens equation (Hung *et al.*, 1991)
$K_1 = 1.3 \cdot 10^{-3}$ mol/l	Equilibrium constants for ammonium fluoride
$K_2 = 1.4 \cdot 10^{-1}$ mol/l	dissolution
$M = 60.2$ g/mol	Molar mass of silicon oxide
$N_\mathrm{A} = 6.02204 \cdot 10^{23}$ 1/mol	Avogadro constant
$R = 8.31451$ J/Kmol	Universal gas constant
$\epsilon_0 = 8.85418 \cdot 10^{-14}$ F/cm	Vaccum permittivity

Table B.3: Overview of system parameters used in this thesis.

Parameter	Explanation
$c_1 = -10$	Constant in the MCGLE
$c_2 = 1.5$	Constant in the MCGLE
$R_\mathrm{cont} = 15.5\,\Omega$	Resistance of the silicon back contact
$\hat{n}_{\mathrm{H_2O}} = 1.342$	Refractive index of the electrolyte (Lewerenz *et al.*, 1989)
$\hat{n}_\mathrm{Si} = 3.85 + 0.02i$	Refractive index of silicon oxide (Lewerenz *et al.*, 1989)
$\hat{n}_{\mathrm{SiO_2}} = 1.34$	Refractive index of silicon (Lewerenz *et al.*, 1989)
$\alpha_\mathrm{A} = 20\,^\circ$	Angle between the transmission axis of the analyzer and the plane of incidence
$\alpha_\mathrm{C} = 45\,^\circ$	Angle between the fast axis of the quarter plate and the plane of incidence
$\alpha_\mathrm{i} = 70\,^\circ$	Angle of incidence
$\alpha_\mathrm{P} = 175\,^\circ$	Angle between the transmission axis of the polarizer and the plane of incidence
$\gamma = 1.55$	Global forcing term in the MCGLE
$\lambda_\mathrm{illu} = 630$ nm	Typical wavelength of the light used for sample illumination
$\lambda_\mathrm{imag} = 470$ nm	Typical wavelength of the light used for sample imaging
$\omega_0 = 3.1$ Hz	Frequency of the uniform oscillations in the MCGLE
$\rho = 1.69$ g/cm^3	Density of silicon oxide obtained from Eq. (4.15)

Table B.4: Overview of symbols used in this thesis.

Symbol	Unit	Explanation
A	$[\mathrm{m}^2]$	Area
$\lvert a\rvert^2$		Amplitude in the Fourier analysis
$\arg(a)$		Phase in the Fourier analysis
$\Delta \arg(a)$		Width of a phase bin
B		Modification term in the MCGLE
C_{cont}	$[\mathrm{F/cm}^2]$	Capacity of the silicon back contact
C_{hh}	$[\mathrm{F/cm}^2]$	Capacity of the Helmholtz layer
C_{ox}	$[\mathrm{F/cm}^2]$	Capacity of the oxide layer
C_{sc}	$[\mathrm{F/cm}^2]$	Capacity of the space charge layer
C_{ss}	$[\mathrm{F/cm}^2]$	Capacity of the surface states
c	[m/s]	Speed of light
c_1		Constant in the MCGLE
c_2		Constant in the MCGLE
c_{inc}		Etch rate increment of the linear fit
$c_{\mathrm{NH_4F}}$	[mol/l]	Bulk ammonium fluoride concentration
c_{opt}		Proportionality factor
D		Exponent of the Drude equation
E	[V/m]	Electrical field in the oxide layer
E_{F}	[J]	Fermi energy
ΔE_{F}	[J]	Difference between Fermi energies of silicon and electrolyte before contact
E_{illu}	[J]	Energy of the sample illumination
E_{P}	[V/m]	Electrical field after the polarizer
E_{vac}	[J]	Vaccum energy
$\hat{\mathbf{E}}$	[V/m]	Electrical field at the camera
e_0	[C]	Elementary charge
F	[As/mol]	Faraday constant
f_1	[Hz]	Frequency of the base mode
$f_{1/2}$	[Hz]	Frequency of the second subharmonic mode
$f_{1/3}$	[Hz]	Frequency of the third subharmonic mode
h	[Js]	Planck constant
I	[A]	Current
J	$[\mathrm{A/m}^2]$	Current density
J_{F}	$[\mathrm{A/m}^2]$	Faradaic reaction current density
J_{mig}	$[\mathrm{A/m}^2]$	Migration current density across the oxide layer
J_{plat}	$[\mathrm{A/m}^2]$	Current density of the plateau
J_{ss}	$[\mathrm{A/m}^2]$	Current density at the steady state
$J_{\overline{\xi}}$	$[\mathrm{A/m}^2]$	Current density calculated from $\overline{\xi}$
K		Constant for Lorentz-Lorens equation (Hung *et al.*, 1991)
K_1	[mol/l]	Equilibrium constants for ammonium fluoride
K_2	[mol/l]	dissolution
k_{sc}	$[1/\mathrm{m}^2\mathrm{s}]$	Rate constant of the oxidation reaction
k_κ	[1/s]	Rate constant of the adjustment of κ
k	[J/K]	Boltzmann constant
L	$[\mathrm{W/m}^2]$	Power density of the illumination light

continued

continued

Symbol	Unit	Explanation
M	[g/mol]	Molar mass of silicon oxide
N_{anod}		Number of charge carriers contributing to the current density
N_{bin}		Oscillators in a certain bin
N_{γ}		Number of photons hitting the electrode surface
$N_{\mathrm{H^+}}$		Number of protons reacting to give hydrogen
N_{tot}		Total number of oscillators
n_1		Refractive index of a first domain
n_2		Refractive index of a second domain
N_{A}	[1/mol]	Avogadro constant
$n_{\mathrm{SiO_2}}$		Amount of silicon oxide
$\hat{n}_{\mathrm{H_2O}}$		Refractive index of the electrolyte
$\hat{n}_{\mathrm{Si}}$		Refractive index of silicon
$\hat{n}_{\mathrm{SiO_2}}$		Refractive index of silicon oxide
P	[s]	Oscillation period
q	[C]	Charge
R	[J/Kmol]	Universal gas constant
R_{cont}	[Ω]	Resistance of the silicon back contact
R_{ext}	[Ω]	Sum of all ohmic resistances
R_{hh}	[Ω]	Resistance of the Helmholtz layer
R_{ox}	[Ω]	Resistance of the oxide layer
R_{sample}	[Ω]	Resistance of the silicon sample
R_{ser}	[Ω]	Series resistance
R_{sol}	[Ω]	Resistance of the electrolyte solution
$\mathbf{R}_x$		Matrix for rotation
$\hat{r}_{\mathrm{p}}$		Parallel component of the reflection coefficient
$\hat{r}_{\mathrm{s}}$		Perpendicular component of the reflection coefficient
$\mathbf{T}_{\hat{r}}$		Jones matrix for reflection
$\mathbf{T}_{\alpha_{\mathrm{A}}}$		Jones matrix for polarization
$\mathbf{T}_{\lambda/4}$		Jones matrix for retardation
t	[s]	Time
t_{max}	[s]	Discrete time instances of the maxima of $\overline{\xi}$
U	[V]	Voltage applied between WE and RE
U_{ccd}	[V]	Voltage of the CCD sensor
U_{fb}	[V]	U at flat-band conditions
U_{ocp}	[V]	U at open-circuit potential
U_{pot}	[V]	Voltage applied between WE and CE
v_{scan}	[mV/s]	Scan rate
W		Complex amplitude in the MCGLE
$\langle W \rangle$		Spatial average of W
W_{r}		Real part of W
Y		Quantum efficiency
z_{L}	[m]	Uniform oxide layer thickness (Mechanism)
$\overline{z}$	[m]	Spatially averaged formed oxide layer thickness
$\overline{z}_{\mathrm{E}}$	[m]	Spatially averaged etched oxide layer thickness
$\left(\dot{\overline{z}}_{\mathrm{E}}\right)_0$	[m/s]	Etch rate at $\Phi_{\mathrm{eff}} = 0$ of the linear fit
$\left(\dot{\overline{z}}_{\mathrm{E}}\right)_{\mathrm{ocp}}$	[m/s]	Initial etch rate during etch back
$\left(\dot{\overline{z}}_{\mathrm{E}}\right)_{\mathrm{osc}}$	[m/s]	Period averaged etch rate during oscillations
$\left(\dot{\overline{z}}_{\mathrm{E}}\right)_{\mathrm{ss}}$	[m/s]	Etch rate during steady states

continued

continued

Symbol	Unit	Explanation
Z_{F}	[Ω]	Faradaic impedance
$\overline{z}_{\mathrm{L}}$	[m]	Spatially averaged oxide layer thickness
α_{i}	[°]	Angle of incidence
α_{t}	[°]	Angle of transmission
α_{A}	[°]	Angle between the transmission axis of the analyzer and the plane of incidence
α_{B}	[°]	Brewster angle
α_{C}	[°]	Angle between the fast axis of the quarter plate and the plane of incidence
α_{P}	[°]	Angle between the transmission axis of the polarizer and the plane of incidence
ϵ		Relative permittivity
ϵ_0	[F/cm]	Vacuum permittivity
η_{H}		Hydrogen evolution efficiency
γ		Global forcing term in the MCGLE
κ	[m/Vs]	Conductivity of the oxide layer
λ_{illu}	[nm]	Typical wavelength of the light used for sample illumination
λ_{imag}	[nm]	Typical wavelength of the light used for sample imaging
ν		Number of charges contributing to the current density per silicon atom
ν_{cap}		Number of captured holes contributing to the current density per silicon atom
ν_{inj}		Number of injected electrons contributing to the current density per silicon atom
ω_0	[Hz]	Frequency of the uniform oscillations in the MCGLE
Φ	[V]	Potential drop
Φ_{B}	[eV]	Energy barrier for the semiconductor charge carriers
Φ_{eff}	[V]	Applied voltage corrected for Φ_{ohm}
Φ_{ext}	[V]	Potential drop across R_{ext}
Φ_{hh}	[V]	Potential drop across the Helmholtz layer in the electrolyte
Φ_{ohm}	[V]	Ohmic potential drop due to R_{ser}
Φ_{ox}	[V]	Potential drop across the oxide layer
Φ_{sc}	[V]	Potential drop across the space charge layer, *i.e.* band bending in the semiconductor
	[V]	
ρ	[g/m]	Density of silicon oxide
ρ_{osc}		Relative frequency density of the phase histogramm
$\Delta\sigma$	[C/m]	Change in charge density from Eq. (4.30)
ξ	[arb.units]	Ellipso-microscopic signal
$\overline{\xi}$	[arb.units]	Spatial average of the ellipso-microscopic signal
ξ_{bg}	[arb.units]	Background ξ of the electrode
ξ_{calc}		Calculated ratio of the light intensity at the camera to the light intensity transmitted by the polarizer
ξ_{cross}	[arb.units]	Time evolution of a cross section of the electrode
$\overline{\xi}_{\mathrm{elec}}$	[arb.units]	Contribution to $\overline{\xi}$ from the electrode
$\overline{\xi}_{\mathrm{elec}}^{\mathrm{ref}}$	[arb.units]	$\overline{\xi}_{\mathrm{elec}}$ of the hydrogen terminated electrode
ξ_{enh}	[arb.units]	Enhanced ellipso-microscopic signal

continued

concluded

Symbol	Unit	Explanation
$\overline{\xi}_J$	[arb.units]	$\overline{\xi}$ calculated from the current density
$\overline{\xi}^{\mathrm{ref}}$	[arb.units]	$\overline{\xi}^{\mathrm{ref}}$ of the hydrogen terminated electrode
$\overline{\xi}_{\mathrm{elec}}$	[arb.units]	Contribution to $\overline{\xi}$ from the electrode surroundings
$\left(\dot{\overline{\xi}}\right)_{\mathrm{init}}$	[arb.units/s]	Initial rate of change of $\overline{\xi}$ during etch back

References

Aggour, M. (**1994**). *Elektrochemische und grenzflächenanalytische Untersuchungen zur Oszillation des Photostroms am Silizium/Elektrolyt-Kontakt.* Ph.D. thesis, Technische Universität Berlin.

Aggour, M., Giersig, M., and Lewerenz, H. J. (**1995**). "Interface condition of n-Si(111) during photocurrent oscillations in NH_4F solutions." *Journal of Electroanalytical Chemistry*, 383(1-2): 67.

Aggour, M., Skorupska, K., Pereira, T. S., Jungblut, H., Grzanna, J., and Lewerenz, H. J. (**2007**). "Photoactive silicon-based nanostructure by self-organized electrochemical processing." *Journal of the Electrochemical Society*, 154(9): H794.

Allen, F. G. and Gobeli, G. W. (**1962**). "Work function, photoelectric threshold, and surface states of atomically clean silicon." *Physical Review*, 127(1): 150.

Arimoto, S., Hasegawa, H., Yamamoto, H., and Ohno, H. (**1988**). "Anodic-oxidation for enhancement of fabrication yield and efficiency of amorphous-silicon solar-cells." *Journal of the Electrochemical Society*, 135(2): 431.

Azzam, R. and Bashara, N. (**1977**). *Ellipsometry and polarized light.* North-Holland, Amsterdam.

Bertram, M. (**2002**). *Controlling turbulence and pattern formation in chemical reactions.* Ph.D. thesis, Technische Universität Berlin.

Bertram, M., Beta, C., Rotermund, H. H., and Ertl, G. (**2003**). "Complex patterns in a periodically forced surface reaction." *Journal of Physical Chemistry B*, 107(35): 9610.

Bertram, M. and Mikhailov, A. S. (**2003**). "Pattern formation on the edge of chaos: Mathematical modeling of CO oxidation on a Pt(110) surface under global delayed feedback." *Physical Review E*, 67(3): 036 207.

Blackwood, D. J., Borazio, A., Greef, R., Peter, L. M., and Stumper, J. (**1992**). "Electrochemical and optical studies of silicon dissolution in ammonium fluoride solutions." *Electrochimica Acta*, 37(5): 889.

Böhm, S., Peter, L. M., Schlichthörl, G., and Greef, R. (**2001**). "Ellipsometric and microwave reflectivity studies of current oscillations during anodic dissolution of p-Si in fluoride solutions." *Journal of Electroanalytical Chemistry*, 500(1-2): 178.

Born, M. and Wolf, E. (**1964**). *Principles of optics: Electromagnetic theory of propagation, interference, and diffraction of light.* Macmillan, New York, 2nd edition.

Carstensen, J., Prange, R., and Föll, H. (**1999**). "A model for current-voltage oscillations at the silicon electrode and comparison with experimental results." *Journal of The Electrochemical Society*, 146(3): 1134.

Carstensen, J., Prange, R., Popkirov, G. S., and Föll, H. (**1998**). "A model for current oscillations in the Si-HF system based on a quantitative analysis of current transients." *Applied Physics a-Materials Science & Processing*, 67(4): 459.

Cattarin, S., Frateur, I., Musiani, M., and Tribollet, B. (**2000**). "Electrodissolution of p-Si in acidic fluoride media - Modeling of the steady state." *Journal of the Electrochemical Society*, 147(9): 3277.

Chazalviel, J. N., da Fonseca, C., and Ozanam, F. (**1998**). "In situ infrared study of the oscillating anodic dissolution of silicon in fluoride electrolytes." *Journal of the Electrochemical Society*, 145(9): 964.

Chazalviel, J. N. and Ozanam, F. (**1992**). "A theory for the resonant response of an electrochemical system - Self-oscillating domains, hidden oscillation, and synchronization impedance." *Journal of the Electrochemical Society*, 139(9): 2501.

Chazalviel, J. N., Ozanam, F., Etman, M., Paolucci, F., Peter, L. M., and Stumper, J. (**1992**). "The p-Si/fluoride interface in the anodic region: Damped and/or sustained oscillations." *Journal of Electroanalytical Chemistry*, 327(1-2): 343.

Conti, M., Meerson, B., Peleg, A., and Sasorov, P. V. (**2002**). "Phase ordering with a global conservation law: Ostwald ripening and coalescence." *Physical Review E*, 65(4): 046 117.

Coullet, P., Lega, J., Houchmanzadeh, B., and Lajzerowicz, J. (**1990**). "Breaking chirality in nonequilibrium systems." *Phys. Rev. Lett.*, 65(11): 1352.

Demierry, P., Etcheberry, A., Rizk, R., Etchegoin, P., and Aucouturier, M. (**1994**). "Defects induced in p-type silicon by photocathodic charging of hydrogen." *Journal of the Electrochemical Society*, 141(6): 1539.

Diggle, J. (**1973**). "Dissolution of oxide phases." In J. Diggle, editor, "Oxides and oxide films," volume 2, page 281. Marcel Dekker, New York.

Eddowes, M. J. (**1990**). "Anodic-dissolution of p-type and n-type silicon - kinetic-study of the chemical mechanism." *Journal of Electroanalytical Chemistry*, 280(2): 297.

Ertl, G. (**1991**). "Oscillatory kinetics and spatio-temporal self-organization in reactions at solid surfaces." *Science*, 254(5039): 1750.

Esteban-Martin, A., Taranenko, V. B., Garcia, J., de Valcarcel, G. J., and Roldan, E. (**2005**). "Controlled observation of a nonequilibrium Ising-Bloch transition in a nonlinear optical cavity." *Physical Review Letters*, 94(22): 223 903.

Foca, E., Carstensen, J., and Föll, H. (**2007**). "Modelling electrochemical current and potential oscillations at the Si electrode." *Journal of Electroanalytical Chemistry*, 603(2): 175.

Föll, H., Carstensen, J., and Foca, E. (**2006**). "Self-induced oscillations in Si and other semiconductors." *International Journal of Materials Research*, 97(7): 1016.

Frigieri, M. (**2007**). *Spatio-temporal pattern formation during the electrooxidation of Si in HF-containing electrolyte.* Master's thesis, Università degli Studi di Modena e Reggio Emilia.

Gellings, P. and Bouwmeester, H., editors (**1997**). *The CRC handbook: of solid state electrochemistry.* CRC, Boca Raton.

Gerischer, H. and Lübke, M. (**1988**). "Electrolytic growth and dissolution of oxide layers on silicon in aqueous solutions of fluorides." *Ber. Bunsenges. Phys. Chem.*, 92: 573.

Grzanna, J., Jungblut, H., and Lewerenz, H. J. (**2000**a). "A model for electrochemical oscillations at the Si vertical bar electrolyte contact Part I. Theoretical development." *Journal of Electroanalytical Chemistry*, 486(2): 181.

Grzanna, J., Jungblut, H., and Lewerenz, H. J. (**2000**b). "A model for electrochemical oscillations at the Si vertical bar electrolyte contact Part II. Simulations and experimental results." *Journal of Electroanalytical Chemistry*, 486(2): 190.

Hasegawa, H., Arimoto, S., Nanjo, J., Yamamoto, H., and Ohno, H. (**1988**). "Anodic-oxidation of hydrogenated amorphous-silicon and properties of oxide." *Journal of the Electrochemical Society*, 135(2): 424.

Hecht, E. (**2002**). *Optics.* Addison Wesley, San Francisco, 4th edition.

Heinrich, A. (**2009**). *Influence of illumination and external resistance on the oscillatory dynamics during the electrochemical oxidation of silicon.* Bachelor's thesis, Technische Universität München.

Hiesgen, R., Aleksandrova, E., Meichsner, G., Wehl, I., Roduner, E., and Friedrich, K. A. (**2009**). "High-resolution imaging of ion conductivity of Nafion membranes with electrochemical atomic force microscopy." *Electrochimica Acta*, 55(2): 423.

Hung, T. F., Wong, H., Cheng, Y. C., and Pun, C. K. (**1991**). "A new design of anodic-oxidation reactor for high-quality gate oxide preparation." *Journal of the Electrochemical Society*, 138(12): 3747.

Jakubowicz, J. (**2003**). "Study of surface morphology of electrochemically etched n-Si (111) electrodes at different anodic potentials." *Cryst. Res. Technol.*, 38(3-5): 313.

Judge, J. S. (**1971**). "Study of dissolution of SiO_2 in acidic fluoride solutions." *Journal of the Electrochemical Society*, 118(11): 1772.

Kim, M. S., Kim, K. K., Kim, S. Y., Kim, Y., Won, Y. H., Choi, Y. I., and Mho, S. I. (**1999**). "In-situ monitoring of anodic oxidation of p-type Si(100) by electrochemical impedance techniques in nonaqueous and aqueous solutions." *Bulletin of the Korean Chemical Society*, 20(9): 1049.

Krischer, K. (**2003**). "Nonlinear dynamics in electrochemical systems." In R. Alkire and D. M. Kolb, editors, "Advances in Electrochemical Science and Engineering," volume 8, page 89. Wiley-VCH, Weinheim.

Kuramoto, Y. (**1984**). *Chemical oscillations, waves and turbulence.* Springer, Berlin.

Landolt, D. (**1987**). "Fundamental aspects of electropolishing." *Electrochimica Acta*, 32(1): 1.

Lehmann, V. (**1996**). "On the origin of electrochemical oscillations at silicon electrodes." *Journal of the Electrochemical Society*, 143(4): 1313.

Lehmann, V. and Föll, H. (**1988**). "Minority-carrier diffusion length mapping in silicon-wafers using a Si-electrolyte-contact." *Journal of the Electrochemical Society*, 135(11): 2831.

Lewerenz, H. J. (**1992**). "Anodic oxides on silicon." *Electrochimica Acta*, 37(5): 847.

Lewerenz, H. J. and Aggour, M. (**1993**). "On the origin of photocurrent oscillation at Si electrodes." *Journal of Electroanalytical Chemistry*, 351(1-2): 159.

Lewerenz, H. J., Jungblut, H., and Rauscher, S. (**2000**). "Surface analysis of the electropolishing layer on Si(111) in ammonium fluoride solution." *Electrochimica Acta*, 45(28): 4615.

Lewerenz, H. J., Skorupska, K., Aggour, M., Stempel, T., and Grzanna, J. (**2009**). "Surface chemistry and electronics of semiconductor-nanosystem junctions I: metal-nanoemitter-based solar cells." *Journal of Solid State Electrochemistry*, 13(2): 185.

Lewerenz, H. J., Stumper, J., Pettenkofer, C., and Greef, R. (**1989**). "Photoelectrochemically synthesized interfacial oxides on silicon - composition and electronic-properties." *Electrochimica Acta*, 34(12): 1729.

Lin, A. L., Bertram, M., Martinez, K., Swinney, H. L., Ardelea, A., and Carey, G. F. (**2000**). "Resonant phase patterns in a reaction-diffusion system." *Physical Review Letters*, 84(18): 4240.

Linke, F. and Merkel, R. (**2005**). "Quantitative ellipsometric microscopy at the glass-water interface." *New Journal of Physics*, 7: 128.

Marts, B., Hagberg, A., Meron, E., and Lin, A. L. (**2006**). "Resonant and nonresonant patterns in forced oscillators." *Chaos*, 16(3).

Matsumura, M. and Morrison, S. R. (**1983**). "Anodic properties of n-Si and n-Ge electrodes in HF solution under illumination and in the dark." *Journal of Electroanalytical Chemistry*, 147(1-2): 157.

Memming, R. (**1964**). "Surface recombination at higher injection levels." *Surface Science*, 1(1): 88.

Memming, R. and Schwandt, G. (**1966**). "Anodic dissolution of silicon in hydrofluoric acid solutions." *Surface Science*, 4(2): 109.

Miethe, I. (**2004**). *Raum-zeitliche Musterbildung bei der anodischen Elektrooxidiation von Silizium in flußsäurehaltigen Elektrolytlösungen.* Diplomarbeit, Freie Universität Berlin.

Morrison, S. (**1980**). *Electrochemistry at semiconductor and oxidized metal electrodes.* Plenum.

Muller, R. (**1991**). "Ellipsometry as an in situ probe for the study of electrode processes." In R. Varma and J. Selman, editors, "Characterization of Electrodes and Electrochemical Processes," The Electrochemical Society. Wiley, New York.

Ozanam, F. and Chazalviel, J. N. (**1993**). "In-situ infrared characterization of the electrochemical dissolution of silicon in a fluoride electrolyte." *Journal of Electron Spectroscopy and Related Phenomena*, 64-5: 395.

Parkhutik, V. (**2001**). "Silicon anodic oxides grown in the oscillatory anodisation regime - kinetics of growth, composition and electrical properties." *Solid-State Electronics*, 45(8): 1451.

Pliskin, W. A. (**1977**). "Comparison of properties of dielectric films deposited by various methods." *Journal of Vacuum Science & Technology*, 14(5): 1064.

Rauscher, S. (**1993**). *Oberflächenumwandlung von kristallinem Silizium in Kontakt mit wässrigen Elektrolyten.* Diplomarbeit, Technische Universität Berlin.

Rauscher, S. (**2000**). *Dynamische Modifizierung von Silizium-Elektrolyt-Grenzflächen und deren oberflächenphysikalische Eigenschaften.* Ph.D. thesis, Brandenburgesche Technische Universität.

Rauscher, S., Dittrich, T., Aggour, M., Rappich, J., Flietner, H., and Lewerenz, H. (**1995**). "Reduced interface state density after photocurrent oscillations and electrochemical hydrogenation of n-Si(111): A surface photovoltage investigation." *Appl. Phys. Lett.*, 66(22): 3018.

Rotermund, H. H., Haas, G., Franz, R. U., Tromp, R. M., and Ertl, G. (**1995**). "Imaging pattern-formation in surface-reactions from ultrahigh-vacuum up to atmospheric pressures." *Science*, 270(5236): 608.

Ruge, I. (**1975**). *Halbleiter-Technologie.* Springer, Berlin.

Schmidt, P. F. and Ashner, J. D. (**1971**). "Tracer investigation of hydroxyls in SiO_2 films on silicon." *Journal of the Electrochemical Society*, 118(2): 325.

Schuster, H. G. (**1988**). *Deterministic chaos: an introduction.* VCH, Weinheim.

Strogatz, S. (**1994**). *Nonlinear dynamics and chaos.* Addison-Wesley Publishing Company, Massachusetts.

Taylor, M., Jolly, M., and Kevrekidis, I. (**1989**). "SCIGMA: stability computations and interactive graphics for invariant manifold analysis." Technical report, Princeton University, Dept. of Chem. Eng.

Turner, D. (**1958**). "Electropolishing silicon in hydrofluoric acid solutions." *Journal of the Electrochemical Society*, 105(7): 402.

Vanag, V. K., Zhabotinsky, A. M., and Epstein, I. R. (**2000**). "Pattern formation in the Belousov-Zhabotinsky reaction with photochemical global feedback." *Journal of Physical Chemistry A*, 104(49): 11 566.

Varela, H., Beta, C., Bonnefont, A., and Krischer, K. (**2005**). "A hierarchy of global coupling induced cluster patterns during the oscillatory H_2 electrooxidation reaction on a Pt ring-electrode." *Physical Chemistry Chemical Physics*, 7(12): 2429.

Yahyaoui, F., Dittrich, T., Aggour, M., Chazalviel, J. N., Ozanam, F., and Rappich, J. (**2003**). "Etch rates of anodic silicon oxides in dilute fluoride solutions." *Journal of the Electrochemical Society*, 150(5): B205.

Yang, L. F., Dolnik, M., Zhabotinsky, A. M., and Epstein, I. R. (**2000**). "Oscillatory clusters in a model of the photosensitive Belousov-Zhabotinsky reaction system with global feedback." *Physical Review E*, 62(5): 6414.

Zhabotinsky, A. M. (**1991**). "A history of chemical oscillations and waves." *Chaos*, 1(4): 379.

Zhang, X. G. (**2001**). *Electrochemistry of silicon and its oxides.* Kluwer Academic.

Zhang, X. G., Collins, S. D., and Smith, R. L. (**1989**). "Porous silicon formation and electropolishing of silicon by anodic polarization in HF solution." *Journal of the Electrochemical Society*, 136(5): 1561.

Publications

Miethe, I., Garcia-Morales, V., and Krischer, K. (**2009**). "Irregular subharmonic cluster patterns in an autonomous photoelectrochemical oscillator." *Phys. Rev. Lett.*, 102(19): 194 101.

Miethe, I., and Krischer, K. (in preparation). "Ellipso-microscopically measured oxide layer during the anodic electrodissolution of p-type silicon"

Miethe, I., and Krischer, K. (in preparation). "Mathematical modeling of the oscillatory anodic electrodissolution of silicon."

Miethe, I., Heinrich, A., Schönleber, K., and Krischer, K. (in preparation). "A new type of current density oscillation during the electrodissolution of n-type silicon."

Acknowledgments

I thank

Katharina Krischer for her marvelous supervision, for providing an excellent scientific environment and for her continual enthusiasm.

Everybody in the Krischer group for many discussions and making working on this thesis an enjoyable experience.

Antoine Bonnefont for his support during the first months.

Vladimir García-Morales for fruitful and intense collaboration.

Matteo Frigieri and Andreas Heinrich for productive cooperation in the laboratory and for their enthusiasm.

Philipp Bauer for years of great cooperation in and outside of the laboratory.

Robert Hölzel for the computer-related teamwork, and for the answers to many theoretical questions.

Jan Siegmeier and Tahmineh Pourrostami for their support and for being outstanding office mates.

Joachim Lewerenz for discussions and the production of semiconductor back contacts.

Markus Haß and Joachim Dörbecker for the intense cooperation during the building of the setup and for their skill in crafting the cell.

Max Glanz, Johannes Schwärzler and Karin Mayet for providing excellent computer facilities and support.

Jacky Mercey for her keen eye and red pen, helping me to improve grammar, spelling and expression.

Tanja Miethe and Henny Riedl for letting me a have a quiet corner in their houses to concentrate on writing.